

DROPLETS,
CAPILLARY INTERACTIONS
AND SELF-ASSEMBLY
FROM THE EQUILIBRIUM SHAPE
OF FLUID-FLUID INTERFACES

G. Soligno

About the cover: Front page, background: sketch of a honeycomb lattice formed by tripole-tripole interacting cubes adsorbed at a fluid-fluid interface. Front page, inset: 3D view and contour plot of the equilibrium shape of the fluid-fluid interface close to a cubic particle with Young's contact angle $\pi/2$ and adsorbed at its equilibrium configuration. Back page, background: sketch of a hexagonal lattice formed by dipole-dipole interacting cubes adsorbed at a fluid-fluid interface. Back page, inset: equilibrium shape of a droplet attached to a rod-like solid particle with non-trivial curvature and with Young's contact angle $\pi/2$.



Utrecht University, the Netherlands, January 2017,

PhD Thesis by Giuseppe Soligno.

Printed by: GVO drukkers & vormgevers B.V.

ISBN: 978-94-6332-124-2

**Droplets, capillary interactions and self-assembly
from the equilibrium shape
of fluid-fluid interfaces**

Druppels, capillaire wisselwerkingen en zelfassemblage
vanuit de evenwichtsvorm
van vloeistof-vloeistofgrensvlakken
(met een samenvatting in het Nederlands)

Proefschrift

ter verkrijging van de graad van doctor aan de Universiteit Utrecht op gezag van de rector magnificus, prof. dr. G.J. van der Zwaan, ingevolge het besluit van het college voor promoties in het openbaar te verdedigen op maandag 23 januari 2017 des middags te 4.15 uur

door

Giuseppe Soligno

geboren op 22 september 1986 te Venosa (Italië)

Promotoren: Prof. dr. R. H. H. G. van Roij
Prof. dr. M. Dijkstra

This thesis was (partly) accomplished with financial support from the Marie Curie Initial Training Network SOMATAI.

CONTENTS

| | Page |
|--|-----------|
| 1 INTRODUCTION | 5 |
| 2 EQUILIBRIUM SHAPE OF FLUID-FLUID INTERFACES | 9 |
| 2.1 INTRODUCTION | 10 |
| 2.2 MEAN CURVATURE OF A SURFACE | 11 |
| 2.3 YOUNG'S LAW AND CONTACT ANGLE | 14 |
| 2.4 YOUNG-LAPLACE EQUATION | 15 |
| 2.5 DERIVATION OF YOUNG-LAPLACE EQUATION AND YOUNG'S LAW BY ENERGY MINIMIZATION | 17 |
| 2.6 ANALYTIC SOLUTIONS OF THE YOUNG-LAPLACE EQUATION . . . | 22 |
| 2.6.1 Shape of a Meniscus Close to a Vertical Wall | 22 |
| 2.6.2 Shape of a 2D Droplet with Negligible Gravity | 25 |
| 2.7 CONCLUSION | 29 |
| 3 LINEARIZED YOUNG-LAPLACE EQUATION | 31 |
| 3.1 INTRODUCTION | 32 |
| 3.2 LINEAR APPROXIMATION | 33 |
| 3.3 MULTIPOLE EXPANSION | 34 |
| 3.4 WETTING OF A VERTICAL CYLINDER | 35 |
| 3.5 YOUNG'S LAW IN THE LINEAR APPROXIMATION | 37 |
| 3.6 FINITE-SIZE EFFECTS | 38 |
| 3.7 AXISYMMETRIC-MENISCUS DIVERGENCES DUE TO INVERSE GRAV- ITY | 40 |
| 3.8 MENISCUS IN A VERTICAL CYLINDRICAL TUBE | 42 |

| | | |
|----------|---|------------|
| 3.9 | CAPILLARY ELASTIC ENERGY BY DISPLACING A PINNED SPHERE | 44 |
| 3.10 | CAPILLARY INTERACTIONS BETWEEN VERTICAL PLATES | 48 |
| 3.11 | 2D-MENISCUS DIVERGENCES DUE TO INVERSE GRAVITY | 52 |
| 3.12 | CONCLUSION | 56 |
| 4 | A NEW NUMERICAL METHOD FOR MINIMUM-ENERGY SURFACES | 59 |
| 4.1 | INTRODUCTION | 60 |
| 4.2 | NUMERICAL METHOD DESCRIPTION | 61 |
| 4.3 | TESTS AND ILLUSTRATIVE RESULTS FOR 2D SYSTEMS | 63 |
| 4.3.1 | Meniscus close to a Vertical Wall | 63 |
| 4.3.2 | Meniscus between Flat and/or Curved Surfaces | 65 |
| 4.3.3 | Capillary Interactions | 67 |
| 4.3.4 | 2D Sessile and Pendant Droplets | 69 |
| 4.4 | TESTS AND ILLUSTRATIVE RESULTS FOR 3D SYSTEMS | 73 |
| 4.4.1 | Test of the Vertical Wall | 74 |
| 4.4.2 | Finite-size Effects | 74 |
| 4.4.3 | Capillary Rise <i>vs</i> Particle Curvature | 77 |
| 4.4.4 | Multipole Expansion | 78 |
| 4.4.5 | Rotation Capillary Forces | 82 |
| 4.5 | EQUILIBRIUM CONFIGURATION OF A SINGLE ADSORBED PARTICLE | 84 |
| 4.5.1 | Heavy Sphere | 85 |
| 4.5.2 | Ellipsoids and Cylinders | 91 |
| 4.6 | CONCLUSION | 94 |
| 4.7 | APPENDIX A | 95 |
| 4.8 | APPENDIX B | 98 |
| 5 | CAPILLARY INTERACTIONS AND SELF-ASSEMBLY OF ADSORBED CUBES | 107 |
| 5.1 | INTRODUCTION | 108 |
| 5.2 | METHOD | 108 |
| 5.3 | SINGLE-ADSORBED CUBE | 110 |
| 5.4 | PAIR INTERACTION | 114 |
| 5.5 | SELF-ASSEMBLY INTO HEXAGONAL AND HONEYCOMB LATTICES . | 116 |
| 5.6 | TEMPERATURE-DENSITY PHASE-DIAGRAM | 122 |
| 5.6.1 | Free Energy of the Fluid Phase | 122 |
| 5.6.2 | Free Energy of the Honeycomb Phase | 124 |
| 5.6.3 | Free energy of the Hexagonal Phase | 125 |
| 5.6.4 | Rotational Energy for Cubes in the Honeycomb and Hexagonal Lattices | 127 |
| 5.6.5 | Common Tangent Construction | 128 |
| 5.6.6 | Temperature-Density Diagram for the x , h and f Phases . | 132 |
| 5.7 | EFFECTS DUE TO TRUNCATION OF THE CUBE SHAPE | 133 |
| 5.8 | CASIMIR-LIKE AND VAN DER WAALS FORCES | 136 |
| 5.9 | CONCLUSION | 138 |

| | | |
|----------|--|------------|
| 6 | WETTING OF DROPLETS ON COMPLEX SUBSTRATES | 139 |
| 6.1 | INTRODUCTION | 140 |
| 6.2 | NUMERICAL METHOD | 140 |
| 6.3 | DROPLETS WETTING NON-TRIVIAALLY-CURVED SOLID PARTICLES | 142 |
| 6.3.1 | Shape of the Solid Particles | 150 |
| 6.3.2 | Energy of a Spherical-cap Droplet | 151 |
| 6.4 | DROPLETS ON HYDROPHILIC ELLIPSOIDAL PATCHES | 152 |
| 6.5 | CONCLUSION | 157 |
| | BIBLIOGRAPHY | 159 |
| | SUMMARY/SAMENVATTING | 165 |
| | ACKNOWLEDGMENTS | 167 |
| | AUTHOR'S PUBLICATIONS | 169 |
| | AUTHOR'S PRESENTATIONS | 171 |
| | ABOUT THE AUTHOR | 173 |

CHAPTER 1

INTRODUCTION

In this thesis we use theoretical and numerical methods to study *Soft Matter* systems where *fluid-fluid interfaces* are involved. The term Soft Matter in general refers to all those fields of science and technology that deal with *soft* materials, i.e. deformable by stimulations with the energy scale of thermal energy at room temperature. The typical characteristic length scale for Soft Matter systems is between a few nanometers and a few millimeters, so quantum effects are negligible in these systems, and classical physics can be used to investigate them. Usually, a Soft Matter system involves at least two different phases, mixed together at a certain length scale (molecular, mesoscopic or macroscopic), and at least one of these phases is *fluid*, i.e. in a liquid or gas state.

In this thesis, more particularly, we consider Soft Matter systems where at least two phases are fluid, and therefore a fluid-fluid interface between these two phases exists. This is actually a very common situation in Soft Matter, and a wide range of examples for this kind of systems can be found e.g. in Ref. [1]. Two different approaches can be used to analyze fluid-fluid interfaces: a *microscopic approach*, i.e. modeling the two fluid phases with density fields, or a *macroscopic approach*, i.e. treating the fluid-fluid interface as a possibly curved 2D surface with zero thickness and which separates the two homogeneous fluid phases. In this thesis, we always follow the second approach. Also, we always study these systems at equilibrium, i.e. following a minimum (free) energy approach, without including fluid-dynamic effects, as not relevant for the experimental equilibrium systems we

intend to model. The key element to investigate the behavior of these systems is the *equilibrium shape* of the fluid-fluid interface. This shape is fixed by the *Young-Laplace Equation*, together with *Young's Law* as a boundary condition. These equations, usually proved through mechanical force-balance arguments, e.g. see Refs. [2–4], can be obtained using a variational principle, e.g. see Refs. [5, 6]. For completeness, in Sec. 2.5 of Chapter 2 we prove this, reporting a compact derivation, partially new to the best of the author's knowledge, in which we minimize the (free) energy of a fluid-fluid-solid system with respect to the fluid-fluid interface shape, and we show that this is equivalent to solving the Young-Laplace Equation and Young's Law.

Typical examples of problems involving fluid-fluid interfaces are those works where fluid droplets are studied, see e.g. Refs. [7–14]. Another very relevant example is given by systems of *colloidal particles*¹ adsorbed at fluid-fluid interfaces. Over a century ago it was already observed that sub-millimeter sized particles strongly adsorb at fluid-fluid interfaces [15, 16], and the bonding potential is usually strong enough to allow stable monolayers of particles [17–19]. Since a pioneering study by Pieranski [20], a lot of interest has been devoted to these quasi-2D systems, which have many applications, e.g. emulsions [21–29], coatings [30, 31], optics [32], and new material development [33]. Because of the contact angle constraint imposed by Young's Law, an adsorbed particle in general induces deformations in the shape of the fluid-fluid interface. These so-called capillary deformations are responsible for capillary interactions between the adsorbed particles [34–41], and therefore they regulate the particle self-assembly at the interface [42–50]. These interactions can be tuned by varying e.g. the particle shape and chemistry [51–54], or the curvature of the fluid-fluid interface [55–60]. A primary step to understand adsorbed-particle systems is the study of an isolated particle at a macroscopically flat fluid-fluid interface. Important issues are the equilibrium configuration of the particle at the interface [61–65] and the adsorption energy [17, 18, 66, 67], which depend on the particle shape and chemical properties. A common approximation (following Pieranski [20]) is to assume the fluid-fluid interface to be flat even when the particle is adsorbed, i.e. to ignore the capillary deformations induced by the particle. In this approximation, which is geometrically far from trivial for non-spherical particles, the (free) energy of the particle configuration follows from the particle surface areas below and above the interface plane, and from the intersection area of the particle with the interface plane. Numerical techniques employed for these calculations are e.g. the Triangular Tessellation method [68–72], and a hit and miss Monte Carlo method [73, 74]. However, we show in this thesis (see Chapter 5 in particular) that neglecting capillary effects can lead to significant overestimates of the energy, and even to erroneous equilibrium configurations for the single-adsorbed particle.

In this thesis, we first provide, in Chapter 2, a theoretical introduction to fluid-

¹The term *colloid*, or colloidal particle, indicates a solid, and possibly soft, particle with size between a nanometer and a millimeter.

fluid interfaces, where we introduce and derive by a variational principle the basic equations that regulate their equilibrium shape, and we show illustrative examples for their application. Then, in Chapter 3, we introduce an approximate theory to analytically solve the Young-Laplace Equation, and we prove with many examples its applicability to a wide range of problems involving fluid-fluid interfaces. The main aim of Chapter 3 is to provide an analytical framework to test and validate our new numerical method for calculating the equilibrium shape of fluid-fluid interfaces by energy minimization. In Chapter 4, which is the core of this thesis, we introduce such a new numerical method, and we provide several illustrative examples to prove the correctness and accuracy of the method for 2D and 3D systems. In particular, with these examples we point out the applicability of the method to study systems of possibly odd-shaped colloidal particles adsorbed at fluid-fluid interfaces, and droplets in contact with solid surfaces, possibly curved and with heterogeneous chemical properties. Finally, in Chapters 5 and 6, we present the most important and innovative results contained in this thesis, obtained through the numerical method introduced in Chapter 4. In particular, in Chapter 5 we show results for the capillary interactions and self-assembly of cubic colloidal particles adsorbed at fluid-fluid interfaces, proving that they self-assemble into thermodynamically-stable honeycomb and hexagonal lattices, as observed experimentally [75, 76]. In Chapter 6, we present results for the equilibrium position of droplets attached to rod-like colloidal particles with non-trivial curvatures, pointing out the fundamental role of the particle geometry, and then results for the equilibrium shape of droplets wetting solid surfaces with heterogeneous chemical properties.

CHAPTER 2

EQUILIBRIUM SHAPE OF FLUID-FLUID INTERFACES

In this Chapter, the concept of a fluid-fluid interface is introduced. The equations that determine its equilibrium shape, i.e. the Young-Laplace Equation and Young's Law, are derived by minimizing the energy of the system with respect to the fluid-fluid interface shape, and the physical implications of such equations are discussed with some examples. Finally, the analytic solution of these equations is calculated in two illustrative problems with a simple geometry: a meniscus close to a vertical wall, and the shape of a 2D droplet in contact with a flat solid surface and in the limit of negligible gravity.

2.1 INTRODUCTION

The main ingredient of this thesis is the interface that separates two immiscible fluids in contact with each other. We study such an interface from a macroscopic point of view, i.e. treating it as a 2D possibly curved surface with null thickness and separating two homogeneous and incompressibleⁱ fluids. Only the equilibrium shape of such interface is considered, i.e. we do not address problems where dynamic effects are involved. However, in principle, quasi-equilibrium dynamics could be extracted from our minimum-energy approach, for example following the approach in Ref. [77]. We neglect capillary waves, i.e. thermal fluctuations of the fluid-fluid interface from its equilibrium profile. Capillary waves can induce Casimir-like forces between particles adsorbed at the fluid-fluid interface [78], but these forces are negligible for the experimental systems of interest, as shown in Section 5.8. When the fluid-fluid interface is in contact with a solid surface, the line tension contribution due to the three-phase contact line is not taken into account, as usually negligible in typical experiments.

Given two fluids, say fluid 1 and fluid 2, if they do not mix (so a fluid-fluid interface separating them forms), it means that the molecules of fluid 1 prefer to interact between themselves rather than with the molecules of fluid 2, and vice versa. At the fluid-fluid interface, however, the molecules of the two fluids are forced to interact with each other, and therefore an energy cost is associated to the formation of the fluid-fluid interface. Given the energy cost E necessary to form a fluid-fluid interface of surface area A , the *surface tension* between fluid 1 and fluid 2 is defined as

$$\gamma \equiv E/A, \quad (2.1)$$

and therefore has the units of an energy over a surface area. This macroscopic parameter γ takes into account the molecular interactions of the two fluids and it is of fundamental importance for the macroscopic description of the fluid-fluid interface. A force interpretation is also possible for the surface tension. From Eq. (2.1) it follows that the work dW to increase the surface area of a fluid-fluid interface by an infinitesimal square of side dx is $dW = \gamma dx^2$. That is, a force of modulus $dF = dW/dx = \gamma dx$ is exerted to move one side of the infinitesimal square by a displacement dx . So $\gamma = dF/dx$ is the (modulus of the) force per unit length necessary to extend the fluid-fluid interface area. The existence of such cohesion forces in fluid-fluid interfaces is the reason why, for example, insects manage to walk on the water surface.

Let Γ be the 2D surface corresponding to the fluid-fluid interface equilibrium shape, and (x, y, z) a generic point belonging to Γ , where a Cartesian coordinate system is introduced with the versor $\hat{\mathbf{z}}$ anti-parallel to the gravity acceleration \mathbf{g} , the so-called *Young-Laplace Equation* states that

$$\nabla \cdot \hat{\mathbf{n}}(x, y, z) = \frac{\Delta P}{\gamma} - \frac{\hat{\mathbf{z}} \cdot (x, y, z)}{\ell^2}, \quad (2.2)$$

ⁱTherefore, the fluid mass density is treated as a constant.

where $\nabla \equiv (\frac{\partial}{\partial x}, \frac{\partial}{\partial y}, \frac{\partial}{\partial z})$, $\hat{\mathbf{n}}(x, y, z)$ is the normal to Γ in (x, y, z) , $\Delta P = P_2 - P_1$ is the difference between the *bulk pressures*ⁱⁱ P_1 and P_2 of the two fluids, and

$$\ell \equiv \sqrt{\frac{\gamma}{g \Delta \rho}} \quad (2.3)$$

is the *capillary length*, with $g = |\mathbf{g}|$, $\Delta \rho \equiv \rho_2 - \rho_1$, and ρ_1, ρ_2 the mass densities of fluid 1 and fluid 2, respectively. The capillary length ℓ sets the length scale for the decay of the fluid-fluid interface deformations due to gravity effects, i.e. due to $\Delta \rho$ (see for example the decay of a meniscus from a vertical wall in Section 2.6.1). If $\ell \rightarrow 0$, then the capillary effects on the system are negligible, and this is the regime $Bo \gg 1$, where the *Bond number* Bo is introduced as $Bo \equiv L^2/\ell^2$, with L a characteristic length of the system. If instead $Bo \leq \mathcal{O}(1)$, then capillarity is relevant, and this is the regime considered in the whole thesis. Often the limit $\ell \rightarrow \infty$ (i.e. $Bo \rightarrow 0$) will be applied, that is when gravity effects on the fluid-fluid interface equilibrium shape become irrelevant. Equation (2.2) will be studied in detail in the rest of the thesis, deriving it by minimizing the energy with respect to the fluid-fluid interface shape, see Section 2.5, and showing analytical and numerical solutions in many different problems.

When the fluid-fluid interface is in contact with a solid surface, the boundary conditions for the interface shape at the three-phase contact points are imposed by Young's Law, as shown in Section 2.3. But first, in the next Section, the concept of surface mean curvature is introduced.

2.2 MEAN CURVATURE OF A SURFACE

Given a curved line in 2D, the *curvature* in a point \mathbf{v} of this curve is $\kappa = \pm 1/R$, where R is the radius of the osculating disc in \mathbf{v} , i.e. the disc that best approximates the curve in a neighborhood of \mathbf{v} (see Fig. 2.1). The sign of κ depends on the parametrization of the curve, i.e. on whether R rotates clockwise or counter-clockwise when moving along the curve in \mathbf{v} . For a curved surface Γ in 3D, the curvature in a point $\mathbf{v} \equiv (x, y, z)$ of Γ can be evaluated for a normal section of Γ , i.e. the intersection of Γ with a plane containing the normal vector $\hat{\mathbf{n}}$ to Γ

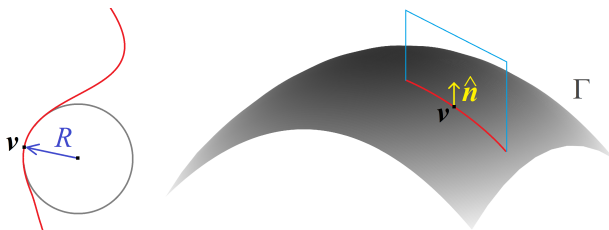


Figure 2.1: (Left) Curvature $\kappa = 1/R$ in the point \mathbf{v} of a curved line in 2D. (Right) Normal section (shown with a red curve) through the point \mathbf{v} of a curved surface Γ in 3D, where $\hat{\mathbf{n}}$ is the normal vector to Γ in \mathbf{v} .

ⁱⁱWith the term *bulk pressure* we refer to the pressure P_i that the fluid i has at the reference level $z = 0$. So, at a height z , the fluid pressure is $P_i - z g \rho_i$, with ρ_i the fluid mass density. If gravity is negligible, then the fluid has pressure P_i everywhere.

in (x, y, z) , see Fig. 2.1. In general, infinite choices for this plane are possible, which result in different values for the curvature. The maximum $\kappa_1 = \pm 1/R_1$ and minimum $\kappa_2 = \pm 1/R_2$ of all the possible values for the curvature in (x, y, z) are called principal curvatures, and R_1, R_2 are the principal radii of curvature. The *mean curvature* H in (x, y, z) is defined as the average of the principal curvatures, that is

$$H(x, y, z) \equiv \frac{\kappa_1(x, y, z) + \kappa_2(x, y, z)}{2}. \quad (2.4)$$

An equivalent definition [79] for the mean curvature H of the surface Γ in the point (x, y, z) is

$$H(x, y, z) = \frac{1}{2} \nabla \cdot \hat{\mathbf{n}}(x, y, z), \quad (2.5)$$

by which the Young-Laplace Equation [Eq. (2.2)] can be rewritten as

$$2H(x, y, z) = \frac{\Delta P}{\gamma} - \frac{\hat{\mathbf{z}} \cdot (x, y, z)}{\ell^2}. \quad (2.6)$$

Note that the mean curvature of a certain surface depends on its shape, but surfaces with different shapes can have the same mean curvature. In Section 2.4 the physical implications of Eq. (2.6) are discussed in more detail. Here we derive some equations for $H(x, y, z)$ which will be useful later on. Just for mathematical simplicity, we assume that Γ can be expressed as a function $h = h(x, y)$, so also $H = H(x, y)$ and $\hat{\mathbf{n}} = \hat{\mathbf{n}}(x, y)$. Then, the normal to the surface $h(x, y)$ can be expressed as

$$\hat{\mathbf{n}}(x, y) = \frac{\nabla[z - h(x, y)]}{|\nabla[z - h(x, y)]|}. \quad (2.7)$$

Using $\nabla[z - h(x, y)] = (-\frac{\partial h}{\partial x}, -\frac{\partial h}{\partial y}, 1)$, from Eq. (2.5) it follows

$$H(x, y) = -\frac{1}{2} \frac{\frac{\partial^2 h}{\partial x^2} \left[1 + \left(\frac{\partial h}{\partial y}\right)^2\right] + \frac{\partial^2 h}{\partial y^2} \left[1 + \left(\frac{\partial h}{\partial x}\right)^2\right] - 2\frac{\partial h}{\partial x} \frac{\partial h}{\partial y} \frac{\partial^2 h}{\partial x \partial y}}{\left[1 + \left(\frac{\partial h}{\partial x}\right)^2 + \left(\frac{\partial h}{\partial y}\right)^2\right]^{\frac{3}{2}}}. \quad (2.8)$$

If the system has translational invariance along the y axis, i.e. $\partial h/\partial y = 0$, then $H = H(x)$, and Eq. (2.8) becomes

$$H(x) = -\frac{1}{2} \frac{\partial^2 h}{\partial x^2} \left[1 + \left(\frac{\partial h}{\partial x}\right)^2\right]^{-\frac{3}{2}}. \quad (2.9)$$

This case corresponds to the limit where one of the principal radii of curvature is infinity. Therefore, for a curved line $h = h(x)$ in 2D, the curvature is given by

$\kappa(x) = 2H(x)$, with $H(x)$ given in Eq. (2.9).

The total surface area of $h(x, y)$ is

$$S[h(x, y)] = \int_D \sqrt{1 + \left(\frac{\partial h}{\partial x}\right)^2 + \left(\frac{\partial h}{\partial y}\right)^2} dx dy, \quad (2.10)$$

with D the domain of $h(x, y)$. The functional derivative of $S[h(x, y)]$ with respect to $h(x, y)$ isⁱⁱⁱ

$$\frac{\delta S[h(x, y)]}{\delta h(x, y)} = 2H(x, y), \quad (2.12)$$

where $H(x, y)$ is expressed by Eq. (2.8).

If $h(x, y)$ is a surface of revolution, i.e. it has rotational invariance around a vertical axis, then it can be written as $h = h(r)$, with $r \equiv \sqrt{x^2 + y^2}$ the distance from such a vertical axis, and Eq. (2.12) assumes a simpler expression. Indeed, using cylindrical coordinates (r, ϕ, z) in Eq. (2.5) and $\hat{\mathbf{n}} = \hat{\mathbf{n}}(r) = \nabla[z - h(r)]/|\nabla[z - h(r)]|$, with $\nabla[z - h(r)] = (-\frac{\partial h}{\partial r}, 0, 1)$, the mean curvature $H = H(r)$ of $h(r)$ results^{iv}

$$H(r) = -\frac{1}{2r} \frac{\partial}{\partial r} \left[\frac{r \frac{\partial h}{\partial r}}{\sqrt{1 + \left(\frac{\partial h}{\partial r}\right)^2}} \right]. \quad (2.13)$$

The surface of $h(r)$ is

$$S[h(r)] = 2\pi \int r \sqrt{1 + \left(\frac{\partial h}{\partial r}\right)^2} dr, \quad (2.14)$$

from which it follows

$$\frac{\delta S[h(r)]}{\delta h(r)} = 4\pi r H(r), \quad (2.15)$$

that is Eq. (2.12) expressed in cylindrical coordinates for a surface of revolution, with $H(r)$ given by Eq. (2.13). Note, from Eq. (2.13), that $H(r)$ can also be written as

$$H(r) = \frac{1}{2} [\kappa_1(r) + \kappa_2(r)], \quad (2.16)$$

ⁱⁱⁱGiven a function $h : \mathbb{R}^N \rightarrow \mathbb{R}$ and a functional $F[h]$ defined as $F[h] = \int d\mathbf{x} f[\mathbf{x}, h(\mathbf{x}), \nabla h(\mathbf{x})]$, with $\mathbf{x} \equiv (x_1, \dots, x_N) \in \mathbb{R}^N$ and $\nabla \equiv (\frac{\partial}{\partial x_1}, \dots, \frac{\partial}{\partial x_N})$, then the functional derivative of F with respect to h is given by

$$\frac{\delta F}{\delta h} = \frac{\partial f}{\partial h} - \nabla \cdot \left[\frac{\partial f}{\partial \left(\frac{\partial h}{\partial x_1}\right)}, \dots, \frac{\partial f}{\partial \left(\frac{\partial h}{\partial x_N}\right)} \right]. \quad (2.11)$$

^{iv}In cylindrical coordinates (r, ϕ, z) , given a function f and a vector field $\mathbf{v} \equiv (v_r, v_\phi, v_z)$, it holds $\nabla f = (\frac{\partial f}{\partial r}, \frac{1}{r} \frac{\partial f}{\partial \phi}, \frac{\partial f}{\partial z})$ and $\nabla \cdot \mathbf{v} = \frac{1}{r} \frac{\partial(r v_r)}{\partial r} + \frac{1}{r} \frac{\partial v_\phi}{\partial \phi} + \frac{\partial v_z}{\partial z}$.

where $\kappa_1(r)$ and $\kappa_2(r)$ are

$$\kappa_1(r) = -\frac{d^2h}{dr^2} \left[1 + \left(\frac{dh}{dr} \right)^2 \right]^{-\frac{3}{2}}, \quad \kappa_2(r) = -\frac{1}{r} \frac{dh}{dr} \sqrt{1 + \left(\frac{dh}{dr} \right)^2}, \quad (2.17)$$

and it can be shown [80] that they are the principal curvatures of $h(r)$. Precisely, $\kappa_1(r)$ is the curvature in a plane containing the vertical axis of symmetry, and $\kappa_2(r)$ is the curvature in a plane orthogonal to the vertical axis of symmetry^v.

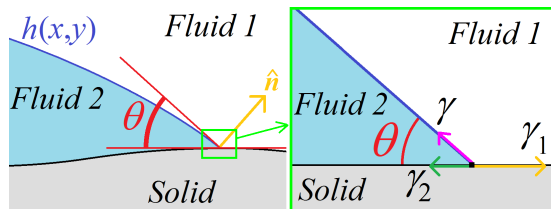
2.3 YOUNG'S LAW AND CONTACT ANGLE

When a fluid-fluid interface is in contact with a solid surface, three surface tensions are involved: the fluid-fluid surface tension γ , and the surface tensions γ_1 and γ_2 of the fluid 1-solid and fluid 2-solid surfaces, respectively. These surface tensions impose at the three-phase contact point a fixed angle θ (called *contact angle* and by convention measured inside fluid 2, see Fig. 2.2) between the tangent to the fluid-fluid interface and the tangent to the solid surface, by *Young's Law*

$$\cos \theta = \frac{\gamma_1 - \gamma_2}{\gamma}. \quad (2.18)$$

Equation (2.18) is valid in the assumption that the solid is undeformable, and that the solid surface, locally at the three-phase contact points, can be considered flat. If instead the solid is deformable, then three different contact angles appear (for example see the limit case of a fluid-fluid-fluid contact point in Section 2.4), but we do not consider this case. In Section 2.5, Young's Law is derived using a minimum-energy principle. However, Eq. (2.18) can also be proved by a simple force-equilibrium argument. Using the force interpretation for the surface tension (see Section 4.1), one realizes that the three-phase contact point must be subjected to three different forces, proportional in modulus to the three surface tensions γ , γ_1 , γ_2 , and with direction tangent to the respective interface (see Fig. 2.2). Then, imposing that the total force acting on the three-phase contact point is zero, as the equilibrium condition requires, trivially leads to Eq. (2.18). Note that Young's Law holds also when gravity is relevant for the system. Indeed the force argument used here applies microscopically at the three-phase contact point, without regard of gravity effects on the fluid-fluid interface shape.

Figure 2.2: Contact angle θ of a fluid-fluid interface with a solid surface, where γ , γ_1 and γ_2 are the fluid-fluid, solid-fluid 1 and solid-fluid 2 surface tensions, respectively. Force balance in the three-phase contact point implies Young's Law [Eq. (2.18)].



^vIndeed $\kappa_2 \rightarrow 0$ in the limit $r \rightarrow \infty$.

2.4 YOUNG-LAPLACE EQUATION

The Young-Laplace Equation [Eq. (2.6)] implies that in any point of a fluid-fluid interface there is a jump $\Delta\Pi$ in the pressure between the two fluids determined by the mean curvature H [Eq. (2.5)] of the interface in that point. Indeed, in hydrostatic equilibrium, any fluid has constant pressure at a constant level z . By definition (see note ii at page 11), the pressures of fluid 1 and fluid 2 at the reference level $z = 0$ are P_1 and P_2 , respectively, such that, at a generic height z , fluid 2 has pressure $P_2^* \equiv P_2 - z g \rho_2$ and fluid 1 has pressure $P_1^* \equiv P_1 - z g \rho_1$. Therefore, across a point (x, y, z) of the fluid-fluid interface there must be a pressure difference given by [see Fig. 2.3(a)]

$$\Delta\Pi(x, y, z) = P_2^* - P_1^* = \Delta P - \hat{\mathbf{z}} \cdot (x, y, z) g \Delta\rho, \quad (2.19)$$

with $\Delta\rho \equiv \rho_2 - \rho_1$ and $\Delta P \equiv P_2 - P_1$. Note that ΔP and z depend on the choice of the reference level $z = 0$, but $\Delta\Pi$ does not, as expected, because it is a physical observable. Using $\ell^{-2} = g \Delta\rho/\gamma$, we can rewrite the Young-Laplace Equation [Eq. (2.6)] as

$$\Delta\Pi(x, y, z) = 2\gamma H(x, y, z), \quad (2.20)$$

which proves that the pressure jump $\Delta\Pi$ across the fluid-fluid interface is determined by the mean curvature of the interface surface. A trivial implication of Eq. (2.20) is that across a flat fluid-fluid interface there is no jump in the pressure, i.e. $\Delta\Pi = 0$, because the mean curvature H of a planar surface is zero.

Note that different surface shapes can have the same mean curvature, therefore Eq. (2.20) alone does not univocally fix the shape of the interface. The solution of

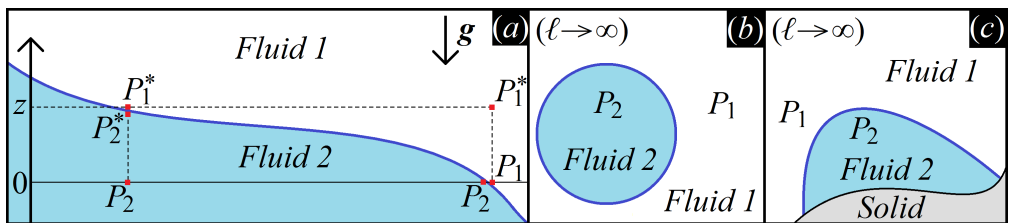


Figure 2.3: (a) For the hydrostatic equilibrium, each fluid has constant pressure at constant heights. We call P_1 and P_2 the pressures at the reference level $z = 0$ of fluid 1 and fluid 2, respectively. At a generic height z , the two fluids have pressures $P_1^* \equiv P_1 - h g \rho_1$ and $P_2^* \equiv P_2 - h g \rho_2$, with ρ_1 and ρ_2 the respective mass densities of the two fluids. Therefore, at the fluid-fluid interface there is a pressure jump $\Delta\Pi = P_2^* - P_1^*$. The Young-Laplace Equation [Eq. (2.6)] relates $\Delta\Pi$ with the mean curvature of the interface. (b) Droplet of fluid 2 inside fluid 1. In the limit of no gravity ($\ell \rightarrow \infty$), the Young-Laplace Equation [Eq. (2.21)] implies a spherical droplet, and that the pressure jump between inside and outside the droplet is fixed by the surface tension γ and the droplet volume V [see Eq. (2.22)]. (c) Sketch of a droplet in contact with a curved solid surface.

the Young-Laplace Equation is unique only if we impose the boundary conditions, given by the fluid volumes and by the Young's contact angle between the fluid-fluid interface and the solid surface. However, given such boundary conditions, typically it is not easy at all, even in problems with very simple geometries, to determine *a priori* the position of the three-phase contact points, i.e. where the fluid-fluid interface touches the given solid surface. For this reason, a much more convenient approach to calculate the equilibrium shape of a fluid-fluid interface is by minimizing the (free) energy of the system with respect to the interface shape. In this way, the solution of the Young-Laplace Equation is obtained, for the given fluid volumes and Young's contact angle of the solid surface, without imposing *a priori* the position of the three-phase contact points (see Section 2.5). A relevant limit is when gravity is negligible, i.e. $\ell \rightarrow \infty$. In this limit, fluid 1 and fluid 2 have, respectively, constant pressure P_1 and P_2 also in the \mathbf{z} direction, and $\Delta\Pi = \Delta P$ everywhere. The Young-Laplace Equation becomes

$$H = \frac{\Delta P}{2\gamma}, \quad (2.21)$$

implying that the mean curvature H of the fluid-fluid interface surface is constant. Therefore, if two fluids are separated by a flat interface, which has null mean curvature, then $\Delta P = 0$. A droplet completely surrounded by another fluid must have a spherical shape [see Fig. 2.3(b)], because this has constant mean curvature^{vi}. The mean curvature of a sphere is $H = 1/R$, with $R = \sqrt[3]{3V/4\pi}$ the sphere radius and V its volume, so Eq. (2.21) implies that the pressure difference ΔP between the inside and the outside of the droplet is given by

$$\Delta P = 2\gamma \sqrt[3]{\frac{4\pi}{3V}}, \quad (2.22)$$

that is ΔP is fixed by γ and the droplet volume V . If the external fluid surrounding a spherical droplet is changed, then in general the surface tension γ changes, so the ΔP between the droplet and the external fluid also changes accordingly to Eq. (2.22), assuming that the volume V of the droplet does not vary (i.e. the fluids are incompressible). Note, however, that the solution of the no-gravity Young-Laplace Equation [Eq. (2.21)] is not necessarily a spherical surface, but just a surface with constant mean curvature. For example, if the droplet is in contact with a curved solid surface, in general it has a non-spherical shape because of the Young's Law boundary conditions [see a sketch in Fig. 2.3(c)]. The ΔP , however, is not affected by the fact that the droplet is completely surrounded by fluid 1 or also in contact with a solid (undeformable) surface. So ΔP can be calculated using Eq. (2.22) also for non-spherical droplets.

^{vi}For symmetry reasons, all the other possible shapes with constant mean curvature are ruled out, because, as gravity is negligible, the system should be invariant by rotating a Cartesian coordinate system with origin in the droplet center of mass. Alternatively, another argument is that the sphere is the closed surface with minimal surface area.

An interesting case is a droplet adsorbed at a flat fluid-fluid interface (say fluid 1 and fluid 2 are the fluid phases forming the flat interface, and fluid 3 is the fluid phase forming the droplet, see Fig. 2.4). Fluid 1 and fluid 2 have the same pressure, as the interface is flat, so the pressure difference inside-outside the droplet is ΔP with both fluid 1 and fluid 2, assuming gravity negligible. However, the surface tension of the droplet with fluid 1 and fluid 2 is different, so, for Eq. (2.21), the droplet spherical curvature has a different radius of curvature in fluid 1 and fluid 2. The resulting shape of the droplet, see Fig. 2.4, is given by two attached spherical caps with the same base and placed, respectively, inside fluid 1 and fluid 2. At the three-phase contact point Young's Law does not hold anymore, because here there are three fluid phases in contact and no solid phase, and three contact angles θ_1 , θ_2 , and θ_3 appear (see Fig. 2.4). Using a force-balance argument for the three-phase contact point, like we did for Young's Law in Section 2.3, it follows that θ_1 , θ_2 , and θ_3 are fixed by the so-called "Neumann triangle" equations

$$\begin{cases} \gamma + \gamma_1 \cos \theta_1 + \gamma_2 \cos \theta_2 = 0, \\ \gamma_1 + \gamma \cos \theta_1 + \gamma_2 \cos \theta_3 = 0, \\ \gamma_2 + \gamma_1 \cos \theta_3 + \gamma \cos \theta_2 = 0. \end{cases} \quad (2.23)$$

where γ is the fluid 1-fluid 2 surface tension, and γ_1 , γ_2 are the surface tensions of the droplet with fluid 1 and fluid 2, respectively. Fluid droplets adsorbed at fluid-fluid interfaces can be considered as the limit case of adsorbed soft (i.e. deformable) solid particles, which are a current active field of research [81–83].

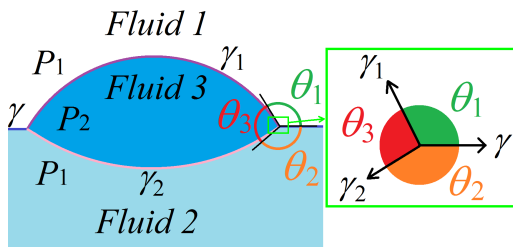


Figure 2.4: For Eq. (2.21), a droplet adsorbed at a flat fluid-fluid interface has a spherical curvature with different radius of curvature above and below the interface. At the three-phase contact point there are three different contact angles, defined by the "Neumann triangle" rule [see Eq. (2.23)].

2.5 DERIVATION OF YOUNG-LAPLACE EQUATION AND YOUNG'S LAW BY ENERGY MINIMIZATION

In this Section we derive the Young-Laplace Equation and Young's Law by minimizing the (free) energy of a fluid-fluid system in contact with a solid at a fixed position. Although such a proof is widely known and accepted (a first version is due to Gauss [84], and more recent versions are shown, e.g., in Refs. [5, 6]), here we present a concise and partially new version for completeness. We consider (see Fig. 2.5) a fixed volume V that contains two demixed fluids, fluid 1 and fluid 2, with fluid 1 lighter than fluid 2. Such volume V is surrounded by

a solid surface with fixed position. We assume the solid to be non-deformable. The volume and mass density are respectively V_1 and ρ_1 for fluid 1, V_2 and ρ_2 for fluid 2, with $V_1 + V_2 = V$. The fluids are in contact with a heat bath that keeps constant the temperature T . We ignore the T dependence from now on, as it is not relevant in our derivation. We introduce a Cartesian coordinate system with the z axis anti-parallel to the gravity acceleration \mathbf{g} . For simplicity we assume that the fluid-fluid interface can be written as a function $h = h(x, y)$, although our derivation can be easily extended for more general surfaces (e.g. with overhangs). The surface area of the solid surface in contact with fluid 1 is $W_1[h]$, and that with fluid 2 is $W_2[h]$, where $[h]$ means a functional dependence with respect to h . The surface tensions associated to the three interfaces fluid 1-fluid 2, solid-fluid 1 and solid-fluid 2 are γ , γ_1 and γ_2 , respectively. We neglect in our analysis the energy contribution due to the three-phase contact line tension, although our derivation can be easily extended to include it. The (free) energy E of this system, hereinafter called energy, is^{vii}

$$E[h] = \gamma S[h] + \gamma_1 W_1[h] + \gamma_2 W_2[h] + E_g[h] + \Omega_1(V_1[h]) + \Omega_2(V_2[h]), \quad (2.24)$$

where $S[h]$ is the surface area of the fluid-fluid interface, $\Omega_1(V_1[h])$ and $\Omega_2(V_2[h])$ are the bulk (free) energies of fluid 1 and fluid 2 respectively, and $E_g[h]$ is the gravitational energy of the system, given by

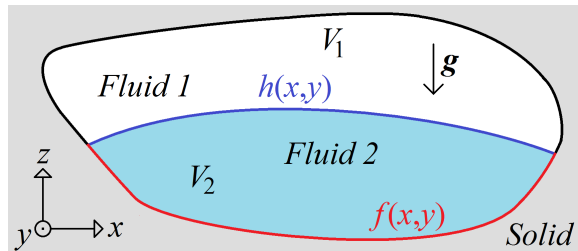
$$E_g[h] = g \rho_1 \int_{V_1[h]} z \, dx \, dy \, dz + g \rho_2 \int_{V_2[h]} z \, dx \, dy \, dz, \quad (2.25)$$

with $g = |\mathbf{g}|$. Note that the integration domains over $V_1[h]$ and $V_2[h]$ are functionals of h .

The total area of the fluid 1-fluid 2 interface is

$$S[h] = \int_D \sqrt{1 + \left(\frac{\partial h}{\partial x}\right)^2 + \left(\frac{\partial h}{\partial y}\right)^2} \, dx \, dy, \quad (2.26)$$

Figure 2.5: Sketch of a fluid-fluid interface. The fluids are bounded by a fixed solid surface. In blue and red are highlighted the fluid 1-fluid 2 and solid-fluid 2 interfaces, which play an important role in the derivation of the Young-Laplace Eq. and Young's Law shown in Section 2.5.



^{vii}In general E depends on the volumes V_1 and V_2 of fluid 1 and fluid 2, respectively, on the solid surface position and on the fluid/fluid, solid/fluid 1 and solid/fluid 2 surface tensions. Here, however, these parameters are considered fixed, so E depends only on the fluid-fluid interface shape h .

where D is the domain of h . The functional derivative of S with respect to h (see Section 2.2) is

$$\frac{\delta S}{\delta h(x, y)} = \nabla \cdot \hat{\mathbf{n}}(x, y), \quad (2.27)$$

where $\hat{\mathbf{n}}(x, y)$ [see Eq. (2.7)] is the unit normal to the surface $h(x, y)$ in the point $[x, y, h(x, y)]$, pointing from fluid 2 toward fluid 1.

We assume now that the solid-fluid 2 interface can be written as a function $f = f(x, y)$. As before, we do this for simplicity, although it is easy to extend the derivation to more general surfaces. Note that f is a functional of h , since f and h are connected at the three-phase contact line. The areas of the solid surfaces in contact with the fluids can be written as

$$W_2[h] = \int_D dx dy \sqrt{1 + \left(\frac{\partial f}{\partial x}\right)^2 + \left(\frac{\partial f}{\partial y}\right)^2}, \quad W_1[h] = W - W_2[h], \quad (2.28)$$

where W is the total surface area of the solid in contact with the fluid-fluid system, and it does not depend on h . Note that the domain of f coincides with that of h . The functional derivative of the solid-fluid surface energy with respect to h is

$$\begin{aligned} \frac{\delta(\gamma_1 W_1 + \gamma_2 W_2)}{\delta h(x, y)} &= \Delta\gamma \int_D du dv \frac{\delta W_2}{\delta f(u, v)} \frac{\delta f(u, v)}{\delta h(x, y)} = \\ &= \Delta\gamma \int_D du dv \nabla \cdot \hat{\mathbf{N}}(u, v) \frac{\delta f(u, v)}{\delta h(x, y)} \equiv \Delta\gamma \Phi(x, y), \end{aligned} \quad (2.29)$$

where we defined the integral as $\Phi(x, y)$ for later convenience, $\Delta\gamma = \gamma_2 - \gamma_1$, and

$$\hat{\mathbf{N}}(x, y) = \frac{\nabla [z - f(x, y)]}{\left| \nabla [z - f(x, y)] \right|} \quad (2.30)$$

is the unit normal to the f surface in $[x, y, f(x, y)]$, pointing from the solid toward fluid 2. The functional derivative $\delta f/\delta h$ is explicitly written as

$$\frac{\delta f(u, v)}{\delta h(x, y)} = \begin{cases} \delta(x - u) \delta(y - v), & \text{if } (x, y) \in \{\mathbf{t}\}, \\ 0, & \text{otherwise,} \end{cases} \quad (2.31)$$

where $\delta(x)$ is the Dirac delta function and $\{\mathbf{t}\}$ is the set of all the points (x, y) where $f(x, y) = h(x, y)$, i.e. such that $[x, y, h(x, y)]$ is a three-phase contact point. Equation (2.25) can be written as

$$E_g[h] = g \rho_1 \int_V z dx dy dz + \frac{g \Delta\rho}{2} \int_D (h^2 - f^2) dx dy \quad (2.32)$$

with $\Delta\rho = \rho_2 - \rho_1$. The functional derivative of E_g with respect to h is

$$\frac{\delta E_g}{\delta h(x, y)} = g \Delta\rho h(x, y). \quad (2.33)$$

Here the $\delta f/\delta h$ term does not appear because its contribution is canceled by the h^2 term.

The bulk (free) energies of fluid 1 and fluid 2 can be written as^{viii}

$$\Omega_1(V_1) + \Omega_2(V_2) = -P_1 V_1[h] - P_2 V_2[h] , \quad (2.34)$$

where P_1 and P_2 are the bulk pressures of fluids 1 and 2, i.e. their pressures at the reference level $z = 0$. Using that

$$V_1[h] = V - V_2[h] \quad , \quad V_2[h] = \int_D dx dy (h - f) , \quad (2.35)$$

we find that

$$\frac{\delta[\Omega_1(V_1) + \Omega_2(V_2)]}{\delta h(x, y)} = -\Delta P , \quad (2.36)$$

with $\Delta P = P_2 - P_1$. The term $\delta f/\delta h$ does not appear here because its contribution is canceled by the h term.

Finally, we use the minimum energy principle to state that the functional derivative with respect to h of the energy E [Eq. (2.24)] is zero at equilibrium, that is

$$\frac{\delta E[h]}{\delta h(x, y)} = 0 . \quad (2.37)$$

Using Eqs. (2.27), (2.29), (2.33), (2.36) we obtain from Eq. (2.37) that

$$\gamma \nabla \cdot \hat{\mathbf{n}}(x, y) + \Delta \gamma \Phi(x, y) + g \Delta \rho h(x, y) - \Delta P = 0 , \quad (2.38)$$

with $\Phi(x, y)$ defined in Eq. (2.29). First we consider this equation for all the $(x, y) \notin \{\mathbf{t}\}$, i.e. where the fluid-fluid interface is not in contact with the solid surface. Here $\Phi(x, y) = 0$, so it follows

$$\gamma \nabla \cdot \hat{\mathbf{n}}(x, y) = \Delta P - g \Delta \rho h(x, y) , \quad (2.39)$$

which is the Young-Laplace Equation introduced in Eq. (2.2).

To derive Young's Law, we take Eq. (2.38) for any $(x, y) \in \{\mathbf{t}\}$, i.e. in a three-phase contact point, obtaining

$$\gamma \nabla \cdot \hat{\mathbf{n}}(x, y) + \Delta \gamma \nabla \cdot \hat{\mathbf{N}}(x, y) = \Delta P - g \Delta \rho h(x, y) . \quad (2.40)$$

We now consider an infinitesimal volume dV located inside fluid 2 and in contact with the three-phase contact line. The volume dV is delimited at one face by the fluid 1-fluid 2 interface, at another face by the fluid 2-solid interface, and at the remaining three faces by planes orthogonal to the fluid 2-solid interface (see Fig. 2.6). We take dV small enough to assume $h(x, y)$ and $f(x, y)$ to be linear, and

^{viii}We are considering homogeneous and incompressible fluids, at fixed temperature and volume.

integrate Eq. (2.40) over dV . The right-hand side of Eq. (2.40) is constant over dV , so its integration gives zero contribution in the limit $dV \rightarrow 0$. Hence we find

$$\int_{dV} \nabla \cdot \left[\hat{\mathbf{n}}(x, y) + \frac{\Delta\gamma}{\gamma} \hat{\mathbf{N}}(x, y) \right] d\mathbf{r} = 0, \quad (2.41)$$

which, upon applying the divergence theorem, yields

$$\mathbf{w}(x, y) \cdot \left[\hat{\mathbf{n}}(x, y) + \frac{\Delta\gamma}{\gamma} \hat{\mathbf{N}}(x, y) \right] = 0, \quad (2.42)$$

where

$$\mathbf{w}(x, y) \equiv \hat{\mathbf{n}}(x, y) dS - \hat{\mathbf{N}}(x, y) dW + \hat{\mathbf{a}} dH + \hat{\mathbf{b}} dA + \hat{\mathbf{c}} dA, \quad (2.43)$$

with $\hat{\mathbf{n}}$, $-\hat{\mathbf{N}}$, $\hat{\mathbf{a}}$, $\hat{\mathbf{b}}$ and $\hat{\mathbf{c}}$ the normals towards outside of the various faces of dV (see Fig. 2.6). The areas of these faces are, respectively, dS , dW , dH , dA and dA . By definition of dV , we have $\hat{\mathbf{n}} \cdot \hat{\mathbf{b}} = \hat{\mathbf{n}} \cdot \hat{\mathbf{c}} = \hat{\mathbf{N}} \cdot \hat{\mathbf{a}} = \hat{\mathbf{N}} \cdot \hat{\mathbf{b}} = \hat{\mathbf{N}} \cdot \hat{\mathbf{c}} = 0$. We call θ the angle formed by the fluid 1-fluid 2 interface with the solid-fluid interfaces, and measured inside fluid 2 (so inside dV). Therefore $\hat{\mathbf{n}} \cdot \hat{\mathbf{a}} = -\sin\theta$, $\hat{\mathbf{n}} \cdot \hat{\mathbf{N}} = \cos\theta$. Then, by definition of the normal, $\hat{\mathbf{n}} \cdot \hat{\mathbf{n}} = \hat{\mathbf{N}} \cdot \hat{\mathbf{N}} = 1$, and hence from Eq. (2.42) it follows that

$$\frac{\Delta\gamma}{\gamma} = \frac{\cos\theta dW + \sin\theta dH - dS}{\cos\theta dS - dW}. \quad (2.44)$$

If we use now that $dH = \sin\theta dS$, we obtain Young's Law [Eq. (2.18)].

We have thus proven that minimizing the energy E of a fluid-fluid-solid system [Eq. (2.24)] with respect to the fluid-fluid interface shape is equivalent to solving simultaneously the Young-Laplace Eq. and Young's Law.

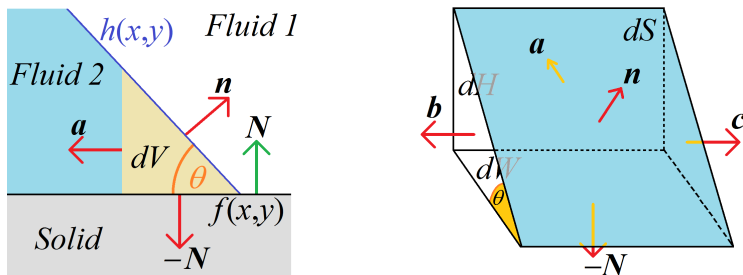


Figure 2.6: Profile and 3D view of the infinitesimal volume dV on which we integrate Eq. (2.40). We chose dV small enough to consider $h(x, y)$ and $f(x, y)$ linear within it. One face of dV is the fluid 1-fluid 2 interface (colored in blue in the picture on the right), and it has normal $\hat{\mathbf{n}}$ and area dS . Another face of dV is the solid-fluid 2 interface, with normal $-\hat{\mathbf{N}}$ and area dW . The remaining three faces of dV are orthogonal to the solid-fluid 2 interface, and have respectively normal $\hat{\mathbf{a}}$, $\hat{\mathbf{b}}$ and $\hat{\mathbf{c}}$ and area dH , dA and dA .

2.6 ANALYTIC SOLUTIONS OF THE YOUNG-LAPLACE EQUATION

In this Section, we study simple-geometry problems where the Young-Laplace Equation can be solved analytically, to illustrate with practical applications the concepts introduced in this Chapter.

2.6.1 SHAPE OF A MENISCUS CLOSE TO A VERTICAL WALL

Here we calculate the equilibrium shape of a fluid-fluid interface, i.e. the *meniscus*, close to a vertical wall. Far from the vertical wall the meniscus is assumed to be flat. First, the energy of the system is minimized with respect to the meniscus height profile, obtaining as a result the 2D Young-Laplace Equation, with Young's Law as boundary condition. Then, such differential equation is explicitly solved, and an analytical expression for the height profile of the meniscus is obtained.

Given a Cartesian coordinate system (x, y, z) , with the z direction anti-parallel to the gravity acceleration \mathbf{g} , a solid vertical surface coinciding with the plane $x = 0$ is introduced. The two coexisting fluids are in the half space $x > 0$, with the fluid-fluid interface described by the height profile $z = h(x, y)$, the fluid 1 placed at $z > h(x, y)$, and the fluid 2 placed at $z < h(x, y)$. The system has translational invariance in the y direction, so $h = h(x)$. Note that gravity cannot be neglected in this problem, otherwise the meniscus could not be infinitely extended for $x \rightarrow \infty$. With γ the fluid-fluid surface tension, and γ_1, γ_2 the surface tensions of the solid with fluid 1 and fluid 2, respectively, the energy E [Eq. (2.24)] of the system is

$$E[h] = \gamma S[h] + \gamma_1 W_1[h] + \gamma_2 W_2[h] + E_g[h], \quad (2.45)$$

where the $-P_1 V_1[h], -P_2 V_2[h]$ terms can be neglected, because we impose a flat meniscus far from the vertical wall, so $P_1 = P_2$ and therefore their sum does not depend on $h(x)$.

With ξ_y the length of the system in the y direction, the wetting energy contribution can be written as

$$\gamma_1 W_1[h] + \gamma_2 W_2[h] = (\gamma_2 - \gamma_1) \xi_y \int_{-\infty}^{+\infty} h \delta(x) dx + C \quad (2.46)$$

with C a constant not depending on $h(x)$, and $\delta(x)$ the Dirac delta function. The fluid-fluid surface energy contribution is

$$\gamma S[h] = \gamma \xi_y \int_{-\infty}^{+\infty} \Theta(x) \sqrt{1 + \left(\frac{\partial h}{\partial x}\right)^2} dx, \quad (2.47)$$

where $\Theta(x)$ is the step function, defined by

$$\Theta(x) \equiv \begin{cases} 0, & \text{if } x < 0, \\ 1, & \text{if } x \geq 0. \end{cases} \quad (2.48)$$

The gravitational energy contribution is

$$E_g[h] = \frac{\gamma \xi_y}{2 \ell^2} \int_{-\infty}^{+\infty} \Theta(x) h^2 dx, \quad (2.49)$$

with ℓ the capillary length [Eq. (2.3)].

The equilibrium height profile of the meniscus has minimum energy $E[h]$ [Eq. (2.45)], from which $\delta E[h]/\delta h = 0$. Therefore, see note iii at page 13, it follows

$$\delta(x) \frac{\gamma_2 - \gamma_1}{\gamma} - \frac{\partial}{\partial x} \left[\Theta(x) \frac{\partial \left(\sqrt{1 + \left(\frac{\partial h}{\partial x} \right)^2} \right)}{\partial \left(\frac{\partial h}{\partial x} \right)} \right] + \frac{\Theta(x) h}{\ell^2} = 0 \quad (2.50)$$

Integrating Eq. (2.50) between $x = 0^-$ and $x = 0^+$ gives

$$\frac{\gamma_2 - \gamma_1}{\gamma} - \frac{\frac{\partial h}{\partial x} \Big|_{0^+}}{\sqrt{1 + \left(\frac{\partial h}{\partial x} \Big|_{0^+} \right)^2}} = 0, \quad (2.51)$$

where the integral over the gravitational term gives a negligible contribution. Introducing, in Eq. (2.51), a new parameter θ by the relation $\cos \theta \equiv (\gamma_1 - \gamma_2)/\gamma$, we obtain

$$\cos \theta \sqrt{1 + \left(\frac{\partial h}{\partial x} \Big|_{0^+} \right)^2} = - \frac{\partial h}{\partial x} \Big|_{0^+} \quad (2.52)$$

$$\Rightarrow \left(\frac{\partial h}{\partial x} \Big|_{0^+} \right)^2 = \frac{1}{\tan^2 \theta} \Rightarrow \frac{\partial h}{\partial x} \Big|_{0^+} = - \frac{1}{\tan \theta}, \quad (2.53)$$

and Eq. (2.53)^{ix} proves that such parameter θ is actually the contact angle formed by the height profile $h(x)$ of the meniscus with the vertical wall (see Fig. 2.7). Therefore, we have proved Young's Law [Eq. (2.18)] for a meniscus close to the

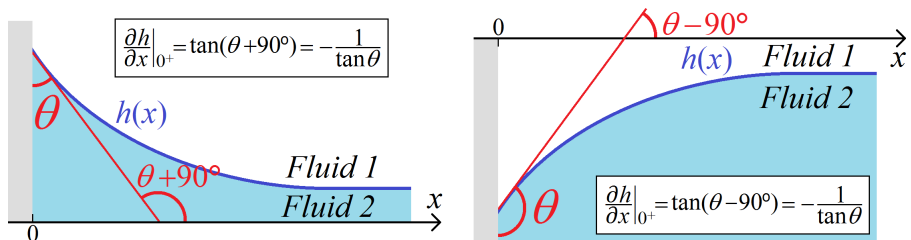


Figure 2.7: Relation between the derivate of the meniscus height profile $h(x)$ in 0^+ and its contact angle θ with the vertical wall.

^{ix}In Eq. (2.53) the solution with the plus sign that comes out after taking the square root has been discarded, because, from Eq. (2.52), the sign of $\frac{\partial h}{\partial x} \Big|_{0^+}$ is opposite to the sign of $\cos \theta$, which has the same sign of $\tan \theta$, as $\theta \in [0, \pi]$.

vertical wall using energy minimization.

To calculate the profile $h(x)$, we consider Eq. (2.50) for $x > 0$, keeping Eq. (2.53) as a boundary condition for $x \rightarrow 0^+$, obtaining

$$\frac{h}{\ell^2} - \frac{\partial^2 h}{\partial x^2} \left[1 + \left(\frac{\partial h}{\partial x} \right)^2 \right]^{-\frac{3}{2}} = 0, \quad (2.54)$$

which is the Young-Laplace Equation [Eq. (2.6)] for $\Delta P = 0$ and $H(x)$ given by Eq. (2.9). Multiplying Eq. (2.54) by $\partial h / \partial x$ and integrating in x , it follows

$$\frac{h^2}{2\ell^2} + \left[1 + \left(\frac{\partial h}{\partial x} \right)^2 \right]^{-\frac{1}{2}} = C', \quad (2.55)$$

where the integration constant is $C' = 1$, because in $x \rightarrow \infty$ we impose the boundary conditions

$$h(+\infty) \rightarrow 0, \quad \left. \frac{\partial h}{\partial x} \right|_{+\infty} \rightarrow 0. \quad (2.56)$$

Then, evaluating Eq. (2.55) in $x \rightarrow 0^+$ and using Young's Law boundary condition, i.e. Eq. (2.53), we obtain

$$h^2(0^+) = 2\ell^2 (1 - \sin \theta). \quad (2.57)$$

From Eqs. (2.54) and (2.55) it follows that, if it exists an $x_0 \in [0^+, +\infty]$ such that $h(x_0) = 0$ or $\partial h(x_0) / \partial x = 0$ or $\partial^2 h(x_0) / \partial x^2 = 0$, then $h(x_0) = \partial h(x_0) / \partial x = \partial^2 h(x_0) / \partial x^2 = 0$. Consequently, either $h(x) = 0$ for any x , or $h(x) \neq 0$ for any x . So, if $h(0^+) > 0$, then $h(x) > 0$ for any x , and so $\partial h / \partial x < 0$ for any x , because h has to decrease to zero at infinity [see Eq. (2.56)] and h cannot have local minima, i.e. $\partial h / \partial x = 0$, otherwise h would be zero everywhere. Using an analogous argument for the case $h(0^+) < 0$, we deduce, finally, that h and $\partial h / \partial x$ must have opposite and constant sign for any x . Exploiting this property together with Eq. (2.53), we can now take the square root of Eq. (2.57) and extract $h_0 \equiv h(0^+)$ with the correct sign choice, that is

$$h_0 = \begin{cases} +\sqrt{2\ell^2 (1 - \sin \theta)}, & \text{if } 0 \leq \theta \leq \pi/2, \\ -\sqrt{2\ell^2 (1 - \sin \theta)}, & \text{if } \pi/2 \leq \theta \leq \pi. \end{cases} \quad (2.58)$$

To calculate $h(x)$, we rewrite Eq. (2.55) as

$$\frac{[2\ell^2 - h^2]^2}{\ell^2 h^2 (4\ell^2 - h^2)} \left(\frac{\partial h}{\partial x} \right)^2 = \frac{1}{\ell^2} \Rightarrow \frac{h^2 - 2\ell^2}{h\sqrt{4\ell^2 - h^2}} \frac{\partial h}{\partial x} = 1, \quad (2.59)$$

where the sign choice, after taking the square root, assures that h and $\partial h/\partial x$ have opposite signs^x. Integrating Eq. (2.59) with respect to x , we obtain^{xi}

$$\operatorname{acosh}\left(\frac{2\ell}{|h|}\right) - \sqrt{4 - \frac{h^2}{\ell^2}} + C''' = \frac{x}{\ell}. \quad (2.61)$$

By evaluating Eq. (2.61) in $x \rightarrow 0^+$, the integration constant C''' is

$$C''' = \sqrt{4 - \frac{(h_0)^2}{\ell^2}} - \operatorname{acosh}\left(\frac{2\ell}{|h_0|}\right). \quad (2.62)$$

In conclusion, the height profile $h(x)$ of a meniscus near the vertical wall, with x the distance from the wall, is given by the following analytic expression where x is expressed with respect to $|h|$

$$\frac{x(|h|)}{\ell} = \operatorname{acosh}\left(\frac{2\ell}{|h|}\right) - \operatorname{acosh}\left(\frac{2\ell}{|h_0|}\right) - \sqrt{4 - \frac{h^2}{\ell^2}} + \sqrt{4 - \frac{(h_0)^2}{\ell^2}}. \quad (2.63)$$

Here h_0 is given by Eq.(2.58). The input parameters fixing $h(x)$ are θ and ℓ . If $0 \leq \theta \leq \pi/2$, then $h_0 \geq 0$ and $0 \leq h(x) \leq h_0$. If $\pi/2 \leq \theta \leq \pi$, then $h_0 \leq 0$ and $h_0 \leq h(x) \leq 0$. Plots of $h(x/\ell)/\ell$ are shown in Fig. 2.8 for several values of θ .

2.6.2 SHAPE OF A 2D DROPLET WITH NEGLIGIBLE GRAVITY

When gravity is negligible, a droplet has (see Section 2.4) a spherical shape if completely surrounded by another fluid, while it has in general a different shape when in contact with a solid surface, because of Young's Law boundary conditions. However, if the solid surface in contact with the droplet is flat, then the droplet keeps a spherical curvature, because a spherical cap shape that satisfies Young's Law with the flat solid surface and that has the droplet volume can always be found. In this Section, for illustrative purposes, we prove this analytically for a 2D droplet^{xii}, by minimizing the energy with respect to the droplet shape and then solving the 2D Young-Laplace Equation.

A Cartesian coordinate system (x, z) is introduced in our 2D space, with the solid surface in $z = 0$ and the 2D droplet on top of it (see Fig. 2.9). We take the z axis passing through the droplet center of mass, and we consider the droplet for $x \geq 0$, assuming the system symmetric for $x \rightarrow -x$. For convenience, we study

^xNote that $[h(x)]^2 - 2\ell^2 \leq 0$ for any x , because $|h(x)| \leq |h_0|$ for any x , with $|h_0|$ given by Eq. (2.58).

^{xi}Note that $\operatorname{acosh}(h) \equiv \ln(h + \sqrt{h^2 - 1})$ and

$$\frac{1}{\ell} \int \frac{h^2 - 2\ell^2}{h\sqrt{4\ell^2 - h^2}} dh = \ln\left[\frac{2\ell}{|h|} + \sqrt{\frac{4\ell^2}{h^2} - 1}\right] - \sqrt{4 - \frac{h^2}{\ell^2}} + C'''. \quad (2.60)$$

^{xii}Which corresponds to a 3D system with translational invariance.

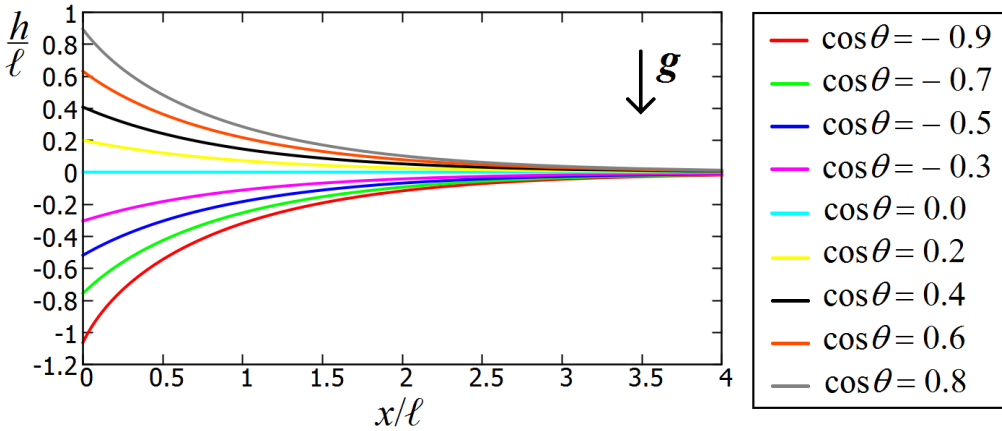


Figure 2.8: Equilibrium shape, as obtained from Eqs. (2.58) and (2.63), of a meniscus close to a vertical wall in $x = 0$, for several values of Young's contact angle θ . The capillary length [Eq. (2.3)] is ℓ , and \mathbf{g} is the gravity acceleration.

the profile $x(z)$ of the droplet (see Fig. 2.9). The surface tension of the solid surface with the droplet and with the external fluid is γ_2 and γ_1 , respectively, and γ is the surface tension of the droplet with the external fluid. The energy of our 2D system expressed as a functional of $x(z)$ is [see Eq. (2.24)]

$$E[x] = E_S[x] + E_W[x] - V[x] \Delta P, \quad (2.64)$$

where the gravitational energy term is neglected as we assume $\ell \rightarrow \infty$,

$$E_S[x] = \gamma \int_{-\infty}^{\infty} \Theta(z) \Theta(h_0 - z) \sqrt{1 + \left(\frac{dx}{dz}\right)^2} dz \quad (2.65)$$

is the energy contribution due to the droplet surface in contact with the external fluid, with $\Theta(z)$ the step function [see Eq. (2.48)], and h_0 the height of the droplet on the z axis, such that $x(h_0) = 0$ (see Fig. 2.9),

$$E_W[x] = (\gamma_2 - \gamma_1) \int_{-\infty}^{+\infty} \delta(z) x dz + C \quad (2.66)$$

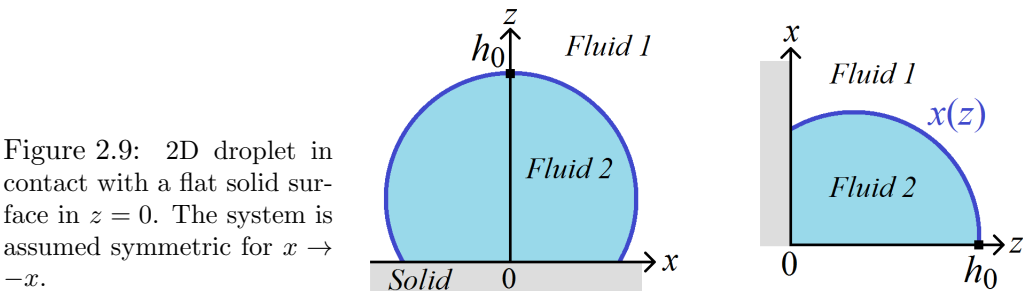


Figure 2.9: 2D droplet in contact with a flat solid surface in $z = 0$. The system is assumed symmetric for $x \rightarrow -x$.

is the wetting energy contribution due to the solid surface, with C a constant and $\delta(z)$ the Dirac delta function, and

$$V[x] = \int_{-\infty}^{+\infty} \Theta(z) \Theta(h_0 - z) x dz \quad (2.67)$$

is the volume of the 2D droplet. At the equilibrium, $\delta E[x]/\delta x = 0$, from which, see note iii at page 13, for $0 \leq z \leq h_0$ it follows

$$\delta(z) \frac{\gamma_2 - \gamma_1}{\gamma} - \frac{d}{dz} \left[\Theta(z) \Theta(h_0 - z) \frac{d \left(\sqrt{1 + \left(\frac{dx}{dz} \right)^2} \right)}{d \left(\frac{dx}{dz} \right)} \right] - \frac{\Delta P}{\gamma} = 0. \quad (2.68)$$

By integrating Eq. (2.68) in z between 0^- and 0^+ , we obtain

$$\frac{\gamma_2 - \gamma_1}{\gamma} - \frac{\frac{dx}{dz} \Big|_{0^+}}{\sqrt{1 + \left(\frac{dx}{dz} \Big|_{0^+} \right)^2}} = 0, \quad (2.69)$$

where the ΔP term gives a negligible contribution. Introducing in Eq. (2.69) the parameter θ by the relation $\cos \theta \equiv (\gamma_1 - \gamma_2)/\gamma$, we obtain, proceeding analogously to the calculations in Eqs. (2.52) and (2.53), that

$$\frac{dx}{dz} \Big|_{0^+} = -\frac{1}{\tan \theta}, \quad (2.70)$$

which proves^{xiii} Young's Law [Eq. (2.18)], i.e. that such a parameter θ is actually the droplet contact angle, see Fig. 2.10. To calculate $x(z)$, we consider Eq. (2.68) for $0 < z \leq h_0$, and keep Eq. (2.70) as boundary condition in $z \rightarrow 0^+$, obtaining

$$-\frac{d^2 x}{dz^2} \left[1 + \left(\frac{dx}{dz} \right)^2 \right]^{-\frac{3}{2}} = \frac{\Delta P}{\gamma}, \quad (2.71)$$

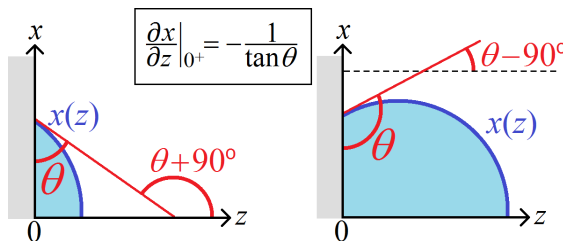


Figure 2.10: Relation between the derivative of the 2D droplet profile $x(z)$ in $z = 0^+$ and the droplet contact angle θ , where the droplet is in contact with a flat surface in $z = 0$.

^{xiii}Note that the same result would have held even if we had included the gravitational energy in Eq. (2.64), because its contribution is negligible when integrating Eq. (2.68) in z between 0^- and 0^+ .

which is, as expected, the no-gravity Young Laplace Equation [Eq. (2.21)] in 2D, so with h_0 expressed by Eq. (2.9). By multiplying Eq. (2.71) by dx/dz and integrating in z , it follows

$$-\frac{1}{\sqrt{1 + \left(\frac{dx}{dz}\right)^2}} = -\frac{\Delta P}{\gamma} x + C. \quad (2.72)$$

We impose the boundary conditions $x(h_0) = 0$, by definition of this system, and

$$\left.\frac{dx}{dz}\right|_{h_0} = \infty, \quad (2.73)$$

because the system is symmetric for $x \rightarrow -x$, and d^2x/dz^2 cannot change sign [from Eq. (2.71)], i.e. the droplet profile cannot form cusps. Therefore, evaluating Eq. (2.72) in h_0 gives $C = 0$. Then, considering Eq. (2.72) for $z \rightarrow 0^+$ and using Eq. (2.70), we obtain:

$$x_0 = R \sin \theta, \quad (2.74)$$

with $x_0 \equiv x(0^+)$ and $R \equiv \gamma/\Delta P$. We rewrite Eq. (2.72) as

$$\frac{(x/R)^2}{1 - (x/R)^2} \left(\frac{dx}{dz}\right)^2 = 1 \quad \Rightarrow \quad \frac{x/R}{\sqrt{1 - (x/R)^2}} \frac{dx}{dz} = s, \quad (2.75)$$

where

$$s = \begin{cases} -1, & \text{if } 0 \leq \theta \leq \pi/2, \\ +1, & \text{if } \pi/2 \leq \theta \leq \pi, \end{cases} \quad (2.76)$$

as implied by Eqs. (2.70) and (2.74). By integrating Eq. (2.75) in z , it follows

$$-R\sqrt{1 - (x/R)^2} = sz + C' \quad (2.77)$$

Calculating Eq. (2.77) for $z \rightarrow 0^+$ and using Eq. (2.74), we obtain $C' = -R \cos \theta$. Then, by squaring both members in Eq. (2.77) and rearranging the terms, it follows

$$x^2 + (z - sR \cos \theta)^2 = R^2, \quad (2.78)$$

which is the equation of a circumference with center in $(x_c, z_c) = (0, sR \cos \theta)$ and radius R , see Figure 2.11. The mean curvature is $H = (2R)^{-1}$, because for a 2D system the other principal radius of curvature is ∞ , so, as we defined $R \equiv \gamma/\Delta P$, it follows $H = \Delta P/(2\gamma)$, as expected from Eq. (2.21). Our 2D droplet is the circular segment in the half-plane $z \geq 0$, so its volume^{xiv} is

$$V = \frac{\theta - \sin \theta \cos \theta}{\Delta P^2} \gamma^2. \quad (2.79)$$

^{xiv}The area of a circular segment is $R^2(\theta - \sin \theta \cos \theta)$, with R the curvature radius and θ the contact angle between the arc and the chord of the circular segment (see Fig. 2.11).

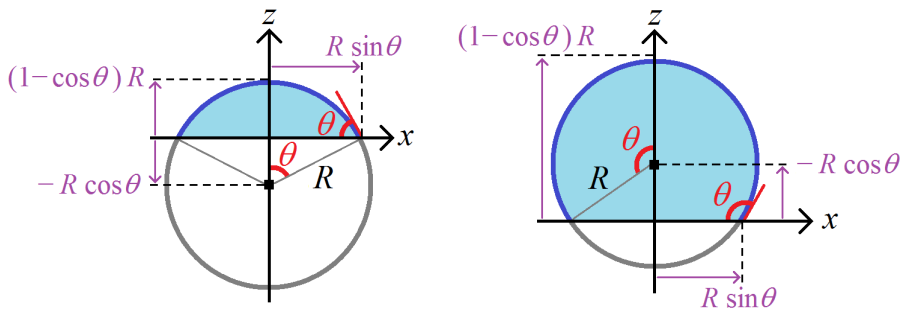


Figure 2.11: Analytic solution [Eq. (2.78)] for the shape of a 2D droplet in the half-plane $z \geq 0$ and in contact with a flat solid surface in $z = 0$, as obtained, in the limit of no gravity, by minimizing the energy E of the system [Eq. (2.64)] and then solving the Young-Laplace Equation [Eq. (2.71)] and Young's Law [Eq. (2.70)]. The Young's contact angle is (left) $\theta \leq \pi/2$ and (right) $\theta \geq \pi/2$. The droplet radius of curvature is $R = \gamma/\Delta P$ and the droplet volume V is given in Eq. (2.79).

2.7 CONCLUSION

In this Chapter, we discussed the relevant equations which determine the equilibrium shape of fluid-fluid interfaces, i.e. the *Young-Laplace Equation* and *Young's Law*. In Section 4.1, we gave an overview of the model we use for fluid-fluid interfaces. Then, we introduced the Young-Laplace Equation and the macroscopic parameters involved in it, i.e. the *surface tension*, the fluid *bulk pressure* difference, and the *capillary length*. In Section 2.2, we discussed the concept of *mean curvature* of a surface, in relation to the Young-Laplace Equation, deriving some relevant expressions. In Section 2.3, the *Young's contact angle* is introduced, and an equation for it, i.e. Young's Law, is derived by a force-balance argument. In Section 2.4, we showed that, across any point of the fluid-fluid interface, a jump in the pressure proportional to the mean curvature of the interface in that point must occur. Then, in the same Section, we discussed the Young-Laplace Equation in the limit of negligible gravity, considering the case of a droplet when completely surrounded by an external fluid, and when adsorbed at the interface between two different fluids. In Section 2.5, we derived the Young-Laplace Equation and Young's Law by minimizing the energy of a fluid-fluid-solid system with respect to the fluid-fluid interface shape, for fixed fluid volumes and solid surface position. Finally, in Sections 2.6.1 and 2.6.2, we considered two illustrative problems with a simple geometry, a meniscus close to a vertical wall and a 2D droplet with negligible gravity and wetting a solid flat surface, and for these we derived, by energy minimization, and then solved analytically the Young-Laplace Equation and Young's Law.

CHAPTER 3

LINEARIZED YOUNG-LAPLACE EQUATION

In this Chapter, we consider the linear approximation of the Young-Laplace Equation, which holds in the limit of small deformations of the fluid-fluid interface shape. To show the applicability of this approximated theory for a wide range of problems involving fluid-fluid interfaces, we present illustrative results for studying a multipole capillary deformation of an adsorbed particle, the wetting of a vertical cylinder, the shape of a meniscus in a vertical cylindrical tube, the force necessary to deform a flat interface by displacing an adsorbed pinned particle orthogonally to the interface, and the capillary force between two vertical plates at an interface. Finally, as main goal of this Chapter, we provide an analytical framework which is exploited in the next Chapter to compare and test the correctness of our numerical results for the equilibrium shape of a fluid-fluid interface.

3.1 INTRODUCTION

In our model, we treat the fluids macroscopically, i.e. as a continuum, and the fluid-fluid interface separating them as a curved surface with zero thickness. In the previous Chapter we introduced the Young-Laplace Equation [Eq. (2.2)], which determines the equilibrium shape of a fluid-fluid interface. The boundary conditions of the fluid-fluid interface at the three-phase contact points, i.e. where the fluid-fluid interface is in contact with solid surfaces, are given by Young's Law [Eq. (2.18)], which fixes the contact angle of the fluid-fluid interface with the solid surface. Solving this Dirichlet problem analytically is usually very complicated, and feasible only in problems with very trivial geometries (see for example Secs. 2.6.1 and 2.6.2, where a meniscus close to a vertical wall and a 2D droplet in absence of gravity and wetting a flat solid surface are considered). Such an analytical difficulty is driven mainly by two reasons: the free boundary problem that arises at the three-phase contact points, whose position is in principle unknown, and the non-linearity of the partial differential equation for the meniscus height profile. In this Chapter we deal with the latter problem by applying the linear approximation to the Young-Laplace Equation, i.e. by neglecting the non-linear terms. We will show that, thanks to this approximation valid in the limit of small deformations of the fluid-fluid interface shape, the linearized Young-Laplace Equation can be easily applied in a much wider range of problems than by considering its exact form. However, note that the main purpose of this Chapter is to introduce an analytical framework which will be exploited to test and validate the correctness of the new numerical method we present in Chapter 4, where the equilibrium shape of a fluid-fluid interface is computed by energy minimization. As we will show, both the difficulties mentioned before are solved in this new numerical method, as the equilibrium position of the three-phase contact line is automatically found by minimizing the energy, and the computed shape of the fluid-fluid interface corresponds to the solution of the exact Young-Laplace Equation. Then, the most interesting and original results of this Thesis will be presented in Chapters 5 and 6, where, using our new numerical method, we predict the equilibrium configuration, capillary interactions and self-assembly of cubic particles adsorbed at fluid-fluid interfaces, and the equilibrium shape of 3D droplets in contact with complex substrates.

In Sec. 3.2, the linearized form of the Young-Laplace Equation is introduced. In Secs. 3.3-3.8, we apply such an equation to study problems with different boundary conditions, obtaining analytical results for the equilibrium shape of the fluid-fluid interface which will be exploited in Chapter 4 to verify our numerical results. Once the equilibrium shape of the fluid-fluid interface is known analytically, with respect to the position of the solid surfaces in the problem, then the capillary force acting on such solid surfaces can also be extracted analytically, and we will show some examples in Secs. 3.9-3.11, mainly for illustrative purpose. In particular, in Sec. 3.9 we compute the capillary force necessary to

displace an adsorbed sphere, pinned at a fluid-fluid interface, in the direction orthogonal to the interface plane. In Ref. [85] experimental results are shown for the case of a sliding three-phase contact line. Here, to stick to the illustrative purpose of these calculations, we assume for simplicity that the three-phase contact line remains fixed on the particle surface during its displacement. Finally, in Secs. 3.10 and 3.11, we present for completeness the 2D linearized Young-Laplace Equation, and we apply it to study the capillary interaction between two vertical walls immersed in a fluid-fluid interface. Other similar applications of the linearized Young-Laplace Equation can be found e.g. in Refs. [86–91], where the capillary force between particles adsorbed at a fluid-fluid interface and with a given pinned three-phase contact line is analytically computed from the meniscus shape. However, note that in these works the position of the three-phase contact line is required as an input parameter. This limits the applicability of such a theory for studying adsorbed particles at fluid-fluid interfaces, equilibrium shapes of droplets in contact with complex substrates, and other similar free boundary problems, which instead can be easily treated by our new numerical method, as we will show in Chapters 4, 5, and 6.

3.2 LINEAR APPROXIMATION

In this Section we introduce the *linear approximation* of the Young-Laplace Equation, valid when the fluid-fluid interface shape is weakly curved. Given a Cartesian coordinate system with z anti-parallel to the gravity acceleration \mathbf{g} , and assuming that the fluid-fluid interface equilibrium shape can be expressed as an height profile $h(x, y)$, the Young-Laplace Equation [Eq. (2.2)] can be written as

$$2H(x, y) = \frac{\Delta P}{\gamma} - \frac{h(x, y)}{\ell^2}, \quad (3.1)$$

where $H(x, y)$, given in Eq. (2.8), is the mean curvature of $h(x, y)$. We remind that (for details see Chapter 2) γ is the fluid-fluid surface tension, ΔP is $P_2 - P_1$, with P_1 , P_2 the bulk pressures of, respectively, fluid 1 (the lightest fluid, and above the interface with respect to z) and fluid 2 (the heaviest fluid, and below the interface with respect to z), and ℓ is the capillary length [Eq. (2.3)].

We consider now the linear approximation, that is

$$\left(\frac{\partial h}{\partial x}\right)^2 \simeq \left(\frac{\partial h}{\partial y}\right)^2 \simeq \frac{\partial h}{\partial x} \frac{\partial h}{\partial y} \ll 1. \quad (3.2)$$

Applying this, Eq. (3.1) becomes

$$\nabla^2 h = \frac{h}{\ell^2} - \frac{\Delta P}{\gamma}. \quad (3.3)$$

that is the *linearized Young-Laplace Equation*.

3.3 MULTIPOLE EXPANSION

Here we apply the linearized Young-Laplace Equation [Eq. (3.3)] to an isolated adsorbed particle at a fluid-fluid interface. The fluid-fluid interface is flat and coincides with the plane $z = 0$ when there is no particle, so $\Delta P = 0$. For convenience, we use the cylindrical coordinate (r, ϕ, z) , with $r \equiv \sqrt{x^2 + y^2}$, ϕ the azimuthal angle, and the z -axis anti-parallel to the gravity and passing through the particle center of mass. So, the fluid-fluid interface height profile is $h = h(r, \phi)$, and Eq. (3.3) becomesⁱ

$$r^2 \frac{\partial^2 h}{\partial r^2} + r \frac{\partial h}{\partial r} + \frac{\partial^2 h}{\partial \phi^2} - r^2 \frac{h}{\ell^2} = 0. \quad (3.4)$$

Assuming we can use variable separation, i.e. that

$$h(r, \phi) = \Psi(r) \Phi(\phi), \quad (3.5)$$

we can rewrite Eq. (3.4) as

$$\frac{r^2}{\Psi} \frac{\partial^2 \Psi}{\partial r^2} + \frac{r}{\Psi} \frac{\partial \Psi}{\partial r} - \frac{r^2}{\ell^2} = -\frac{1}{\Phi} \frac{\partial^2 \Phi}{\partial \phi^2}. \quad (3.6)$$

The two members in Eq. (3.6) depend on different variables, therefore they must be equal to the same constant, that is

$$\pm m^2 = -\frac{1}{\Phi} \frac{\partial^2 \Phi}{\partial \phi^2}, \quad (3.7)$$

$$\pm m^2 = \frac{r^2}{\Psi} \frac{\partial^2 \Psi}{\partial r^2} + \frac{r}{\Psi} \frac{\partial \Psi}{\partial r} - \frac{r^2}{\ell^2}, \quad (3.8)$$

with $m \in \mathbb{R}$. From Eq. (3.7), the case $-m^2$ can be excluded, becauseⁱⁱ a periodic solution for $\Phi(\phi)$ is required, as $\Phi(\phi + 2\pi) = \Phi(\phi)$. The solution of

$$-\frac{1}{\Phi} \frac{\partial^2 \Phi}{\partial \phi^2} = +m^2, \quad (3.9)$$

for a given m , is

$$\Phi_m(\phi) = C_m \cos(m\phi - B_m) \quad (3.10)$$

where B_m, C_m are integration constants. The periodicity condition $\Phi(\phi + 2\pi) = \Phi(\phi)$ imposes that $m \in \mathbb{N}$.ⁱⁱⁱ Therefore, considering in Eq. (3.8) the case $+m^2$ and $m \in \mathbb{N}$, we obtain

$$r^2 \frac{\partial^2 \Psi}{\partial r^2} + r \frac{\partial \Psi}{\partial r} - \left(\frac{r^2}{\ell^2} + m^2 \right) \Psi = 0, \quad (3.11)$$

ⁱIn polar coordinates (r, ϕ) , given a function $f(r, \phi)$, it holds $\nabla^2 f = \frac{\partial^2 f}{\partial r^2} + \frac{1}{r} \frac{\partial f}{\partial r} + \frac{1}{r^2} \frac{\partial^2 f}{\partial \phi^2}$.

ⁱⁱThe solution of $(-1/\Phi)(\partial^2 \Phi/\partial \phi^2) = -m^2$ is $\Phi(\phi) = A e^{\phi/m} + B e^{-\phi/m}$, which is not periodic.

ⁱⁱⁱIndeed $\cos(m\phi + B) = \cos[m(\phi + 2\pi) + B]$ only if $m \in \mathbb{N}$.

which is the *modified Bessel equation of order m* ,^{iv} and its solution for a given m is

$$\Psi_m(r) = D_m I_m(r/\ell) + E_m K_m(r/\ell) \quad (3.12)$$

where I_m and K_m are the *modified Bessel functions* of the first and second kind respectively, and D_m, E_m are integration constants. So, the solution of Eq. (3.6) for a given $m \in \mathbb{N}$ is $h(r, \phi) = \Psi_m(r) \Phi_m(\phi)$. As any $m \in \mathbb{N}$ holds, the general solution of Eq. (3.6) is a linear combination of all these, that is

$$h(r, \phi) = \sum_{m=0}^{\infty} [D_m I_m(r/\ell) + E_m K_m(r/\ell)] C_m \cos(m\phi - B_m). \quad (3.13)$$

As the fluid-fluid interface is flat for $r \rightarrow \infty$, we impose the boundary condition $h(r \rightarrow \infty, \phi) = 0$, implying $D_m = 0$ for any m , because $I_m(r \rightarrow \infty) = \infty$.

In conclusion, defining $A_m \equiv C_m E_m$ in Eq. (3.13), the fluid-fluid interface equilibrium shape $h(r, \phi)$ around an adsorbed particle, using the linear approximation [Eq. (3.2)], is

$$h(r, \phi) = A_0 K_0(r/\ell) + \sum_{m=1}^{\infty} A_m K_m(r/\ell) \cos(m\phi - B_m). \quad (3.14)$$

The integration constants A_m and B_m , for any $m \in \mathbb{N}$, are to be determined by the boundary conditions on the particle surface. In analogy with the electromagnetism, Eq. (3.14) is often referred to as *multipole expansion* of the fluid-fluid interface height profile, with the $m = 0, m = 1, m = 2, m = 3$, etc. terms being, respectively, the *monopole, dipole, quadrupole, hexapole*, etcetera. Note, however, that for adsorbed particles at fluid-fluid interfaces opposite charges repel each other and equal charges attract each other, oppositely to electric charges. This phenomenon, which induces capillary interactions between adsorbed particles, will be discussed in details in Chapter 5, where in particular we will present results for hexapolar interactions between adsorbed cubes.

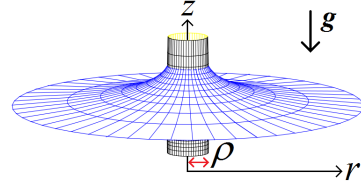
In Chapter 4, Sec. 4.4.4, we present results for an adsorbed sphere with a pinned undulated three-phase contact line that generates capillary deformations given by Eq. (3.14), and we compare these analytical results with the numerical predictions obtained by the method introduced in Chapter 4.

3.4 WETTING OF A VERTICAL CYLINDER

We consider here the same system of the previous section, i.e. a particle adsorbed at a flat fluid-fluid interface, but assuming that the height profile of the fluid-fluid

^{iv}The modified Bessel equation of order m is $x^2 \frac{d^2 f}{dx^2} + x \frac{df}{dx} - (a^2 x^2 + m^2) f = 0$, with $x > 0$, and its solution is given by $f = A \cdot I_m(x/a) + B \cdot K_m(x/a)$, with I_m and K_m the m -th order modified Bessel function of the first and second kind, respectively. The ordinary Bessel equation, instead, is $x^2 \frac{d^2 f}{dx^2} + x \frac{df}{dx} + (a^2 x^2 + m^2) f = 0$, with $x > 0$, and has solution $f = A \cdot J_m(x/a) + B \cdot Y_m(x/a)$, with J_m and Y_m the m -th order Bessel function of the first and second kind, respectively.

Figure 3.1: Sketch of an infinitely-high vertical solid cylinder (black grid), with radius ρ , in contact with a fluid-fluid interface (blue grid) with height profile $h(r)$, where r is the distance from the cylinder symmetry axis. The gravity is in the direction opposite to z .



interface deformations induced by the particle is invariant with respect to ϕ , i.e. $h = h(r)$. Therefore, Eq. (3.4) becomes

$$\frac{d^2 h}{dr^2} + \frac{1}{r} \frac{dh}{dr} - \frac{h}{\ell^2} = 0, \quad (3.15)$$

which is the modified Bessel equation of order zero. The solution of Eq. (3.15) is

$$h = A \cdot I_0(r/\ell) + B \cdot K_0(r/\ell), \quad (3.16)$$

where I_0 and K_0 are the 0-th order modified Bessel functions of the first and second kind respectively. As the interface is flat for $r \rightarrow \infty$, and $I_0(r \rightarrow \infty) = \infty$, we impose the boundary condition $A = 0$.

We assume now that the adsorbed particle is a solid cylinder in vertical position and infinitely high, with symmetry axis coinciding with the z axis, and with radius ρ (see Fig. 4.11). The integration constant B can be evaluated using Young's Law as a boundary condition on the cylinder surface. By geometrical consideration, we would impose for $h(r)$ the condition $dh/dr|_{r=\rho} = -1/\tan \theta$, in analogy to Eq. (2.53) for the height profile of a meniscus close to a vertical wall, see Fig. 2.7. However, as we are using the linear approximation for $h(r)$ [Eq. (3.2)], also Young's Law holds in an approximated form, that is

$$\left. \frac{dh}{dr} \right|_{\rho} = -\cos \theta. \quad (3.17)$$

This is proved in Section 3.5, using energy minimization. Applying Eq. (3.17) to Eq. (3.16), it follows

$$B \left. \frac{dK_0(r/\ell)}{dr} \right|_{r=\rho} = -\cos \theta. \quad (3.18)$$

Using that $dK_0(ax)/dx = -a K_1(ax)$, we obtain

$$B = \frac{\cos \theta}{K_1(\rho/\ell)} \ell. \quad (3.19)$$

Therefore, the solution $h(r)$ of Eq. (3.15) is given by

$$\frac{h}{\ell} = \frac{K_0(r/\ell)}{K_1(\rho/\ell)} \cos \theta. \quad (3.20)$$

Calculating Eq. (3.20) in $r = \rho$, and defining $h_0 \equiv h(\rho)$, we obtain

$$\frac{h_0}{\ell} = \frac{K_0(\rho/\ell)}{K_1(\rho/\ell)} \cos \theta. \quad (3.21)$$

In Fig. 4.13 of Chapter 4, the analytic behavior of h_0/ℓ [Eq. (3.21)] is shown with respect to ρ/ℓ , for $\cos \theta = 0.9$ and several values of ρ , and compared with the numerical results from the method introduced in Chapter 4.

3.5 YOUNG'S LAW IN THE LINEAR APPROXIMATION

Considering the same system of the previous section, see Fig. 4.11, we show here that the linear approximation for $h(r)$ [Eq. (3.2)] implies that Young's Law holds in the approximated form given in Eq. (3.17).

The energy E [Eq. (2.24)] of our fluid-fluid-cylinder system is

$$\begin{aligned} E[h(r)] = & \frac{\pi \gamma}{\ell^2} \int_0^{+\infty} \Theta(r - \rho) r h^2 dr - 2\pi \gamma \cos \theta \int_0^{+\infty} r h \delta(r - \rho) dr + \\ & + 2\pi \gamma \int_0^{+\infty} \Theta(r - \rho) r \sqrt{1 + \left(\frac{dh}{dr}\right)^2} dr, \end{aligned} \quad (3.22)$$

where the terms are, respectively, the fluid-fluid interface gravitational energy, the solid-fluid wetting energy, and the fluid-fluid surface energy, with γ the fluid-fluid surface tension, ℓ the capillary length, $\delta(x)$ the Dirac delta, $\Theta(x)$ given by Eq. (2.48), and $\cos \theta$ given by Eq. (2.18). At the equilibrium $\delta E/\delta h = 0$, from which (see note iii at page 13) it follows

$$\Theta(r - \rho) \frac{r h}{\ell^2} - r \delta(r - \rho) \cos \theta - \frac{d}{dr} \left[\frac{r \Theta(r - \rho) \frac{dh}{dr}}{\sqrt{1 + \left(\frac{dh}{dr}\right)^2}} \right] = 0. \quad (3.23)$$

Integrating Eq. (3.23) with respect to r between ρ^- and ρ^+ gives

$$\cos \theta \sqrt{1 + \left(\frac{dh}{dr}\bigg|_{\rho^+}\right)^2} = - \frac{dh}{dr}\bigg|_{\rho^+}, \quad (3.24)$$

which is an analogous equation to Eq. (2.52) for the meniscus close to the vertical wall, so it would imply for $h(r)$ that $dh/dr|_{r=\rho} = -1/\tan \theta$, in analogy to Eq. (2.53). However, as we are using the linear approximation [Eq. (3.2)], then Eq. (3.24) implies (3.17), that is Young's Law in the linear approximation.

3.6 FINITE-SIZE EFFECTS

In this Section we study the effects of having a finite-size system, rather than a fluid-fluid interface infinitely extended and flat far from the center. For this purpose, we consider the system described in Sec. 3.4, i.e. a vertical cylinder adsorbed at a fluid-fluid interface, but now we introduce a cylindrical vertical wall, with radius R , contact angle α , and with the same symmetry axis of the solid vertical cylinder, that externally surrounds the fluid-fluid interface, see Fig. 3.2. Therefore, we cannot impose $\Delta P = 0$ like in the previous Sections^v, so, from the linearized Young-Laplace Equation [Eq. (3.3)], for an axisymmetric system it follows that

$$\frac{d^2 h}{dr^2} + \frac{1}{r} \frac{dh}{dr} - \frac{h + C}{\ell^2} = 0 \quad , \quad \text{with} \quad C \equiv -\frac{\Delta P}{\gamma} \ell^2 . \quad (3.25)$$

which is the more general version of Eq. (3.15) for non-zero ΔP , and its solution is^{vi}

$$h(r) = A I_0(r/\ell) + B K_0(r/\ell) - C . \quad (3.26)$$

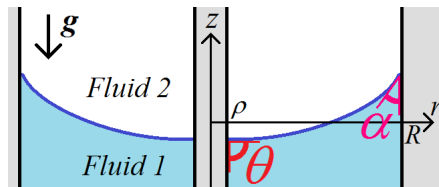
Here we cannot set $A = 0$, like in Sec. 3.4, because the system is extended only until $r = R$. The linearized Young's Law [Eq. (3.17)] in $r = R$ gives

$$\left. \frac{dh(r)}{dr} \right|_R = A \left. \frac{dI_0(r/\ell)}{dr} \right|_R + B \left. \frac{dK_0(r/\ell)}{dr} \right|_R = \cos \alpha . \quad (3.27)$$

Note that in Eq. (3.27) the sign of $\cos \alpha$ is opposite than the sign of $\cos \theta$ in Eq. (3.17), because here the derivative of $h(r)$ is taken on the inner side of the wall with respect to r . The other boundary condition is given by the linearized Young's Law [Eq. (3.17)] in $r = \rho$, that is

$$\left. \frac{dh(r)}{dr} \right|_\rho = A \left. \frac{dI_0(r/\ell)}{dr} \right|_\rho + B \left. \frac{dK_0(r/\ell)}{dr} \right|_\rho = -\cos \theta , \quad (3.28)$$

Figure 3.2: Sketch of a meniscus in a vertical cylindrical tube with radius R and Young's contact angle α , with a vertical solid cylinder of radius ρ and Young's contact angle θ placed in the center. The system is axisymmetric with respect to the z axis.



^vNote that imposing $\Delta P = 0$ for an infinitely-extended system with a flat fluid-fluid interface far from the center is equivalent to fix the volume of the two fluids such that $h(r \rightarrow \infty) = 0$.

^{vi}Note that, if a function h^* is solution of a differential equation with the form $F[d^2h/dx^2, dh/dx] + ah = 0$, with F generic functional, then $h^* - C$ is solution of the differential equation $F[d^2h/dx^2, dh/dx] + a(h + C) = 0$, with C a constant.

with θ the Young's contact angle of the solid cylinder. Using $dK_0(ax)/dx = -aK_1(ax)$ and $dI_0(ax)/dx = aI_1(ax)$, from Eqs. (3.27) and (3.28) we obtain

$$\frac{A}{\ell} = \frac{K_1(\rho/\ell) \cos \alpha + K_1(R/\ell) \cos \theta}{I_1(R/\ell) K_1(\rho/\ell) - I_1(\rho/\ell) K_1(R/\ell)}, \quad (3.29)$$

$$\frac{B}{\ell} = \frac{I_1(\rho/\ell) \cos \alpha + I_1(R/\ell) \cos \theta}{I_1(R/\ell) K_1(\rho/\ell) - I_1(\rho/\ell) K_1(R/\ell)}. \quad (3.30)$$

If $R \rightarrow \infty$, using $K_1(\infty) = 0$ and $I_1(\infty) = \infty$, we correctly obtain $A = 0$ and that Eq. (3.30) reduces to Eq. (3.19), as found in Sec. 3.4.

The integration constant C is to be determined by setting the volume of the fluids. We impose the fluid volumes such that, if the fluid-fluid interface is flat, it corresponds with the plane $z = 0$, that is

$$2\pi \int_{\rho}^R h(r) r dr = 0, \quad (3.31)$$

from which we obtain^{vii}

$$C = 2\ell^2 \frac{R \cos \alpha + \rho \cos \theta}{R^2 - \rho^2}. \quad (3.32)$$

Some illustrative results of the height profile $h(r)$, as obtained by Eq. (3.26), with A, B, C given by, respectively, Eq. (3.29), (3.30), (3.32), are plotted in Fig. 3.3, for $\rho = 0.1\ell$, $R = 2\ell$ and various Young's contact angles α and θ . In the limit case of $\cos \alpha = \cos \theta$, Eq. (3.32) becomes

$$C = 2\ell^2 \frac{\cos \alpha}{R - \rho}. \quad (3.33)$$

Note that C can also be interpreted as the capillary rise of the meniscus^{viii} inside the vertical cylindrical tube, of radius R and Young's contact angle $\cos \alpha$, with a solid vertical cylinder in its center (i.e. with the same symmetry axis) of radius ρ and Young's contact angle $\cos \theta$. As a matter of fact, if $\rho = 0$, i.e. no vertical cylinder in present inside the vertical cylindrical tube, then Eqs. (3.32) and (3.33) reduce to Jurin's Law [92], as discussed in Sec. 3.8.

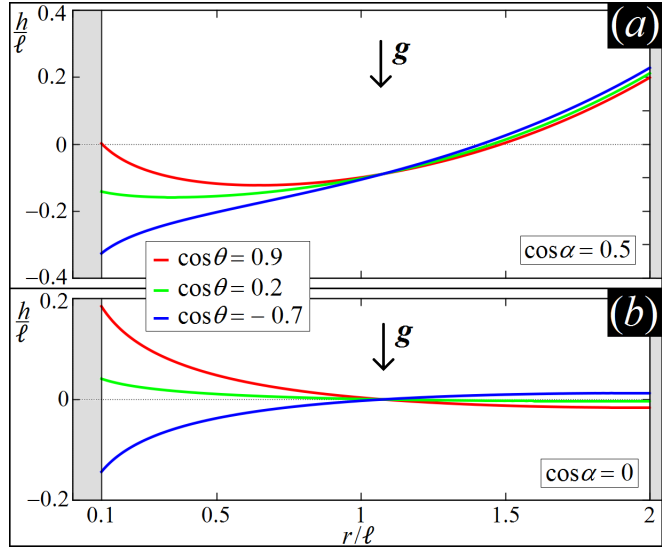
Applying Eq. (3.26) in $r = \rho$ and $r = R$, we obtain

$$h_0 = A [I_0(\rho/\ell) - I_0(R/\ell)] + B [K_0(\rho/\ell) - K_0(R/\ell)], \quad (3.34)$$

^{vii}Equation (3.31) is $A \int_{\rho}^R I_0(r/\ell) r dr + B \int_{\rho}^R K_0(r/\ell) r dr - C \int_{\rho}^R r dr = 0$, from which $A [\ell r I_1(r/\ell)]_{\rho}^R + B [-\ell r K_1(r/\ell)]_{\rho}^R - C \left[\frac{r^2}{2} \right]_{\rho}^R = 0$. Then, writing explicitly A [Eq. (3.29)] and B [Eq. (3.30)], it follows Eq. (3.32).

^{viii}Indeed, if we set $\Delta P = 0$, we are imposing that the fluid-fluid interface must be flat at $z = 0$, and so $z = 0$ becomes the level of the fluid-fluid interface far outside from the tube. Also, if $\Delta P = 0$ is set, then the meniscus profile $h(r)$ is shifted by C above $z = 0$, because Eq. (3.16) holds for $h(r)$, instead of Eq. (3.26), and this explain why C in Eq. (3.32) is the capillary rise of a meniscus in a vertical cylindrical tube with a solid vertical cylinder in its center.

Figure 3.3: Height profile $h(r)$ [Eq. (3.26)] of a meniscus in a cylindrical tube with Young's contact angle α and radius $R = 2\ell$, and with a vertical cylinder in the center of Young's contact angle θ and radius $\rho = 0.1\ell$ (see Fig. 3.2). In (a) $\cos\alpha = 0.5$, and in (b) $\cos\alpha = 0$. The volumes of the two fluids are such that a flat interface corresponds to $z = 0$. The system is axisymmetric with respect to the z axis, i.e. $r = 0$. The capillary length is ℓ .



with $h_0 \equiv h(\rho) - h(R)$. In Fig. 4.12 of Chapter 4, we show the full height profile $h(r)$ [Eq. (3.26)] and the capillary rise h_0 [Eq. (3.34)] for various R and ρ , for $\cos\theta = 0.9$ and $\cos\alpha = 0$, and we compare them with the numerical predictions obtained by the method introduced in Chapter 4.

3.7 AXISYMMETRIC-MENISCUS DIVERGENCES DUE TO INVERSE GRAVITY

Mainly for mathematical curiosity, in this Section we consider the same system treated in the previous Section, see Fig. 3.2, but now we invert the direction of gravity.^{ix} We will show that, in this (in principle unstable) situation, the height profile of the interface is characterized by undulations which diverge for certain values of R/ℓ . Note that, as we are using the linear approximation of the Young-Laplace Equation, these predictions become less reliable when substantial perturbations of the fluid-fluid interface height profile arise. In our model, fluid 2, i.e. the heaviest fluid, is below the interface (with respect to z), and fluid 1, i.e. the lightest fluid, is above the interface. However, by inverting the gravity direction, which is now parallel to z , the Young-Laplace Equation [Eq. (2.2)] becomes

$$\nabla \cdot \hat{\mathbf{n}}(x, y, z) = \frac{\Delta P}{\gamma} + \frac{\hat{\mathbf{z}} \cdot (x, y, z)}{\ell^2}, \quad (3.35)$$

^{ix}Experimentally, this situation in principle can be achieved by placing the heaviest fluid above the lightest fluid in a container. This would be a metastable situation of course, as at the equilibrium the heaviest fluid prefers to be lower, with respect to the gravity, than the lightest fluid. However, if the energy barrier to be overcome for shifting the positions of the two fluids is high enough, then the system remains in this metastable state.

that is, the term proportional to ℓ^{-2} has changed sign. Consequently, the system sketched in Fig. 3.2 is now described, rather than by Eq. (3.25), by

$$\frac{d^2 h}{dr^2} + \frac{1}{r} \frac{dh}{dr} + \frac{h - C}{\ell^2} = 0 \quad , \quad \text{with} \quad C \equiv -\frac{\Delta P}{\gamma} \ell^2 . \quad (3.36)$$

Equation (3.36) is the 0-th order Bessel equation, whose solution is (see note iv at page 35 and vi at page 38)

$$h = A \cdot J_0(r/\ell) + B \cdot Y_0(r/\ell) + C , \quad (3.37)$$

with J_0 and Y_0 the 0-th order Bessel functions of the first and second kind respectively. With θ and α the contact angles of $h(r)$ with the central cylinder in $r = \rho$ and with the external wall in $r = R$, respectively, the boundary conditions to fix A and B , analogously to the previous Section, are

$$\left. \frac{dh(r)}{dr} \right|_R = A \left. \frac{dJ_0(r/\ell)}{dr} \right|_R + B \left. \frac{dY_0(r/\ell)}{dr} \right|_R = \cos \alpha , \quad (3.38)$$

$$\left. \frac{dh(r)}{dr} \right|_\rho = A \left. \frac{dJ_0(r/\ell)}{dr} \right|_\rho + B \left. \frac{dY_0(r/\ell)}{dr} \right|_\rho = -\cos \theta . \quad (3.39)$$

Using $dJ_0(ax)/dx = -a J_1(ax)$ and $dY_0(ax)/dx = -a Y_1(ax)$, we obtain

$$\frac{A}{\ell} = -\frac{Y_1(\rho/\ell) \cos \alpha + Y_1(R/\ell) \cos \theta}{Y_1(\rho/\ell) J_1(R/\ell) - Y_1(R/\ell) J_1(\rho/\ell)} , \quad (3.40)$$

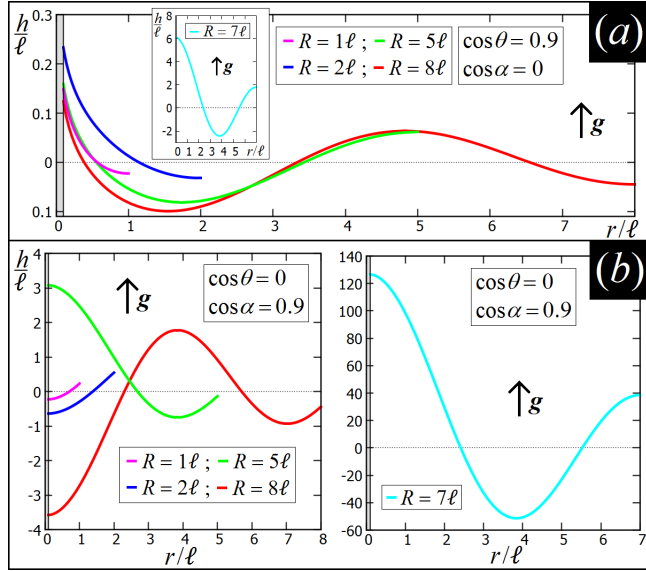
$$\frac{B}{\ell} = \frac{J_1(\rho/\ell) \cos \alpha + J_1(R/\ell) \cos \theta}{Y_1(\rho/\ell) J_1(R/\ell) - Y_1(R/\ell) J_1(\rho/\ell)} . \quad (3.41)$$

As boundary condition to determine C , we fix the fluid volumes by Eq. (3.31), obtaining that C is given by Eq. (3.32).^x

Some illustrative results of the height profile $h(r)$, as obtained by Eq. (3.37), with A , B , C given by, respectively, Eq. (3.40), (3.41), (3.32), are plotted in Fig. 3.4, for $\rho = 0.1 \ell$, and (a) $\cos \theta = 0.9$ and $\cos \alpha = 0$, (b) $\cos \theta = 0$ and $\cos \alpha = 0.9$. As shown, in this (unstable) situation of reversed gravity, the equilibrium height profile of the meniscus is characterized by (static) undulations. Also, the amplitude of these undulations depends on R/ℓ , and diverges for certain values of R/ℓ (see for example the case $R = 7 \ell$ in Fig. 3.4, where the predicted capillary rise on the vertical cylinder supposedly should be of the order of 100ℓ). Clearly, this intriguing behavior of the meniscus equilibrium height profile is connected with the fact that we are dealing with an unstable system, as the gravity is reversed, and so the heaviest fluid, which is below the fluid-fluid interface, would

^xEquation (3.31) is $A \int_\rho^R J_0(r/\ell) r dr + B \int_\rho^R Y_0(r/\ell) r dr + C \int_\rho^R r dr = 0$, from which $A [\ell r J_1(r/\ell)]_\rho^R + B [\ell r Y_1(r/\ell)]_\rho^R + C \left[\frac{r^2}{2} \right]_\rho^R = 0$. Then, writing explicitly A [Eq. (3.40)] and B [Eq. (3.41)], it follows Eq. (3.32).

Figure 3.4: Height profile $h(r)$ [Eq. (3.37)] of a meniscus in a cylindrical tube with Young's contact angle α and radius R , and with a vertical solid cylinder in the center with Young's contact angle θ and radius $\rho = 0.1 \ell$ (see Fig. 3.2). In (a) $\cos \theta = 0.9$, $\cos \alpha = 0$ and in (b) $\cos \theta = 0$, $\cos \alpha = 0.9$. The fluid below the interface is the heaviest, however the gravity direction is inverted, i.e. \mathbf{g} is parallel to the z axis (see note ix at page 40). Note that the solutions diverge for certain values of R/ℓ .



prefer to stay above it. This phenomenon is known as Rayleigh-Taylor instability [93], and dynamic effects need to be included to describe it more accurately. Note, also, that the quality of the linear approximation for the Young-Laplace Equation is poorer when substantial deformations of the fluid-fluid interface shape arise. The main aim of this Section was just to explore the consequences of inverting the sign of the gravitational force term in the Young-Laplace Equation, mainly for mathematical interest. For the same purpose, in Sec. 3.11 we consider the inverted-gravity case for a meniscus with translational symmetry, instead of rotational symmetry, obtaining analogous physical predictions to this Section.

3.8 MENISCUS IN A VERTICAL CYLINDRICAL TUBE

In Sec. 3.4 we applied the linearized Young-Laplace Equation [Eq. (3.3)] to study a vertical solid cylinder in contact with an infinitely extended flat fluid-fluid interface. Then, in Secs. 3.6 and 3.7, we introduced an external vertical cylindrical wall enclosing our system. In this Section we remove the solid vertical cylinder in the center, but we keep the external vertical cylindrical wall. In this way, we study the shape of a meniscus in a vertical cylindrical tube, as sketched in Fig. 3.5.

The height profile $h(r)$ of the meniscus, with r the distance from the symmetry axis, is given by Eq. (3.26). Said R the cylindrical tube radius and α its Young's contact angle, the boundary condition in $r = R$ is given by Eq. (3.27). Then, in $r = 0$ we impose, for symmetry reason, the boundary condition

$$\left. \frac{dh(r)}{dr} \right|_{r=0} = 0, \quad (3.42)$$

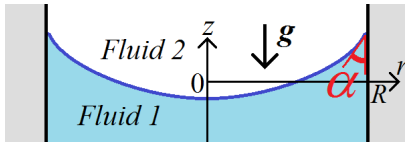


Figure 3.5: Sketch of a meniscus in a vertical cylindrical tube with radius R and Young's contact angle α . The system is axisymmetric with respect to the z axis.

which gives

$$A I_1(0) - B K_1(0) = 0. \quad (3.43)$$

From Eq. (3.27) and (3.43), using $I_1(0) = 0$, we obtain

$$\frac{A}{\ell} = \frac{\cos \alpha}{I_1(R/\ell)}, \quad \frac{B}{\ell} = 0. \quad (3.44)$$

As boundary condition for the fluid volume, we use

$$2\pi \int_0^R h(r) r dr = 0, \quad (3.45)$$

from which^{xi}

$$\frac{C}{\ell} = 2 \frac{\ell}{R} \cos \alpha. \quad (3.46)$$

Note that Eq. (3.46) is *Jurin's Law* [92], with C representing the capillary rise in a vertical cylindrical tube, of Young's contact angle α , immersed in a flat fluid-fluid interface (for the same argument presented in note viii at page 39). This proves that the approximation of a spherical curvature for the meniscus in a cylindrical tube, used to derive Jurin's Law, is equivalent to the linear approximation, i.e. Eq. (3.2). Some illustrative results of the height profile $h(r)$, as obtained by Eq. (3.26), with A, B, C given by Eqs. (3.44) and (3.46), are plotted in Fig. 3.6(a), for $R = 2\ell$ and various Young's contact angles α .

Finally, analogously to Sec. 3.7, we consider, mainly for mathematical interest, the metastable situation in which the gravity direction is inverted (see note ix at page 40). The equilibrium profile $h(r)$ of the fluid-fluid interface is given by Eq. (3.37), and the boundary conditions for A and B are given by Eq. (3.38) for $r = R$ and by Eq. (3.42) for $r = 0$. So, using that $J_1(0) = 0$, we obtain

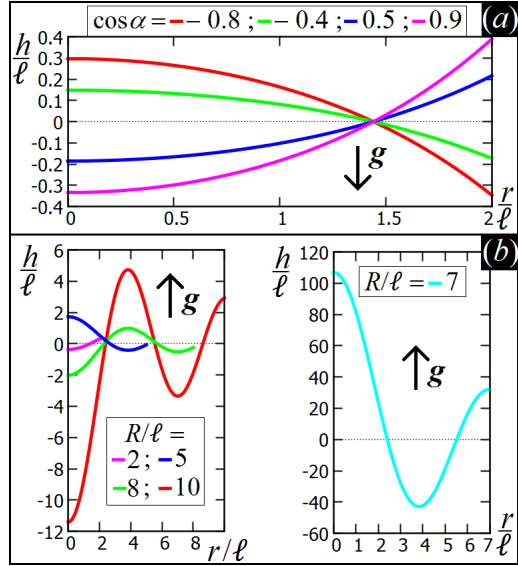
$$\frac{A}{\ell} = -\frac{\cos \alpha}{J_1(R/\ell)}, \quad \frac{B}{\ell} = 0. \quad (3.47)$$

As boundary condition to determine C , we fix the fluid volumes by Eq. (3.45), obtaining that C is given by Eq. (3.46).^{xii} Some illustrative results of the height profile $h(r)$, as obtained by Eq. (3.37), with A, B, C given by Eqs. (3.47)

^{xi}Equation (3.45) for $h(r)$ given by Eq. (3.26) is $A \int_0^R I_0(r/\ell) r dr - C \int_0^R r dr = 0$, from which $A \ell R I_1(R/\ell) - C R^2/2 = 0$. Then, writing explicitly A [Eq. (3.44)], it follows Eq. (3.46).

^{xii}Equation (3.45) for $h(r)$ given by Eq. (3.37) is $A \int_0^R J_0(r/\ell) r dr + C \int_0^R r dr = 0$, from which $A \ell R J_1(R/\ell) + C R^2/2 = 0$. Then, writing explicitly A [Eq. (3.47)], it follows Eq. (3.46).

Figure 3.6: Height profile $h(r)$ of a meniscus in a vertical cylindrical tube with radius R and Young's contact angle α , (a) for $R = 2$ and various values of $\cos \alpha$, and (b) for $\cos \alpha = 0.5$ and various values of R . The fluid below the interface is the heaviest. However, while in (a) the gravity is antiparallel to the z axis, in (b) the case of inverse gravity, i.e. \mathbf{g} parallel to the z axis, is considered (see note ix at page 40). As shown, (static) undulations in the meniscus height profile arise in (b), with their amplitude diverging for certain values of R . This mathematical behavior of $h(r)$ is due to the unstable physical situation we are dealing with, as the heaviest fluid, which is below the interface, prefers to stay above it when gravity is reversed.



and (3.46), are plotted in Fig. 3.6(b), for $\cos \alpha = 0.5$ and various values of R . Analogously to Sec. 3.7, we observe that the equilibrium height profile of the meniscus is characterized by (static) undulations, with a diverging amplitude for certain values of R/ℓ . A more appropriate study of such a fluid-fluid system should take into account also dynamic effects, and this only-equilibrium analysis of the inverse-gravity case was done mainly for mathematical curiosity.

3.9 CAPILLARY ELASTIC ENERGY BY DISPLACING A PINNED SPHERE

We consider in this Section an isolated spherical particle adsorbed at a flat fluid-fluid interface. At the equilibrium, the sphere adjusts the height of its center of mass to form a contact angle θ with the flat interface, see Fig. 3.7(a), as imposed by Young's Law [Eq. (2.18)]. In this configuration (which has minimum energy, as we numerically prove in Sec.4.5.1) the sphere manages to fulfill Young's Law without deforming the flat fluid-fluid interface, for any Young's contact angle θ .^{xiii} We now assume that the three-phase contact line is pinned on the sphere surface at its equilibrium position. Therefore, if the sphere is displaced in a direction orthogonal to the fluid-fluid interface plane, the three-phase contact line moves together with the sphere, inducing deformations in the interface [see a sketch in Fig. 3.7(b)]. In this Section, we use the linearized Young-Laplace Equation to predict the shape of these deformations, and then we calculate the force to

^{xiii}Note that, instead, an anisotropic particle adsorbed at a fluid-fluid interface in general needs to deform the interface, to fulfill Young's Law along the whole three-phase contact line. And the same is true for a spherical particle adsorbed at a curved fluid-fluid interface.

displace the sphere orthogonally to the interface plane.

At the equilibrium, the height z_c of the sphere center on mass on the $z = 0$ plane, corresponding to the flat fluid-fluid interface, is given by [see Fig. 3.7(a)]

$$z_c = -\rho \cos \theta , \quad (3.48)$$

with ρ the sphere radius. By changing the height of the sphere center of mass from z_c [Eq. (3.48)] to $z_c + \Delta z$, we induce capillary deformations with cylindrical symmetry with respect to the axis orthogonal to the $z = 0$ plane and passing through the sphere center of mass. Using the linear approximation, the height profile $h(r)$ of these capillary deformations, with r the distance from the symmetry axis, is given by Eq. (3.16), which is the solution of the axisymmetric linearized Young-Laplace Equation [Eq. (3.15)], where $\Delta P = 0$ because we are assuming a flat fluid-fluid interface far from the sphere. Using that $h(\infty) = 0$, it follows $A = 0$ in Eq. (3.16), obtaining

$$h = B \cdot K_0(r/\ell) . \quad (3.49)$$

The boundary condition to determine B in Eq. (3.49) is the position of the three-phase contact line, that is

$$h(\rho \sin \theta) = \Delta z . \quad (3.50)$$

where $r = \rho \sin \theta$ is the distance from the symmetry axis of the three-phase contact line [see Fig. 3.7(a)]. Using Eq. (3.50), from Eq. (3.49) it follows that

$$B = \frac{\Delta z}{K_0(\rho \sin \theta/\ell)} . \quad (3.51)$$

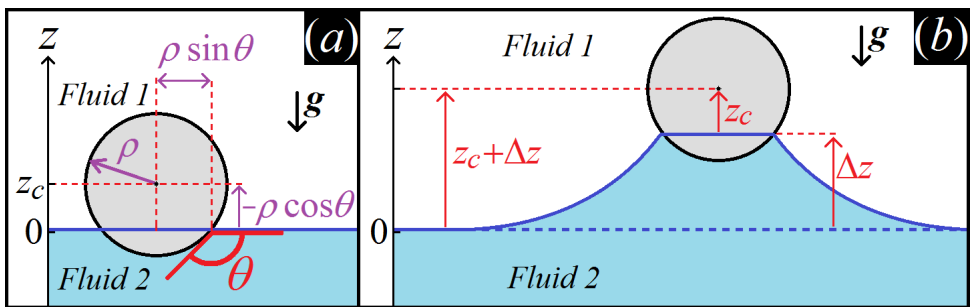


Figure 3.7: (a) Equilibrium position of a spherical particle, with radius ρ and Young's contact angle θ , adsorbed at a flat fluid-fluid interface. (b) Deformations induced in the interface by displacing the sphere of Δz in the direction orthogonal to the interface. The three-phase contact line is assumed to be pinned at its equilibrium position. Note that, to keep the sphere in this out-of-equilibrium configuration, we are exerting a force, therefore in this situation the contact angle between the sphere surface and the fluid-fluid interface does not fulfill Young's Law. The z axis, here for convenience shown at the side, passes through the sphere center of mass.

In Fig. 3.8 the height profile $h(r)$ is shown for various Δz , for $\rho = 0.001\ell$ and $\theta = \pi/2$. The energy E [Eq. (2.24)], with respect to the displacement Δz of the sphere, is

$$E(\Delta z) = \gamma [S(\Delta z) - \Gamma + W_1 \cos \theta] + E_g(\Delta z), \quad (3.52)$$

with γ the fluid-fluid surface tension, $S(\Delta z)$ the total surface area of the fluid-fluid interface, Γ the area of the $z = 0$ plane (which represents the fluid-fluid interface when no sphere is adsorbed), W_1 the sphere surface area wet by the fluid above the interface given by ^{xiv}

$$W_1 = 2\pi \rho^2 (1 - \cos \theta), \quad (3.53)$$

and $E_g(\Delta z)$ the gravitational energy of the fluid-fluid interface. Note that the reference level $E = 0$ is shifted with respect to Eq. (2.24) such that here $E(\Delta z)$ is zero when the sphere is desorbed from the interface and immersed in the fluid below the interface. The pressure terms in Eq. (2.24) do not contribute to Eq. (3.52) because $\Delta P = 0$. In Eq. (3.52) the particle position varies, so in principle the particle weight contribution should be added to E , but here we consider that the particle weight negligible.^{xv} Explicitly, $S(\Delta z)$ and $E_g(\Delta z)$ are:

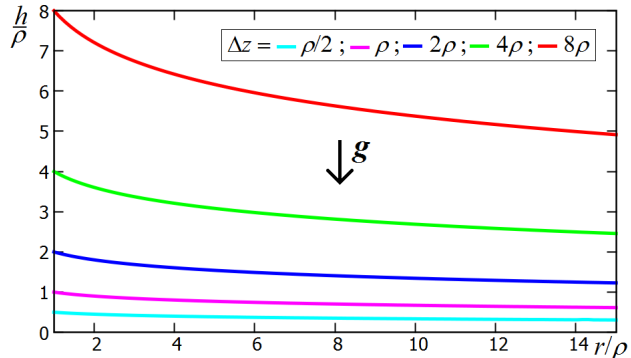
$$S(\Delta z) = 2\pi \int_{\rho \sin \theta}^{\infty} r \sqrt{1 + \left(\frac{dh}{dr}\right)^2} dr, \quad (3.54)$$

$$E_g(\Delta z) = \frac{\gamma \pi}{\ell^2} \int_{\rho \sin \theta}^{\infty} r h^2 dr, \quad (3.55)$$

where $h(r)$ [Eq. (3.49)] depends on Δz through B [Eq. (3.51)]. Using the linear approximation, $S(\Delta z)$ can be written as ^{xvi}

$$S(\Delta z) \simeq 2\pi \int_{\rho \sin \theta}^{\infty} r dr + \pi \int_{\rho \sin \theta}^{\infty} r \left(\frac{dh}{dr}\right)^2 dr, \quad (3.56)$$

Figure 3.8: Height profile $h(r)$ [Eq. (3.49)] of the capillary deformations induced by displacing a sphere, pinned at the interface, by Δz along the z axis, orthogonal to the interface and passing through the sphere center of mass, with r the distance from z . The sphere has Young's contact angle $\theta = \pi/2$ and radius $\rho = 0.001\ell$.



^{xiv}Note that W_1 is a constant, as we are assuming a pinned triple contact line.

^{xv}In Sec. 4.5.1 we discuss this approximation in detail, showing its range of validity.

^{xvi}Note that $\sqrt{1+x^2} = 1 + x^2/2 + \mathcal{O}(x^4)$.

and using that the first term at the second member of Eq. (3.56) is $\Gamma - \pi (\rho \sin \theta)^2$, we can express $\Delta S(\Delta z) \equiv S(\Delta z) - \Gamma$ as

$$\Delta S(\Delta z) \simeq \pi \int_{\rho \sin \theta}^{\infty} r \left(\frac{dh}{dr} \right)^2 dr - \pi (\rho \sin \theta)^2. \quad (3.57)$$

Using Eqs. (3.49), (3.51), (3.53), (3.55), (3.57), and that $dK_0(ax)/dx = -a K_1(x)$, we can rewrite Eq. (3.52) as

$$E(\Delta z) = \frac{\pi \gamma}{\ell^2} B^2 \int_{\rho \sin \theta}^{\infty} r [K_1^2(r/\ell) + K_0^2(r/\ell)] dr + \gamma \rho^2 c, \quad (3.58)$$

where we defined

$$c \equiv 2\pi (1 - \cos \theta) \cos \theta - \pi \sin^2 \theta. \quad (3.59)$$

Eq. (3.58) has the form of a parabola in the $[E, \Delta z]$ space, that is

$$E(z_c) = \gamma \rho^2 \left[\Psi \left(\frac{\Delta z}{\rho} \right)^2 + c \right], \quad (3.60)$$

where we defined

$$\Psi \equiv \frac{\pi}{\ell^2 [K_0(\rho \sin \theta/\ell)]^2} \int_{\rho \sin \theta}^{\infty} r [K_1^2(r/\ell) + K_0^2(r/\ell)] dr, \quad (3.61)$$

that is ^{xvii}

$$\Psi = \pi \frac{K_1(\rho \sin \theta/\ell)}{K_0(\rho \sin \theta/\ell)} \frac{\rho \sin \theta}{\ell}. \quad (3.62)$$

Finally, from Eq. (3.60) we obtain the force $F \equiv dE/d(\Delta z)$ necessary to move the particle center of mass with a displacement Δz in the z direction, that is

$$F(\Delta z) = k \Delta z. \quad (3.63)$$

Therefore $F(\Delta z)$ is an elastic force, because linear in Δz , with spring constant given by

$$k = 2\gamma \Psi. \quad (3.64)$$

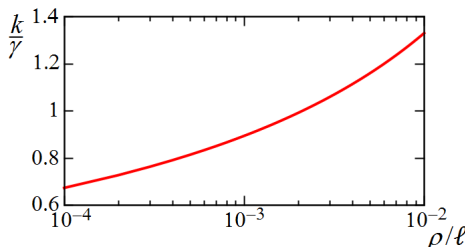


Figure 3.9: Spring constant k [Eq. (3.64)], with respect to ρ/ℓ , of the elastic force $F = k \Delta z$ [Eq. (3.63)] necessary to move a sphere, pinned at the interface, by Δz orthogonally to the interface plane. The sphere has radius ρ and Young's contact angle $\pi/2$, γ is the fluid-fluid surface tension, and ℓ is the capillary length.

^{xvii} $\int x [K_0^2(x/a) + K_1^2(x/a)] dx = -a x K_0(ax) K_1(ax)$.

Note that, as expected, $F(\Delta z) = 0$ when $\Delta z = 0$, i.e. when the sphere is at its equilibrium configuration, with its center of mass height given by $z_c = -\rho \cos \theta$. In Fig. 3.9, the spring constant k [Eq. (3.64)] of the elastic force $F(\Delta z)$ [Eq. (3.63)] is plotted with respect to ρ/ℓ , for a sphere with Young's contact angle $\pi/2$.

3.10 CAPILLARY INTERACTIONS BETWEEN VERTICAL PLATES

In this Section we apply the linearized Young-Laplace Equation to calculate the capillary force between two vertical plates adsorbed at a fluid-fluid interface, see Fig. 3.10. First, we calculate the equilibrium shape of the meniscus between the plates. Then, by analogous procedure to the previous Section, we compute the energy of the system with respect to the distance between the two vertical plates, and from this we extract the capillary force acting between the plates.

Using a Cartesian coordinate system with the z axis antiparallel to the gravity \mathbf{g} , the two solid surfaces in contact with the meniscus are in $x = 0$ and $x = D$, respectively, see Fig. 3.10. The system has translational invariance along the y axis. Therefore, the linearized Young-Laplace Equation [Eq. (3.3)] becomes

$$\frac{d^2 h}{dx^2} = \frac{h + C}{\ell^2}, \quad (3.65)$$

where we defined

$$C \equiv -\frac{\Delta P}{\gamma} \ell^2. \quad (3.66)$$

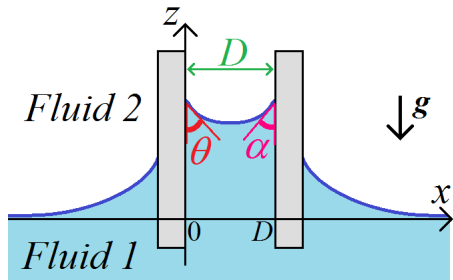
The solution of Eq. (3.65) is (see note ii at page 34 and vi at page 38)

$$h = A e^{x/\ell} + B e^{-x/\ell} - C, \quad (3.67)$$

where A and B are constants to be determined by the boundary conditions of Young's Law in $x = 0$ and $x = D$. Analogously to Eqs. (3.27), (3.28), such boundary conditions are

$$\left. \frac{dh(x)}{dx} \right|_0 = -\cos \theta, \quad \left. \frac{dh(x)}{dx} \right|_D = \cos \alpha, \quad (3.68)$$

Figure 3.10: Sketch of two vertical plates, with surface-to-surface distance D , at a fluid-fluid interface. The system has translational invariance orthogonally to the $[x, z]$ plane. Plots of the meniscus between the plates, with respect to the Young's contact angles θ (in $x = 0$) and α (in $x = D$), are shown in Fig. 3.11. The capillary force F [Eq. (3.83)] with respect to D is shown in Fig. 3.12(b).



where θ and α are Young's contact angles of the solid surface in $x = 0$ and $x = D$, respectively (see Fig. 3.10). From Eq. (3.68), it follows

$$\frac{A}{\ell} = \frac{\cos \alpha + \cos \theta e^{-D/\ell}}{e^{D/\ell} - e^{-D/\ell}}, \quad \frac{B}{\ell} = \frac{\cos \alpha + \cos \theta e^{D/\ell}}{e^{D/\ell} - e^{-D/\ell}}. \quad (3.69)$$

To determine C , we impose that the volumes of the fluids between the two plates are such that a flat meniscus would correspond to the $z = 0$ plane, that is

$$\int_0^D h(x) dx = 0, \quad (3.70)$$

from which^{xviii}

$$\frac{C}{\ell} = (\cos \theta + \cos \alpha) \frac{\ell}{D}. \quad (3.71)$$

Plots of $h(x)$ [Eq. (3.67)], for A, B, C given by Eqs. (3.69) and (3.71), are shown in Fig. 3.11 for $D = \ell$ and some values of θ and α . Note that C [Eq. (3.71)] represents the capillary rise of a meniscus between two vertical plates, for the same argument presented in note viii at page 39. As a matter of fact, Eq. (3.71) in the limit $\theta = \alpha$ becomes

$$C = \frac{2\ell^2}{D} \cos \theta \quad (3.72)$$

which is the capillary rise of a meniscus between two vertical plates in the approximation of a cylindrical shape for the meniscus (see Sec. 4.3.3), proving that such an approximation is equivalent to linearize the Young-Laplace Equation.^{xix} To calculate the capillary force between the two plates, it is more realistic to fix the fluid bulk pressures, rather than fixing the volume by Eq. (3.70). Assuming that the fluid-fluid interface is flat and coincides with $z = 0$ for $x \rightarrow \pm\infty$, see Fig. 3.10, it follows $\Delta P = 0$, which implies $C = 0$ in Eq. (3.67). The energy E

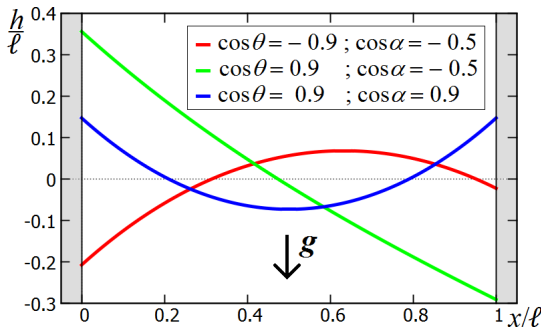


Figure 3.11: Height profile $h(x)$ of a meniscus between two solid vertical surfaces in $x = 0$ and $x = D$, with Young's contact angles θ and α , respectively, as obtained by Eq. (3.67), with A, B, C given by Eqs. (3.69) and (3.71). The fluid volumes are such that a flat meniscus would correspond to $z = 0$. The capillary length is ℓ .

^{xviii}Equation (3.70) for $h(x)$ given by Eq. (3.67) is $A \int_0^D e^{x/\ell} dx + B \int_0^D e^{-x/\ell} dx - C \int_0^D dx = 0$, from which $[A \ell e^{x/\ell} - B \ell e^{-x/\ell}]_0^D = C D$. Then, writing explicitly A and B [Eq. (3.69)], it follows Eq. (3.71).

^{xix}Analogously, in Sec. 3.8 we noted, about Jurin's Law, that the spherical shape approximation for a meniscus in a vertical tube corresponds to linearize the Young-Laplace Equation.

[Eq. (2.24)] of the system given by the fluid-fluid interface with the two adsorbed vertical plates depends on the surface-to-surface distance D between the vertical plates, and explicitly is^{xx}

$$E = \xi_y \gamma [S_o + S - h_0 \cos \theta - h_D \cos \alpha] + E_g, \quad (3.73)$$

where ξ_y is the length of the system in the y direction, γ is the fluid-fluid surface tension, $h_0 \equiv h(0)$ and $h_D \equiv h(D)$ explicitly are

$$h_0 = A + B, \quad h_D = A e^{D/\ell} + B e^{-D/\ell}, \quad (3.74)$$

S_o is the (1D) surface area of the fluid-fluid interface outside the plates (i.e. for $x < 0$ and $x > D$), S is the (1D) surface area of the meniscus between the plates and given by

$$S = \int_0^D \sqrt{1 + \left(\frac{dh}{dx}\right)^2} dx, \quad (3.75)$$

and E_g is the gravitational energy and given by

$$E_g = \frac{\gamma \xi_y}{2\ell^2} \int_0^D h^2 dx. \quad (3.76)$$

As we are assuming a flat fluid-fluid interface for $x \rightarrow \pm\infty$, the shape of the meniscus outside the plates does not depend on D , so its surface area can be written as

$$S_o = \Gamma - D, \quad (3.77)$$

with Γ a constant not depending on D . Using the approximation of small perturbations, we can write S as (see note xvi at page 46)

$$S \approx D + \frac{1}{2} \int_0^D \left(\frac{dh}{dx}\right)^2 dx, \quad (3.78)$$

which, writing $h(x)$ explicitly [Eq. (3.67)] for $C = 0$, is

$$\frac{S}{\ell} = \frac{A^2}{4\ell^2} \left(e^{\frac{2D}{\ell}} - 1\right) - \frac{B^2}{4\ell^2} \left(e^{-\frac{2D}{\ell}} - 1\right) + \frac{D}{\ell} \left(1 - \frac{AB}{\ell^2}\right). \quad (3.79)$$

The gravitational energy E_g [Eq. (3.76)], writing $h(x)$ explicitly [Eq. (3.67)] for $C = 0$, is

$$\frac{E_g}{\gamma \xi_y \ell} = \frac{A^2}{4\ell^2} \left(e^{\frac{2D}{\ell}} - 1\right) - \frac{B^2}{4\ell^2} \left(e^{-\frac{2D}{\ell}} - 1\right) + \frac{D}{\ell} \frac{AB}{\ell^2}. \quad (3.80)$$

So, using Eqs. (3.74), (3.77), (3.79), (3.80), it follows that E [Eq. (3.73)] with

^{xx}Note that here the reference level $E = 0$ is shifted by a constant with respect to Eq. (2.24).

respect to A , B , D is

$$\begin{aligned} \frac{E}{\gamma \xi_y \ell} &= \frac{A^2}{2\ell^2} \left(e^{\frac{2D}{\ell}} - 1 \right) - \frac{B^2}{2\ell^2} \left(e^{-\frac{2D}{\ell}} - 1 \right) + \\ &+ \frac{\Gamma}{\ell} - \frac{A+B}{\ell} \cos \theta - \frac{A e^{\frac{D}{\ell}} + B e^{-\frac{D}{\ell}}}{\ell} \cos \alpha. \end{aligned} \quad (3.81)$$

Then, writing explicitly A and B [Eq. (3.69)], we obtain^{xxi}

$$\frac{E}{\gamma \xi_y \ell} = -\frac{\cos^2 \alpha + \cos^2 \theta}{2 \tanh(D/\ell)} - \frac{\cos \alpha \cos \theta}{\sinh(D/\ell)}, \quad (3.82)$$

where we neglected the Γ/ℓ term, as it is just an additive constant. Plots of E [Eq. (3.82)] are shown in Fig. 3.12(a), with respect to D , for some values of θ

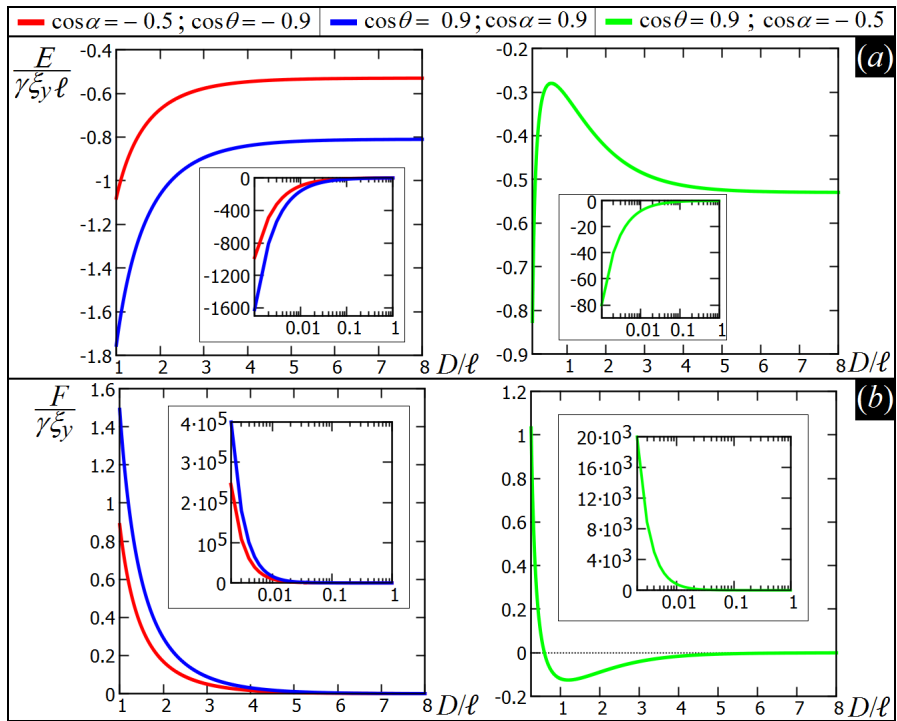


Figure 3.12: Plot of (a) the energy E [Eq. (3.82)] and (b) the capillary force $F \equiv dE/dD$ [Eq. (3.83)] for two vertical plates adsorbed at a fluid-fluid interface and at a surface-to-surface distance D (see Fig. 3.10). The insets show the close-range $D < \ell$, with D/ℓ in logarithmic scale. Note that the two plates attract each other if F is positive, repel if F is negative, and are at equilibrium if $F = 0$. The Young's contact angle of the two plates are, respectively, θ and α , the fluid-fluid surface tension is γ , the capillary length is ℓ , and the length of the system in the translational invariant direction is ξ_y .

^{xxi} $\sinh(x) = (e^x - e^{-x})/2$, $\cosh(x) = (e^x + e^{-x})/2$, $\tanh(x) = \sinh(x)/\cosh(x)$.

and α . Finally, from Eq. (3.82), we calculate the capillary force $F \equiv dE/dD$ between the two vertical plates, obtaining^{xxii}

$$\frac{F}{\gamma \xi_y} = \frac{\cos^2 \alpha + \cos^2 \theta}{2 \sinh^2(D/\ell)} + \frac{\coth(D/\ell)}{\sinh(D/\ell)} \cos \alpha \cos \theta. \quad (3.83)$$

Plots of F [Eq. (3.83)] with respect to D , for some values of θ and α , are shown in Fig. 3.12(b). As shown, the two plates attract each other when $\cos \theta$ and $\cos \alpha$ have the same sign, and the higher their modulus, the stronger the attraction. Instead, for $\cos \theta$ and $\cos \alpha$ with opposite signs, there is a maximum in E [Eq. (3.82)] for a certain distance D^* between the plates, therefore the plates repel each other if $D > D^*$, and they attract each other if $D < D^*$. In the limit case $\cos \theta = -\cos \alpha$, the maximum in the energy E [Eq. (3.82)] is in $D = 0$, therefore the plates repel each other for any D .

3.11 2D-MENISCUS DIVERGENCES DUE TO INVERSE GRAVITY

Inspired by the results in Section 3.7, in this Section we verify if the fluid-fluid interface of a system with translational invariance has divergent undulations if we invert the direction of the gravity force (see note ix at page 40), analogously to the axisymmetric case. We consider the same system of the previous section, i.e. a meniscus between two vertical plates at a surface-to-surface distance D and with Young's contact angle θ and α , respectively (see Figure 3.10). However, here we impose the gravity force to be parallel to the z axis. As the fluid below the fluid-fluid interface (with respect to z) is the heaviest, this situation is in principle unstable. A more accurate analysis of this system should include the dynamics of the fluids. Also, note that the linear approximation becomes less precise when the fluid-fluid interface shows substantial deformations. The study we report in this Section is mainly for mathematical curiosity, to explore the consequences of changing the sign of the gravity term in the Young-Laplace Equation.

Since we inverted the gravity direction, the Young-Laplace Equation is expressed by Eq. (3.35) and not by Eq. (2.2). Therefore, its linearized 2D version [Eq. (3.65)] becomes

$$\frac{d^2 h}{dx^2} = -\frac{h - C}{\ell^2}, \quad (3.84)$$

with C defined by Eq. (3.66). The solution of Eq. (3.84) is ^{xxiii} (see also note vi at page 38)

$$h = A e^{ix/\ell} + B e^{-ix/\ell} + C. \quad (3.85)$$

^{xxii} $\coth(x) = 1/\tanh(x)$.

^{xxiii} The solution of $d^2 h/dx^2 = -h/\ell^2$ is $h(x) = a \cos(b+x/\ell)$. Using Euler's formula $\exp(ix) = \cos(x) + i \sin(x)$, it follows $\cos(x) = [\exp(ix) + \exp(-ix)]/2$, from which we can rewrite $h(x)$ as $h(x) = A \exp(ix/\ell) + B \exp(-ix/\ell)$. Here a , b , A , B , are all integration constants.

The boundary conditions to determine A and B , obtained imposing Young's Law in $x = 0$ and $x = D$, are expressed by Eq. (3.68), and, for $h(x)$ given by Eq. (3.85), they imply

$$\frac{A}{\ell} = -i \frac{\cos \alpha + \cos \theta e^{-iD/\ell}}{e^{iD/\ell} - e^{-iD/\ell}} \quad , \quad \frac{B}{\ell} = -i \frac{\cos \alpha + \cos \theta e^{iD/\ell}}{e^{iD/\ell} - e^{-iD/\ell}} \quad . \quad (3.86)$$

As boundary condition to determine C , we fix the fluid volumes by Eq. (3.70), obtaining that C is given by Eq. (3.71).^{xxiv} The height profile $h(x)$ [Eq. (3.85)], with A and B [Eq. (3.86)] explicitly written, is^{xxv}

$$\frac{h}{\ell} = \frac{C}{\ell} - \frac{\cos \alpha}{\sin(D/\ell)} \cos\left(\frac{x}{\ell}\right) - \frac{\cos \theta}{\sin(D/\ell)} \cos\left(\frac{x-D}{\ell}\right) \quad . \quad (3.87)$$

Plots of $h(x)$ [Eq. (3.85)], for A , B , C given by Eqs. (3.86) and (3.71), are shown in Fig. 3.13 for several values of D/ℓ and for (a) $\cos \theta = \cos \alpha = 0.2$, (b) $\cos \theta = 0.2$, $\cos \alpha = -0.2$. As speculated, the meniscus equilibrium height profile $h(x)$ shows (static) undulations, analogously to the axisymmetric case presented in Section 3.7. Such an intriguing behavior is clearly connected to the unstable situation considered, because the heaviest fluid, below the interface with respect to z , would prefer to stay above, as the gravity is parallel to the z axis. Note that $h(x)$ is not defined for $D = n\pi\ell$, with n any integer, because of the $1/\sin(D/\ell)$ term in Eq. (3.87).

We are interested now in calculating the capillary force between the vertical plates, for this reversed-gravity system. Therefore, we impose $\Delta P = 0$ to have a flat interface far outside the plates, implying $C = 0$ in Eq. (3.85). Analogously to Section 3.10, where we considered the capillary force between two vertical plates with the usual direction of the gravity (i.e. antiparallel to z), the energy E of the system is given by Eq. (3.73). However, in the present case, the meniscus height profile is given by Eq. (3.85), with $C = 0$. So, by analogous calculations to Section 3.10, the various terms of E [Eq. (3.73)] result

$$\frac{h_0}{\ell} = A/\ell + B/\ell \quad , \quad (3.88)$$

$$\frac{h_D}{\ell} = \frac{A}{\ell} e^{iD/\ell} + \frac{B}{\ell} e^{-iD/\ell} \quad , \quad (3.89)$$

$$\frac{S_o + S}{\ell} = i \frac{A^2}{4\ell^2} \left(e^{i\frac{2D}{\ell}} - 1 \right) - i \frac{B^2}{4\ell^2} \left(e^{-i\frac{2D}{\ell}} - 1 \right) + \frac{D A B}{\ell \ell^2} + \frac{\Gamma}{\ell} \quad , \quad (3.90)$$

$$\frac{E_g}{\gamma \xi_y \ell} = -i \frac{A^2}{4\ell^2} \left(e^{i\frac{2D}{\ell}} - 1 \right) + i \frac{B^2}{4\ell^2} \left(e^{-i\frac{2D}{\ell}} - 1 \right) + \frac{D A B}{\ell \ell^2} \quad . \quad (3.91)$$

Using Eqs. (3.88), (3.89), (3.90), (3.91), it follows that E [Eq. (3.73)] with

^{xxiv}Equation (3.70) for $h(x)$ given by Eq. (3.85) is $A \int_0^D e^{ix/\ell} dx + B \int_0^D e^{-ix/\ell} dx + C \int_0^D dx = 0$, from which $\left[i B \ell e^{-ix/\ell} - i A \ell e^{ix/\ell} \right]_0^D = -C D$. Then, writing explicitly A and B [Eq. (3.86)], it follows Eq. (3.71).

^{xxv}Using $\cos(x) = [\exp(ix) + \exp(-ix)]/2$ and $\sin(x) = i[\exp(-ix) - \exp(ix)]/2$.

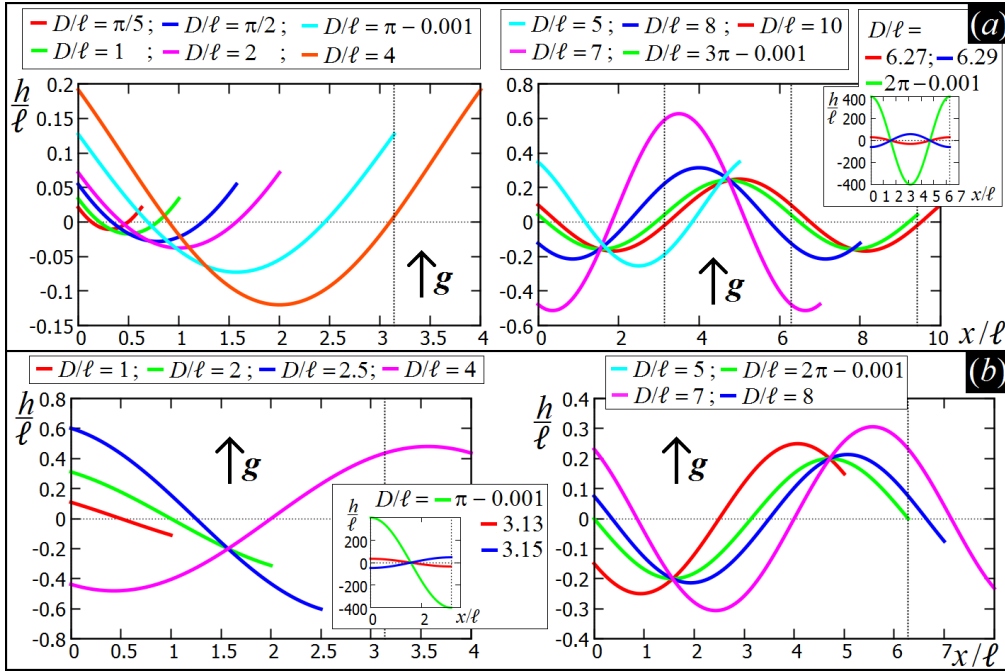


Figure 3.13: Height profile $h(x)$ of a meniscus between two vertical solid surfaces in $x = 0$ and $x = D$ (see Fig. 3.10), as obtained by Eq. (3.85), with A, B, C given by Eqs. (3.86) and (3.71). The Young's contact angles, θ in $x = 0$ and α in $x = D$, are given by (a) $\cos \theta = \cos \alpha = 0.2$, (b) $\cos \theta = 0.2$, $\cos \alpha = -0.2$. The fluid volumes are such that a flat meniscus corresponds to $z = 0$. The capillary length is ℓ . Here the gravity is inverted, i.e. \mathbf{g} is parallel to the z axis (see note ix at page 40), with the fluid below the interface being the heaviest. The dotted vertical lines indicate π/ℓ and its multiples. Note that $h(x)$ is not defined in $D = n\ell\pi$, with n any integer [see Eq. (3.85)].

respect to A, B, D is

$$\frac{E}{\gamma \xi_y \ell} = 2 \frac{D A B}{\ell \ell^2} - \left(\frac{A}{\ell} + \frac{B}{\ell} \right) \cos \theta - \left(\frac{A}{\ell} e^{i \frac{D}{\ell}} + \frac{B}{\ell} e^{-i \frac{D}{\ell}} \right) \cos \alpha + \frac{\Gamma}{\ell}. \quad (3.92)$$

Then, writing explicitly A and B [Eq. (3.86)], we obtain

$$\begin{aligned} \frac{E}{\gamma \xi_y \ell} = & \left[\frac{D/\ell}{2 \sin^2(D/\ell)} + \cot(D/\ell) \right] (\cos^2 \alpha + \cos^2 \theta) + \\ & + \frac{2 + (D/\ell) \cot(D/\ell)}{\sin(D/\ell)} \cos \alpha \cos \theta, \end{aligned} \quad (3.93)$$

where we neglected Γ/ℓ , as just an additive constant. Plots of E [Eq. (3.93)] are shown in Fig. 3.14, where we report also the capillary force $F \equiv dE/dD$ obtained

from Eq. (3.93), and explicitly given by

$$\begin{aligned} \frac{F}{\gamma \xi_y} = & - \left[\frac{1 + 2(D/\ell) \cot(D/\ell)}{2 \sin^2(D/\ell)} \right] (\cos^2 \alpha + \cos^2 \theta) + \\ & + \left\{ \frac{\cot(D/\ell)}{\sin(D/\ell)} - \frac{\cos(D/\ell)}{\sin^2(D/\ell)} \left[2 + \frac{D/\ell}{\tan(D/\ell)} \right] - \frac{D/\ell}{\sin^3(D/\ell)} \right\} \cos \alpha \cos \theta. \end{aligned} \quad (3.94)$$

As shown in Fig. 3.14(a), for $\cos \theta = 0.1$ and $\cos \alpha = -0.2$ the energy E [Eq. (3.93)] positively diverges for $D \rightarrow n\pi\ell$, with n any integer, because for such a D this theory predicts a divergent meniscus height profile. In the cases $\cos \theta = \cos \alpha = 0.2$ and $\cos \theta = -\cos \alpha = 0.2$, instead, the meniscus height profile, and consequently the energy E , diverges only for $D \rightarrow 2\pi\ell$ and $D \rightarrow (2n+1)\pi\ell$, respectively. As shown in Fig. 3.14(b), the capillary force F [Eq. (3.94)] drives the two plates at equilibrium distances D , corresponding to the energy minima, and recurring once every $\pi\ell$ in the case $\cos \theta = 0.1$ and $\cos \alpha = -0.2$, and once every $2\pi\ell$ in the cases $\cos \theta = \pm \cos \alpha$. We remark, however, that we are dealing with an unstable system, because the heaviest fluid, below the interface with respect to z , would prefer to stay above, as the gravity is parallel to z . This phenomenon is known as Rayleigh-Taylor instability [93], and dynamic effects need

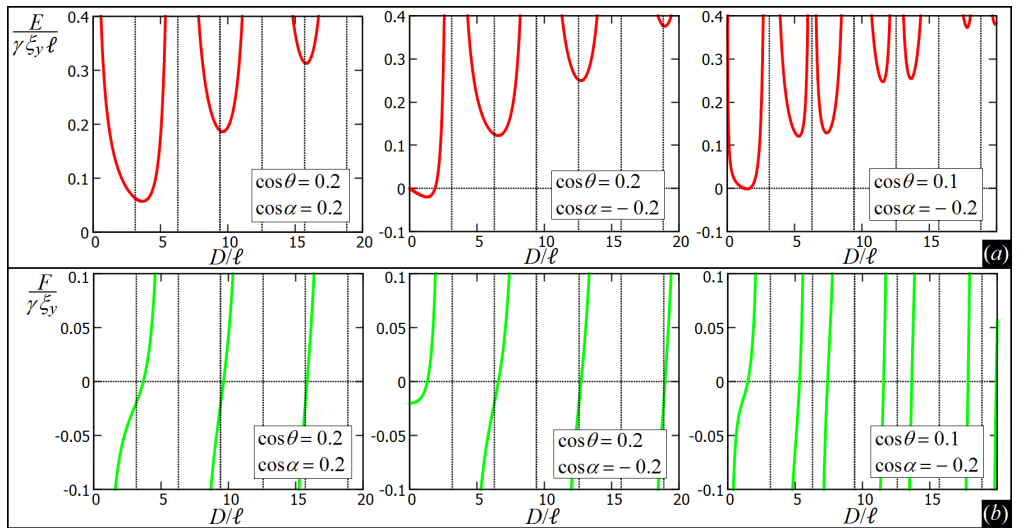


Figure 3.14: Energy E [Eq. (3.93)] and capillary force $F \equiv dE/dD$ [Eq. (3.94)] for two vertical plates adsorbed at a fluid-fluid interface and at a surface-to-surface distance D . This system is sketched in Fig. 3.10, but here the case with inverse gravity, i.e. \mathbf{g} parallel to the z axis, is considered (see note ix at page 40). Note that the two plates attract each other if F is positive, repel if F is negative, and are at equilibrium if $F = 0$. The Young's contact angles, θ in $x = 0$ and α in $x = D$, are given by (a) $\cos \theta = \cos \alpha = 0.2$, (b) $\cos \theta = 0.2$, $\cos \alpha = -0.2$. The fluid-fluid surface tension is γ , the capillary length is ℓ , and the length of the system in the translational invariant direction is ξ_y . The dotted vertical lines indicate π/ℓ and its multiples.

to be included to describe it more accurately. In addition, we are using the linear approximation of the Young-Laplace Equation, which holds for small deformations of the meniscus height profile, while here non-linear effects of the meniscus shape seem important. The main aim of this Section, and alike of Section 3.7, was just to explore the consequences of inverting the sign of the gravitational force in the Young-Laplace Equation, mainly for mathematical interest.

3.12 CONCLUSION

In this Chapter we presented the linearized Young-Laplace Equation [Eq. (3.3)], which is an approximated and easier-to-solve version of the Young-Laplace Equation [Eq. (2.2)] for small deformations of the fluid-fluid interface shape.

In Sec. 3.3, we derived a solution of such an equation in the form of a multipole expansion [see Eq. (3.14)], to describe the deformation field induced in the height profile of a fluid-fluid interface by an adsorbed particle with a pinned three-phase contact line of given position. This result is at the base of several theoretical works in the literature, e.g. Refs. [86–91], where the capillary force between adsorbed particles generating a given deformation field is analytically computed. In Sec. 3.4 we studied the wetting of a vertical solid cylinder at a flat fluid-fluid interface infinitely extended, and in Sec. 3.6 we investigated the finite-size effects due to an external vertical wall enclosing the system. In Sec. 3.8, we studied the height profile of a meniscus in a cylindrical vertical tube, and showed that the linearized Young-Laplace Equation implies Jurin’s Law. These results will be exploited in the next Chapter, where we introduce a new numerical method for the equilibrium shape of a fluid-fluid interface, to test and verify the correctness of our numerical predictions.

From the analytical expression of the meniscus height profile, the capillary force acting in a system can also be analytically derived. To show an illustrative application of this, in Sec. 3.9 we compute the force necessary to deform a flat fluid-fluid interface by displacing an adsorbed sphere, pinned at the interface, in the direction orthogonal to the interface plane. As shown, such a force [Eq. (3.63)] is elastic in nature, with spring constant k [Eq. (3.64)]. In Ref. [85] experimental results are shown for the case of a sliding three-phase contact line. Here, as the purpose of these calculations was mainly illustrative, we assumed for simplicity a fixed three-phase contact line on the particle surface. Then, in Sec. 3.10, also for illustrative purpose and for completeness, we calculated the capillary force between two vertical plates adsorbed at a flat fluid-fluid interface, and possibly with different contact angles. According to the sign of the deformations induced by the plates in the interface, i.e. if they are depressions or rises, the two plates can attract or repel each other.

Finally, in Secs. 3.7, 3.8, and 3.11, we explored the consequences of inverting the sign of the gravity force in the Young-Laplace Equation. As a result, the equilibrium shape of the meniscus is characterized by (static) undulations, which diverge

in amplitude for certain sizes of the system. As we mentioned, this analysis was done mainly for mathematical curiosity, and more accurate physical predictions, which go beyond the purpose of this Thesis, should include also the dynamics of the fluids, as the treated system is unstable (Rayleigh-Taylor instability [93]). The main goal of this Chapter was to provide an analytical framework to compare the numerical results for the equilibrium shape of fluid-fluid interfaces obtained from the method we will introduce in the next Chapter. Indeed, despite the simplification introduced by the linear approximation, a major complication still remains in solving the Young-Laplace Equation for many applications, e.g. adsorbed particles at a fluid-fluid interface, that is the position of the three-phase contact points is in principle unknown. This free boundary problem will be solved by the numerical approach introduced in the next Chapter.

CHAPTER 4

A NEW NUMERICAL METHOD FOR MINIMUM-ENERGY SURFACES

In this Chapter, we introduce a new numerical method to calculate the equilibrium shape of a fluid-fluid interface by minimizing the (free) energy of the system. First, we illustrate the basic mechanism of the method (leaving a more detailed description of its implementation to the Appendixes at the end of the Chapter), then we present illustrative results in 2D and 3D to validate the correctness and precision of the method, and show its applicability to a wide range of problems involving fluid-fluid interface. In particular, we prove the applicability of our method for studying capillary deformations induced by colloidal particles adsorbed at flat fluid-fluid interfaces.

4.1 INTRODUCTION

Explicit knowledge of the fluid-fluid interface shape is required in many different problems of Soft Matter or related fields. For example, to study the capillary interactions between particles adsorbed at a fluid-fluid interface, the capillary deformations induced by the particles in the interface shape need to be predicted. As shown in Chapter 2, the equilibrium shape of a fluid-fluid interface is fixed by the Young-Laplace Equation [Eq. (2.2)], with Young's Law [Eq. (2.18)] imposed as boundary condition in the three-phase contact points, i.e. where the fluid-fluid interface is in contact with a solid surface. Analytical solutions of such an equation are possible only in problems with very trivial geometries, e.g. a meniscus close to a vertical wall, or a 2D droplet wetting a flat substrate and in absence of gravity, see Secs. 2.6.1 and 2.6.2. By applying the linear approximation to the Young-Laplace Equation, as shown in Chapter 3, analytic solutions in terms of Bessel functions can be obtained in a wider range of problems. However, even in this approximation, a main issue remains for practical applications to particles adsorbed at the interface, that is the position of the three-phase contact line, i.e. where Young's Law boundary conditions are applied, is not known a priori. To approach this *free boundary problem* [94], an alternative route arises from Sec. 2.5, where we showed that calculating the shape of a fluid-fluid interface that minimizes the energy E [Eq. (2.24)] is equivalent to solving the Young-Laplace Equation and, simultaneously, the boundary conditions given by Young's Law. In this Chapter, we introduce a new numerical method to calculate such a shape, given as input parameters the volume of the two fluids and the shape, position and Young's contact angle of the solid surfaces in the system.

Other numerical methods to calculate the equilibrium shape of a fluid-fluid interface as a minimum-energy surface already exist. A widely used software in the Soft Matter community is Surface Evolver [95]. A hybrid energy-minimization method specifically developed to study equilibrium shapes of droplets wetting hydrophilic-hydrophobic patterned surfaces was recently introduced in Ref. [96]. However, the choice of developing independently a new numerical method, with a home-made code written from scratch, allowed us to easily adapt the method for studying all the problems presented in this thesis, involving in particular one or many particles with various shapes adsorbed at fluid-fluid interfaces, or droplets wetting non-trivially-curved (and, possibly, chemically heterogeneous) solid surfaces. The method is simply implementable, and an illustrative algorithm for its implementation in 2D and 3D is reported at the end of this Chapter, in Appendix A and B, respectively.

Alternatively, more general approaches which include also the dynamics of the fluids can be used to compute fluid-fluid interface shapes, for example numerical methods which solve the two-phase Navier-Stokes Equation for sharp interfaces [97–99] or diffuse interfaces [100], Lattice-Boltzmann simulations [18, 101–104], Molecular Dynamics [105–108] and Dissipative Particle Dynamics [109] ap-

proaches, and various Diffuse Interface models [110–112]. Each of these methods has its own pros and cons. In general, compared to energy minimization approaches, they all require much more computational time, and they are more imprecise and less reliable in calculating the fluid-fluid interface shape in the equilibrium limit, as they are focused on the dynamics of the fluids. Therefore, as in this thesis we do not include fluid dynamic effects and we are interested only in equilibrium shapes of fluid-fluid interfaces, we will follow a minimum-energy approach.

4.2 NUMERICAL METHOD DESCRIPTION

In this Section we describe the basic mechanism of our new numerical method to predict the equilibrium shape of a fluid-fluid interface. An illustrative algorithm to implement this method is reported in Appendix A for 2D systems (i.e. with translational symmetry, such that the fluid-fluid interface can be represented by a curved line in a 2D space), and in Appendix B for 3D systems (i.e. such that the fluid-fluid interface is a curved surface in a 3D space).

The basic idea of the method is to find the shape of the fluid-fluid interface that minimizes the (free) energy E [Eq. (2.24)]. This is done by numerically calculating the interface shape that minimizes the potential

$$\Xi_0 \equiv \gamma S + \gamma_1 W_1 + \gamma_2 W_2 + g \rho_1 \int_{V_1} z dx dy dz + g \rho_2 \int_{V_2} z dx dy dz, \quad (4.1)$$

with the constraint that the volumes V_1 and V_2 of fluid 1 and fluid 2 have a fixed input value. Here S , W_1 and W_2 are the area of the fluid 1-fluid 2, solid-fluid 1 and solid-fluid 2 interface, respectively. Note that S , W_1 , W_2 , V_1 , V_2 and Ξ_0 are functionals of the fluid-fluid interface shape. From the Lagrange multipliers theorem, it follows that we are minimizing, with respect to the interface shape, the energy

$$E = \Xi_0 - P_1 V_1 - P_2 V_2, \quad (4.2)$$

with the Lagrange multipliers P_1 and P_2 depending on the choice of V_1 and V_2 . The energy E in Eq. (4.2) is, indeed, the energy potential E defined in Eq. (2.24), with P_1 and P_2 the bulk pressure of fluid 1 and fluid 2, respectively. As proved in Sec. 2.5, the shape that minimizes E is the solution of the Young-Laplace Equation and Young's Law, i.e. is the equilibrium shape of the fluid-fluid interface. For convenience, instead of Ξ_0 [Eq. (4.1)], we numerically minimize, by keeping the fluid volumes constant, the potential $\Xi \equiv \Xi_0 - \Xi_C$, with $\Xi_C \equiv \gamma_1 \Sigma + g \rho_1 \int_V z dx dy dz$, $\Sigma \equiv W_1 + W_2$ and $V \equiv V_1 + V_2$, that is

$$\Xi = \gamma \left[S - W_2 \cos \theta + \ell^{-2} \int_{V_2} z d\mathbf{r} \right], \quad (4.3)$$

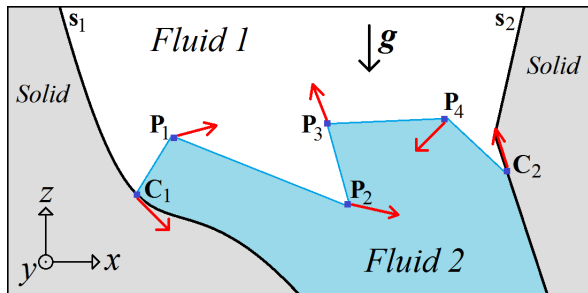
where $\cos \theta$ is defined using Young's Law [Eq. (2.18)] and ℓ is the capillary length

[Eq. (2.3)]. Note that Ξ_C does not depend on the fluid-fluid interface shape, so minimizing Ξ or Ξ_0 with respect to the interface shape is equivalent. Therefore, given the fluid volumes and the position of the solid surfaces, the input parameters that determine the equilibrium shape of the fluid-fluid interface are ℓ and $\cos \theta$.ⁱ

To focus on the basic mechanism of the method, we now describe its operating principles for systems with translational invariance along the Cartesian coordinate y , so that the fluid-fluid interface can be represented by a 2D profile. An illustrative algorithm to implement our method for more general 3D systems without symmetries is reported in Appendix B. We represent the interface profile using a set of points forming a 1D grid, as shown in Fig. 4.1. We indicate the two extreme points of the grid with \mathbf{C}_1 and \mathbf{C}_2 , which are constrained to stay on the imposed solid boundaries of the fluid-fluid system. We call *free points* the remaining points \mathbf{P}_i , with $i = 1, \dots, N$, and these are allowed to be wherever outside the solids in the (x, z) -plane. The interface is given by the set of segments linking any two consecutive points (by definition \mathbf{P}_{i+1} is consecutive to \mathbf{P}_i , \mathbf{P}_1 to \mathbf{C}_1 and \mathbf{C}_2 to \mathbf{P}_N). The fluid volume is set by the initial positions of the grid points. The interface equilibrium shape follows from the positions of the points that minimize Ξ [Eq. (4.3)] fulfilling the constraint of a fixed volume for the fluids. To find these positions, we apply a Simulated Annealing algorithm [113], that is an adaptation of a Monte Carlo method where a temperature-like parameter is introduced and gradually lowered during the simulation. This drives the system toward its minimum energy configuration in a way that resembles an annealing process, from which the name of the method. In our model we change randomly the point positions, keeping the fluid volumes V_1 and V_2 constant and not allowing unphysical configurations (for details see Appendixes A and B). Every configuration change is then accepted with probability

$$\mathcal{P} \equiv \begin{cases} 1, & \text{if } \Delta \Xi < 0 \\ \exp\left(-\frac{\Delta \Xi}{k_B T}\right), & \text{if } \Delta \Xi \geq 0 \end{cases} \quad (4.4)$$

Figure 4.1: Sketch of a fluid-fluid interface represented by a set of points P_1, P_2, \dots, P_N and attached to the solid walls in C_1 and C_2 . In the simulation, these points are moved until the configuration that minimizes Ξ [Eq. (4.3)], for the fixed volumes V_1 and V_2 of the fluids, is found.



ⁱBy definition, see Eq. (2.18) and Fig. 2.2, the Young's contact angle θ is taken inside fluid 2, which is by convention the heaviest of the two fluids and stays below the interface.

where $\Delta\Xi$ is the variation of Ξ [Eq. (4.3)] between the old and the new configuration of the points, T is the temperature-like control parameter, and k_B is the Boltzmann constant. In the simulation, these configuration changes are performed continuously while T is gradually lowered starting from an initial T_0 . When T reaches zero, the simulation ends. Thanks to the randomness involved, the Simulated Annealing has the advantage of providing escape routes out of metastable states, unlike energy-gradient methods. However, the speed of the T decrement and the initial value T_0 must be chosen slow and high enough, respectively, to ensure the minimum is found. To avoid metastable states, $k_B T_0$ needs to be much bigger than the energy barrier of these states. An adequate choice of T_0 and its decrement speed depend also on the discrepancy between the initial configuration of the points and the final solution. As a general rule: the slower is the decrement of T , the better is the approximation of the final solution. If different equivalent global minima of the energy are present, then the method finds randomly only one of these. A detailed description of an illustrative algorithm to implement our method for 2D and 3D systems is reported in Appendix A and B, respectively. Note that, in principle, our method can be adapted to work at constant pressure instead of at constant volume, by removing the constraint of a fixed volume, and by minimizing the potential E [Eq. (4.2)], instead of Ξ [Eq. (4.3)]. This can be useful, for example, for studying particles adsorbed at curved fluid-fluid interfaces.

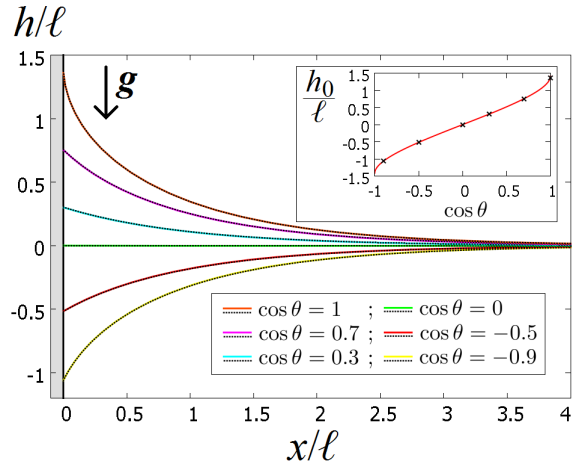
4.3 TESTS AND ILLUSTRATIVE RESULTS FOR 2D SYSTEMS

In this Section we illustrate results obtained from our method for 2D systems, using the algorithm described in Appendix A. The main aim is to validate our method with simple tests and show that it is applicable to a wide range of physical problems involving the equilibrium shape of fluid-fluid interfaces. All the systems shown here have translational invariance in the y direction, i.e. in the direction pointing out of the paper. The simulation parameters (N , T_0 , etc.) used in the algorithm of Appendix A for all the calculations in this Section are reported in Table 4.1.

4.3.1 MENISCUS CLOSE TO A VERTICAL WALL

First, to prove the accuracy of the method, we consider the case of a fluid-fluid interface in the half-space $x > 0$ close to a vertical wall located in the plane $x = 0$. As shown in Sec. 2.6.1, the height profile $h(x)$ of the meniscus is expressed by the inverse relation in Eq. (2.63). In Fig. 4.2 we show the interface profiles obtained from our numerical method with $N = 28$ free points of the grid for different values of $\cos\theta$. For comparison, we also plot the corresponding analytical solutions of Eq. (2.63), which are indistinguishable from our numerical curves. To reproduce the flatness of the meniscus for $x \rightarrow \infty$, we placed another vertical wall with contact

Figure 4.2: Height profiles $h(x)$ of fluid-fluid menisci with capillary length ℓ close to a vertical wall in the plane $x = 0$, for different contact angles θ . The full lines are obtained numerically from our algorithm and shifted in z to have the same asymptotic height for $x \rightarrow \infty$. The dotted lines are the analytical solutions from Eq. (2.63), indistinguishable from the numerical curves. In the inset, the numerical values of the capillary rise h_0 (black crosses) are compared with the analytic result (full line) of Eq. (2.58).



angle $\pi/2$ at $x = 20\ell$ (i.e. far beyond the scale of Fig. 4.2). All the numerical and analytical solutions shown are slightly shifted in z such that $h(20\ell) = 0$. The inset of Fig. 4.2 also shows excellent agreement between our numerical results and the analytic expression Eq. (2.58) of the contact height.

In Fig. 4.3 we study the influence of the number of points on the solution. We consider the system of Fig. 4.2 for the case $\cos \theta = 0.9$, and we show in Fig. 4.3 the numerical solutions we obtain using a grid with (a) $N = 3$, (b) $N = 8$, (c) $N = 18$, (d) $N = 38$ free points, respectively. For convenience the solution is shown for $0 \leq x \leq 10\ell$, while the right limit of the system is in $x = 20\ell$, so not all the points of the solution are visible in the figure. We see that even for a few points our numerical solution matches fairly well with the analytical one (dotted line). It is interesting to note that the density of points is higher where the interface is curved and lower in the flat region. The initial configuration, however, was an equally-spaced grid on the x -axis. Therefore during the simulation the points have spontaneously migrated to increase their density on the curved part of the interface. This disposition allows the points to optimize the energy and in this way to find the deepest minimum. In the insets of each graph of Fig. 4.3 we plot the energy Ξ [Eq. (4.3)] of the system with respect to the number of cyclesⁱⁱ performed in the simulated annealing process. The energy converges towards a minimum value in all the simulations, with a lower energy at higher number of grid points N , i.e. the approximation of the numerical solution improves by increasing N . Therefore, a good way to choose a proper value for N is to repeat the simulation using higher values of N , until the energy of the final solution does not vary anymore (within the desired precision). The relatively small number of points needed to describe the interface here is important to generalize to 3D systems, where a 2D grid is required to represent the interface.

ⁱⁱIn the algorithm reported in Appendix A, one cycle is completed every time the step “ l ” is executed.

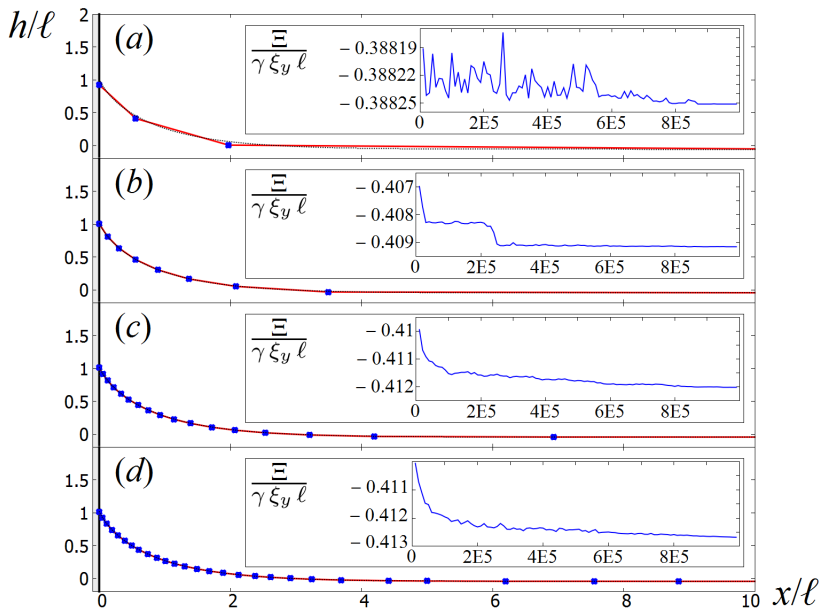


Figure 4.3: Height profile $h(x)$ of a fluid-fluid meniscus close to a vertical wall in $x = 0$ with contact angle θ and $\cos\theta = 0.9$. We show the numerical solutions obtained using a grid with varying number of free points [(a): $N = 3$; (b): $N = 8$; (c): $N = 18$; (d): $N = 38$] and the points are plotted in the graph. On the right in the half-space $x > 20\ell$ the fluid-fluid system is limited by a vertical wall with contact angle $\pi/2$. For convenience we show the solution only in the region $0 \leq x \leq 10\ell$. The dotted lines are the analytical solutions from Eq. (2.63) shifted in z to match our solutions at $x = 20\ell$. The initial configuration of the points is an equally-spaced grid on the x -axis. The final profiles indicate migration of the points during the simulation to pack more on the curved part of the interface. The insets show the behavior of the energy Ξ [Eq. (4.3), with ξ_y the length of the system in y] with respect to the number of cycles performed in the simulation. These graphs prove that during the simulation the system evolves toward configurations with lower energy, the more so for a larger number of grid points N .

4.3.2 MENISCUS BETWEEN FLAT AND/OR CURVED SURFACES

Our numerical method is very general and allows to consider solid boundaries of any shape, which is important for future studies of odd-shaped colloidal particles. Here we provide some examples, presenting results for fluid-fluid menisci located between inclined walls and/or curved solid surfaces. In Fig. 4.4 we show some numerical solutions for the shape of a meniscus between two inclined walls. The two walls are symmetric with respect to a central vertical axis, and, as expected, also the solutions fulfill this symmetry. Another indication of the correctness of our method is given by the contact angle that each numerical solution forms with the two solid surfaces. The geometrical value, say θ^* , of the contact angle of the meniscus with each solid surface is calculated from the positions of the point of the interface grid constrained on that surface and its first neighbor (\mathbf{P}_1

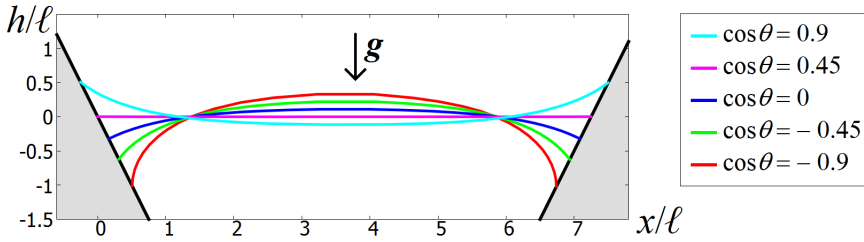
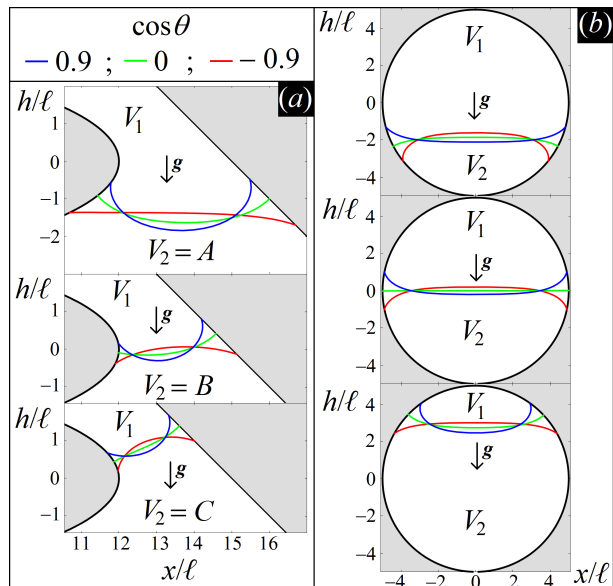


Figure 4.4: Height profiles $h(x)$ of fluid-fluid menisci between two inclined walls, with ℓ the capillary length. Each line is a solution obtained numerically from our algorithm using a certain value of $\cos \theta$ in the potential Ξ [Eq. (4.3)]. The volumes of the fluids are the same for every solution.

for \mathbf{C}_1 and \mathbf{P}_N for \mathbf{C}_2 , see Fig. 4.1). The obtained values of $\cos \theta^*$ for each solution match very well with the input parameter $\cos \theta$ in Ξ [Eq. (4.3)]. In particular, we find that $|\cos \theta^* - \cos \theta| < 0.05$ in all cases. A higher precision can be achieved by increasing the number of points N of the interface. In Fig. 4.5 we present analogous results for fluid-fluid menisci located (a) between a solid curved surface and an inclined wall, and (b) inside a cylindrical cavity with symmetry axis pointing out of the paper. In both these systems the numerical solutions are obtained using different values of $\cos \theta$, and different volumes for fluid 2 (the fluid below). We see that, as expected, the meniscus adapts its shape upon changing the fluid volume to keep its contact angles with the external surfaces constant. We point out, again, that we are not imposing a priori this constraint for the contact angles of the meniscus, but this is automatically obtained upon minimizing the energy Ξ [Eq. (4.3)] of the system.

Figure 4.5: Height profiles $h(x)$ of fluid-fluid menisci (a) between a solid curved surface and an inclined wall, and (b) inside a cylindrical cavity with symmetry axis pointing out of the paper. Each line is a solution obtained numerically from our algorithm using a certain value of $\cos \theta$ in the potential Ξ [Eq. (4.3)], with ℓ the capillary length. In each graph, the solutions are obtained by assigning a different volume V_2 to fluid 2, i.e. the one below the interface, with (a) $A < B < C$, and (b) from top to bottom $V_2/V = 0.23$, $V_2/V = 0.5$, and $V_2/V = 0.83$.



4.3.3 CAPILLARY INTERACTIONS

Here we present results on the capillary interaction between two vertical and parallel walls, although solid surfaces with any other shape can be taken into account as well. In Fig. 4.6 we consider a system of two vertical walls, each of width ℓ , immersed in the fluid-fluid interface and at a surface-to-surface distance D from each other. The origin of the x axis is in the middle between the two walls. The whole fluid-fluid system is enclosed between two external vertical walls in the half-planes $x < -15\ell$ and $x > 15\ell$, respectively, far beyond the scale of the graphs in Fig. 4.6. Three one-dimensional grids of points are necessary to represent the interface: one set between the two inner central walls and the other two between the external walls and the central walls. During the simulation, fluid 2 can exchange volume between these three regions, but the sum of the volumes below the three interfaces is kept constant. The central wall on the left has contact angle θ_l , the one on the right θ_r . We assign a contact angle $\theta = \pi/2$ to the two external walls, to induce a flat meniscus far from the two central walls in order to mimic an infinitely extended system. To consider in our model the presence of solid surfaces with different contact angles, we generalize Ξ [Eq. (4.3)] as

$$\Xi = \gamma \left[S - \sum_k W_2(k) \cos \theta_k + \ell^{-2} \int_{V_2} z \, d\mathbf{r} \right], \quad (4.5)$$

where the k -sum is over all the walls, θ_k is the contact angle of the k -th solid surface and $W_2(k)$ is its surface area in contact with fluid 2. In Fig. 4.6 we have $k = 2$, with the two walls referred to as left (l) and right (r). The shape of the fluid-fluid interface is calculated for several surface-to-surface distances between the left and right wall, using as contact angles (a) $\cos \theta_l = \cos \theta_r = 0.8$, (b) $\cos \theta_l = \cos \theta_r = -0.5$, and (c) $\cos \theta_l = 0.8$, $\cos \theta_r = -0.5$. In Fig. 4.6(a) we see the capillary rise of the interface obtained by decreasing D , and in Fig. 4.6(b) we see the capillary drop. The height of the capillary rise is greater than the depth of the capillary drop - at the same D - because in the former case the contact angle has a larger absolute value. In case (c), we see the interface shape due to the interplay between a capillary rise and drop. For each of the cases (a), (b), (c) of Fig. 4.6, we report on the very right the effective potential $\Xi(D)$ and the force $F(D)$ of the capillary interaction between the two central walls, defined as $F \equiv d\Xi/dD$. Here $\Xi(D)$ [Eq. (4.5)] is computed from the equilibrium shape of the fluid-fluid interface as described in Appendix A. In the insets we show $\Xi(D)$ shifted to be zero at $D = 5\ell$. We consider F only for $D \leq 5\ell$, such that the minimum distance between the central walls and the external walls always exceeds 10ℓ . So we can reasonably assume that the effects of the external walls on F are negligible. For both the cases (a) and (b) we see an attractive force. In (a) the force is stronger than in (b) because the absolute value of the contact angle is greater. In (c) we observe a repulsive force at large separations due to the fact that $\cos \theta_l$ and $\cos \theta_r$ have different signs. However, there is a maximum in

$\Xi(D)$ for $D \simeq 0.5 \ell$ and so an attractive force between the walls exists when they are closer than about 0.5ℓ . This is caused by the different absolute value of $\cos \theta_l$ and $\cos \theta_r$ which generates a slight capillary rise for small D , as we can see in Fig. 4.6 (c). In Fig. 4.7 we report the D dependence of the capillary rise h_c between the two walls at $x = 0$, for the cases (a) and (b) of Fig. 4.6. The reference level $z = 0$ is the height of the interface at $x = \pm 15\ell$. Our numerical values (symbols) are compared with the approximate analytical result (line) given by

$$h_c = \frac{2 \ell^2}{D} \cos \theta . \quad (4.6)$$

Eq. (4.6) follows from the approximation that the meniscus between two narrow vertical walls has a cylindrical shapeⁱⁱⁱ. To check this, use that the mean curvature

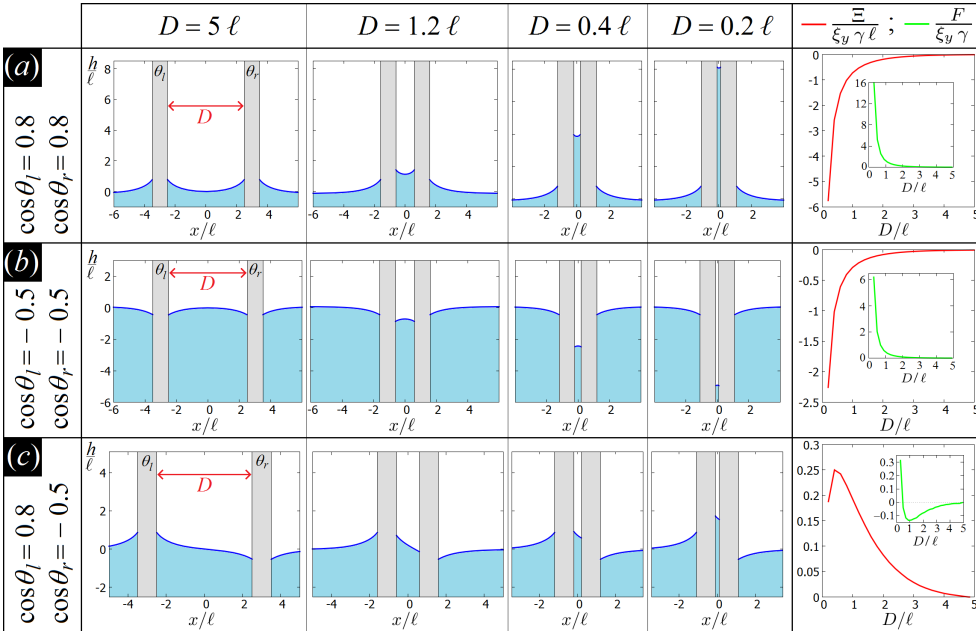


Figure 4.6: (Left) Height profile of a horizontal fluid-fluid interface in contact with two vertical walls of width equal to the capillary length ℓ . The system has translational invariance in the y direction, i.e. perpendicularly to the plane, and it is limited by two external walls with contact angles $\pi/2$ in the half-spaces $x > 15\ell$ and $x < -15\ell$, beyond the scale of the plot. The central wall on the left has contact angle θ_l , the one on the right θ_r . The interface shape is calculated numerically by our method and it is shown for different surface-to-surface distances D between the walls, for (a) $\cos \theta_l = \cos \theta_r = 0.8$, (b) $\cos \theta_l = \cos \theta_r = -0.5$, (c) $\cos \theta_l = 0.8$, $\cos \theta_r = -0.5$. (Right) The effective interaction potential $\Xi(D)$ [Eq. (4.5)] of the system, with γ the fluid-fluid surface tension and ξ_y the length of the system in the y direction. The capillary force $F(D) \equiv d\Xi/dD$ acting between the walls is plotted in the insets.

ⁱⁱⁱIndeed, if the distance between the two walls is much smaller than the capillary length, then gravity effects are small and so the mean curvature of the meniscus is almost constant.

$\nabla \cdot \hat{\mathbf{n}}/2$ of a surface can be written as $-(R_1^{-1} + R_2^{-1})/2$, where R_1 and R_2 are the two principal radii of curvature. For the central point of a meniscus with cylindrical shape $R_1 = R$, with R the radius of the circular section of the cylinder, and $R_2 = \infty$. Then applying Eq. (2.2) for $x \rightarrow \pm 15\ell$, it follows $\Delta P = 0$, because here $\nabla \cdot \hat{\mathbf{n}} = 0$, as the interface is flat, and $h = 0$ for the choice of the reference level. So the Young-Laplace Equation [Eq. (2.2)] for the central point of the meniscus becomes: $1/R = h_c/\ell^2$. Eq. (4.6) follows using that $D = 2R \cos \theta$ [see Fig. 4.6 (c), right panel]. The agreement of our numerical values with Eq. (4.6) is quite good for $D < \ell$, confirming that the approximation of a cylindrical shape for the meniscus is good for small D .

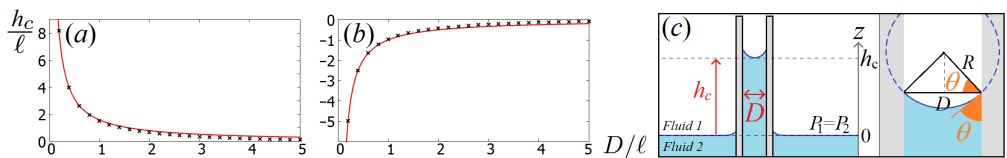


Figure 4.7: Capillary rise h_c of the central point of a meniscus between two vertical walls for (a) $\cos \theta = 0.8$ and (b) $\cos \theta = -0.5$, with respect to the surface-to-surface distance D between the walls (the meniscus equilibrium shape is shown for some values of D in Fig. 4.6). The symbols are our numerical values, the line is the analytical result from Eq. (4.6), obtained by approximating the meniscus with a cylindrical shape. Our results confirm that the larger is D , the poorer is this approximation. In (c) a meniscus with a cylindrical shape is sketched.

4.3.4 2D SESSILE AND PENDANT DROPLETS

In this Section we show that our numerical method is usable also for studying equilibrium shapes of droplets wetting flat or curved solid surfaces, including, possibly, the effects of gravity. Note that here we consider only 2D droplets, while results for 3D droplets are presented in Chapters 7 and 8. In Fig. 4.8(a) we report the equilibrium shape of a 2D sessile droplet on a flat solid surface. The droplet is formed by fluid 2, which is the heavier of the two fluids. The numerical solutions are computed using different values of the capillary length ℓ and the contact angle θ in Ξ [Eq. (4.3)]. For a fixed γ , decreasing ℓ means increasing $\Delta\rho$ [see Eq. (2.3)]. Indeed, in each graph of Fig. 4.8, for droplets with the same volume and contact angle, the effect of the gravity on the droplet shape increases by lowering ℓ . As shown, our method is able to treat also cases with very low wettability [see the case $\cos \theta = -0.9$ in Fig. 4.8(a)]. As another indication of the correctness of the method, the equilibrium shapes are symmetric with respect to a central symmetry axis (in the figure the solutions are shifted in x to align their symmetry axes). In Fig. 4.8(b) we show analogous results, but obtained

Note, however, that gravity is not negligible in this system.

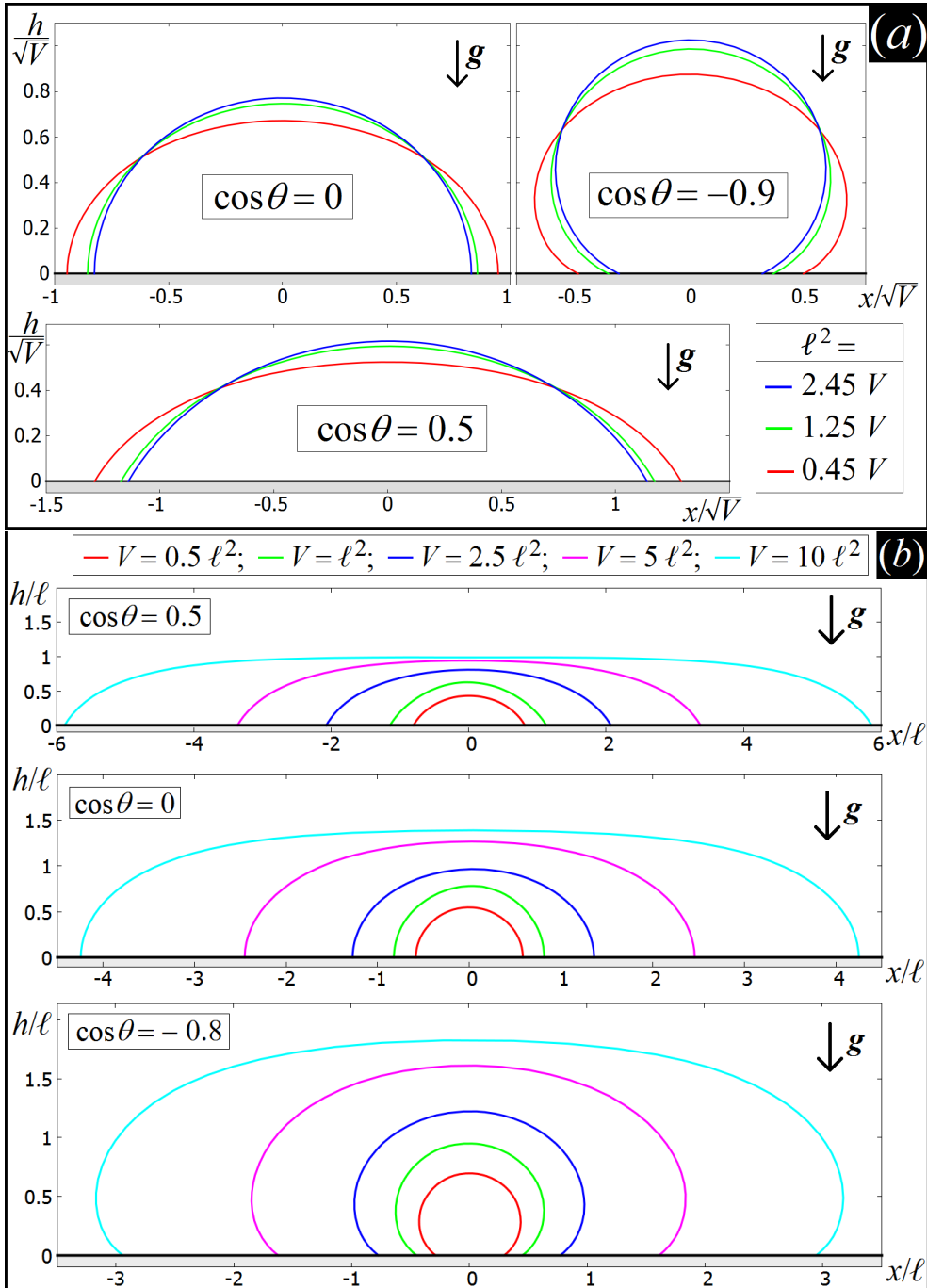


Figure 4.8: Equilibrium height profile $h(x)$ of a 2D sessile droplet on a flat solid surface. The fluid forming the droplet is heavier than the fluid outside. The solutions are obtained numerically from our method using different values of $\cos\theta$ in Ξ [Eq. (4.3)]. (a) The capillary length ℓ is varied, while the 2D volume V of the droplet is kept fixed. As expected, our solutions show, for a fixed $\cos\theta$, an increasing flattening of the droplet shape with decreasing ℓ . (b) The capillary length ℓ is kept fixed, and V is tuned.

using a fixed value of ℓ and tuning the volume of the droplet. Note that, as analytically proved in Sec. 2.6.2, a 2D droplet wetting a flat solid surface has a circular segment shape in the limit $\ell \rightarrow \infty$ (or, equivalently, $V \rightarrow 0$).

In Fig. 4.9 we show equilibrium shapes of 2D droplets pending (a)-(b) from a flat horizontal solid surface and (c) from a highly curved solid surface. Here, fluid 2 forms a droplet that is located above the lighter fluid 1. The droplet does not fall down because it is wetting an upper solid surface that keeps it in mechanical and thermodynamical metastable equilibrium. Such a situation is obtained in our model by changing the sign of the gravity vector, i.e. expressing Ξ as

$$\Xi = \gamma \left[S - W_2 \cos \theta - \ell^{-2} \int_{V_2} z \, d\mathbf{r} \right], \quad (4.7)$$

instead of using Eq. (4.3). Note that also a sessile droplet formed by a fluid lighter than the surrounding fluid has an energy given by Eq. (4.7), with the minus sign multiplying ℓ^2 due to a negative $\Delta\rho$ [see Eq. (2.3)]. Therefore, the results we present for pendant droplets are likewise valid for sessile droplets lighter than the surrounding fluid.

In Fig. 4.9(a) the equilibrium shapes of pendant droplets from a flat solid surface are numerically obtained using different values of ℓ and $\cos \theta$, for a fixed droplet volume V . In Fig. 4.9(b) analogous results are shown, but varying the 2D volume V of the pendant droplet and keeping constant ℓ . As an indication of the correctness of our method, the equilibrium shapes are symmetric with respect to a central symmetry axis (in the plots, the solutions are shifted in x to align their axes). As expected, these results show that by decreasing ℓ in (a) and increasing V in (b), the effect of gravity on the droplet shape becomes stronger. If ℓ is too low, or V too big, then all the free points of the interface grid, instead of going toward an asymptotic shape, keep going in the direction of \mathbf{g} until the simulation stops. This corresponds to the physical situation in which gravity is too strong, so the pendant droplet is not stable and prefers to detach itself or partially fall down. Note, however, that unstable pendant droplets could still seem stable using our method, if the simulated annealing is not slow enough or T_0 not high enough, because the grid points get frozen in a metastable state before they manage to fall down. For a 2D droplet pending from a flat solid surface the stability condition can easily be found analytically. Indeed, see Fig. 4.9(c), the modulus of the total surface tension force keeping the droplet attached to the solid is $2\gamma \sin \theta$, while $F_g = g V \Delta\rho = \gamma V / \ell^2$ is the modulus of the gravitational force pulling the droplet down. So the 2D pendant droplet is unstable if $V > 2\ell^2 \sin \theta^{\text{iv}}$.

In Fig. 4.9(d) we show analogous results, but for the equilibrium shape of droplets pending from a highly curved solid surface. The solid surface is symmetric with respect to a central symmetry axis, and indeed - for fixed $\cos \theta$, ℓ , and droplet volume - two different solutions exist, one being the mirror image of the other

^{iv}For a 3D droplet pending from a flat surface, this condition becomes $V > d\pi\ell^2 \sin \theta$, with d the diameter of the circular solid surface wet by the droplet.

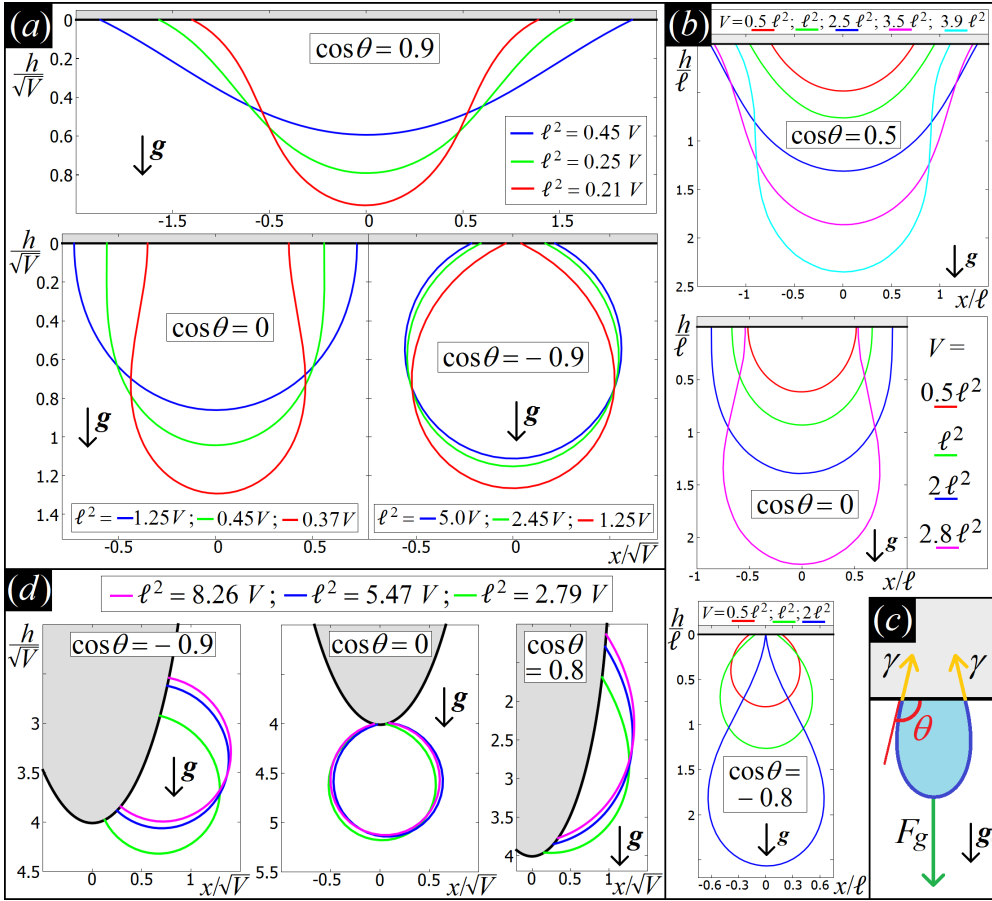


Figure 4.9: Equilibrium height profile $h(x)$ of 2D pendant droplets. The fluid forming the droplet is heavier than the fluid outside. The solutions are obtained numerically from our method using different values of $\cos\theta$ in Ξ [Eq. (4.7)]. (a)-(b) 2D pendant droplets from a flat solid surface. In (a) the capillary length ℓ is varied, while the 2D volume V of the droplet is kept fixed. As expected, our solutions show, for a fixed $\cos\theta$, an increasing flattening of the droplet shape with decreasing ℓ . In (b) the capillary length ℓ is kept fixed, and V is tuned. (c) Sketch of a droplet pending from a flat surface. The droplet is unstable if the gravitational force pulling it down is stronger than the surface tension force keeping it attached to the solid. (d) 2D droplets pending from a highly curved solid surface. Here the droplet volume is constant and ℓ is tuned. As shown, by tuning $\cos\theta$, the droplet prefers to wet a solid surface with different curvature.

with respect to this axis (in a single simulation our method finds randomly one of these two solutions, and in the graphs we show only the solutions on one side of the solid surface). Note that the minimum-energy equilibrium shape of the pendant droplet changes its position on the curved surface by tuning $\cos\theta$. For high contact angles the droplet prefers a lowly curved convex surface, for low contact angles it prefers a highly curved convex surface. This allows the droplet to have a

shape as close as possible to a circle, while fulfilling Young's Law. Therefore the final position of the droplet on the heterogeneously curved solid surface is given by an interplay between gravitational force, fluid-fluid and fluid-solid interactions.

4.4 TESTS AND ILLUSTRATIVE RESULTS FOR 3D SYSTEMS

Our primary goal is to apply our numerical method to study micro and nano-sized colloidal particles adsorbed at a fluid-fluid interface. In Appendix B we report a detailed description of an illustrative basic algorithm to implement our method for the equilibrium shape of a fluid-fluid interface, flat if no particles are present, when in contact with an isolated 3D colloidal particle with a given position and orientation. In this Section we present results obtained through this algorithm, to validate and verify the correctness and accuracy of the method for 3D systems,

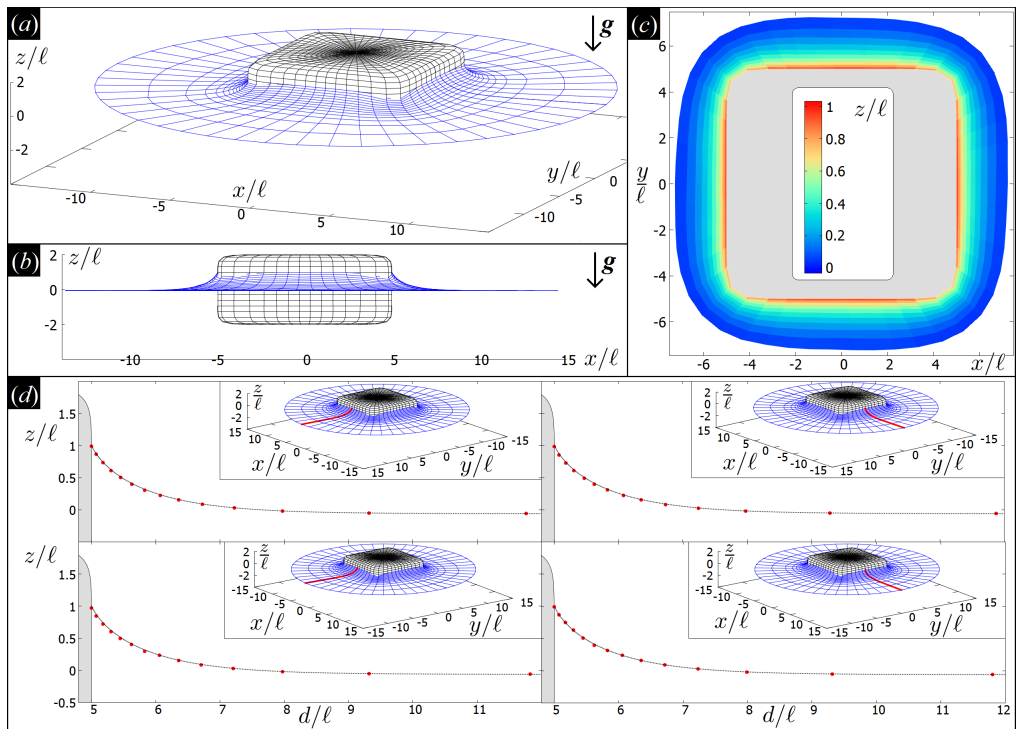


Figure 4.10: (a) 3D view, (b) profile view and (c) contour plot of the height profile of the fluid-fluid interface (blue grid), as obtained from our numerical method, close to a parallelepiped-shaped solid particle (black grid) with fixed position and Young's contact angle θ ($\cos \theta = 0.9$). (d) 2D height profiles of the fluid-fluid interface along the red lines shown in the insets, where the red dots are the interface grid points. With d we indicate the distance from the z axis. The system is externally surrounded by a vertical cylindrical wall, at a distance 15ℓ from the central axis, with Young's contact angle $\pi/2$. The dotted line is the analytical solution of Eq. (2.63), shifted in z to match our numerical solution in $d = 15\ell$.

and to show its applicability to adsorbed solid particles at fluid-fluid interfaces.

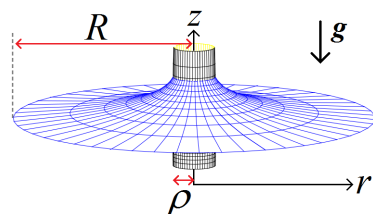
4.4.1 TEST OF THE VERTICAL WALL

To test the correctness of our method, we calculate here the deformations of a fluid-fluid interface close to a vertical wall. As proved in Sec. 2.6.1, the height profile of the fluid-fluid interface with respect to the distance from the wall can be expressed analytically by the inverse relation in Eq. (2.63). To obtain this situation in our model, we consider (see Fig. 4.10) a parallelepiped-shaped solid particle with center of mass in $(0, 0, 0)$, in horizontal position, with height 4ℓ and sides of length 10ℓ aligned to the x and y directions respectively, where ℓ is the capillary length [Eq. (2.3)], and a Cartesian coordinate system (x, y, z) with z anti-parallel to the gravity \mathbf{g} is introduced. The particle has a fixed position, and the deformation of the fluid 1-fluid 2 interface is computed, using our method, with respect to the desired Young's contact angle θ . The fluid volumes are defined by the initial position of the fluid-fluid interface in the simulation, which is the $z = 0$ plane. Each vertical face of the particle is large enough with respect to ℓ to be considered as a vertical wall, at least toward its center, far from the edges. Therefore, we expect that the meniscus along the x and y axes follows Eq. (2.63). The whole particle-fluid-fluid system is enclosed by a vertical cylindrical wall at distance $R = 15\ell$ from the origin, and with Young's contact angle $\pi/2$. In Fig. 4.10 we show the equilibrium shape of the fluid-fluid interface for $\cos\theta = 0.9$. In Fig 4.10(d) we compare the height profiles of the meniscus along the x and y axes with Eq. (2.63), showing an excellent agreement.

4.4.2 FINITE-SIZE EFFECTS

To exploit our method for studying colloidal particles adsorbed at flat fluid-fluid interface, we consider a fluid-fluid interface surrounded by an external vertical wall with Young's contact angle $\pi/2$, and then we compute the equilibrium shape of the interface when colloidal particles with a certain position and orientation are placed at the interface (see Appendix B for details). As we want to model a flat fluid-fluid interface far from the particles, it is important to estimate how far the external wall is to be placed from the particles to avoid that its presence

Figure 4.11: Sketch of the system considered in Sec. 4.4.2: a infinitely-high vertical solid cylinder (black grid), with radius ρ and Young's contact angle θ , in contact with a fluid-fluid interface (blue grid) with height profile $h(r)$, with r the distance from the cylinder symmetry axis. Externally, the fluid-fluid interface is surrounded in $r = R$ by a vertical wall (not shown in the picture) with Young's contact angle $\pi/2$. The gravity direction is opposite to z .



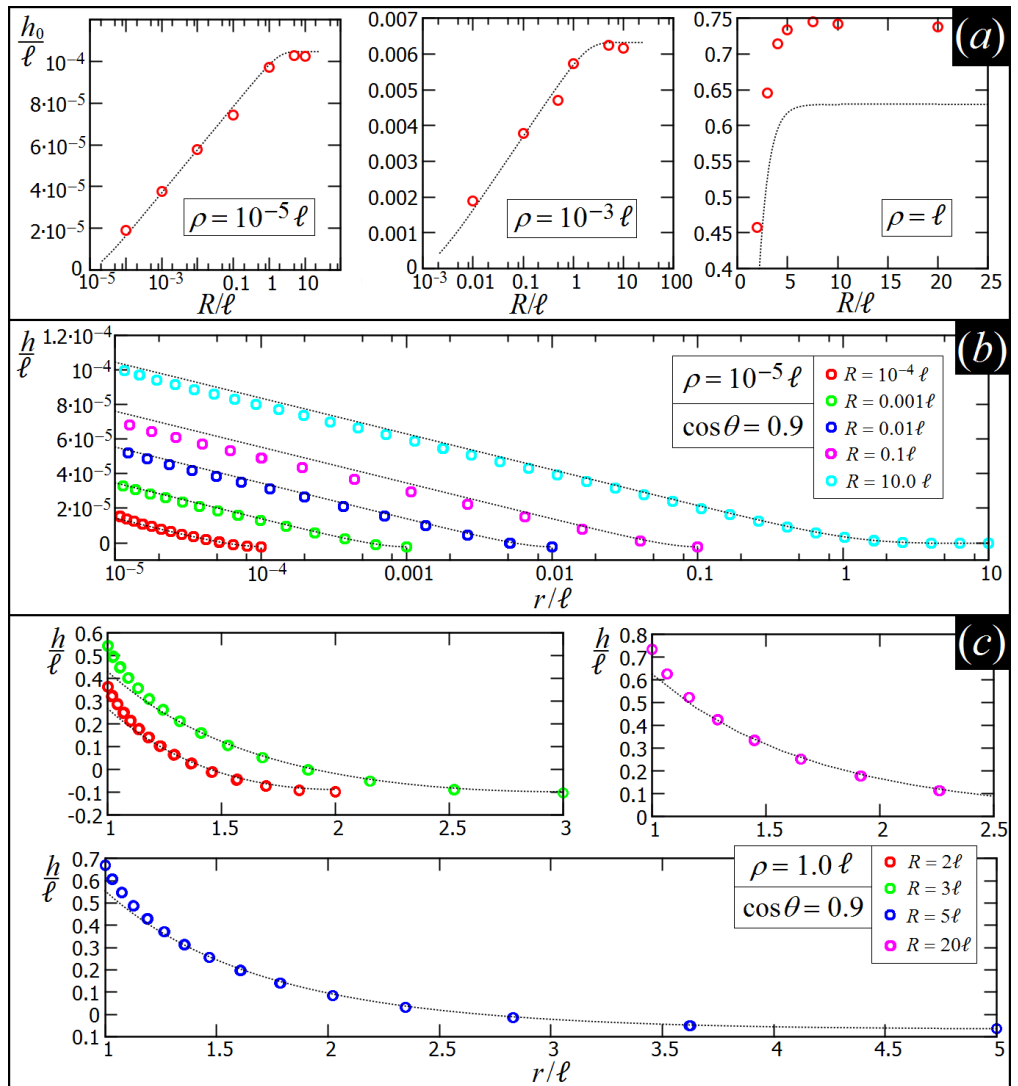


Figure 4.12: (a) Capillary rise h_0 [Eq. (4.8)] of a meniscus on a vertical cylinder with radius ρ and Young’s contact angle θ (with $\cos\theta = 0.9$), with respect to the radius R of the vertical wall enclosing the system and with Young’s contact angle $\pi/2$. The dotted line is the analytical prediction [Eq. (3.34)] obtained using the linear approximation for the Young-Laplace Equation, which matches fairly well our numerical results (circles) for $\rho = 10^{-5}\ell$ and $\rho = 10^{-3}\ell$. Instead, for $\rho = \ell$, Eq. (3.34) is less accurate, because here the amplitude of the capillary deformations is of the order of ℓ , so the linear approximation is poorer. (b)-(c) Height profile $h(r)$ of the fluid-fluid interface between the external wall in $r = R$, and the vertical cylinder of radius (b) $\rho = 10^{-5}\ell$, and (c) $\rho = \ell$. The circles are the grid points as obtained by our numerical method, while the dotted line is the analytical prediction of Eq. (3.26), obtained by the linearized Young-Laplace Equation.

affects the results. For this purpose, we consider here (see Fig. 4.11) a solid (infinitely-high) vertical cylinder of radius ρ with symmetry axis coinciding with the z axis. The fluid-fluid interface, described by the height profile $h(r)$, with $r = \sqrt{x^2 + y^2}$, externally is in contact with a vertical cylindrical wall in $r = R$, and with Young's contact angle $\pi/2$. By our numerical method, we calculate the equilibrium shape of the fluid-fluid interface for $\cos\theta = 0.9$, with θ the Young's contact angle of the vertical solid cylinder in the center. In Fig. 4.12(a), the capillary rise h_0 , given by

$$h_0 \equiv h(\rho) - h(R), \quad (4.8)$$

is plotted with respect to R .^v Our numerical results (circles) are compared with the analytical prediction of Eq. (3.34) for h_0 , obtained using the linear approximation for the Young-Laplace Equation (see Sec. 3.6). The analytical prediction matches fairly well our numerical results for $\rho = 10^{-5}\ell$ and $\rho = 10^{-3}\ell$. Instead, for $\rho = \ell$, Eq. (3.34) is less accurate, because in this case the amplitude of the capillary deformations is of the order of ℓ , so the linear approximation is poorer. Figure 4.12(a) shows that for $R \gtrsim 5\ell$ the effects of the external wall on the system are negligible, because the capillary rise h_0 is constant in this regime. This is true for all the values of ρ considered, i.e. $\rho = \ell$, $\rho = 10^{-3}\ell$, and $\rho = 10^{-5}\ell$, so ℓ is the characteristic length that sets the interaction range between the external wall and the solid cylinder in the center. Note, however, that here we consider an infinitely-high solid cylinder, allowing h_0 to be much bigger than ρ , while the capillary deformations close to colloidal particles adsorbed at the interface are necessarily limited by the particle size.^{vi} In Fig. 4.12(b)-(c) we show, for $\rho = 10^{-5}\ell$ and $\rho = \ell$, the height profile $h(r)$ for several values of R , as obtained by our numerical method (circles) and by the analytical prediction of Eq. (3.26). As shown, in the case $\rho = \ell$ the linear approximation is less precise in predicting $h(r)$ than in the case $\rho = 10^{-5}\ell$, where the exact solution, neglecting the numerical approximations, is given by the minimum energy solution obtained by our numerical method.

^vNote that is the fluid-fluid interface height profile $h(r)$ that changes by tuning R .

^{vi}In the limit of negligible gravity, i.e. $\ell \rightarrow \infty$, the particle size is the characteristic length that sets the amplitude of the capillary deformations induced by the adsorbed particles, and so it also sets the range of the capillary interactions between the particles. In Chapter 5, this situation is studied in detail.

4.4.3 CAPILLARY RISE *vs* PARTICLE CURVATURE

In this Section we study the capillary rise of a meniscus on a vertical cylinder with respect to the cylinder radius of curvature. The system considered is the same of the previous Section, see Fig. 4.11, with θ the Young's contact angle of the vertical cylinder, ρ the radius of the cylinder and R the radius of the external vertical wall (with Young's contact angle $\pi/2$) surrounding the system. We set $R = \rho + 10\ell$, which is, as proved in the previous Section, big enough to avoid finite-size effects on the system. In Fig. 4.13, we show, for $\cos \theta = 0.9$, the capillary rise $h_0 = h(\rho)$, as obtained by our numerical method (red dots), and as obtained by the analytical prediction of Eq. (3.21) (black line), from the linearized Young-Laplace Equation.^{vii} As shown, the agreement between our numerical results and the analytical predictions is excellent for $\rho < 0.1\ell$, while it becomes slightly worse for bigger ρ , as here the linear approximation of the Young-Laplace Equation is poorer.

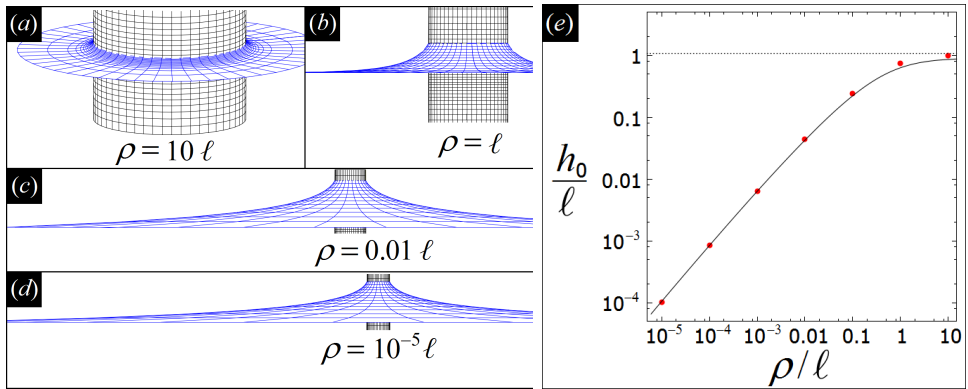


Figure 4.13: In (a), (b), (c), (d), we show a 3D view of the fluid-fluid interface equilibrium shape (blue grid) close to a vertical cylinder (black grid) with Young's contact angle θ and radius ρ , as obtained by our numerical method, for $\cos \theta = 0.9$ and $\rho = 10\ell$, $\rho = \ell$, $\rho = 0.01\ell$, and $\rho = 10^{-5}\ell$, respectively, with ℓ the capillary length. In (e) we show the capillary rise h_0 (i.e. the height of the meniscus in contact with the cylinder on the level of the interface far away from the cylinder) as obtained by our numerical method (red dots), and as obtained by Eq. (3.21) (black line). The horizontal dotted line is the capillary rise of a meniscus on a vertical wall with $\cos \theta = 0.9$, as obtained by Eq. (2.58), and corresponds to the case $\rho/\ell \rightarrow \infty$.

^{vii}Note that here, as we are choosing R big enough to avoid finite size effects, we obtain from our numerical method that $h(R) \approx 0$, and therefore the capillary rise is $h_0 \equiv h(\rho) - h(R) \approx h(\rho)$. For this reason, to compare our numerical results with the analytical predictions of the linearized Young-Laplace Equation, we can use Eq. (3.21), which holds for $R = \infty$.

4.4.4 MULTIPOLE EXPANSION

In this Section we study the multipole expansion [Eq. (3.14)] introduced in Chapter 3 to describe the height profile $h(r, \phi)$ of the capillary deformations induced by a particle adsorbed at a flat fluid-fluid interface. For this purpose, we consider a spherical particle at the interface, and a pinned undulated three-phase contact line on the sphere surface. Given the position of the pinned three-phase contact line, we calculate by our numerical method the equilibrium shape of the fluid-fluid interface, using the algorithm described in Appendix B, and we compare these numerical results with the analytical predictions of Eq. (3.14).

In our model, the sphere center of mass height is $z_c = 0$, with the $z = 0$ plane corresponding to the flat fluid-fluid interface. The z axis is antiparallel to the gravity and passes through the sphere center of mass, r is the radial distance from the z axis, and ϕ is the azimuthal angle with respect to the z axis. The sphere has radius $\rho = 0.01\ell$, with ℓ the capillary length. The pinned three-phase contact line height profile $h(r, \phi)$ is described by

$$h(r_0, \phi) = A_0 K_0(r_0/\ell) + \sum_{m=1}^4 A_m K_m(r_0/\ell) \cos(m\phi - B_m), \quad (4.9)$$

where r_0 is the radial distance of the three-phase contact line, and we assume it as a constant not depending on ϕ .^{viii} In Figs. 4.14, 4.15, 4.16, 4.17, 4.18, 4.19, and 4.20, we show $h(r, \phi)$, as obtained numerically from our method, for different values of A_i and B_j (for $i = 0, \dots, 4$, $j = 1, \dots, 4$) in Eq. (4.9). We also compare these numerical results with the analytical predictions of Eq. (3.14), obtained from the linearized Young-Laplace Equation. In Eq. (3.14) we use the coefficients A_i and B_j used in Eq. (4.9) for $i = 0, \dots, 4$, $j = 1, \dots, 4$, and we set to zero the coefficients for $i > 4$, $j > 4$. In the left and central panels of such figures, we show the height profile $h(r, \phi)$ for a fixed r and with respect to ϕ , where the red circles are the numerical results from our method, and the black dotted line is the analytical prediction of Eq. (3.14). In the right panels of such figures, we show a contour plot and a 3D view of interface equilibrium shape close to the particle, as obtained by our numerical method. In Figs. 4.14, 4.15, 4.16, 4.17, and 4.18, is shown, respectively, a monopolar, dipolar, quadrupolar, hexapolar and octapolar capillary deformation field induced by the sphere in the flat fluid-fluid interface. In Figs. 4.19 and 4.20, the capillary deformation field is defined by combining different multipoles. As shown, a multipole with a lower order decays slower than a multipole with a higher order. Therefore, far away from the sphere, the height profile of the interface, with respect to ϕ and at a constant r , corresponds to the multipole with lowest order appearing in Eq. (4.9).

^{viii}This is actually not true. The radial distance $r_0(\phi)$ of the three-phase contact line on the sphere surface in general depends on ϕ (it would be constant if we had a vertical cylinder). However, defining r_0 as the average value of $r_0(\phi)$ with respect to ϕ , we will consider only three-phase contact lines where $r_0(\phi)$ varies of max 2% – 3% from r_0 , so we can approximate $r_0(\phi)$ with r_0 .

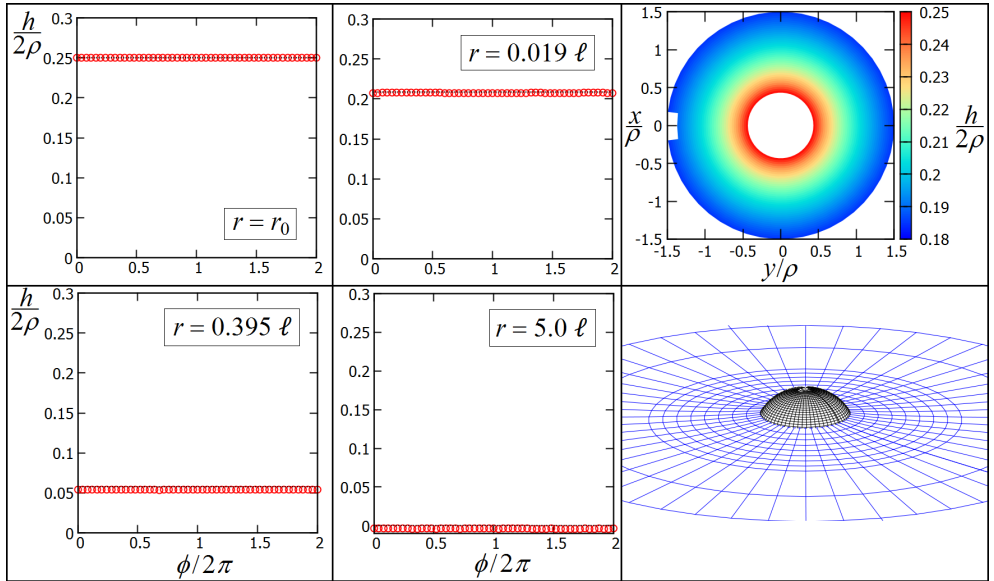


Figure 4.14: Height profile $h(r, \phi)$ of a fluid-fluid interface induced by a sphere with a pinned three-phase contact line given by $h(r_0, \phi) = 0.5 \rho$, which is Eq. (4.9) using $A_0 = 0.5\rho/K_0(r_0/\ell)$, $A_1 = 0$, $A_2 = 0$, $A_3 = 0$, $A_4 = 0$, $B_1 = 0$, $B_2 = 0$, $B_3 = 0$, $B_4 = 0$, and $r_0 = 0.864 \rho$.

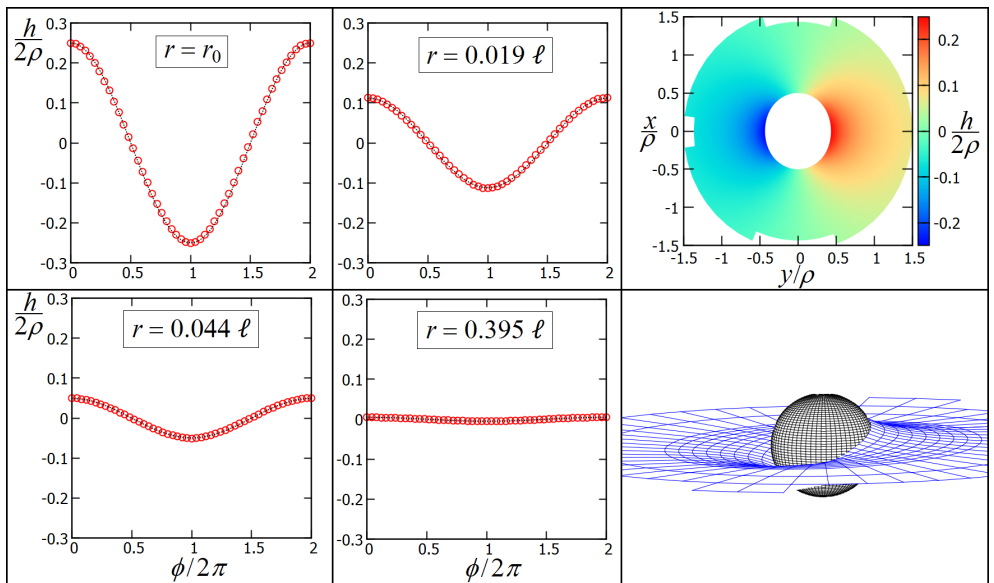


Figure 4.15: Height profile $h(r, \phi)$ of a fluid-fluid interface induced by a sphere with a pinned three-phase contact line given by $h(r_0, \phi) = 0.5 \rho \cos(\phi)$, which is Eq. (4.9) using $A_0 = 0$, $A_1 = 0.5\rho/K_1(r_0/\ell)$, $A_2 = 0$, $A_3 = 0$, $A_4 = 0$, $B_1 = 0$, $B_2 = 0$, $B_3 = 0$, $B_4 = 0$, and $r_0 = 0.864 \rho$.

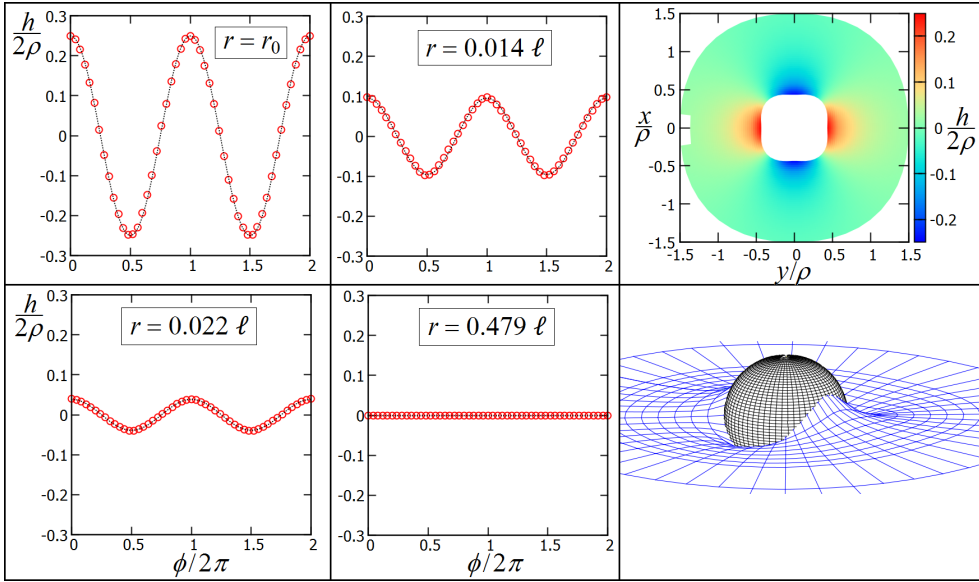


Figure 4.16: Height profile $h(r, \phi)$ of a fluid-fluid interface induced by a sphere with a pinned three-phase contact line given by $h(r_0, \phi) = 0.5 \rho \cos(2\phi)$, which is Eq. (4.9) using $A_0 = 0$, $A_1 = 0$, $A_2 = 0.5\rho/K_2(r_0/\ell)$, $A_3 = 0$, $A_4 = 0$, $B_1 = 0$, $B_2 = 0$, $B_3 = 0$, $B_4 = 0$, and $r_0 = 0.864 \rho$.

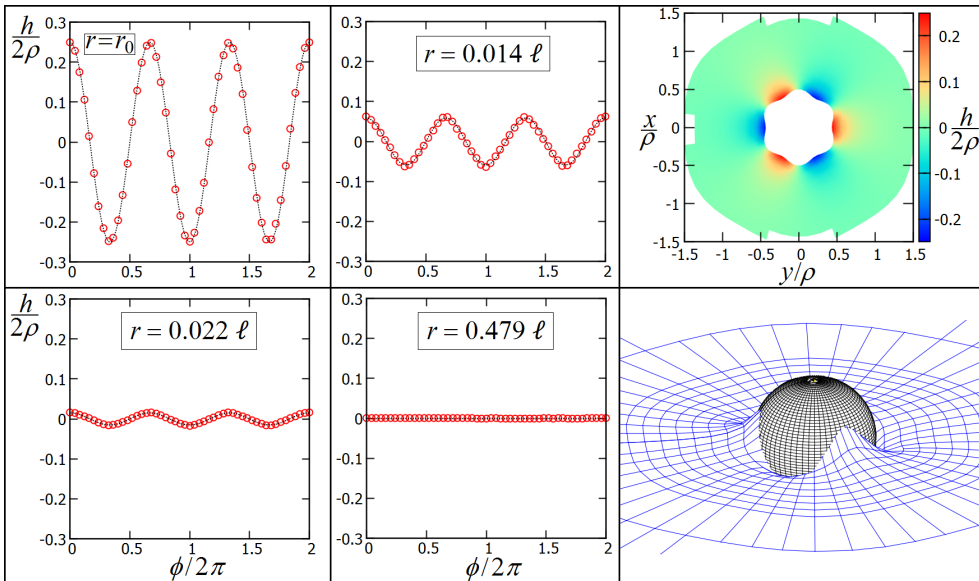


Figure 4.17: Height profile $h(r, \phi)$ of a fluid-fluid interface induced by a sphere with a pinned three-phase contact line given by $h(r_0, \phi) = 0.5 \rho \cos(3\phi)$, which is Eq. (4.9) using $A_0 = 0$, $A_1 = 0$, $A_2 = 0$, $A_3 = 0.5\rho/K_3(r_0/\ell)$, $A_4 = 0$, $B_1 = 0$, $B_2 = 0$, $B_3 = 0$, $B_4 = 0$, and $r_0 = 0.864 \rho$.

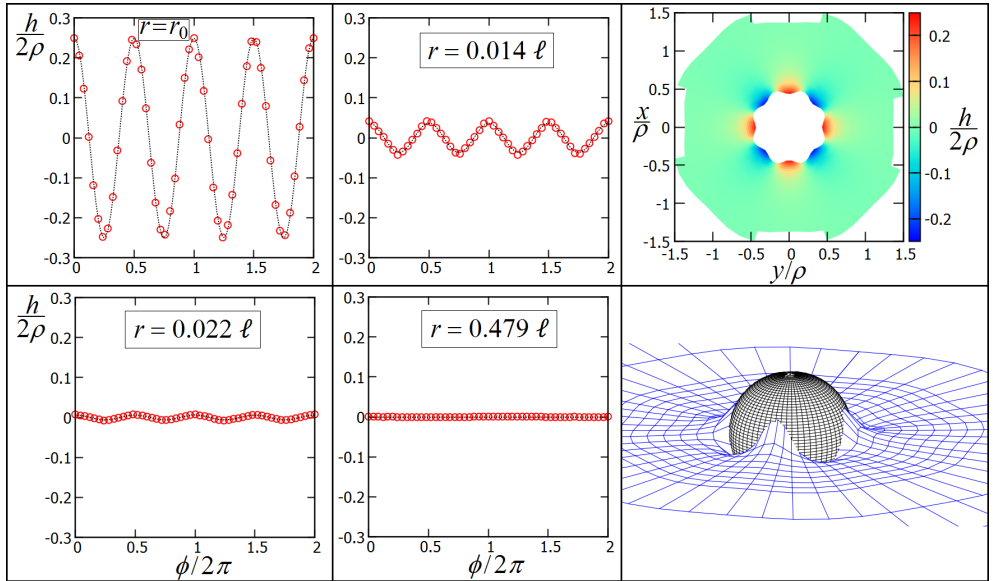


Figure 4.18: Height profile $h(r, \phi)$ of a fluid-fluid interface induced by a sphere with a pinned three-phase contact line given by $h(r_0, \phi) = 0.5 \rho \cos(4\phi)$, which is Eq. (4.9) using $A_0 = 0$, $A_1 = 0$, $A_2 = 0$, $A_3 = 0$, $A_4 = 0.5\rho/K_4(r_0/\ell)$, $B_1 = 0$, $B_2 = 0$, $B_3 = 0$, $B_4 = 0$, and $r_0 = 0.864 \rho$.

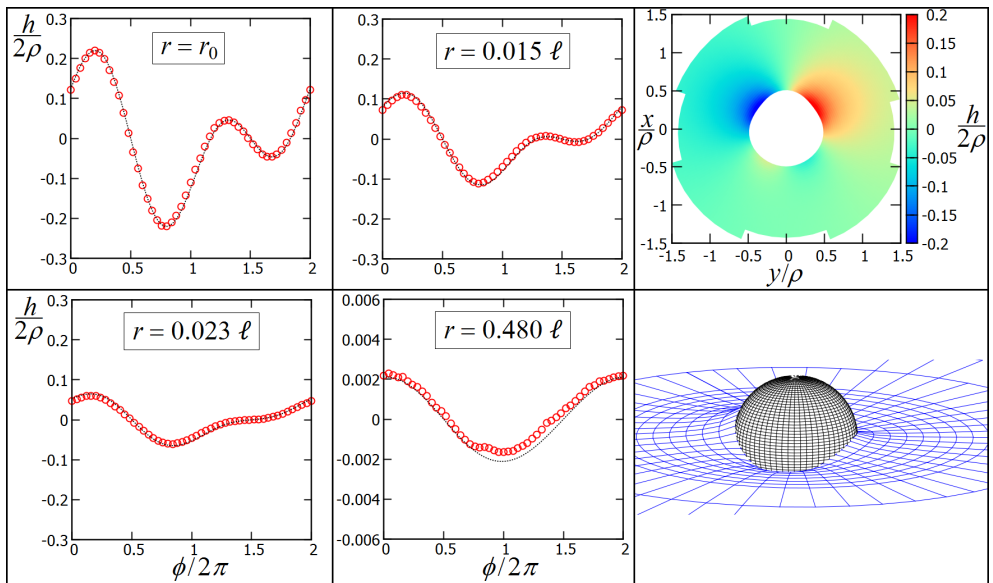


Figure 4.19: Height profile $h(r, \phi)$ of a fluid-fluid interface induced by a sphere with a pinned three-phase contact line given by $h(r_0, \phi) = 0.25 \rho [\cos(\phi) + \cos(2\phi - \pi/2)]$, which is Eq. (4.9) using $A_0 = 0$, $A_1 = \rho/[4K_1(r_0/\ell)]$, $A_2 = \rho/[4K_2(r_0/\ell)]$, $A_3 = 0$, $A_4 = 0$, $B_1 = 0$, $B_2 = \pi/2$, $B_3 = 0$, $B_4 = 0$, and $r_0 = 0.968 \rho$.

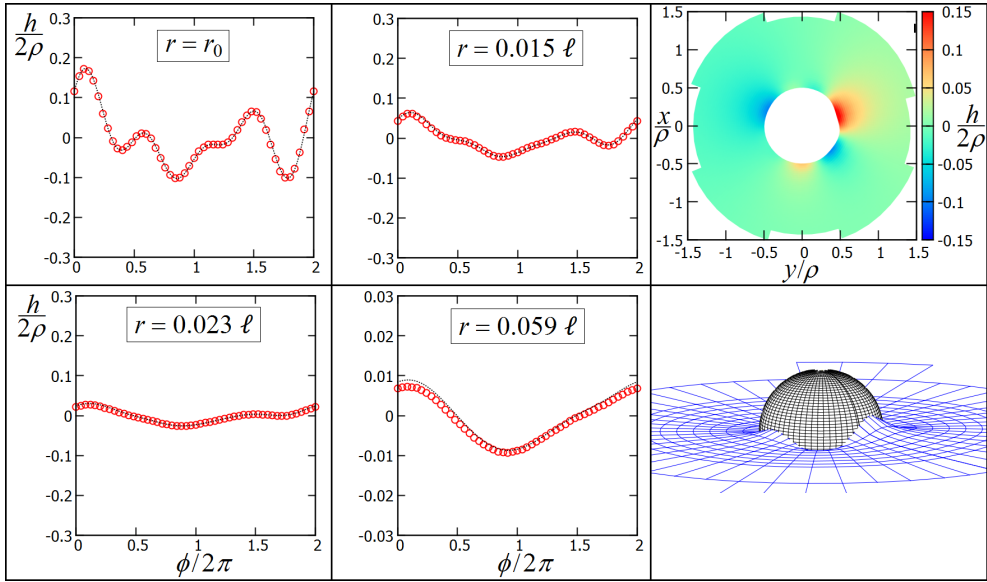


Figure 4.20: Height profile $h(r, \phi)$ of a fluid-fluid interface induced by a sphere with a pinned three-phase contact line given by $h(r_0, \phi) = 0.1 \rho [\cos(\phi) + \cos(2\phi - \pi/2) + \cos(3\phi - \pi/4) + \cos(4\phi - 2\pi/7)]$, which is Eq. (4.9) using $A_0 = 0$, $A_1 = 0.1\rho/K_1(r_0/\ell)$, $A_2 = 0.1\rho/K_2(r_0/\ell)$, $A_3 = 0.1\rho/K_3(r_0/\ell)$, $A_4 = 0.1\rho/K_4(r_0/\ell)$, $B_1 = 0$, $B_2 = \pi/2$, $B_3 = \pi/4$, $B_4 = 2\pi/7$, and $r_0 = 0.975 \rho$.

4.4.5 ROTATION CAPILLARY FORCES

As an additional illustrative application of our numerical method, we calculate here the capillary forces preventing a sphere, adsorbed at a fluid-fluid interface and with a pinned three-phase contact line, to rotate its vertical axis from the equilibrium configuration. This situation can be studied experimentally, for example, by considering adsorbed spherical particles with a rough surface and a magnetic dipole. Because of the rough surface, the three-phase contact line is likely to be pinned, and, by switching on and off a magnetic field, the sphere rotates to align its magnetic dipole axis. However, as the three-phase contact line is pinned, the sphere rotation induces capillary deformations in the fluid-fluid interface, therefore the magnetic force necessary to rotate the particle has to compensate the capillary forces preventing such deformations.

To study this situation, we apply the algorithm described in Appendix B to calculate the equilibrium shape of a fluid-fluid interface around a sphere with radius $\rho = 0.005 \ell$ and center of mass height z_c at the interface reference level $z = 0$. At the equilibrium the fluid-fluid interface is undeformed by the sphere, and the three-phase contact line corresponds to the intersection of the sphere with the flat interface plane $z = 0$. Assuming that the Young's contact angle is $\pi/2$, the three-phase contact line is a circle of radius ρ . We use the algorithm described in Appendix B to calculate the equilibrium shape of the fluid-fluid interface ob-

tained by keeping a pinned three-phase contact line on the sphere while rotating the sphere by a polar angle α . The energy E [Eq. (2.24)] of the fluid-fluid-particle system, computed from the equilibrium configuration of the fluid-fluid interface (see details in Appendix B), is reported in Fig. 4.21 with respect to the particle rotation α . Note that here we shifted the reference level of E such that $E = 0$ corresponds to the equilibrium configuration of the sphere.

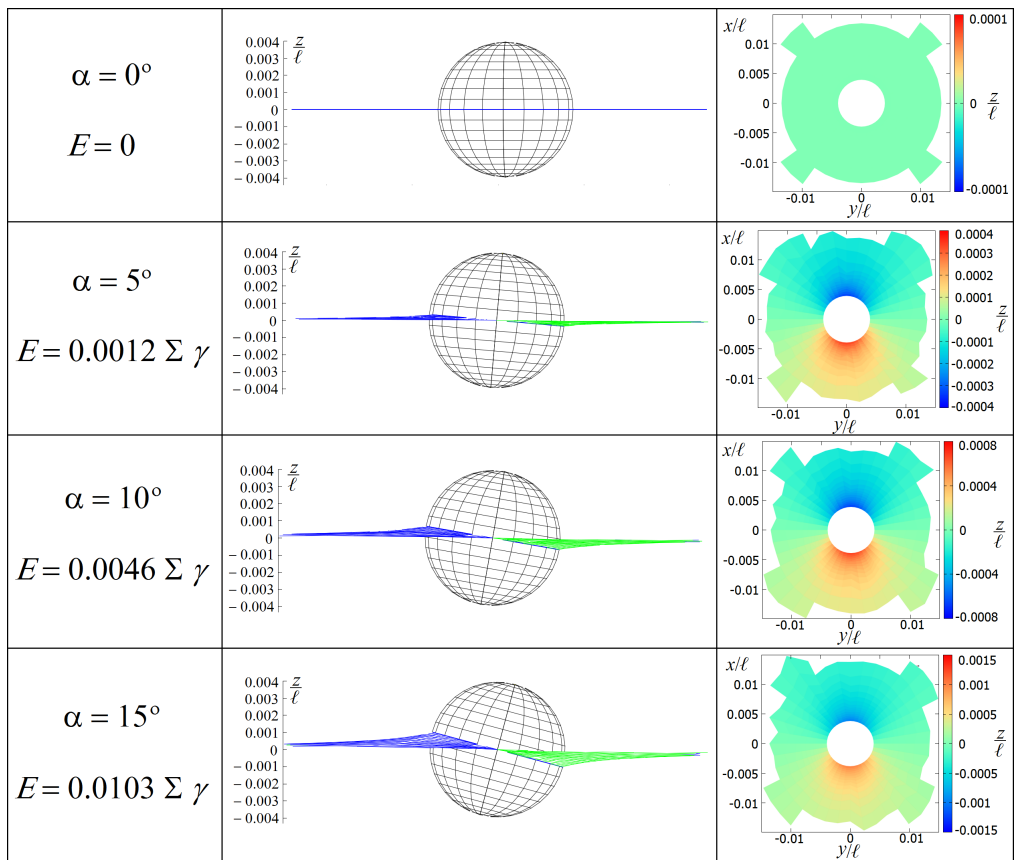


Figure 4.21: Given a sphere adsorbed at a fluid-fluid interface, with Young’s contact angle $\pi/2$, radius $\rho = 0.005\ell$, surface area Σ , and three-phase contact line pinned at the sphere equilibrium configuration, we show here the energy E to rotate the sphere by tilting its vertical axis by an angle α . In the central and right panels we show a 3D view and a contour plot of the equilibrium shape of the fluid-fluid interface close to the sphere, for each α , as obtained by our numerical method. The energy E [Eq. (2.24)] is computed by the equilibrium shape of the fluid-fluid interface, with reference level $E = 0$ shifted in $\alpha = 0$.

4.5 EQUILIBRIUM CONFIGURATION OF A SINGLE ADSORBED PARTICLE

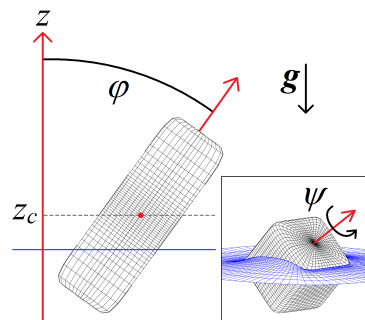
An important application of our numerical method is the prediction of the equilibrium configuration for a (3D) colloidal particle, possibly odd-shaped, adsorbed at a flat fluid-fluid interface. In this Section, first it is explained how the algorithm described in Appendix B is exploited for this purpose, and then we present illustrative results for spheres, ellipsoids and cylinders.

In our model, the fluid-fluid interface is flat and coincides with the plane $z = 0$ when no particle is adsorbed^{ix}, and it is delimited at its boundary by a vertical wall with Young's contact angle $\pi/2$. This vertical wall is placed far enough from the adsorbed particle to not affect the system, such that our results hold for a fluid-fluid interface that is infinitely extended and flat far from the particle. Once a particle with a given shape is placed at the interface and the equilibrium shape of the interface is computed, the energy E [Eq. (2.24)] of this fluid-fluid-particle system can be extracted, and its value depends on z_c , φ and ψ , where z_c is the height of the particle center of mass on the interface reference level $z = 0$, φ is the polar angle of the particle vertical axis with the interface, and ψ is the particle internal Euler angle around its vertical axis (see Fig. 4.22). For convenience, we shift by a constant the reference level of E [Eq. (2.24)] to be zero when the particle is desorbed in fluid 2 (i.e. the heaviest fluid, below the interface), obtaining

$$E = \gamma \left(S - A + W_1 \cos \theta + \frac{1}{\ell^2} \int_{V_2} z dV \right), \quad (4.10)$$

where the volume-pressure terms in Eq. (2.24) are neglected in Eq. (4.10), as we are considering a flat fluid-fluid interface, so $\Delta P = 0$. Here, γ is the fluid-fluid surface tension, ℓ is the capillary length [Eq. (2.3)], S and A are the surface areas of the fluid-fluid interface with and without particle, respectively, W_1 is the portion of the particle surface area in contact with fluid 1, θ is the particle

Figure 4.22: Configuration of a colloidal particle (black grid) adsorbed at a fluid-fluid interface (blue grid). The height of the particle center of mass on the interface reference level $z = 0$ (here indicated by the blue line) is z_c , and the polar angle of the particle vertical axis with the interface plane is φ . The insets shows the internal Euler angle ψ around the vertical axis of a cubic particle adsorbed at a fluid-fluid interface (blue grid).



^{ix}Note that this defines the fluid volumes, which are kept constant during the minimization of the potential Ξ [Eq. (4.3)] with respect to the fluid-fluid interface shape (for details see Appendix B).

Young's contact angle [Eq. (2.18)], and V_2 is the volume of fluid 2. If the particle is desorbed in fluid 2, then $W_1 = 0$, $S = A$, and $\int_{V_2} z dV = 0$, because without particle the interface coincides with the $z = 0$ plane, so E [Eq. (4.10)] is 0. Instead, if the particle is desorbed in fluid 1, it follows $E = \gamma \Sigma \cos \theta$, with Σ the particle total surface area.

To sum up, the algorithm described in Appendix B is used to calculate the equilibrium shape of the fluid-fluid interface, for a given configuration (z_c, φ, ψ) of the particle. Then, from the interface equilibrium shape, the energy $E(z_c, \varphi, \psi)$ [Eq. (4.10)] is calculated, as described in Appendix B. We repeat this procedure for all the possible different configurations (z_c, φ, ψ) of the particle, and the minimum value of $E(z_c, \varphi, \psi)$ indicates the particle equilibrium adsorption configuration.^x

4.5.1 HEAVY SPHERE

In the expression for the fluid-fluid-particle energy E [Eq. (4.10)], the position of the solid surfaces in the system is assumed constant. However, if the particle configuration (z_c, φ, ψ) at the interface is changed, then the gravitational energy contribution due to the particle weight should in principle be included in E . In this Section we study the influence of the particle weight, by showing results for an heavy sphere.

With respect to the model described in Sec. 4.5, the gravitational potential energy E_p of the solid particle at the fluid-fluid interface is

$$E_p = m_p g z_c, \quad (4.11)$$

with z_c the height of the particle center of mass on the interface reference level, m_p the particle mass, and g the gravity acceleration modulus. For convenience, we write $g = \gamma/(\ell^2 \Delta\rho)$, and $m_p = V_p \rho_p$, with V_p and ρ_p the particle volume and mass density, respectively, obtaining

$$E_p = \frac{\gamma}{\ell^2} \frac{\rho_p}{\Delta\rho} V_p z_c. \quad (4.12)$$

Therefore, by adding E_p to the total energy E [Eq. (4.10)] of the system, we obtain

$$E = \gamma (S - A + W_1 \cos \theta) + \frac{\gamma}{\ell^2} \left(\frac{\rho_p}{\Delta\rho} V_p z_c + \int_{V_2} z dV \right). \quad (4.13)$$

For simplicity, we consider here a spherical particle with diameter σ , such that the energy E [Eq. (4.13)] depends only on z_c , and not on ϕ and ψ . Using the algorithm in Appendix B, we compute the energy $E(z_c)$ [Eq. (4.13)] from the equilibrium shape of the fluid-fluid interface for many values of z_c in the interval $[-\sqrt{3}\sigma/2, \sqrt{3}\sigma/2]$, and we assume the sphere desorbed from the interface for z_c

^xNumerically it is, of course, not possible to consider continuously all the possible values of z_c, φ, ψ , so one needs to sample them discretely, with intervals small enough to not miss energy minima.

outside this interval.^{xi}

First, we consider the case where the particle weight is negligible, i.e. E_p [Eq. (4.12)] is zero, and therefore the energy E is given by Eq. (4.10). In Fig. 4.23(a), we show the energy $E(z_c)$ [Eq. (4.13)] for a sphere with radius $\sigma/2 = \ell$ and $\cos \theta = 0.5$. To show the effects of capillary deformations, we plot for the same system also the energy as obtained through the Triangular Tessellation Technique (TTT), a numerical method [114] where the energy for the given particle configuration is computed in the approximation of no capillary deformations, i.e. assuming the interface flat everywhere, even when the particle is adsorbed. As shown, the energy through our method is lower, for a given z_c , than as computed by the TTT, because the capillary deformations allow the system to optimize the energy at the most. Indeed the approximation of a flat interface everywhere, used in the TTT, in general breaks Young's Law [Eq. (2.18)]. However, a spherical particle at a height $z_c = -(\sigma/2) \cos \theta$ on the interface plane keeps with a flat fluid-fluid interface a contact angle θ along the whole three-phase contact line [see Fig. 3.7(a)]. The results in Fig. 4.23 show that such a z_c corresponds to the minimum E . The TTT predictions for the minimum energy configuration coincide with the results of our method, obviously, as in the minimum energy configuration the sphere does not deform the interface, so the flat interface approximation becomes exact in this particular case. In Fig. 4.23(b) we show analogous results, but for $\cos \theta = -0.5$, i.e. with the sphere preferring to wet the fluid above the interface.^{xii} To study how the capillary deformation effects on the energy depend on ℓ , in Fig. 4.23(c) we show the energy $E(z_c)$ [Eq. (4.10)] for a sphere with radius $\sigma/2 = 0.1\ell$, $\sigma/2 = 0.01\ell$, $\sigma/2 = 0.001\ell$, and $\sigma/2 = 10^{-4}\ell$, and for $\cos \theta = 0.5$ and $\cos \theta = -0.5$. As shown, by decreasing $\sigma/2$ until 0.001ℓ , the energy E , in units of $\Sigma \gamma$ and for a given z_c , also decreases, in agreement with the idea that the flat interface approximation used by the TTT corresponds to the limit $\ell \rightarrow 0$.

^{xi}So we are assuming that the sphere is desorbed in fluid 1, i.e. above the interface, if $z_c > \sqrt{3}\sigma/2$, and it is desorbed in fluid 2, i.e. below the interface, if $z_c < -\sqrt{3}\sigma/2$. In principle, the energy E [Eq. (4.13)] should be checked also for z_c outside this interval, by calculating the equilibrium fluid-fluid interface shape for such a z_c , and then the particle should be considered desorbed from the interface only if E is higher than the energy of the particle desorbed in, respectively, fluid 1, i.e. $E = \gamma \Sigma \cos \theta$, and in fluid 2, i.e. $E = 0$.

^{xii}With $E^+(z_c)$ the energy [Eq. (4.10)] of a particle with Young's contact angle θ , the energy $E(z_c)$ [Eq. (4.10)] of the same particle but with Young's contact angle $\pi - \theta$ is $E(z_c) = E^+(-z_c) - \cos \theta \Sigma \gamma$.

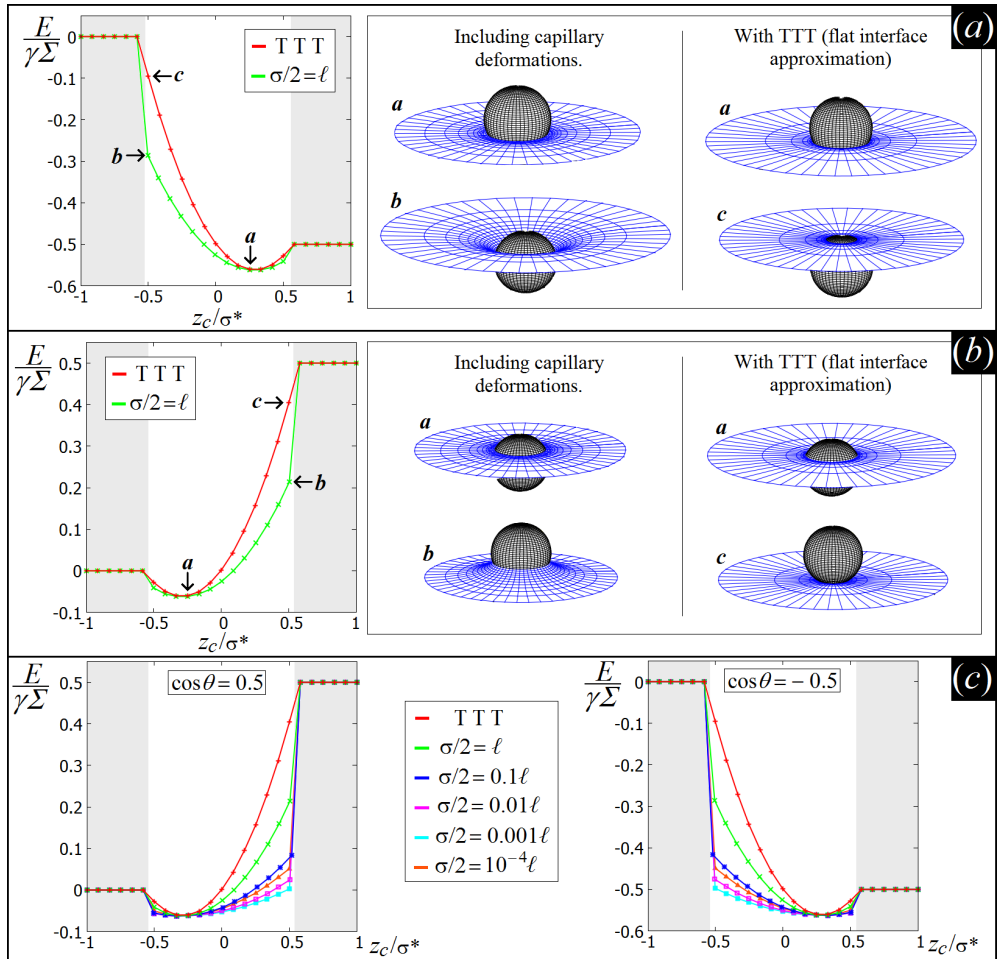


Figure 4.23: (a) Energy $E(z_c)$ [Eq. (4.10)], of a spherical particle with radius $\sigma/2 = \ell$ and $\cos\theta = 0.5$ adsorbed at a flat fluid-fluid interface, with respect to the sphere center of mass height z_c on the interface plane, with ℓ the capillary length, θ the Young's contact angle, Σ the sphere total surface area, γ the fluid-fluid surface tension, and $\sigma^* \equiv \sqrt{3}\sigma/2$. The results obtained by the TTT, i.e. neglecting capillary deformations, are compared with the results obtained by our numerical method (see Appendix B), i.e. calculating the fluid-fluid interface equilibrium shape for each z_c considered. In the energy minimum, the predictions of the two methods coincide, as for such a z_c the sphere keeps the interface flat. In the gray areas we assume the particle desorbed from the interface (see note xi at page 86). In the inset, we show 3D views of the fluid-fluid interface shape close to the particle, as obtained by our method (left) and in the TTT (right). (b) Analogous results to (a), but for $\cos\theta = -0.5$. (c) The results of (a) and (b) are here compared with the energy $E(z_c)$ [Eq. (4.10)] of a sphere with $\sigma/2 = 0.1\ell$, $\sigma/2 = 0.01\ell$, $\sigma/2 = 0.001\ell$, and $\sigma/2 = 10^{-4}\ell$, respectively.

Now we study the influence of the sphere weight on its equilibrium configuration. Therefore, we need to add the term E_p [Eq. (4.12)] to the energy $E(z_c)$ shown in Fig. 4.23. In Figs. 4.24, 4.25, 4.26, the energy $E(z_c)$ [Eq. (4.13)] of a spherical particle with radius $\sigma/2 = \ell$, $\sigma/2 = 0.1\ell$, and $\sigma/2 = 0.01\ell$, respectively, is plotted for $\cos\theta = 0.5$ and $\cos\theta = -0.5$, and for some values of $\rho_p/\Delta\rho$. As shown, the sphere equilibrium configuration, i.e. the z_c corresponding to the minimum E , changes by tuning $\rho_p/\Delta\rho$. In particular, we obtain, as expected, that, by increasing ρ_p , the z_c with minimum energy decreases, i.e. the particle prefers to stay lower with respect to the interface plane.^{xiii} Note that, as we introduced the particle weight contribution E_p [Eq. (4.12)], the plots of $E(z_c)$ for $\cos\theta$ and $-\cos\theta$ are not specular anymore. Indeed, for $\cos\theta = -0.5$ the sphere prefers to wet the fluid above, therefore it needs a higher weight to desorb from the interface than for $\cos\theta = 0.5$, as the graphs show. These results show that, for $\sigma/2 = 0.1\ell$, we need $\rho_p/\Delta\rho \geq \mathcal{O}(10)$ to see significant effects of the particle weight on the minimum-energy configuration, while, for $\rho = \ell$, important effects are observed for $\rho_p/\Delta\rho \geq \mathcal{O}(1)$. Finally, for $\sigma/2 = 0.01\ell$, particle weight effects on $E(z_c)$ appears totally negligible for $\rho_p/\Delta\rho \leq \mathcal{O}(100)$.

In conclusion, we have shown that $\rho_p/\Delta\rho$ is the parameter that determines if the particle weight can be neglected or not in the energy E [Eq. (2.24)] of a fluid-fluid-particle system, given the particle size with respect to ℓ . For a typical experimental system of solid particles at a liquid-liquid interface, we can estimate a mass density $\rho_1 = 900 \text{ kg/m}^3$ for fluid 1, $\rho_2 = 1000 \text{ kg/m}^3$ for fluid 2, and $\rho_p = 2500 \text{ kg/m}^3$ for the solid particles, implying $\rho_p/\Delta\rho \simeq 25$. If instead we consider a liquid-air interface, we can estimate $\rho_1 = 1 \text{ kg/m}^3$ for fluid 1, i.e. the air, obtaining $\rho_p/\Delta\rho \simeq 2.5$. The capillary length ℓ is typically a few millimeters. Therefore on an order-of-magnitude base we can conclude that, to determine the particle equilibrium configuration in such experimental systems (i.e. $2.5 \lesssim \rho_p/\Delta\rho \lesssim 25$), the particle weight is negligible for a particle size $\sigma \leq \mathcal{O}(10 \mu\text{m})$, while there is an interplay between particle weight and wetting energy for $\sigma = \mathcal{O}(100 \mu\text{m})$, and the particle weight becomes completely dominant over the wetting energy for $\sigma \geq \mathcal{O}(1 \text{ mm})$.

^{xiii}On the other hand, it seems also that the lower $\Delta\rho$, the more important the weight of the particle, and, in the limit $\Delta\rho \rightarrow 0$, the parameter $\rho_p/\Delta\rho$ diverges. However, note that the $\Delta\rho$ is fixed by the capillary length ℓ [Eq. (2.3)], and $\Delta\rho = 0$ implies $\ell = \infty$.

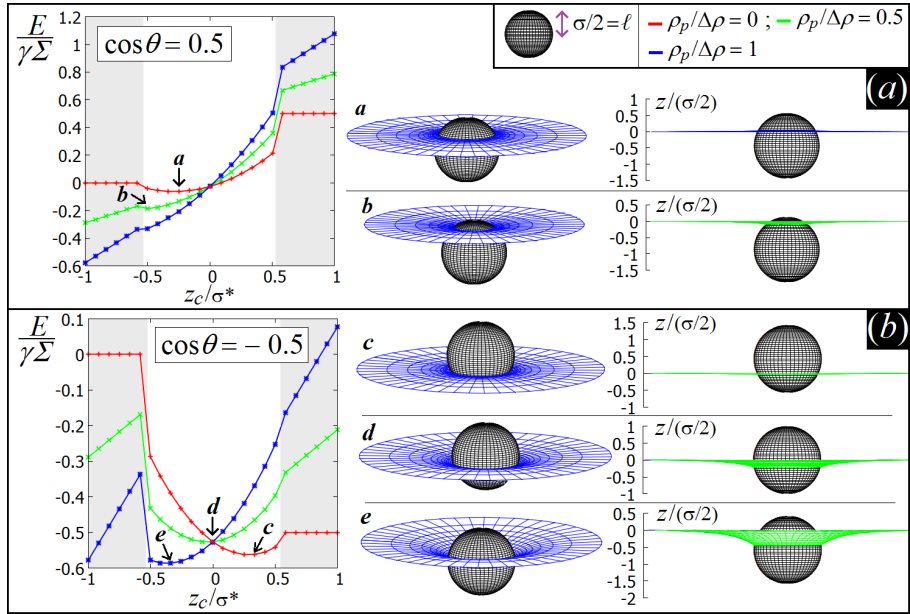


Figure 4.24: Energy $E(z_c)$ [Eq. (4.13)] of an adsorbed sphere with radius $\sigma/2 = \ell$, and including its weight contribution E_p [Eq. (4.12)], for (a) $\cos\theta = 0.5$ and (b) $\cos\theta = -0.5$, with respect to the sphere center of mass height z_c on the interface plane, for some values of $\rho_p/\Delta\rho$. Here ρ_p is the particle mass density, $\Delta\rho = \rho_2 - \rho_1$ is the difference of the mass densities of the two fluids, ℓ is the capillary length, θ is Young's contact angle, Σ is the sphere total surface area, γ is the fluid-fluid surface tension, and $\sigma^* \equiv \sqrt{3}\sigma/2$. On the right, 3D and profile views of the interface equilibrium shape close to the sphere, as obtained by our numerical method, are shown for some values of z_c .

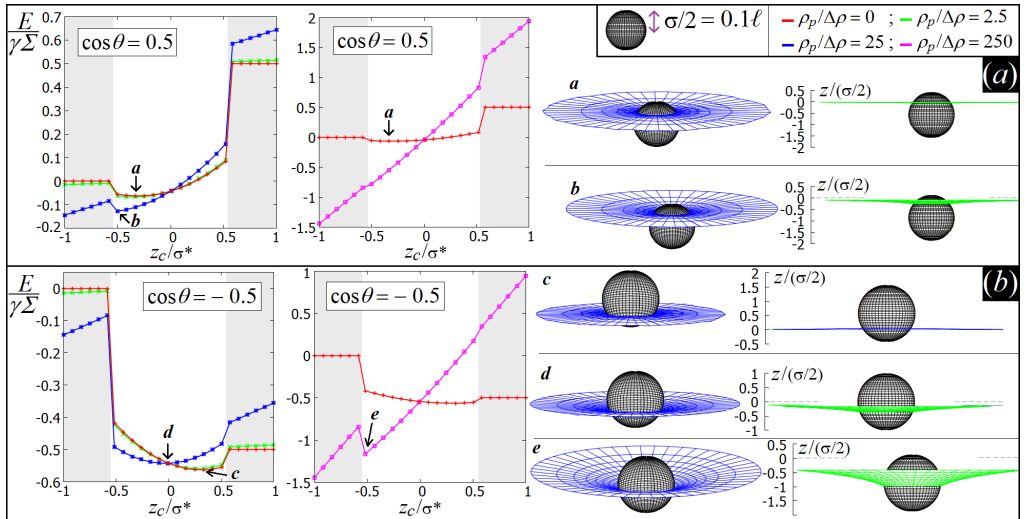


Figure 4.25: The same results of Fig. 4.24 are shown here, but for a sphere radius $\sigma/2 = 0.1\ell$.

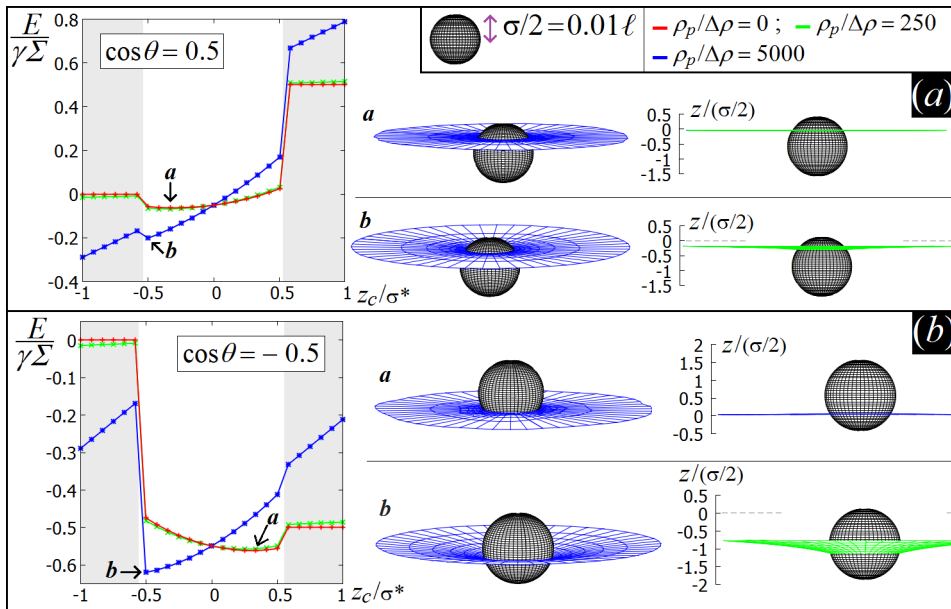


Figure 4.26: The same results of Fig. 4.24 are shown here, but for a sphere radius $\sigma/2 = 0.01\ell$.

4.5.2 ELLIPSOIDS AND CYLINDERS

As shown in the previous Section, a spherical particle adsorbed at the equilibrium at a flat fluid-fluid interface does not generate, if the particle weight is negligible, capillary deformations, regardless of the Young's contact angle θ , because the sphere can adjust the height of its center of mass to match the desired contact angle with the flat interface along the whole three-phase contact line.

Now we consider, instead, the equilibrium adsorption configuration of an ellipsoid of aspect ratio 3 and minor axis $\sigma = 0.02\ell$ [see Fig. 4.27(a)], with ℓ the capillary length. We assume the particle weight negligible. The predictions obtained from our numerical method are reported in Fig. 4.28, and they show that, for this shape, the particle does generate capillary deformations at the interface, if Young's contact angle is different from $\pi/2$.

Analogously, we consider the equilibrium adsorption configuration of a cylinder of aspect ratio 2 and diameter $\sigma = 0.02\ell$ [see Fig. 4.27(b)]. We assume again the particle weight negligible. The predictions obtained from our numerical method are reported in Fig. 4.29. Also in this case, they show that the cylinder does generate capillary deformations at the interface, if Young's contact angle is different from $\pi/2$.

The reason why ellipsoids and cylinders deform the interface is Young's Law. Indeed, the contact angle between the particle surface and the fluid-fluid interface needs to match along the whole three-phase contact line the Young's contact angle given in Eq. (2.18), and for such particle shapes this is not possible with a flat interface. Only when the Young's contact angle is $\pi/2$, cylinders and ellipsoids adsorb at the interface without inducing capillary deformations. Interestingly, if adsorbed particles with a cubic shape are considered, then it is for a Young's contact angle close to $\pi/2$ that the particle, at the equilibrium, generates capillary deformations in the interface, while for a Young's contact angle far from $\pi/2$ the interface remains basically undeformed. This will be shown in Chapter 5, where we will also see that such capillary deformations induced by the cubic particles have an hexapolar geometry, and we will study the induced capillary interactions and self-assembly. Note that in this Section we showed that ellipsoids and cylinders, instead, generate capillary deformations with a quadrupolar geometry, see Figs. 4.28 and 4.29.

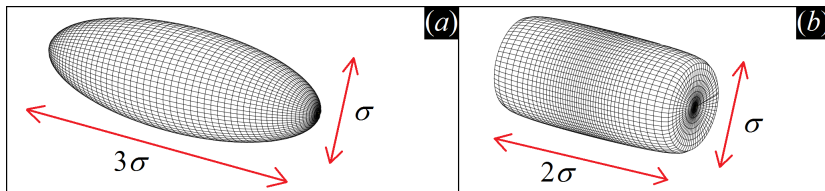


Figure 4.27: (a) Ellipsoid with aspect ratio 3 and minor axis σ . (b) Cylinder with aspect ratio 2 and diameter σ .

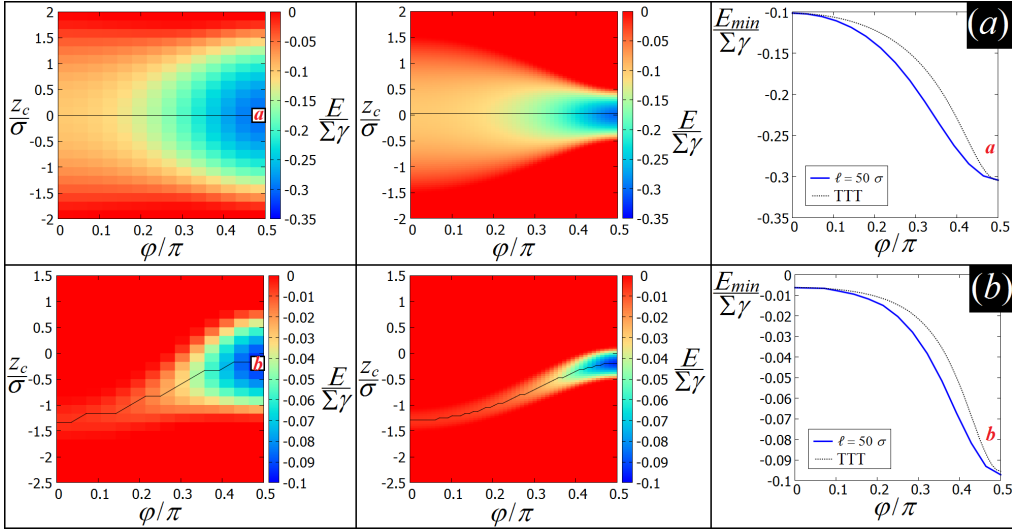
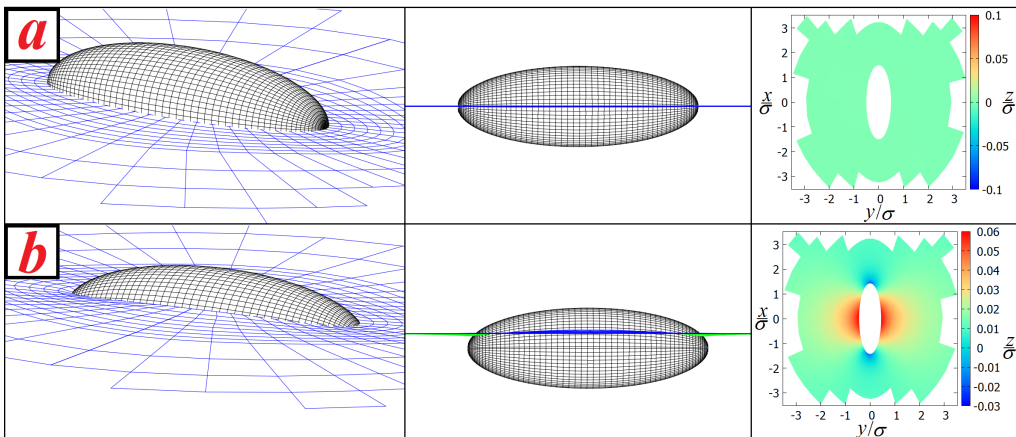


Figure 4.28: Left panels: adsorption energy $E(z_c, \phi)$ [Eq. (4.10)] for an ellipsoid of aspect ratio 3 and minor axis $\sigma = 0.02\ell$, with Young's contact angle θ , for (a) $\cos \theta = 0$ and (b) $\cos \theta = 0.5$, as obtained by our numerical method. Central panels: same, but as obtained by the Triangular Tessellation Technique (TTT), i.e. neglecting capillary deformations effects. Right panels: $E_{min}(\phi)$, obtained by minimizing $E(z_c, \phi)$ over z_c , with the minimum- z_c path highlighted in the contour plots with a black line. The blue line represents the results from our numerical method, while the dotted black line represents the results from the TTT. Here Σ is the total surface area of the particle, and γ the fluid-fluid surface tension. In **a** and **b** we show a 3D view, profile view, and contour plot of the equilibrium shape of the fluid-fluid interface close to the particle, as obtained numerically by our method, for the particle configuration indicated by the labels on the left graph of $E(z_c, \phi)$. Note that these are the minimum energy configurations of the particle.



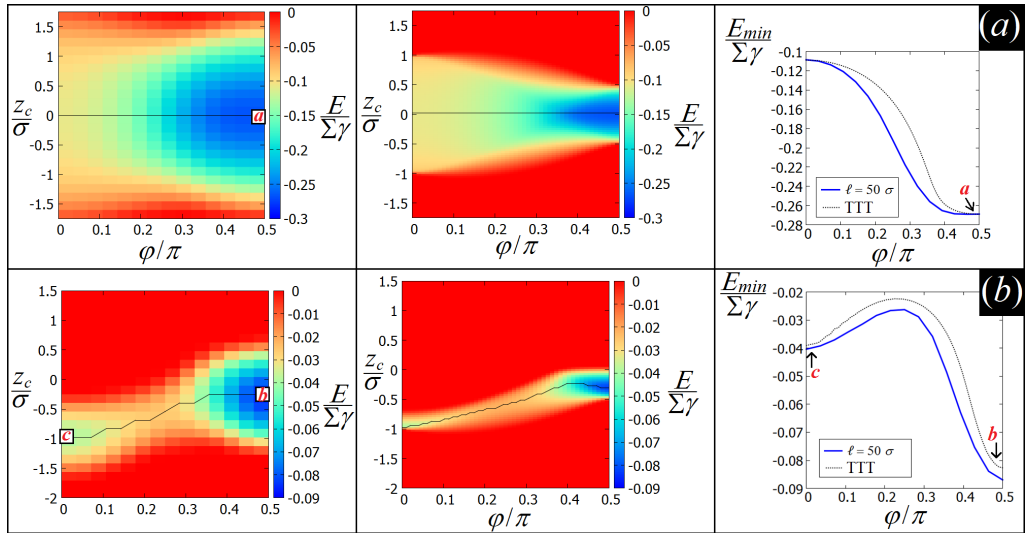
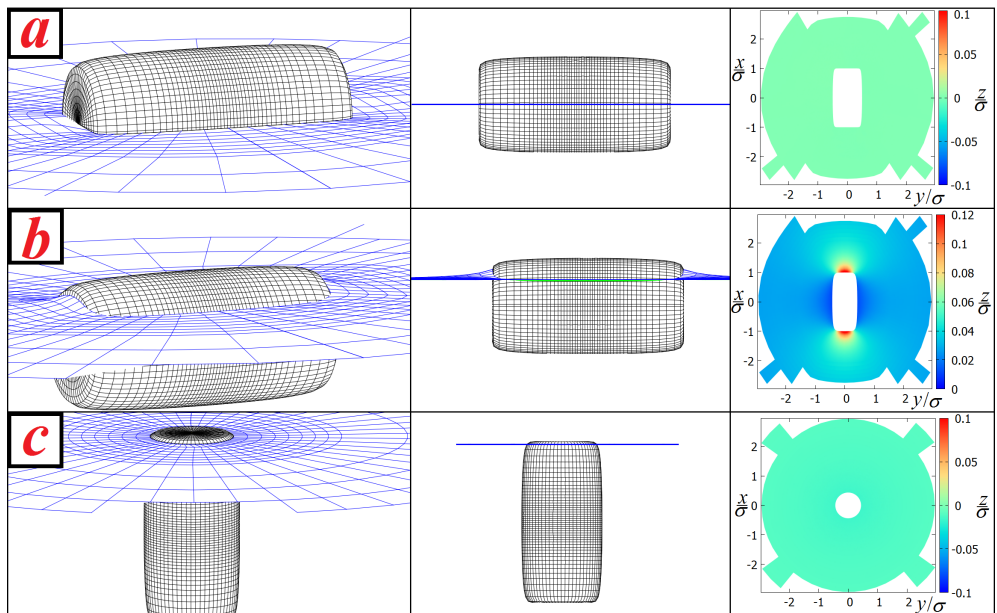


Figure 4.29: Left panels: adsorption energy $E(z_c, \phi)$ [Eq. (4.10)] for a cylinder of aspect ratio 2 and diameter $\sigma = 0.02\ell$, with Young's contact angle θ , for (a) $\cos\theta = 0$ and (b) $\cos\theta = 0.5$, as obtained by our numerical method. Central panels: same, but as obtained by the Triangular Tessellation Technique (TTT), i.e. neglecting capillary deformations effects. Right panels: $E_{min}(\phi)$, obtained by minimizing $E(z_c, \phi)$ over z_c , with the minimum- z_c path highlighted in the contour plots with a black line. The blue line represents the results from our numerical method, while the dotted black line represents the results from the TTT. Here Σ is the total surface area of the particle, and γ the fluid-fluid surface tension. In **a**, **b**, and **c** we show a 3D view, profile view, and contour plot of the equilibrium shape of the fluid-fluid interface close to the particle, as obtained numerically by our method, for the particle configuration indicated by the labels on the left graph of $E(z_c, \phi)$. Note that **a** and **b** are the minimum energy configurations of the particle, while **c** is a metastable state.



4.6 CONCLUSION

In this Chapter, we introduced a new numerical method to calculate the equilibrium shape of a fluid-fluid interface in the presence of external solid surfaces and possibly gravity, describing it and showing illustrative results in 2D and 3D.

Firstly, in Sec. 4.2, we explained the basic mechanism of our method, providing in Appendix A and B a detailed description of an illustrative algorithm to implement the method in 2D and 3D, respectively.

In Sec. 4.3, we presented illustrative results in 2D, to validate our method, and to show its applicability to a wide range of problems. In Sec. 4.3.1, we proved the correctness of our numerical method, showing an excellent agreement between numerical and analytical solutions for a meniscus close to a vertical wall. In Sec. 4.3.2, we reported the shape of menisci in contact with vertical or inclined walls and solid curved surfaces, to show the possibility of considering any kind of shape for the solid surfaces in contact with the interface. In Sec. 4.3.3, we exploited our method to study the capillary rise and the capillary interactions between two vertical plates adsorbed at a flat fluid-fluid interface. In Sec. 4.3.4, we applied our numerical method to study the equilibrium shape of 2D droplets. Results for 3D droplets, as obtained by our numerical method, will be shown in Chapter 6. In Sec. 4.3, we presented illustrative results in 3D, to validate our method also in 3D, and, in particular, to prove its applicability for studying colloidal particles adsorbed at fluid-fluid interfaces. In Sec. 4.4.1, we proved the correctness of the method in 3D by comparing the analytical and numerical predictions for a meniscus close to a parallelepiped particle with sides large enough (with respect to the capillary length ℓ) to be considered as vertical walls. In Sec. 4.4.2, we studied the finite-size effects in our model, to estimate which size we need for our interface to reproduce a flat and infinitely extended one. In Sec. 4.4.3, we studied the wetting of a vertical cylinder adsorbed at a flat fluid-fluid interface, calculating the capillary rise of the meniscus and comparing our numerical results with the analytical predictions of the linearized Young-Laplace Equation. In Sec. 4.4.4, we computed the height profile of the capillary deformations in a flat fluid-fluid interface induced by an adsorbed particle with a pinned three-phase contact line, showing that it can be described as a superposition of multipoles with different orders. In Sec. 4.4.5, we computed the energy necessary to deform a flat fluid-fluid interface by rotating the vertical axis of a sphere with a pinned three-phase contact line.

Finally, in Sec. 4.5, we applied our numerical method to compute the equilibrium adsorption configuration of an adsorbed particle at a flat fluid-fluid interface. In Sec. 4.5.1, we studied the influence of the particle weight on the equilibrium height of a sphere adsorbed at the interface, and in Sec. 4.5.2 we reported the equilibrium adsorption configuration for ellipsoids and cylinders with various Young's contact angles.

4.7 APPENDIX A

Here we report a detailed description of an illustrative algorithm to implement our numerical method in 2D. The basic mechanism of the algorithm is explained in Sec. 4.2. Results obtained through this algorithm are presented in Sec. 4.3. The physical system of interest has translational invariance along y , with the gravity anti-parallel to z . Therefore we consider a (x, z) -plane and we minimize the potential $\varepsilon \equiv \Xi/(\gamma \xi_y)$ with respect to the fluid-fluid interface shape, where Ξ is defined by Eq. (4.3), and ξ_y is the length of the system along y . The algorithm is the following:

- a) Assuming we have two solid surfaces that enclose our system, we introduce the two parametric functions $\mathbf{s}_1(u)$ and $\mathbf{s}_2(v)$ [with u, v scalars, and $\mathbf{s}_1, \mathbf{s}_2$ belonging to the (x, z) -plane] to define these surfaces. Between the two solid surfaces there is the fluid-fluid system, outside a solid, as shown in Fig. 4.1.
- b) We set the initial positions of the free points \mathbf{P}_i ($i = 1, \dots, N$) in the space between $\mathbf{s}_1(u)$ and $\mathbf{s}_2(v)$, and of the extreme points \mathbf{C}_1 and \mathbf{C}_2 on the surface of the solid 1 and solid 2 respectively. The interface is given by the set of segments linking any two consecutive points. By definition \mathbf{P}_{i+1} is consecutive to \mathbf{P}_i , \mathbf{P}_1 to \mathbf{C}_1 and \mathbf{C}_2 to \mathbf{P}_N . These initial positions define also the volume of the two fluids.
- c) The annealing temperature T , introduced in Eq. (4.4), is set to its initial value T_0 .
- d) A point is randomly selected. If the selected point is a free point, say \mathbf{P}_i , it is moved in the (x, z) -plane by the displacement (δ_x, δ_z) to its new position \mathbf{P}'_i [see Fig. 4.30(a)], where δ_x, δ_z are randomly selected within $[-\delta_{max}/2, \delta_{max}/2]$. If the segment $\mathbf{P}'_i\mathbf{P}_i$ crosses a solid surface or the interface, then the move is rejected and the program goes to step “l”. If the selected point is \mathbf{C}_k ($k = 1, 2$), it is moved along \mathbf{s}_k (in one of the two possible directions, randomly chosen) until it covers a path of length δ , where δ is randomly chosen within $[0, \delta_{max}/2]$. Given its new position \mathbf{C}'_k , if the segment $\mathbf{C}'_k\mathbf{P}_1$ or $\mathbf{P}_N\mathbf{C}'_k$ crosses the interface, then the move is rejected and the program goes to step “l”.
- e) The variation $\delta\varepsilon_g$ of the gravitational term of ε due to the point move in step “d)” is calculated. If the point moved is a free point, say P_i , then: $\delta\varepsilon_g = a\hat{G}(\mathbf{A}\mathbf{P}_i\mathbf{B}) + b\hat{G}(\mathbf{A}\mathbf{P}'_i\mathbf{B})$, where \mathbf{A} and \mathbf{B} are the two closest neighbors of \mathbf{P}_i on the interface, and $\hat{G}(\mathbf{A}\mathbf{B}\mathbf{C})$ is the gravitational energy of the triangle \mathbf{ABC} , scaled with ξ_y and γ , and it is computed as

$$\hat{G}(\mathbf{A}\mathbf{B}\mathbf{C}) = \frac{\hat{A}(\mathbf{A}\mathbf{B}\mathbf{C})}{\ell^2} \frac{(\mathbf{A} + \mathbf{B} + \mathbf{C}) \cdot \mathbf{z}}{3}, \quad (4.14)$$

where $\hat{A}(\mathbf{ABC})$ is the area of the triangle \mathbf{ABC} . Then $a, b = \pm 1$, where [see Fig. 4.30 (a)] b is equal to the sign of $[(\mathbf{A} - \mathbf{B}) \times (\mathbf{A} - \mathbf{P}'_i)] \cdot \hat{\mathbf{y}}$, with $\hat{\mathbf{y}}$ the normal in the y direction (i.e. pointing out of the paper). Then $a = b$ if the segment $\mathbf{P}_i\mathbf{P}'_i$ intersects the line passing through the segment \mathbf{AB} , otherwise $a = -b$. If the point moved is \mathbf{C}_k ($k = 1, 2$), then the area between $\mathbf{s}_1, \mathbf{C}'_1\mathbf{P}_1$ and $\mathbf{C}_1\mathbf{P}_1$ (or $\mathbf{s}_2, \mathbf{C}'_2\mathbf{P}_N$ and $\mathbf{C}_2\mathbf{P}_N$) is decomposed into a certain number of triangles T_f [see Fig. 4.30 (b)], and $\delta\varepsilon_g = \pm \sum_f \hat{G}(T_f)$, with the sign “ \pm ” positive if fluid 2 is gaining volume (moving \mathbf{C}_k in \mathbf{C}'_k), otherwise negative.

- f) The interface surface variation δS due to the point move in step “d)” is calculated as the length variation of the segments forming the interface (and it is negative if the total length of the segments was decreased, positive otherwise).
- g) If the point moved in “d)” is \mathbf{C}_k ($k = 1, 2$), then the variation in the k -th solid surface wet by fluid 2 is computed as $\delta W_2(k) = \pm \left| \int_{\mathbf{C}_k}^{\mathbf{C}'_k} \mathbf{s}_k(u) du \right|$, with “ \pm ” positive if fluid 2 is gaining volume (moving \mathbf{C}_k in \mathbf{C}'_k), otherwise negative. If the point moved in “d)” is a free point, then $\delta W_2(k) = 0$.
- h) The volume variation δV of the fluid 2 is calculated. If the point moved in “d)” was a free point, say \mathbf{P}_i , then: $\delta V = a \hat{A}(\mathbf{AP}_i\mathbf{B}) + b \hat{A}(\mathbf{BP}_i\mathbf{A})$, where \mathbf{A} and \mathbf{B} are the two closest neighbors of \mathbf{P}_i on the grid, $\hat{A}(\mathbf{ABC})$ is the area of the triangle \mathbf{ABC} , and $a, b = \pm 1$. The signs of a and b are computed as described in step “e)”. If the point moved in “d)” was \mathbf{C}_k ($k = 1, 2$), then the area between $\mathbf{s}_1, \mathbf{C}'_1\mathbf{P}_1$ and $\mathbf{C}_1\mathbf{P}_1$ (or $\mathbf{s}_2, \mathbf{C}'_2\mathbf{P}_N$ and $\mathbf{C}_2\mathbf{P}_N$) is decomposed in a certain number of triangles T_f [see Fig. 4.30 (b)] and $\delta V = \pm \sum_f \hat{A}(T_f)$, with “ \pm ” positive if fluid 2 is gaining volume (moving \mathbf{C}_k in \mathbf{C}'_k), otherwise negative.
- i) Another point is randomly selected and it is moved to compensate the volume variation calculated in step “h)”. Just for simplicity, in this step we choose only free points. Say \mathbf{P}_j is the selected point. Firstly the point \mathbf{O} at a distance $l \equiv 2|\delta\tilde{V}|/|\mathbf{AB}|$ from the segment \mathbf{AB} is calculated [see

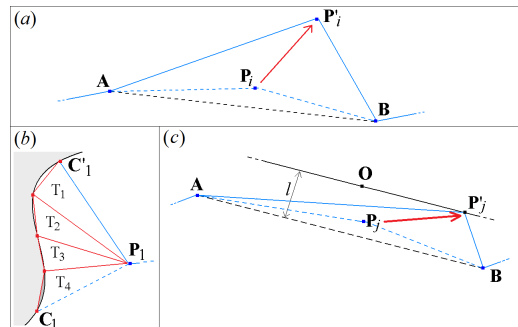


Figure 4.30: (a) Movement of a free point; (b) decomposition in triangles of the area between $\mathbf{s}_1, \mathbf{C}'_1\mathbf{P}_1$ and $\mathbf{C}_1\mathbf{P}_1$; (c) free point movement to generate the desired variation in the volume of fluid 2.

Fig. 4.30 (c)], where \mathbf{A} and \mathbf{B} are the two closest neighbors of \mathbf{P}_j , $\delta\tilde{V} = \delta V + \mathbf{A}\mathbf{P}_j \times \mathbf{A}\mathbf{B}/2$. The side of \mathbf{O} with respect to the segment \mathbf{AB} is such that $\mathbf{AO} \times \mathbf{AB}$ has the same sign as $\delta\tilde{V}$. Then the new position \mathbf{P}'_j is found moving \mathbf{O} by a random amount $\delta \in [0, \delta_{max}/2]$ in one of the two directions parallel to \mathbf{AB} (which direction is randomly chosen). In this way the total volume variation due to the moves in this step and in step “d)” is zero. If the segment $\mathbf{P}'_j\mathbf{P}_j$ crosses a solid surface or the interface, then the move is forbidden and the program goes to the step “l)”.

- j) The variations due to the move in step “i)” in the gravitational part of ε and in the fluid-fluid surface (respectively $\delta\varepsilon'_g$ and $\delta S'$) are computed as described in the steps “e)” and “f)”. Then the total variation in the functional ε due to the moves in the steps “d)” and “i)” is calculated as: $\delta\varepsilon = \delta\varepsilon_g + \delta\varepsilon'_g + \delta S + \delta S' - \cos\theta_k \delta W_2(k)$, where θ_k is the Young’s contact angle of the k – th solid surface.
- k) With a probability \mathcal{P} [with $\Delta\Xi = \gamma\xi_y \delta\varepsilon$, see Eq. (4.4)] the new configuration of the system is accepted, otherwise the two points moved respectively in step “d)” and “i)” return to their previous positions.
- l) The program returns to step “d)”. Every M times this step is performed, T is decreased by an amount δT . If $T \leq 0$, then the simulation ends.

To efficiently run this algorithm and obtain the correct solution, it is necessary to choose properly all the simulation parameters involved (T , T_0 , N , δ_{max} , M , δT). In principle a good choice of this set can be found only heuristically. However this problem, which is intrinsic to the method, needs to be faced only in a first stage. Then the method can be applied systematically to a certain class of problems by keeping the same structure of parameters, with at most some minor adjustments. In Table 4.1 we report all the simulation parameter values that we used for the results of Sec. 4.3.

This algorithm can be adapted to simulate a system where two or more 1D grids of points are necessary to represent the interface (like in Sec. 4.3.3). The necessary modifications are: in step “b)” defining all the solid surfaces, grids of points, and two constrained points for each grid, and in the step “i)” choosing the free point randomly from every grid, to allow the exchange of volume between the regions below the different grids.

For the results of Sec. 4.3.3 (Fig. 4.6), the energy $\Xi = \varepsilon\gamma\xi_y$ [Eqs. (4.3) and (4.5)] of the equilibrium shape of the fluid-fluid interface is computed as

$$\varepsilon = \varepsilon_g + S - \sum_k W_2(k) \cos\theta_k \quad (4.15)$$

where S , $W_2(k)$ and ε_g respectively are: the fluid-fluid surface, the k – th solid-fluid 2 surface and the gravitational part of ε (all referred to the final solution, i.e. the equilibrium shape of the meniscus). They are computed updating their

initial values as $S + \delta S + \delta S'$, $W_2(k) + \delta W_2(k)$ and $\varepsilon_g + \delta\varepsilon_g + \delta\varepsilon'_g$ in step “ k ” every time a new configuration is accepted.

To obtain the results of Sec. 4.3.4 for the pendant droplets (Fig. 4.9), the algorithm is modified to minimize Eq. (4.7) instead of Eq. (4.3). This is done simply by changing the signs of $\delta\varepsilon_g$ and $\delta\varepsilon'_g$ in step “ j ”.

| Fig. | N | $\frac{k_B}{\gamma \ell^2} T_0$ | $\frac{k_B}{\gamma \ell^2} \delta T$ | M |
|----------------|---------|---------------------------------|--|----------------|
| 4.2,4.4,4.5(b) | 28 | 10^{-5} | 10^{-7} | 10^5 |
| 4.3 | several | 10^{-5} | 10^{-7} | 10^5 |
| 4.5(a) | 28 | 0.01 | 10^{-4} if $T > 10^{-4}$, otherwise $5 \cdot 10^{-7}$ | $2 \cdot 10^5$ |
| 4.6 | 13 | 0.11 | 10^{-4} if $T > 10^{-4}$, otherwise 10^{-7} | $3 \cdot 10^5$ |
| 4.8,4.9(a) | 48 | 0.01 | 10^{-4} if $T > 10^{-4}$, otherwise $5 \cdot 10^{-7}$ | $2 \cdot 10^5$ |
| 4.9(b) | 38 | 0.01 | 10^{-4} if $T > 10^{-4}$, otherwise $5 \cdot 10^{-7}$ | $2 \cdot 10^5$ |

Table 4.1: Simulation parameters used in the various results shown in Sec. 4.3. In all the simulations, δ_{max} is set to 0.5ℓ . About Fig. 4.6, N is referred to each one of the three grids of points. Each simulation was performed on an ordinary office PC and required few minutes to be completed.

4.8 APPENDIX B

Here we report a detailed description of an illustrative algorithm to implement our numerical method for studying a single adsorbed 3D solid particle adsorbed at a fluid-fluid interface. The fluid-fluid interface is flat when there are no particles. As usual, we call fluid 2 the heavier fluid, i.e. the fluid below the interface, and fluid 1 the fluid above. The basic mechanism of the algorithm is explained in Sec. 4.2. Results obtained through this algorithm are presented in Sec. 4.3. In our model, we introduce a Cartesian coordinate system with z axis anti-parallel to the gravity direction. The solid particle is placed approximately in the center of the system, and the particle surface is approximated using a grid of triangles, see Fig. 4.31. The fluid-fluid interface is also represented by a grid of triangles, whose vertexes form a 2D grid of points which is disposed around the particle like it is shown in the example of Fig. 4.32. Each point of this grid is labeled as $\mathbf{p}(h, k)$, with $h = 1, 2, \dots, N_h$, $k = 1, 2, \dots, N_k$, where the indexes h and k vary along the two directions of the grid (see Fig. 4.32). The points with $h = N_h$ are constrained to move on the particle surface. The points with $h = 1$ are constrained to move

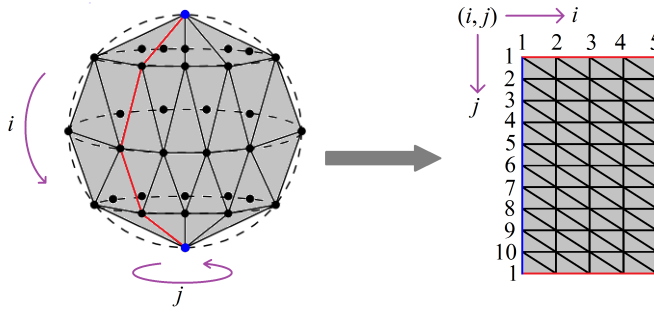


Figure 4.31: Triangular 2D grid used to represent the surface of a 3D particle. In this example, a 5×10 grid is used.

on the external vertical wall, that has a cylindrical shape with radius R and it encloses the fluid-fluid-particle system. So, R is the distance of the system boundary from the origin. To reproduce a flat and infinitely extended interface far from the particle, this external wall has Young's contact angle $\pi/2$. During the simulation, each $\mathbf{p}(h, k)$ point of the fluid-fluid interface grid is constrained to move along a given radial direction with respect to the center of the grid. This direction is the same for all points with the same k . In detail, the algorithm is the following:

- a) The particle surface is defined using a grid of triangles (see Fig. 4.31) with $N_p \times N_p$ points. For simplicity we assume here convex particle shapes only. We use a super-quadratic equation to define the particle surface for a particle with center of mass in the origin and with $\varphi = \psi = z_c = 0$, where z_c is the height of the particle center of mass on the interface reference level,

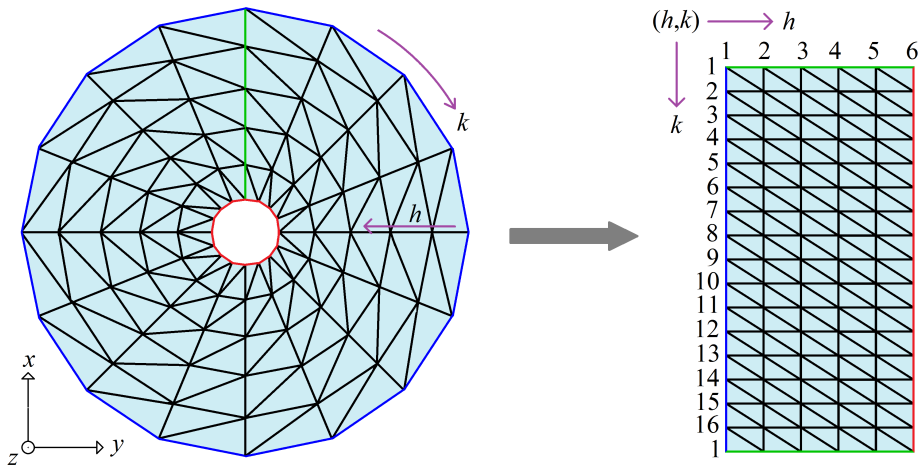


Figure 4.32: Top view of the initial 2D grid representing the fluid-fluid interface at which a colloidal particle (in the center) is adsorbed. Each point of the grid is in the plane $z = 0$ in the initial configuration, with the gravity direction perpendicular to such a plane. In this example, the grid is 6×16 , that is $N_h = 6$, $N_k = 16$, and the colloidal particle has a cylindrical shape.

φ is the polar angle of the particle vertical axis with the interface, and ψ is the internal Euler angle that defines the particle rotation around its vertical central axis (see Fig. 4.22). Then, the particle surface points are rotated and shifted to obtain the desired configuration (φ, ψ, z_c) . For convenience, the particle is also shifted in the x and y directions to match \mathbf{c} with the origin, where \mathbf{c} is the center of the intersection between the particle and the $z = 0$ plane.

- b) The grid of points representing the fluid-fluid interface is defined as shown in Fig. 4.32. A generic point of this grid is $\mathbf{p}(h, k)$, with $h = 1, 2, \dots, N_h$, $k = 1, 2, \dots, N_k$. Firstly, each point $\mathbf{p}(N_h, k)$ is defined on the particle surface, i.e. in one of the triangles forming the particle surface grid. The initial position of these points is chosen such that $p_z(N_h, k) = 0$, and such that the distance $|\mathbf{p}(N_h, j) - \mathbf{p}(N_h, j + 1)|$ is (approximately) constant for any choice of j . This initial position of each $\mathbf{p}(N_h, k)$ defines also the radial direction

$$\alpha_k \equiv \text{atan}2[p_y(N_h, k), p_x(N_h, k)] \quad (4.16)$$

along which the other k -th points are constrained to move, where $\text{atan}2(y, x)$ denotes the angle of the vector (x, y) with the x -axis, positive if counter-clockwise. Then, the initial positions of the other points are defined as

$$\mathbf{p}(h, k) \equiv f(h) [\cos(\alpha_k), \sin(\alpha_k), 0]. \quad (4.17)$$

Here $f(h)$ is a monotonic function that decreases from the maximum value R in $h = 1$ to the minimum value of $r_{min}(k)$ in $h = N_h - 1$, where $r_{min}(k)$ is 1.05 times the distance of the initial position of $\mathbf{p}(N_h, k)$ from the origin.

- c) T is set to its initial value T_0 .
- d) A point $\mathbf{p}(h, k)$ is randomly selected. If $h = 1$, the random value $\delta_z \in [-\delta_{max}/2, \delta_{max}/2]$ is chosen and the point is moved in the real space by the displacement $(0, 0, \delta_z)$. So $\mathbf{p}(1, k)$ moves only vertically along the external solid wall. If $1 < h < N_h$, the random values $\delta, \delta_z \in [-\delta_{max}/2, \delta_{max}/2]$ are chosen and the point is moved in the real space by the displacement $(\delta \cos \alpha_k, \delta \sin \alpha_k, \delta_z)$. In this way, $\mathbf{p}(h, k)$ moves randomly in the three-dimensional space, but it keeps the same radial direction α_k with respect to the center of the grid. If $h \geq j$,^{xiv} it is checked if the segment $\mathbf{p}(j, k)\mathbf{p}(j + 1, k)$ intersects the particle.^{xv} If so, the move is rejected and the program goes to step “ m ”. If $h = N_h$, the point $\mathbf{p}(N_h, k)$ is randomly moved on the

^{xiv}As standard choice we use $j = N_h - 3$. In general, the lower is j , the safer is the code, but of course the slower is the simulation.

^{xv}A way to do this is considering several points along the segment $\mathbf{p}(j, k)\mathbf{p}(j + 1, k)$, and verifying that they all stay outside the particle. To check if a generic point \mathbf{p} is outside the particle, the closest triangle to \mathbf{p} of the particle surface is selected, and a point \mathbf{t} belonging to this triangle is chosen. If the sign of $(\mathbf{t} - \mathbf{p}) \cdot \mathbf{n}$ is opposite to the sign of $(\mathbf{t} - \mathbf{c}) \cdot \mathbf{n}$, with \mathbf{n} the normal to the triangle and \mathbf{c} the center of mass of the particle, then \mathbf{p} is considered outside the particle, otherwise inside. This method works only for convex particle shapes.

particle surface. For doing this, firstly, a triangle belonging to the particle surface grid is selected randomly among the following 18 triangles:

$$\begin{aligned}
& (i-1, j-1), (i-1, j), (i, j); (i-1, j-1), (i, j-1), (i, j); \\
& (i, j-1), (i, j), (i+1, j); (i, j-1), (i+1, j-1), (i+1, j); \\
& (i+1, j-1), (i+1, j), (i+2, j); (i+1, j-1), (i+2, j-1), (i+2, j); \\
& (i-1, j), (i-1, j+1), (i, j+1); (i-1, j), (i, j), (i, j+1); \\
& (i, j), (i, j+1), (i+1, j+1); (i, j), (i+1, j), (i+1, j+1); \\
& (i+1, j), (i+1, j+1), (i+2, j+1); (i+1, j), (i+2, j), (i+2, j+1); \\
& (i-1, j+1), (i-1, j+2), (i, j+2); (i-1, j+1), (i, j+1), (i, j+2); \\
& (i, j+1), (i, j+2), (i+1, j+2); (i, j+1), (i+1, j+1), (i+1, j+2); \\
& (i+1, j+1), (i+1, j+2), (i+2, j+2); (i+1, j+1), (i+2, j+1), (i+2, j+2);
\end{aligned}$$

where each triangle is indicated by the coordinates of its three vertexes on the particle surface grid (see Fig. 4.31), and where the position of $\mathbf{p}(N_h, k)$ before being moved is located inside the triangle $(i, j), (i, j+1), (i+1, j+1)$ or $(i, j), (i+1, j), (i+1, j+1)$. Then, given the real space positions $\mathbf{A}, \mathbf{B}, \mathbf{C}$ of the vertexes of the selected triangle, the point $\mathbf{p}(N_h, k)$ is moved in $\mathbf{A} + (1-r_1)\mathbf{B} + (1-r_2)\mathbf{C}$, where r_1, r_2 are random numbers between 0 and 1, and such that $r_1 + r_2 \leq 1$. If the projection on the x, y plane of the new position of $\mathbf{p}(N_h, k)$ is outside the angle $\Delta\alpha$ on the x, y plane, with vertex in the origin, and centered around the α_k radial direction, then the move is rejected and the program goes to step “m)”. This check is done to keep the points on the particle surface aligned (approximately, within the angle $\Delta\alpha$) along the same line of the other points of the grid with the same k . Also, it is checked if the segment $\mathbf{p}(N_h, k)\mathbf{p}(N_h - 1, k)$ intersects the particle, and, if it does, the move is rejected and the program goes to step “m)”.

- e) The fluid-fluid interface surface variation δS due to the move of $\mathbf{p}(h, k)$ in step “d)” is calculated as the sum of the area variations of the six grid triangles with respectively vertexes: $\mathbf{p}(h, k)\text{-}\mathbf{p}(h, k-1)\text{-}\mathbf{p}(h-1, k-1)$, $\mathbf{p}(h, k)\text{-}\mathbf{p}(h-1, k)\text{-}\mathbf{p}(h-1, k-1)$, $\mathbf{p}(h, k)\text{-}\mathbf{p}(h-1, k)\text{-}\mathbf{p}(h, k+1)$, $\mathbf{p}(h, k)\text{-}\mathbf{p}(h, k+1)\text{-}\mathbf{p}(h+1, k+1)$, $\mathbf{p}(h, k)\text{-}\mathbf{p}(h+1, k)\text{-}\mathbf{p}(h+1, k+1)$, $\mathbf{p}(h, k)\text{-}\mathbf{p}(h+1, k)\text{-}\mathbf{p}(h, k-1)$. For the points $\mathbf{p}(h, k)$ on the boundary of the grid (i.e. $h = 1$ or $h = N_h$) only the three existing triangles are considered.
- f) The volume variation δV of fluid 2 induced by the move of $\mathbf{p}(h, k)$ in step “d)” is computed. We refer from now on with \mathbf{p}_o to the old real space position of $\mathbf{p}(h, k)$, i.e. before the move in step “d)”, and with \mathbf{p}_n to its new position. To compute δV , the following procedure can be used

- > The volumes $\Omega_1, \Omega_2, \Omega_3$ and Ω_4 of the four tetrahedrons with one vertex given by \mathbf{p}_o and the other three vertexes given respectively by $\mathbf{p}(h, k-1)\text{-}\mathbf{p}(h-1, k-1)\text{-}\mathbf{p}(h-1, k)$, $\mathbf{p}(h, k-1)\text{-}\mathbf{p}(h-1, k)\text{-}\mathbf{p}(h, k+1)$,

$\mathbf{p}(h+1, k)$ - $\mathbf{p}(h, k-1)$ - $\mathbf{p}(h, k+1)$, $\mathbf{p}(h, k+1)$ - $\mathbf{p}(h+1, k+1)$ - $\mathbf{p}(h+1, k)$ are computed.

- > The volumes Ω'_1 , Ω'_2 , Ω'_3 and Ω'_4 of the same four tetrahedrons considered before, but using \mathbf{p}_n instead of \mathbf{p}_o as one of their vertexes, are computed ^{xvi}.
- > $\delta V = \sum_{i=1}^4 (a_i \Omega_i + b_i \Omega'_i)$, with $a_i, b_i = \pm 1$. To calculate the signs of a_i and b_i for the i -th tetrahedrons Ω_i and Ω'_i , we firstly define the normal vector \mathbf{n}_i to the triangular face opposite to the \mathbf{p}_n or \mathbf{p}_o vertex of Ω_i and Ω'_i . The direction of \mathbf{n}_i is from fluid 2 toward fluid 1. Note that Ω_i and Ω'_i have a common triangular base and the fourth vertex different and given in one case by \mathbf{p}_n and in the other case by \mathbf{p}_o . We call \mathbf{w} one of the common vertexes that Ω_i and Ω'_i have. Then b_i is given by the sign of $\mathbf{n}_i \cdot (\mathbf{p}_n - \mathbf{w}_i)$. If $\mathbf{n}_i \cdot (\mathbf{p}_n - \mathbf{w}_i)$ has the same sign of $\mathbf{n}_i \cdot (\mathbf{p}_o - \mathbf{w}_i)$, then $a_i = b_i$, otherwise $a_i = -b_i$.

If the point $\mathbf{p}(h, k)$ moved in step “d)” is on the boundary of the grid (i.e. $h = 1$ or $h = N_h$), then only the two existing tetrahedrons are considered in the procedure described above.

- g) The variation δE_g induced by the move of $\mathbf{p}(h, k)$ in step “d)” in the fluid-fluid interface gravitational energy is computed. This procedure can be implemented analogously to the previous step, i.e. $\delta E_g = \sum_{i=1}^4 (a_i \hat{G}_i + b_i \hat{G}'_i)$, with $a_i, b_i = \pm 1$. Here \hat{G}_i is the gravitational energy of the tetrahedrons with one vertex given by \mathbf{p}_o , and the other three given, respectively for each i , by $\mathbf{p}(h, k-1)$ - $\mathbf{p}(h-1, k-1)$ - $\mathbf{p}(h-1, k)$, $\mathbf{p}(h, k-1)$ - $\mathbf{p}(h-1, k)$ - $\mathbf{p}(h, k+1)$, $\mathbf{p}(h+1, k)$ - $\mathbf{p}(h, k-1)$ - $\mathbf{p}(h, k+1)$, $\mathbf{p}(h, k+1)$ - $\mathbf{p}(h+1, k+1)$ - $\mathbf{p}(h+1, k)$. Then, \hat{G}'_i is the gravitational energy of the same tetrahedrons, but with one vertex given by \mathbf{p}_n instead of \mathbf{p}_o . To calculate the signs of a_i and b_i , the same method described in step “f)” can be used. The gravitational energy \hat{G} of a tetrahedron is given by

$$\hat{G} = \frac{\gamma}{\rho^2} \Omega c_z,$$

with Ω the volume of the tetrahedron and c_z the z component of the tetrahedron center of mass \mathbf{c} .

- h) If the point $\mathbf{p}(h, k)$ moved in step “d)” has $h = N_h$, i.e. it is a point constrained on the surface on the particle, then the variation $\delta W = \pm(A_1 + A_2)$ in the particle surface area wet by fluid 2 is calculated. Here A_1 is the area of the triangle with vertexes \mathbf{p}_o , \mathbf{p}_n and $\mathbf{p}(N_h, k-1)$, while A_2 is the

^{xvi}For a generic tetrahedron with vertexes \mathbf{A} , \mathbf{B} , \mathbf{C} , \mathbf{D} , its volume V is given by $V = |\mathbf{a} \cdot (\mathbf{b} \times \mathbf{c})|/6$, where: $\mathbf{a} = \mathbf{A} - \mathbf{B}$, $\mathbf{b} = \mathbf{A} - \mathbf{C}$, $\mathbf{c} = \mathbf{A} - \mathbf{D}$.

area of the triangle with vertexes \mathbf{p}_o , \mathbf{p}_n and $\mathbf{p}(N_h, k + 1)$.^{xvii} The sign is positive if, by moving \mathbf{p}_o to \mathbf{p}_n , the fluid 2 is increasing the particle surface area that it is wetting, otherwise the sign is negative.^{xviii}

- i*) Another point $\mathbf{p}(l, m)$, different from the point $\mathbf{p}(h, k)$ of step “*d*”, is randomly selected. For simplicity, we take here only $1 < l < N_h$. This point is moved to compensate the volume variation δV of fluid 2 generated by the displacement of $\mathbf{p}(h, k)$ in step “*d*” and computed in “*f*”. We call \mathbf{q}_o the old position of $\mathbf{p}(l, m)$, and \mathbf{q}_n its new position. To calculate \mathbf{q}_n we impose that

$$\delta V = \frac{1}{6} (\mathbf{q}_n - \mathbf{q}_o) \cdot \sum_{i=1}^6 (\mathbf{A}_i - \mathbf{q}_o) \times (\mathbf{A}_{i+1} - \mathbf{q}_o), \quad (4.18)$$

where $\mathbf{A}_1, \mathbf{A}_2, \mathbf{A}_3, \mathbf{A}_4, \mathbf{A}_5$ and \mathbf{A}_6 are respectively the positions of $\mathbf{p}(l - 1, m - 1)$, $\mathbf{p}(l, m - 1)$, $\mathbf{p}(l + 1, m)$, $\mathbf{p}(l + 1, m + 1)$, $\mathbf{p}(l, m + 1)$, $\mathbf{p}(l - 1, m)$, and $\mathbf{A}_7 \equiv \mathbf{A}_1$. So Eq. (4.18) implies

$$q_n(z) - q_o(z) = \frac{(q_o(x) - q_n(x))V(x) + (q_o(y) - q_n(y))V(y) + 6\delta V}{V(z)}, \quad (4.19)$$

where $\mathbf{V} = \sum_{i=1}^6 (\mathbf{A}_i - \mathbf{q}_o) \times (\mathbf{A}_{i+1} - \mathbf{q}_o)$, $\mathbf{V} = (V(x), V(y), V(z))$, $\mathbf{q}_n = (q_n(x), q_n(y), q_n(z))$ and $\mathbf{q}_o = (q_o(x), q_o(y), q_o(z))$. Therefore, a random number $\delta \in [-\delta_{max}/2, \delta_{max}/2]$ is chosen, then \mathbf{q}_n is obtained moving \mathbf{q}_o by the displacement

$$[\delta \cos \alpha_k, \delta \sin \alpha_k, q_n(z) - q_o(z)], \quad (4.20)$$

where $q_n(z) - q_o(z)$ is given in Eq. (4.19). If $l \geq j$, it is checked if the segment $\mathbf{p}(j, m)\mathbf{p}(j + 1, m)$ intersects the particle [analogously to the procedure described in step “*d*”], and, if it does, then the move is rejected and the program goes to step “*m*”.

- j*) The fluid-fluid interface surface variation $\delta S'$ due to the move of $\mathbf{p}(l, m)$ in step “*i*” is computed as described for the calculation of δS in step “*e*” (just with l and m in place of h and k).
- k*) The variation $\delta E'_g$ induced by the move of $\mathbf{p}(l, m)$ in step “*i*” in the fluid-fluid interface gravitational energy is computed as described in step “*g*” (just with l and m in place of h and k).

^{xvii}Note that, using this procedure to compute δW , we are approximating the particle surface area using a set of triangles that is not the same we used in step “*a*” to define the particle surface. However, as we move the points on the particle surface from one triangle only to its closest neighbors, the order of the approximation involved is the same. The higher is the number of triangles used in step “*a*” to define the particle surface, the better is the approximation involved in the calculation of the particle surface wet by fluid 2.

^{xviii}This can be checked simply by verifying which is the higher between \mathbf{p}_o and \mathbf{p}_n , with respect to z . However, this procedure needs to be adapted if the particle has a not-convex shape, or if one expects the interface to overstep the particle.

- l) The variation $\delta\Xi = \gamma(\delta S + \delta S' - \cos\theta \delta W) + \delta E_g + \delta E'_g$ in the potential Ξ [Eq. (4.3)] is computed. Then, with a probability

$$\mathcal{P} \equiv \begin{cases} 1, & \text{if } \delta\Xi < 0 \\ \exp\left\{-\frac{\delta\Xi}{k_B T}\right\}, & \text{if } \delta\Xi \geq 0 \end{cases} \quad (4.21)$$

the new configuration of the system is accepted, otherwise the two points moved respectively in step “d)” and “i)” return to their previous positions.

- m) The program returns to step “d)”. Every M times this step is performed, T is decreased by an amount δT . If $T \leq 0$, then the simulation ends.

Possibly, this algorithm can be used to calculate the equilibrium shape of a fluid-fluid interface for a pinned three-phase contact line. In this case, the only adaptations consist in choosing only points with $h < N_h$ in step “d)”, and in defining the initial position of the points constrained on the particle surface with the desired position for the pinned three-phase contact line.

Once the equilibrium shape of the fluid-fluid interface is obtained, the energy E [Eq. (2.24)] of the fluid-fluid-particle system can be computed. For convenience, we shift the reference level of E such that $E = 0$ corresponds to the particle desorbed in fluid 2, and we compute E as defined in Eq. (4.10). The various terms of Eq. (4.10) are computed, from the obtained equilibrium shape of the fluid-fluid interface at the end of the simulation, as it follows

- $A = \pi R^2$.
- S is computed, at the end of the simulation, as the sum of the areas of all the triangles forming the fluid-fluid interface grid, plus the sum of the areas of the circular segments formed by each segment $\mathbf{p}(1, k) \mathbf{p}(1, k+1)$ with the vertical cylindrical wall of radius R enclosing the system. ^{xix}
- To compute W_1 , we check, at the end of the simulation, if the center of mass of each triangle of the particle surface grid is higher or lower (in z) with respect to its closest interface grid point constrained on the particle surface, i.e. to its closest $\mathbf{p}(N_h, k)$ (with $k = 1, \dots, N_k$). Then W_1 is obtained summing all the areas of the triangles that have resulted higher. ^{xx}

^{xix}To be precise, we use the projection of the segment $\mathbf{p}(1, k) \mathbf{p}(1, k+1)$ on the $z = 0$ plane to do this calculation. The approximation involved in this way is negligible because close to the external wall the fluid-fluid interface is almost flat.

^{xx}There is of course an approximation involved in this procedure, but it can be reduced by using a high-enough number of triangles to define the particle surface and a high-enough number of fluid-fluid interface grid points constrained on the particle surface. Possibly, more sophisticated calculations can be introduced to improve the approximation. Also, for particles almost completely immersed in one of the two fluids, this procedure may cause mistakes, and therefore requires adjustments.

- At the beginning of the simulation, E_g is set to its initial value zero, because the interface is flat.^{xxi}. Then, to calculate its final value (i.e. corresponding to the equilibrium shape of the fluid-fluid interface), we simply update E_g during the simulation by adding, each time a new point configuration is accepted in step “ l ”, the contributions δE_g and $\delta E'_g$ calculated in the steps “ g ” and “ k ” of the algorithm^{xxii}.

^{xxi}There is a small approximation in this assumption, because we are neglecting the presence of the particle that removes a small portion of volume from both fluids. The real $E_g = 0$ configuration would be a flat interface without the particle. However, the approximation is very small, especially for ℓ much greater than the particle size, and it affects only the reference level of the energy we measure.

^{xxii}Note that this method would not have work, for example, to compute W_1 , because each contribution δW computed in step “ h ” during the simulation is approximated. Its approximation is negligible for the computation of δE in step “ l ”, however, if W_1 is calculated updating its initial value by using δW each time a new configuration is accepted, then the approximation involved on the final value of δW is, in general, not negligible, due to the high number of cycles performed in a simulation (generally from $O(10^5)$ to $O(10^7)$). For E_g , this problem does not hold, because the calculation of δE_g and $\delta E'_g$ does not involve approximations.

CHAPTER 5

CAPILLARY INTERACTIONS AND SELF-ASSEMBLY OF ADSORBED CUBES

In this Chapter we exploit the numerical method introduced in Chapter 4 to study the capillary interactions and self-assembly of cubic particles adsorbed at a fluid-fluid interface. Firstly, we predict the capillary deformations induced by the cubes for various Young's contact angles, showing that capillarity is crucial not only for quantitative but also for qualitative predictions of the equilibrium configurations of a single cube. For a Young's contact angle close to $\pi/2$, we show that a single-adsorbed cube generates a hexapolar interface deformation with three rises and three depressions. Thanks to the 3-fold symmetry of this hexapole, strongly directional capillary interactions drive the cubes to self-assemble into hexagonal or graphene-like honeycomb lattices. By a simple free-energy model, we predict a density-temperature phase diagram in which both the honeycomb and hexagonal lattice phases are present, as stable states.

5.1 INTRODUCTION

In the previous Chapter we introduced a new numerical method to calculate the equilibrium shape of a fluid-fluid interface in contact with solid surfaces in a given position, and, in particular, we pointed out its applicability to study adsorbed particles at fluid-fluid interfaces, showing results for the equilibrium configuration of adsorption for a sphere, a cylinder, and an ellipsoid, respectively. In this Chapter, we delve deeper into adsorbed particles at fluid-fluid interfaces, by studying their capillary interactions and self-assembly. At the equilibrium, as shown in Chapter 4, a particle adsorbed at the interface may induce capillary deformations in the fluid-fluid interface height profile, as a consequence, for example, of gravity (see Sec. 4.5.1), or of its anisotropic shape (see Sec. 4.5.2). These capillary deformations induce capillary interactions between the adsorbed particles [34–38, 40, 41], regulating the particle self-assembly at the interface [42–50]. In this Chapter, in particular, we exploit our numerical method to study particles with a cubic shape. Very recent experiments (see Refs. [75, 76, 115]) have shown that adsorbed nanocubes with truncated corners can assemble into hexagonal and graphene-like honeycomb lattices. The origin of these structures is unknown, although ligand adsorption and van der Waals forces between specific facets of the truncated cubes have been suggested [75]. Here, however, we show that generic cubic particles with homogeneous surface properties generate hexapolar capillary deformations which can be largely responsible for the observed structures, as we argue. Therefore, cubes of other materials or dimensions could also form similar structures. Firstly, we will investigate the equilibrium configuration of a single-adsorbed cubic particle, for various Young’s contact angles. Then, we will study for many adsorbed cubes the capillary interactions and self-assembly, due to the capillary deformations induced by the cubes in the interface height profile, obtaining finally a temperature-density phase diagram for the adsorbed cubes at the interface, where both the honeycomb and hexagonal lattice phases appear as thermodynamically stable states.

5.2 METHOD

In this Section, we briefly illustrate the method exploited for the numerical calculations reported in this Chapter (for a more detailed description, see Chapter 4). In our model, we consider a fluid-fluid interface which is flat and coincides with the plane $z = 0$ when no particle is adsorbed. Then, we introduce a rigid particle with a fixed position and orientation defined by the polar angle φ of the particle’s vertical axis with the interface normal, the internal Euler angle ψ around the particle’s vertical axis, and the height z_c of the particle’s center of mass on the $z = 0$ level (see Fig. 5.1). Possibly, more than one particle can be introduced. In such a case, for each i -th particle, also the coordinates x_i and y_i of the particle’s center of mass in the $z = 0$ plane, and the azimuthal angle

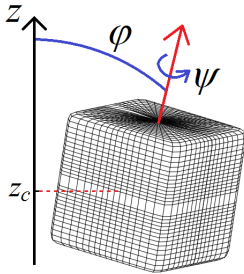


Figure 5.1: Configuration of a cubic particle (black grid) at a fluid-fluid interface, which corresponds to the plane $z = 0$ when no particle is adsorbed. The height of the cube center of mass is z_c , the polar angle of the cube vertical axis with the interface plane is φ , and the internal Euler angle around the cube vertical axis is ψ .

α_i of the particle's vertical axis with respect to the $z = 0$ plane, need to be specified. The whole particle(s)-fluid-fluid system is surrounded by an external vertical wall at a distance much larger than the particle size, to avoid finite size effects, and with Young's contact angle $\pi/2$, to induce a flat interface far from the particles. Given the fixed position(s) and orientation(s) of the particle(s), defined by $\mathbf{\Omega} = \{z_{c_i}, \varphi_i, \psi_i, x_i, y_i, \alpha_i\}_{i=1}^N$, with N the number of particles, we numerically calculate (for details see Chapter 4) the fluid-fluid interface equilibrium shape by representing the interface by a grid of points, and exploiting a Simulated Annealing algorithm [113] to calculate the positions of these points that minimize the energy E [Eq. (2.24)] of the fluid-fluid-particle(s) system, given the fixed volumes of the two fluids. For convenience, in this Chapter we use E_N , with N the number of adsorbed particles at the interface, to indicate the energy E of the fluid-fluid-particle(s) system expressed in Eq. (2.24), and we shift it by a constant such that $E_N = 0$ when all the particles are desorbed from the interface and completely immersed in the fluid below it, with respect to z . Also, we neglect the fluid-fluid interface gravitational energy and the particle weight, as they both are not relevant for the experimental systems of interest.¹ Therefore, from Eq. (2.24) we obtain

$$E_N(\mathbf{\Omega}) = \gamma [S(\mathbf{\Omega}) - A + W(\mathbf{\Omega}) \cos \theta] , \quad (5.1)$$

where $S(\mathbf{\Omega})$ and A are the total areas of the fluid-fluid interface with and without particle(s), respectively, $W(\mathbf{\Omega})$ is the total surface area of the particle(s) in contact with the fluid above the interface, and θ is Young's contact angle, defined by Eq. (2.18) from the three surface tensions in the system, i.e. γ (fluid-fluid), γ_1 (particle-fluid 1), γ_2 (particle-fluid 2), and taken inside fluid 2 (i.e. the fluid below the interface, with respect to z). The pressure-volume terms of the energy do not appear in Eq. (5.1), because here $\Delta P = 0$, as the fluid-fluid interface is flat when no particles are adsorbed. Note that γ and θ are input parameters in Eq. (5.1). As proven in Sec. 2.5 of Chapter 2, the interface shape that minimizes E_N , for the given volume of the fluids, is the solution of the Young-Laplace Equation [Eq. (2.21)], with Young's Law [Eq. (2.18)] as boundary condition, i.e. it is the equilibrium shape of the fluid-fluid interface. Note that the equilibrium position of the three-phase contact line is automatically found by the minimization of

¹However, they can be easily included in our numerical method, as we showed in Chapter 4.

E_N , i.e. it is not imposed a priori. The fluid-fluid interface equilibrium shape, as numerically obtained by our method, forms an angle with the particle surface that matches the input angle θ introduced in Eq. (5.1). Such a geometrical constraint is also not imposed a priori in the method, but automatically found by minimizing the energy E_N .

5.3 SINGLE-ADSORBED CUBE

In this Section, we show results for a single-adsorbed cubic particle with smooth edges (see Fig. 5.1) and side length $L \ll \ell$, where typically the capillary length ℓ is of the order of 1 mm. Since we are using a macroscopic fluid-fluid model, we are also assuming that L is much larger than the fluid-fluid interface thickness. So, the results we present generally hold for micron-to-nanometer sized cubes. To define the shape of the cubic particle, we use a super-quadratic equation. Precisely, the position of each point $\mathbf{p}(u, v) \equiv [p_x(u, v), p_y(u, v), p_z(u, v)]$ of the grid defining the cube surface is obtained by varying the parameters u, v in the interval $[0, 1]$, with

$$\begin{aligned} p_x &= \frac{\cos(u\pi - \pi/2) \cos(2v\pi)}{|\cos(u\pi - \pi/2) \cos(2v\pi)|} |\cos(2v\pi)|^{\frac{1}{10}} |\cos(u\pi - \pi/2)|^{\frac{1}{10}} , \\ p_y &= \frac{\cos(u\pi - \pi/2) \sin(2v\pi)}{|\cos(u\pi - \pi/2) \sin(2v\pi)|} |\sin(2v\pi)|^{\frac{1}{10}} |\cos(u\pi - \pi/2)|^{\frac{1}{10}} , \\ p_z &= \frac{\sin(u\pi - \pi/2)}{|\sin(u\pi - \pi/2)|} |\sin(u\pi - \pi/2)|^{\frac{1}{10}} . \end{aligned} \quad (5.2)$$

Then, the set of all the points \mathbf{p} is rotated and translated to obtain the desired position and orientation of the cube at the interface. In Fig. 5.2, we show E_1 [Eq. (5.1)], minimized over z_c , with respect to φ and ψ , for various Young's contact angles θ . The coordinates z_c, φ, ψ which locally minimize $E_1(z_c, \varphi, \psi)$ correspond to an equilibrium or metastable configuration of the cube. We found that these are (slight perturbations of) the three configurations defined in Fig. 5.3: $\{100\}$, when one face of the cube points upward (i.e. $\varphi = 0$); $\{110\}$, when one edge between two faces of the cube points upward (i.e. $\varphi = \pi/4, \psi = 0$); $\{111\}$ when one corner between three faces of the cube points upward (i.e. $\varphi = \pi/4, \psi = \pi/4$). To point out the importance of capillarity even for these single particle calculations, in Fig. 5.5(a) we compare the energy E_1 , with respect to φ and minimized over z_c and ψ , as obtained by our numerical method, with the same predictions but obtained from the Triangular Tessellation technique (TTT) [116], in which capillary deformation effects are neglected. For a given configuration (z_c, φ, ψ) of the cube, the energy E_1 calculated by the TTT is always higher, as expected. More interestingly, we found that neglecting capillarity leads, for $\cos \theta \leq 0.2$, to the wrong equilibrium orientation of the cube: the TTT predicts the $\{110\}$ as equilibrium orientation, whereas our method finds the $\{111\}$. For $\cos \theta = 0.3$ and $\cos \theta = 0.5$, i.e. for a larger affinity of the cube with the heaviest fluid, both our

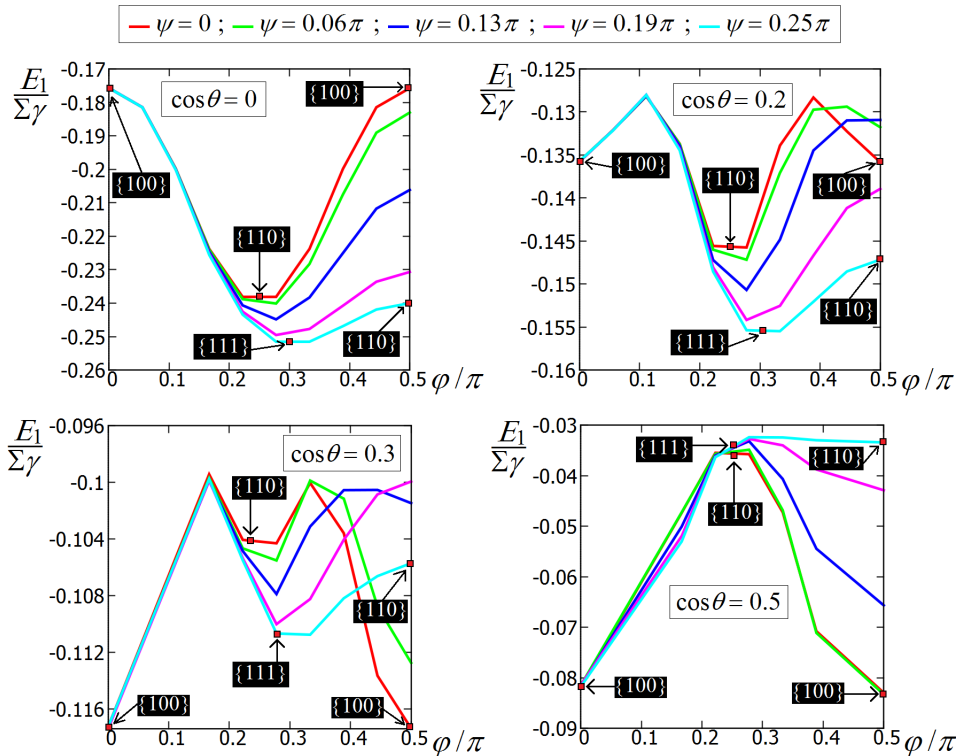


Figure 5.2: Energy E_1 [Eq. (5.1)] of a single adsorbed cube with side L , minimized over z_c and with respect to φ and ψ (see Fig. 5.1), for various Young's contact angles θ . We plot E_1 in units of $\gamma\Sigma$, with Σ the cube's total surface area. For a typical fluid-fluid surface tension $\gamma = 0.01$ N/m, we have $\Sigma\gamma \approx 350 k_B T$ for $L = 5$ nm, and $\Sigma\gamma \approx 1.5 \cdot 10^7 k_B T$ for $L = 1 \mu\text{m}$. The minima in the energy corresponds to the equilibrium and metastable configurations z_c , φ , ψ of the cube. The $\{100\}$, $\{110\}$, $\{111\}$ marks indicate the orientations of the cube at the interface, corresponding to (slight perturbations of) the definitions in Fig. 5.3.

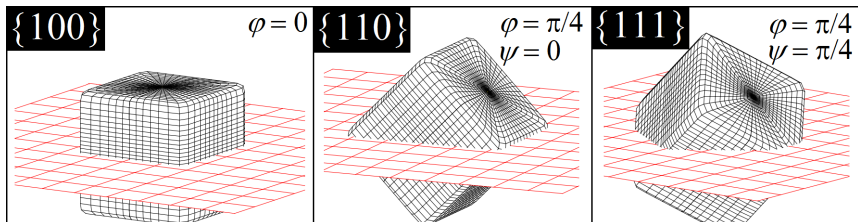


Figure 5.3: Definitions of the $\{100\}$, $\{110\}$, and $\{111\}$ orientations for a cube (black grid) adsorbed at a flat fluid-fluid interface, with the red grid representing a plane parallel to the flat interface, i.e. to $z = 0$. The polar angle of the cube vertical with the $z = 0$ plane is φ , and the internal Euler angle of the cube around its vertical axis is ψ , see Fig. 5.1.

numerical method and the TTT predict that the $\{100\}$ becomes the minimum energy orientation, with the cube almost completely immersed in the lower fluid. Interestingly, we find for $\cos\theta \leq 0.2$ that the cube, which has the $\{111\}$ orientation at the equilibrium, generates a hexapolar capillary deformation in the fluid-fluid interface, with three rises and three depressions in a 3-fold symmetric disposition [see Fig. 5.5(b)]. Instead, for $\cos\theta \geq 0.3$, where the cube has the $\{100\}$ orientation at the equilibrium, no significant capillary deformations are induced in the fluid-fluid interface [see Fig. 5.5(b)]. Note that, for $\cos\theta = 0.3$, the $\{111\}$ still appears as a metastable configuration, though.

In Fig. 5.4(a) we report, for a single adsorbed cube with one of the three orientations $\{100\}$, $\{110\}$, $\{111\}$ as defined in Fig. 5.3, the energy E_1 computed through our numerical method and minimized over z_c , with respect to the particle contact angle θ . As confirmed by the results in Fig. 5.2, between $\cos\theta = 0.2$ and $\cos\theta = 0.3$ there is a cross-over in the energy E_1 for the $\{100\}$ and $\{111\}$ orientation, such that the $\{111\}$ shifts with the $\{100\}$ as the minimum energy orientation. We also see that the $\{111\}$ remains energetically more favorable than the $\{110\}$, although their energies are very close. In 5.4(b) we show the same results, but obtained by neglecting capillary deformations, i.e. using the TTT. In this approximation, the $\{110\}$ appears energetically more favorable than the $\{111\}$ for $\cos\theta < 0.3$, in contradiction with the results from our method, as shown in Fig. 5.4 (a). This proves that neglecting capillary deformation effects can lead to erroneous equilibrium configurations of the particle.

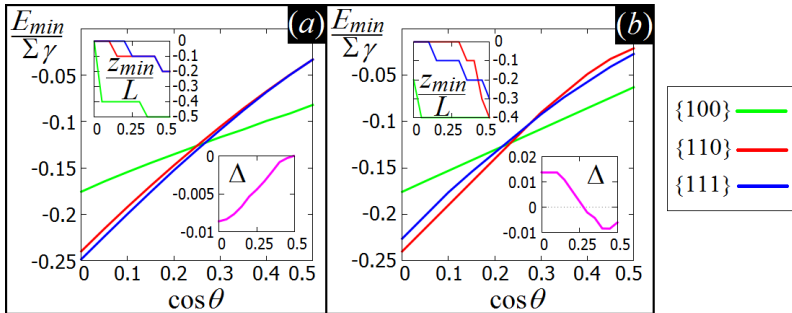


Figure 5.4: Energy $E_{min}(\cos\theta)$, which is E_1 [Eq. (5.1)] minimized over z_c , of a single adsorbed cube with side L at a fluid-fluid interface, with a fixed orientation (i.e. fixed φ and ψ) given, respectively, by the three orientations defined in Fig. 5.3, i.e. $\{100\}$ (green line), $\{110\}$ (red line), and $\{111\}$ (blue line). The total surface area of the cube is Σ , and the fluid-fluid surface tension is γ . In (a) the results are obtained through our numerical method, i.e. including capillary deformations. In (b) the results are obtained by the TTT [116], i.e. neglecting capillarity. The top insets, in both graphs, show z_{min} , i.e. the z_c corresponding to the minimum E_1 , for the three cube orientations considered, with respect to $\cos\theta$. The bottom insets, in both graphs, show $\Delta \equiv [E_{min}(\{111\}) - E_{min}(\{110\})]/\Sigma\gamma$, i.e. the difference of E_{min} for the cube in the $\{111\}$ and in the $\{110\}$ orientation, with respect to $\cos\theta$. As shown, neglecting capillarity (see graph on the right) leads to a completely different prediction.

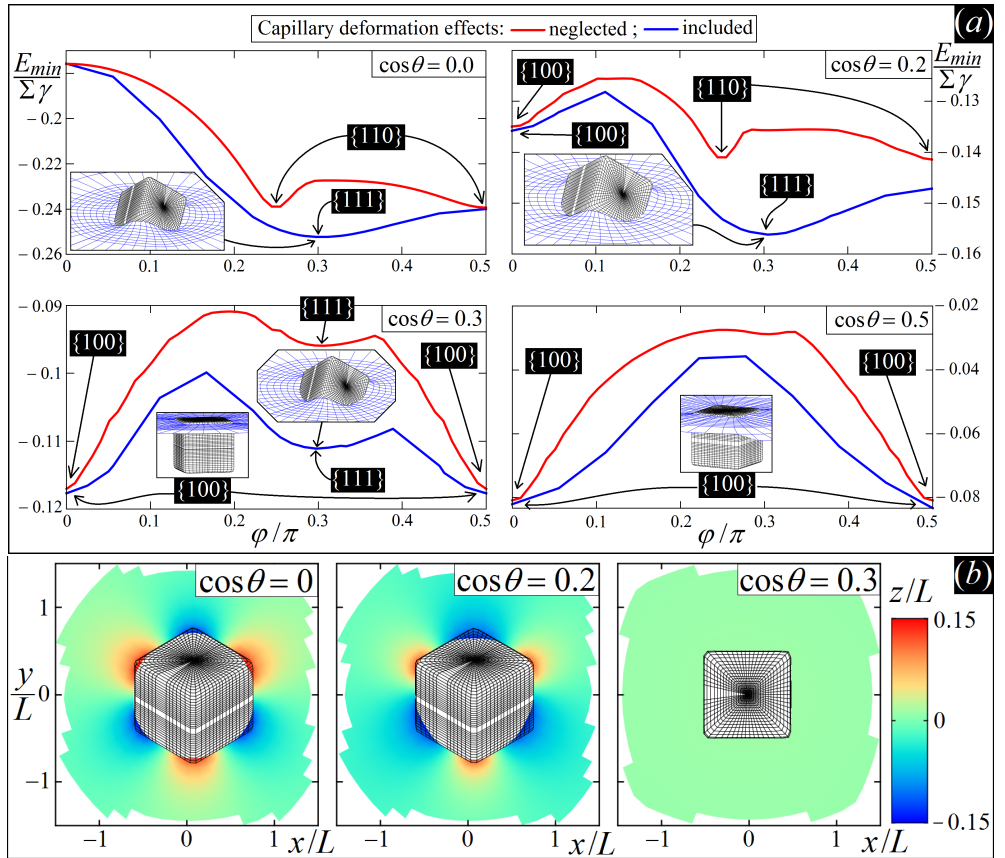


Figure 5.5: (a) Energy $E_{min}(\varphi)$, which is E_1 [Eq. (5.1)] minimized over z_c and ψ , of a single adsorbed cube with side L , for various Young's contact angles θ . We plot E_{min} in units of $\gamma\Sigma$, with Σ the cube's total surface area and γ the fluid-fluid surface tension (see also Fig. 5.2). The minima in the energy corresponds to the equilibrium and metastable configurations z_c , φ , ψ of the cube. The $\{100\}$, $\{110\}$, and $\{111\}$ marks indicate the orientations of the cube at the interface, corresponding to (slight perturbations of) the definitions in Fig. 5.3. The blue lines are the results obtained through our numerical method, i.e. including capillary deformation effects. The red lines are the results obtained through the TTT [116], i.e. neglecting capillarity. In the insets we show, for the particle equilibrium and metastable configurations, a 3D view of the interface shape (blue grid) close to the particle (black grid), as calculated by our method. (b) Contour plots, for the global minimum energy configuration of the cube for the various θ considered, of the interface height profile deformed by the particle, as obtained by our numerical method. For $\cos\theta = 0$ and $\cos\theta = 0.2$, a hexapolar capillary deformation emerges, while for $\cos\theta = 0.3$ the interface is essentially undeformed. The case $\cos\theta = 0.5$, not shown, is basically identical to the case $\cos\theta = 0.3$. The plane $z = 0$ corresponds to the fluid-fluid interface when no particle is adsorbed.

5.4 PAIR INTERACTION

Having established, in the previous Section, the equilibrium configuration of a single-adsorbed cube, we study in this Section the pair interaction between two cubes adsorbed at a fluid-fluid interface.

To study capillary interactions between adsorbed particles, we define the *capillary interaction energy per particle*

$$\tilde{E}_N \equiv \frac{E_N}{N} - E_1, \quad (5.3)$$

where N is the number of adsorbed particles at the fluid-fluid interface, and E_N [Eq. (5.1)] is the energy of the fluid-fluid-particle(s) system, and it is calculated numerically from the equilibrium shape of the fluid-fluid interface, which is computed through our numerical method for the given input parameters [position(s) of the particle(s), Young's contact angle θ , and volume of the fluids]. Note that

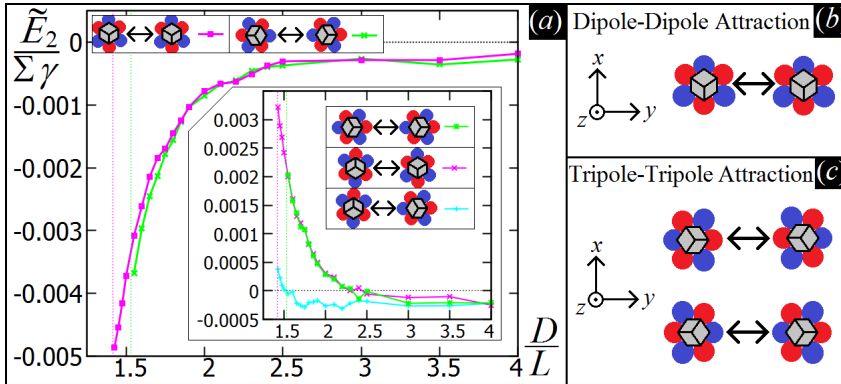


Figure 5.6: (a): Interaction energy per particle \tilde{E}_2 (Eq. (5.3)) of two $\{111\}$ -oriented adsorbed cubes with side L and Young's contact angle $\theta = \pi/2$, as a function of the distance D between their centers of mass, for five relative azimuthal orientations of their hexapolar capillary deformations in the interface plane, indicated by the sketches, where blue spots are depressions and red spots are rises of the interface height profile. The energy is plotted in units of $\gamma \Sigma$, with Σ the cube's total surface area and γ the fluid-fluid surface tension. The main graph shows the two attractive configurations, where a red-blue dipole approaches another red-blue dipole (violet curve), and a red-blue-red tripole approaches another red-blue-red tripole (green curve). The inset shows the two repulsive counterparts and an almost *neutral* dipole-tripole pair. The violet and green vertical dotted lines represent the cube contact distance for the dipole-dipole and tripole-tripole attachments, respectively. As $\cos \theta = 0$, the system is invariant under exchange of red and blue. (b)-(c): Sketch of the two possible relative orientations of the hexapoles generated by the two cubes that induce attraction between them: (i) *dipole-dipole* orientation, such that a set of two spots (one red and one blue) of one cube overlaps with the same set of two spots of another cube, (ii) *tripole-tripole* orientation, such that a set of three spots (blue-red-blue or red-blue-red) of one cube overlaps with the same set of three spots of another cube.

$\tilde{E}_N = 0$ when only one particle is adsorbed ($N = 1$), or when N adsorbed particles do not interact with each other, such that $E_N = N E_1$.

For cubes with $\cos \theta \geq 0.3$, which are adsorbed in the $\{100\}$ configuration and induce negligible deformations [see Fig. 5.5(b)], we do not expect capillary interactions, in agreement with experiments of cubes with $\cos \theta \approx 0.3$ and $L \approx 1 \mu\text{m}$ [117]. Therefore, cubes with such a contact angle tend to assemble into tetragonal possibly closed-packed structures [118].

More interesting is the case $\cos \theta \leq 0.2$, where cubes are adsorbed in the $\{111\}$ configuration and induce a hexapolar deformation in the height profile of the interface, with 3 depressions and 3 risesⁱⁱ [see Fig. 5.5(b)]. In Fig. 5.6(a) we study, for two adsorbed cubes ($N = 2$) with $\cos \theta = 0$, the interaction energy per particle

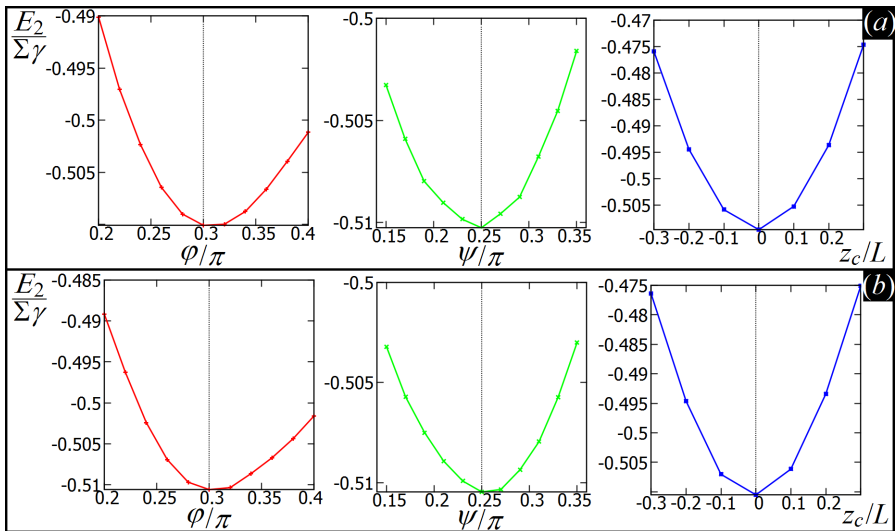


Figure 5.7: Energy E_2 [Eq. (5.1)] for a system of two adsorbed cubes with side L , surface area Σ , Young's contact angle $\theta = \pi/2$, adsorbed at the interface with the equilibrium configuration (i.e. the values of φ , ψ and z_c , see Fig. 5.1) computed for a single cube. The cubes have a distance $D = 1.6 L$ between their centers of mass, i.e. close to their contact distance. As shown in Fig. 5.5(b) for $\cos \theta = 0$, each cube in this configuration induces in the interface height profile a hexapolar capillary deformation. Here the reciprocal azimuthal orientation of the hexapoles generated by the cubes is such that the cubes are (a) dipole-dipole and (b) tripole-tripole interacting [see Fig. 5.6(b)-(c)]. The energy E_2 plotted here (in units of $\Sigma\gamma$, with γ the fluid-fluid surface tension) is obtained by varying the value of, respectively, φ , ψ and z_c for one of the two cubes, from its equilibrium value for a single-adsorbed cube, represented by the dotted vertical line. As shown, the equilibrium values of φ , ψ and z_c are still the same now that we are considering two cubes close to each other. This proves that the capillary interactions between the cubes do not affect the equilibrium configuration φ , ψ , z_c of each cube, calculated for a single adsorbed cube.

ⁱⁱSimilar predictions have also been made for cubes adsorbed at thin films [119].

\tilde{E}_2 [Eq. (5.3)], with respect to the center of mass distance D between the cubes, for several relative azimuthal orientations of the hexapolar capillary deformations generated by the two cubes in the fluid-fluid interface height profile. To illustrate the azimuthal orientation of each hexapole in the interface plane, we indicate a rise in the interface height profile with a red spot, and a depression with a blue spot. Figure 5.6 shows that two cubes attract each other when their orientations allow them to overlap spots with the same color, whereas the cubes repel each other when spots of unlike color overlap. This was to be expected, because the fluid-fluid surface area decreases by overlapping spots of identical color, while it increases when a rise and a depression approach each other. In these calculations, we kept z_c , φ , ψ of each cube fixed to their values for a single-adsorbed cube at $\cos\theta = 0$, as we verified that these are hardly influenced by the presence of the other cubes (see Fig. 5.7). From the behavior of $\tilde{E}_2(D)$ in Fig. 5.6(a), we note that there are two kinds of orientations that allow the two cubes to attract each other: (i) a ‘dipole-dipole’ attraction [Fig. 5.6(b)], when a set of two spots (one red and one blue) of one cube overlaps with the same set of two spots of another cube, and (ii) a ‘tripole-tripole’ attraction [Fig. 5.6(c)], when a set of three spots (blue-red-blue or red-blue-red) of one cube overlaps with the same set of three spots of another cube. As shown in Fig. 5.6(a), the interaction strength \tilde{E}_2 for these two different orientations is essentially the same, for $\cos\theta = 0$. However, the contact distance for dipole-dipole interacting cubes is smaller than for tripole-tripole interacting cubes. Therefore, two $\{111\}$ -oriented cubes minimize the interaction energy \tilde{E}_2 by a dipole-dipole bond, while the tripole-tripole bond is metastable.

5.5 SELF-ASSEMBLY INTO HEXAGONAL AND HONEYCOMB LATTICES

In the previous Section, we showed that two cubes adsorbed with the $\{111\}$ orientation, i.e. generating a hexapolar capillary deformation in the fluid-fluid interface height profile [see Fig. 5.5(b)], attract each other only through two possible reciprocal azimuthal orientations of their hexapole in the interface plane, namely dipole-dipole and tripole-tripole orientation, respectively (see Fig. 5.6). In this Section we consider, for $\cos\theta = 0$, many cubes ($N \gg 2$) adsorbed with the $\{111\}$ orientation at the interface, and we study the ordered structures they can form. If the cubes bond to each other only through the dipole-dipole orientation, then an hexagonal lattice is formed, with all the dipole-dipole bonds satisfied, see Fig. 5.8(a). Instead, if the cubes bond to each other only through the tripole-tripole orientation, then an honeycomb lattice is formed, with all the tripole-tripole bonds satisfied, see Fig. 5.8(b). Note that the holes of this honeycomb lattice are all filled with either depressions or rises, frustrating the inclusion of another $\{111\}$ -oriented hexapole-generating cube (see Fig. 5.9), and therefore preventing this honeycomb lattice to become an hexagonal lattice. We consider

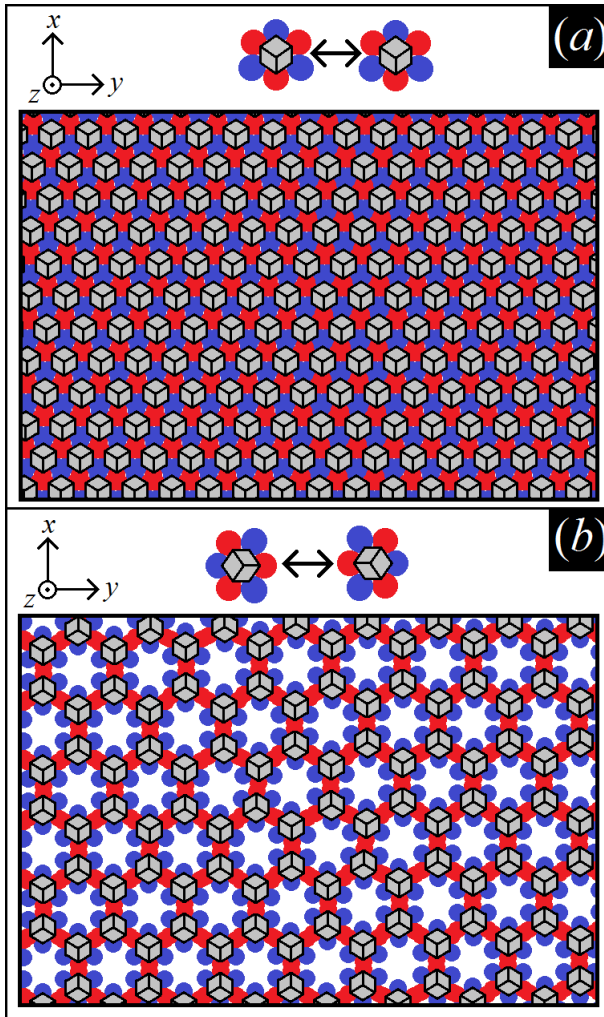


Figure 5.8: Sketch (a) of the honeycomb lattice formed by tripole-tripole interacting cubes, and (b) of the hexagonal lattice formed by dipole-dipole interacting cubes. The cubes, with Young's contact angle $\theta = \pi/2$, are adsorbed at the fluid-fluid interface with the $\{111\}$ equilibrium orientation, therefore inducing a hexapolar capillary deformation in the interface height profile [see Fig. 5.5(b)]. Here, each red spot represents a rise induced by the cubes in the interface height profile, and each blue spot represents a depression in the interface height profile. As $\cos\theta = 0$, the system is symmetric with respect to z , i.e. by shifting red with blue. Particle-particle distances are only schematic. Note that, in the hexagonal lattice, all cubes have the same azimuthal orientation of their vertical axis with respect to the interface plane, whereas in the honeycomb lattice each neighbor is rotated by π .

now the limit $N \rightarrow \infty$ for the $\{111\}$ -oriented hexapole-generating cubes adsorbed at the fluid-fluid interface. In Fig. 5.10(a) we show the interaction energy per particle \tilde{E}_∞ [Eq. (5.3)] for a periodic extension of the hexagonal and honeycomb lattice, formed by dipole-dipole and tripole-tripole attached cubes, respectively, with respect to the center of mass distance D between two closest-neighbor cubes in the lattice. To perform this calculation, we apply our numerical method to a lattice unit cell, which is rectangular with $N = 2$ for the honeycomb lattice, and hexagonal with $N = 1$ for the hexagonal lattice. At the boundary of these unit cells, instead of placing as usual a solid vertical wall with Young's contact angle $\pi/2$, we impose periodic boundary conditions for the height profile of the fluid-fluid interface. For the hexagonal lattice, the height profile of the interface is the same on each couple of opposite sides of the hexagonal cell [see Fig. 5.10(b)]. For the honeycomb lattice, the height profile of the interface is the same on the two short sides of the rectangular cell. Each long side of the rectangular cell is

divided in two halves, and the height profile of the interface is the same on the first half of one long side and on the second half of the other long side [see Fig. 5.10(c)]. Contour plots of the interface height profile, as obtained numerically by our method, are shown in Fig. 5.11 for the hexagonal and honeycomb lattice unit cells, for various values of D .

The results of Fig. 5.10(a) show that, for a given distance D , the hexagonal lattice with dipole-dipole interacting cubes (called phase x) has a lower energy per particle \tilde{E}_∞ than the honeycomb lattice with tripole-tripole interacting cubes (called phase h). In addition, phase x can reach a smaller lattice spacing than phase h , lowering even more the interaction energy per particle \tilde{E}_∞ , because the contact distance is smaller for dipole-dipole attached cubes than for tripole-tripole attached cubes. Hence, it is tempting to conclude that the equilibrium structure consists of touching cubes in phase x , while the phase h of touching cubes is a metastable state, because it locally minimizes \tilde{E}_∞ (about the metastability of phase h , see also Fig. 5.12). However, this reasoning on the basis of the capillary energy is correct only if *translational* and *rotational entropy* contributions can be ignored, which is only the case in the low-temperature or large-particle regime, where $\gamma\Sigma/k_B T$ is sufficiently large (with γ the fluid-fluid surface tension, Σ the cube total surface area, k_B the Boltzmann constant and T the temperature of the system). Given the interaction energy scale of about $-0.02\gamma\Sigma$ per particle in the close-packed phase x , as shown in Fig. 5.10(a), and given a typical free-energy scale of approximately $10 k_B T$ per particle for hard disks at packing fractions varying from rather dilute to close-packed, one arrives at a rough estimate of a balance of capillary and entropic contributions for $\gamma\Sigma/k_B T \approx 500$. Therefore, we conclude that, for $\gamma\Sigma \gg 500 k_B T$ we are in the regime where capillary interactions dominate over entropic forces. Hence, in this limit the cubes assemble in the close-packed phase x , because such a structure has the lowest capillary interaction energy per particle. However, in the regime $\gamma\Sigma \approx 500 k_B T$, we expect entropic forces to be of the same order of capillary interaction forces. So the phase h , favored by entropy because, compared to phase x , it has a lower density per unit area of adsorbed cubes at the interface, may become the phase energetically most favorable in this regime, if entropic effects for the adsorbed cubes are included. These conclusions are elaborated more quantitatively in the next Section, where an approximated free-energy model is introduced to take into account both capillary and entropic contributions to the energy of the x and h phases, and a temperature-density phase diagram for the adsorbed cubes at the fluid-fluid interface is obtained.

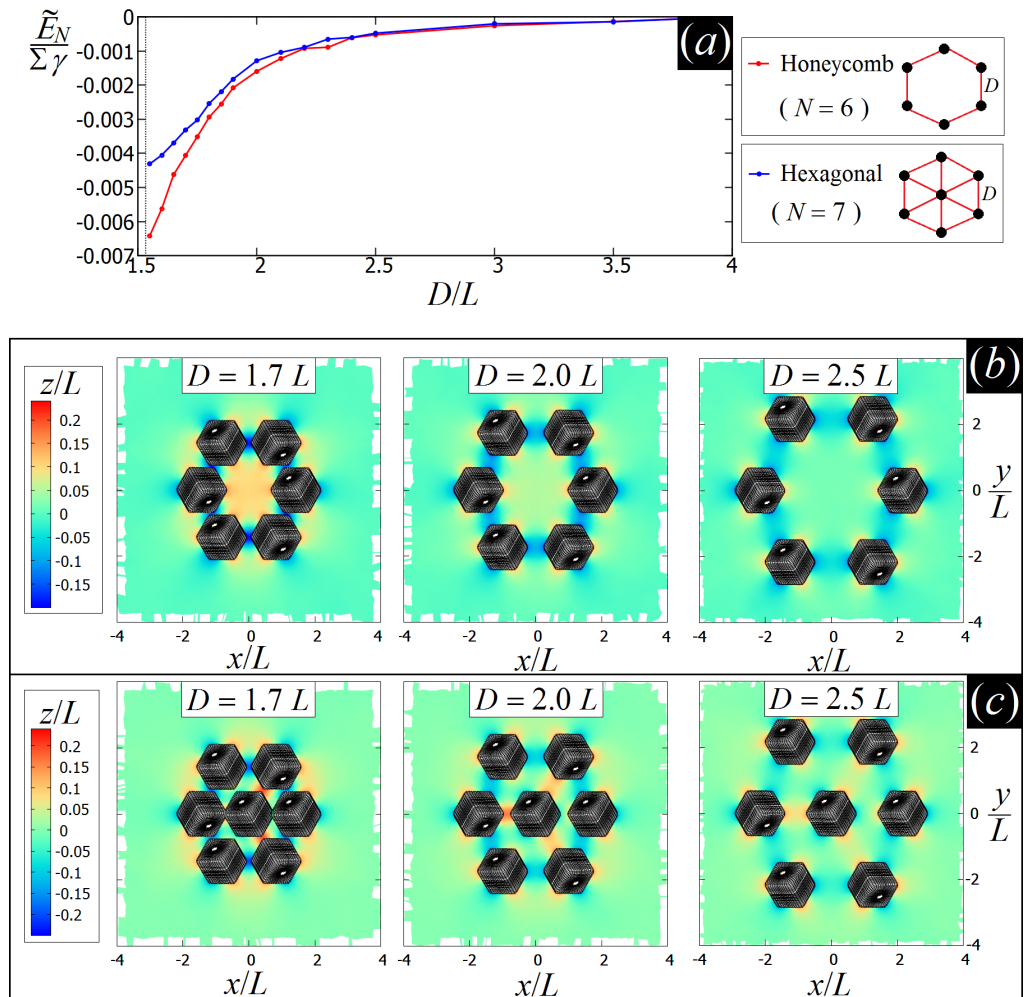


Figure 5.9: (a): Interaction energy per particle \tilde{E}_N [Eq. (5.3)] for $N = 6$ and $N = 7$ cubes, adsorbed at the interface with the $\{111\}$ orientation and tripole-tripole interacting, with side L , surface area Σ , and Young's contact angle $\theta = \pi/2$. As shown, \tilde{E}_N for the 6-particle system [i.e. corresponding to the honeycomb assembly, see (b)] is lower than for the 7-particle system [i.e. corresponding to the hexagonal assembly, see (c)]. Therefore, tripole-tripole interacting cubes prefer to assemble into a honeycomb lattice instead than into a hexagonal lattice. As a matter of fact, in the hexagonal assembly [see (c)] the central cube cannot attach through an attractive tripole-tripole interaction with all its six neighbors, but it is forced to experience repulsive interaction with some of them. (b)-(c): Contour plots of the interface height profile, as obtained through our numerical method, for $N = 6$ and $N = 7$ adsorbed cubes, respectively, for various distances D between the centers of mass of two closest cubes. The azimuthal orientations of the cubes are such that the cubes interact through the tripole-tripole orientation [see also Fig. 5.6(c)]. The plane $z = 0$ corresponds to the interface when no particle is adsorbed.

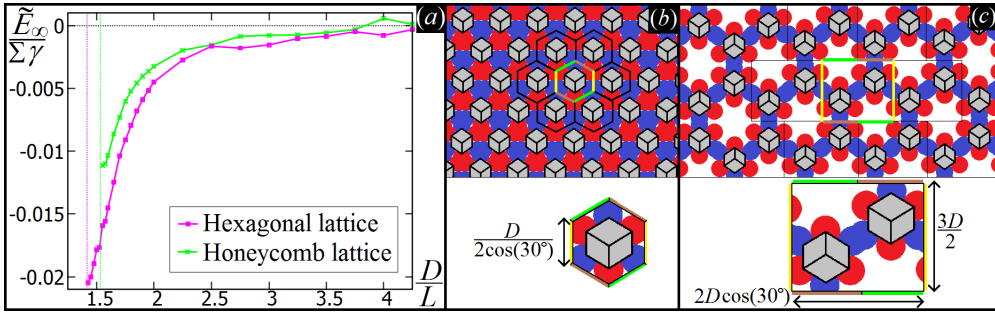


Figure 5.10: (a) Interaction energy per particle \tilde{E}_∞ [Eq. (5.3)] for a periodic hexagonal lattice formed by dipole-dipole interacting cubes (violet curve), and for a periodic honeycomb lattice formed by tripole-tripole interacting cubes, with respect to D , i.e. the distance between the centers of mass of two closest-neighbor cubes. (b)-(c) Sketch of the lattice unit cells considered in our numerical method to reproduce the lattices. The periodic boundary conditions applied to these unit cells are indicated by the colors of the sides of the cell, that is sides of the cell with the same color (yellow, green and brown) have to the same interface height. Contour plots of the interface height profile in these unit cells are shown in Fig. 5.11.

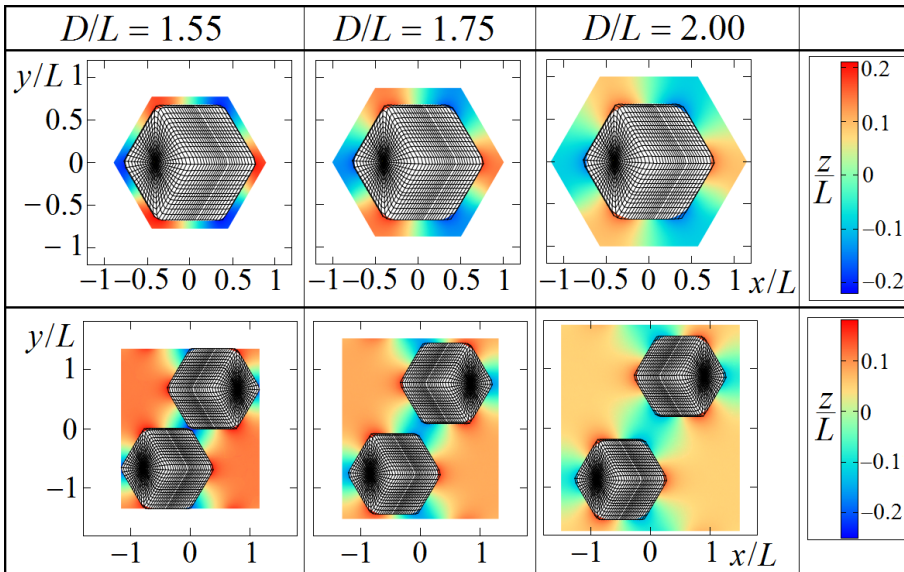


Figure 5.11: Contour plots of the interface height profile, as obtained through our numerical method, for the unit cells of the hexagonal and honeycomb lattices [see Fig. 5.10(b)-(c)] formed by adsorbed cubes dipole-dipole and tripole-tripole interacting, respectively, for different distances D between the centers of mass of two closest-neighbor cubes in the lattice. Each cube has side L , contact angle $\theta = \pi/2$, total surface area Σ , and it is adsorbed at its equilibrium configuration, i.e. with the $\{111\}$ orientation, generating a hexapolar capillary deformation in the interface height profile. The plane $z = 0$ corresponds to the interface when no particle is adsorbed.

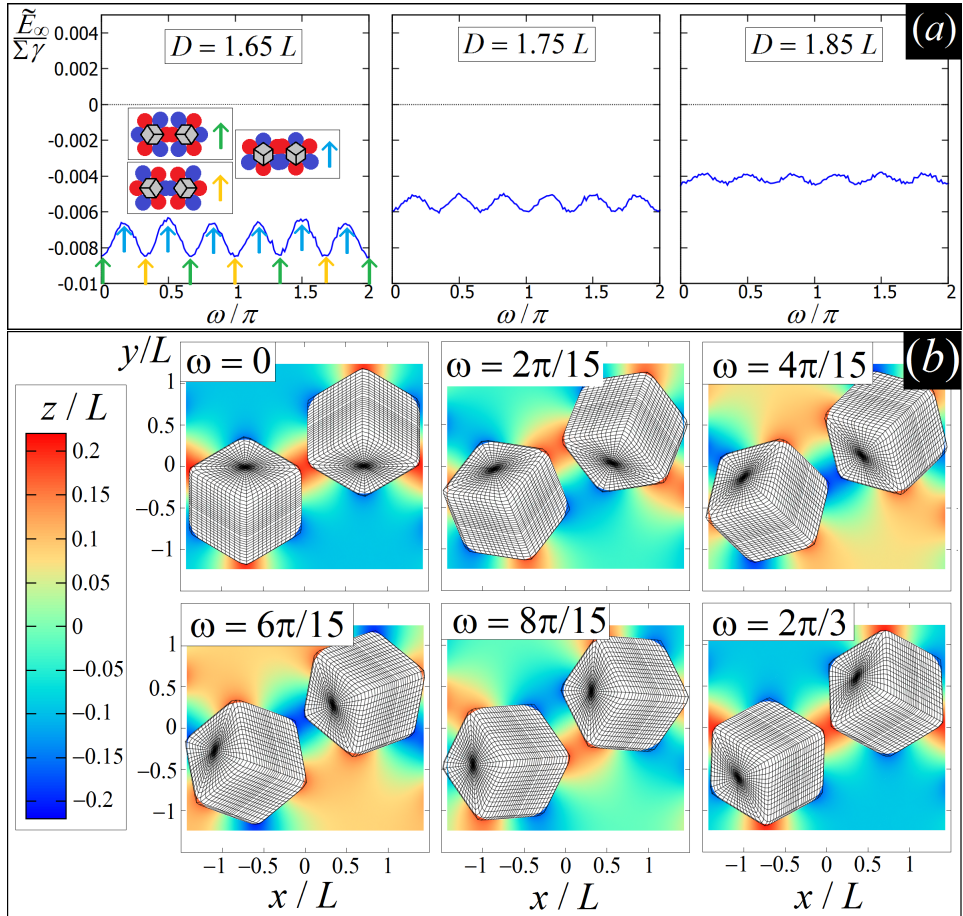


Figure 5.12: (a) Interaction energy per particle \tilde{E}_∞ [Eq. (5.3)] for an honeycomb lattice formed by adsorbed $\{111\}$ -oriented tripole-tripole interacting cubes with side L , contact angle $\theta = \pi/2$, and total surface area Σ , with respect to the rotation ω of the azimuthal angle of the vertical axis of each cube from its equilibrium value. Each cube is rotated in the opposite angular direction with respect to its closest neighbors. By tuning simultaneously ω for each cube, the cubes shift from tripole-tripole to dipole-dipole attachments. Each graph correspond to a different lattice spacing, with D the distance between the centers of mass of two closest-neighbour cubes. The minima in \tilde{E}_∞ , with respect to ω , correspond to the tripole-tripole attachments, while the maxima correspond to the dipole-dipole attachments (see the marks in the graph on the left). Therefore, the honeycomb lattice formed by tripole-tripole interacting cubes is a metastable structure, as an energy barrier prevent it to evolve into an honeycomb lattice with dipole-dipole interacting cubes, which would in turn evolve into an hexagonal lattice with dipole-dipole interacting cubes. (b) Contour plots of the interface height profile, as obtained through our numerical method, for the unit cell of the honeycomb lattice, for $D = 1.65L$ and different values of ω , i.e. the rotation of the azimuthal angle of the vertical axis of each cube from its equilibrium value, corresponding to tripole-tripole interacting cubes. The plane $z = 0$ corresponds to the interface when no particle is adsorbed.

5.6 TEMPERATURE-DENSITY PHASE-DIAGRAM

In the previous Section we calculated the capillary interaction energy per particle \tilde{E}_∞ [Eq. (5.3)] for an honeycomb lattice of adsorbed tripole-tripole interacting cubes, and for an hexagonal lattice of adsorbed dipole-dipole interacting cubes, with respect to the lattice spacing. As a result, we obtained that the close-packed hexagonal lattice has the lowest \tilde{E}_∞ , and therefore it is a candidate for the equilibrium structure, while the close-packed honeycomb lattice is metastable, as it locally minimizes \tilde{E}_∞ . However, the close-packed honeycomb lattice has a lower density of adsorbed cubes per unit area than the close-packed hexagonal lattice. Therefore, for certain temperatures and densities, the cubes could prefer the honeycomb arrangement, if the configurational entropy of the cubes is also taken into account. To verify this, we define, for adsorbed $\{111\}$ -oriented hexapole-generating cubes with $\cos\theta = 0$, a free energy expression, depending on T (temperature), N (number of adsorbed cubes), and A (area of the unperturbed fluid-fluid interface), where both entropic and capillary contributions are included. Assuming that the cubes adsorbed at the interface can be in three possible phases, i.e. a 2D disordered fluid phase (phase f), a honeycomb lattice phase with the cubes tripole-tripole interacting (phase h), and a hexagonal lattice crystal phase with the cubes dipole-dipole interacting (phase x), in Secs. 5.6.1, 5.6.2, and 5.6.3, we define a free energy F_f , F_h and F_x , for each of these three phases, respectively. Then, in Sec. 5.6.6, we show a temperature-density phase diagram for the adsorbed cubes at the interface extracted from the free energy of these three phases.

5.6.1 FREE ENERGY OF THE FLUID PHASE

We assume that, when the $\{111\}$ -oriented adsorbed cubes are in the fluid phase (phase f), they behave approximately like an hard-disk fluid. That is

$$F_f \approx F_{hd}^{(f)}, \quad (5.4)$$

where $F_{hd}^{(f)}(N, A, T)$ is the free energy of a fluid phase of N hard disks of radius R in a 2D space of total area A and at a temperature T . Using the standard *Taylor expansion scaled-particle theory* [120], we can write

$$\frac{F_{hd}^{(f)}}{A(k_B T)} = \frac{N}{A} \left[\ln \left(\frac{N}{A} \pi R^2 \right) - 1 \right] - \frac{N}{A} \ln \left(1 - \frac{N}{A} \pi R^2 \right) + \frac{(2\pi R N/A)^2}{4\pi(1 - \pi R^2 N/A)}, \quad (5.5)$$

where the first term is the entropic ideal-gas contribution and the rest is due to the hard-disk interactions. In our approximated model, the area and perimeter of the hard disk become the area and perimeter of the intersection between the flat interface and a cube adsorbed at its equilibrium configurationⁱⁱⁱ. As numerically

ⁱⁱⁱThat is, as $\cos\theta = 0$, the cube is $\{111\}$ -oriented and with center of mass height at the interface level, see Sec. 5.3.

computed, these are

$$(2\pi R)^2 \approx 3.07 \Sigma, \quad (5.6)$$

$$\pi R^2 \approx 0.23 \Sigma, \quad (5.7)$$

with Σ the cube total surface area. Note that Eq. (5.6) implies $R \approx 0.279\sqrt{\Sigma}$, while Eq. (5.7) implies $R \approx 0.271\sqrt{\Sigma}$. This slight inconsistency occurs because we are treating our adsorbed cubes as hard disks. For convenience, we introduce the normalized density

$$\vartheta^* \equiv \frac{\vartheta}{\vartheta_x}, \quad (5.8)$$

where the density ϑ per unit area of the adsorbed cubes is defined as

$$\vartheta \equiv \Sigma \frac{N}{A}, \quad (5.9)$$

and $\vartheta_x \approx 3.24$ is the closest packing value^{iv} of ϑ for the phase x , as numerically computed. Given the distance D between the centers of mass of two closest-neighbor cubes of the lattice, for the hexagonal lattice with hexagonal unit cell of side $D/\sqrt{3}$ and $N = 1$ cube [see Fig. 5.10(b)], ϑ^* is related to D by $\vartheta^* = 2\Sigma/(\vartheta_x D^2 \sqrt{3})$. Instead, for the honeycomb lattice with rectangular unit cell of long side $D\sqrt{3}$, short side $3D/2$, and $N = 2$ cubes [see Fig. 5.10(c)], ϑ^* is related to D by $\vartheta^* = 4\Sigma/(3\vartheta_x \sqrt{3} D^2)$.

Finally, for a system of N adsorbed cubes in the f phase, we obtain

$$\frac{F_f}{A\gamma} = \frac{k_B T}{\Sigma\gamma} \vartheta_x \left[\vartheta^* \ln \left(\frac{0.23\vartheta^*}{1/\vartheta_x - 0.23\vartheta^*} \right) - \vartheta^* + \frac{3.07(\vartheta^*)^2}{4\pi(1/\vartheta_x - 0.23\vartheta^*)} \right]. \quad (5.10)$$

In the free energy F_f [Eq. (5.10)] we are taking into account only the entropy of the cubes, without including the contribution to the energy due to the capillary interactions, which we assume to consist of positive and negative contributions that cancel. Indeed, the fluid phase occurs for cubes with a rather low density^v or with a random azimuthal orientation of their vertical axis^{vi}. A 2D system of N hard disks with radius R is in the fluid phase when its area A is greater than $1.328 A_0$ [121], where $A_0 \equiv 2N\sqrt{3}R^2$ is the closest packing area of the system. In our approximate analogy for the $\{111\}$ -oriented adsorbed cubes, where A_0/A is given by ϑ^* , we obtain that the adsorbed cubes are in the fluid phase for $\vartheta^* \lesssim 1/1.328$. So, we estimate that the expression in Eq. (5.10) for the free energy F_f of the cubes in the disordered fluid phase is reliable for $\vartheta^* \lesssim 0.75$.

^{iv}That is, when the dipole-dipole interacting cubes are at their contact distance.

^vSuch that particle-particle distances are, on average, large enough that the capillary interactions are negligible.

^{vi}Therefore, the hexapolar capillary deformations induced by the adsorbed cubes in the fluid-fluid interface height profile have random reciprocal azimuthal orientations. Consequently, the cubes exert both attractive and repulsive capillary interactions to each other, giving on average a negligible contribution to the total free energy.

5.6.2 FREE ENERGY OF THE HONEYCOMB PHASE

For the tripole-tripole interacting cubes assembled in the honeycomb lattice (phase h), we assume the free energy F_h can be expressed as

$$F_h \approx N \tilde{E}_N^{(h)} - N k_B T \ln Z_{or}^{(h)} + F_{hd}^{(f)} \quad (5.11)$$

where $\tilde{E}_N^{(h)}$ is the capillary interaction energy per particle [Eq. (5.3)] for the phase h , and it is computed through our numerical method and reported in Fig. 5.10(a) for $N \rightarrow \infty$. The last term in Eq. (5.11), i.e. $F_{hd}^{(f)}$, is the free energy of an hard-disk fluid [Eq. (5.5)], and it takes into account the translational entropy contributions to the energy of the adsorbed cubes in phase h . The second term in Eq. (5.11), i.e. $-N k_B T \ln Z_{or}^{(h)}$, is the rotational entropy contribution to the free energy due to the azimuthal orientation of the vertical axis of the cubes in the interface plane. Indeed, in this lattice phase, any i -th cube ($i = 1, \dots, N$) has a fixed azimuthal orientation α_i of its vertical axis. We assume that the cubes can experience only small angular variations ω in α_i , with an energy cost $U(\omega) \approx C_h(\vartheta^*) \omega^2/2$, where the rotational spring constant $C_h(\vartheta^*)$ depends on the honeycomb lattice density ϑ^* , and it is computed in Sec. 5.6.4 and given in Eq. (5.19). Using this approximation, the orientation partition function $Z_{or}^{(h)}$ of a single cube can be written as

$$Z_{or}^{(h)} = \frac{3}{2\pi} \int_{-\pi/3}^{\pi/3} e^{-U(\omega)/k_B T} d\omega = \frac{3}{4} \sqrt{\frac{2 k_B T}{\pi C_h(\vartheta^*)}} \xi [C_h(\vartheta^*)], \quad (5.12)$$

where

$$\xi [C_h(\vartheta^*)] \equiv 2 \operatorname{Erf} \left[\frac{\pi}{3} \sqrt{\frac{1}{2} \frac{C_h(\vartheta^*)}{\Sigma \gamma} \frac{\Sigma \gamma}{k_B T}} \right], \quad (5.13)$$

and $\operatorname{Erf}(x)$ is the *error function*. As shown in Fig. 5.13, for the whole range of parameters that we consider, $\xi [C_h(\vartheta^*)] \approx 2$, such that the integral in Eq. (5.12) is actually a Gaussian integral. In Eq. (5.12), the factor 3 and the integration between $[-\pi/3, \pi/3]$ takes into account that, for any i -th cube, there are three equivalent minimum energy azimuthal orientations, which are $\alpha_i, \alpha_i + 2\pi/3$, and

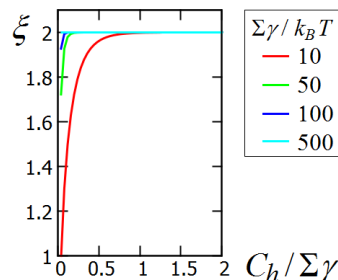


Figure 5.13: Behavior of $\xi [C_h]$ [Eq. (5.13)] for different values of $\Sigma \gamma / k_B T$. As shown, for $\Sigma \gamma / k_B T \geq 100$ we can consider $\xi \approx 2$ always.

$\alpha_i + 4\pi/3$. So, from Eq. (5.11) we obtain

$$\begin{aligned} \frac{F_h}{A\gamma} &= \vartheta_x \vartheta^* \frac{\tilde{E}_N^{(h)}}{\Sigma\gamma} + \vartheta_x \frac{k_B T}{\Sigma\gamma} \left[\vartheta^* \ln \left(\frac{0.23\vartheta^*}{1/\vartheta_x - 0.23\vartheta^*} \right) - \vartheta^* + \right. \\ &\quad \left. + \frac{3.07(\vartheta^*)^2}{4\pi(1/\vartheta_x - 0.23\vartheta^*)} + \frac{\vartheta^*}{2} \ln \left(\frac{2\pi C_h(\vartheta^*) \Sigma\gamma}{9 \Sigma\gamma k_B T} \right) \right]. \end{aligned} \quad (5.14)$$

The close-packing value of ϑ for the honeycomb lattice, i.e. when the tripole-tripole interacting cubes are at their contact distance, is $\vartheta_h \approx 1.83$, as computed numerically, corresponding to $\vartheta^* \approx 0.56$.

5.6.3 FREE ENERGY OF THE HEXAGONAL PHASE

For the dipole-dipole interacting cubes assembled in the hexagonal lattice (phase x), we assume the free energy F_x can be expressed as

$$F_x \approx N \tilde{E}_N^{(x)} - N k_B T \ln Z_{or}^{(x)} + F_{hd}^{(x)}, \quad (5.15)$$

where $\tilde{E}_N^{(x)}$ is the capillary interaction energy per particle [Eq. (5.3)] for the phase x , and it is computed through our numerical method and reported in Fig. 5.10(a) for $N \rightarrow \infty$. The second term in Eq. (5.15), i.e. $-N k_B T \ln Z_{or}^{(x)}$, is the rotational entropy contribution to the free energy due to the azimuthal orientation of the vertical axis of the cubes in the interface plane, and it is calculated analogously to the honeycomb lattice case (see Sec. 5.6.2), with the rotational spring constant for the hexagonal lattice $C_x(\vartheta^*)$ computed in Sec. 5.6.4 and given in Eq. (5.21). The last term, i.e. $F_{hd}^{(x)}(N, A, T)$, is the entropic free energy of a solid phase of N hard disks with radius R in a 2D space of total area A and at a temperature T , and it takes into account the translational entropy contributions to the energy of the adsorbed cubes in the phase x . Following Ref. [121], we have

$$F_{hd}^{(x)} = N k_B T \left[2.73 \ln \left(\frac{A_0}{A} \right) - 2 \ln \left(1 - \frac{A_0}{A} \right) + 2.33 \frac{A}{A_0} - 0.75 \frac{A^2}{A_0^2} - 1.475 \right], \quad (5.16)$$

where $A_0 = 2\sqrt{3}NR^2$ is the closest packing area for a system of N hard disks with radius R . For our cubes in the hexagonal phase, we replace A_0/A with ϑ^* , obtaining finally for F_x [Eq. (5.15)] that

$$\begin{aligned} \frac{F_x}{A\gamma} &= \vartheta_x \vartheta^* \frac{\tilde{E}_N^{(x)}}{\Sigma\gamma} + \vartheta_x \frac{k_B T}{\Sigma\gamma} \left[2.73 \vartheta^* \ln \vartheta^* - 2 \vartheta^* \ln (1 - \vartheta^*) + \right. \\ &\quad \left. + 2.33 - \frac{0.75}{\vartheta^*} - 1.475 \vartheta^* + \frac{\vartheta^*}{2} \ln \left(\frac{2\pi C_x(\vartheta^*) \Sigma\gamma}{9 \Sigma\gamma k_B T} \right) \right]. \end{aligned} \quad (5.17)$$

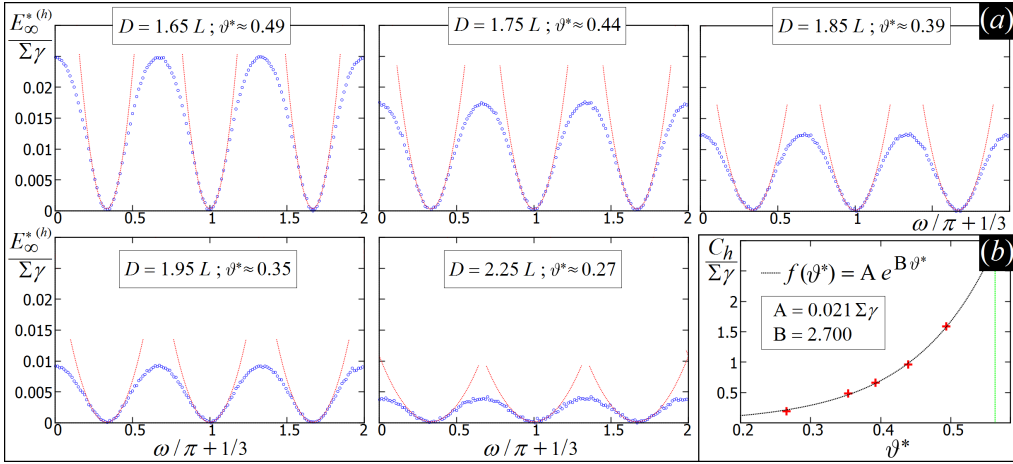
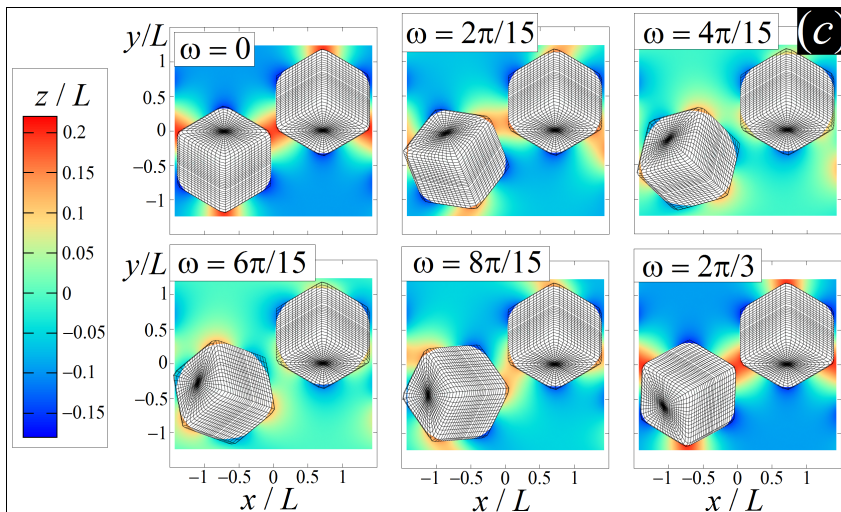


Figure 5.14: (a) Energy $E_\infty^{*(h)}$ [Eq. (5.18)] for an honeycomb lattice unit cell [see Fig. 5.10(c)] with tripole-tripole interacting cubes, where the azimuthal orientation of the vertical axis of one cube is rotated by ω from its equilibrium value, for several values of the distance D between the centers of mass of two closest-neighbor cubes. The Young's contact angle is $\pi/2$, the cube total surface is Σ , and the cube side is L . The red dotted curves represent the fit around each minimum of $E_\infty^{*(h)}$ with $a_h(\vartheta^*) + \omega^2 C_h(\vartheta^*)/2$. (b) Values of $C_h(\vartheta^*)$, as obtained for the various D considered. The dotted curve is the fit of these values using $A e^{B\vartheta^*}$. The green vertical line corresponds to $1.83/\vartheta_x$, i.e. the value of ϑ^* for the honeycomb lattice phase at its closest packing density. (c) Contour plots of the interface height profile, as obtained through our numerical method, for the honeycomb lattice unit cell in the case $D = 1.65L$, for different values of ω . The plane $z = 0$ correspond to the fluid-fluid interface when no cubes are adsorbed.



5.6.4 ROTATIONAL ENERGY FOR CUBES IN THE HONEYCOMB AND HEXAGONAL LATTICES

We consider in this Section $\{111\}$ -oriented hexapole generating cubes, with $\cos \theta = 0$, adsorbed at the interface and arranged in honeycomb or hexagonal lattices, and we study the energy to rotate the azimuthal angle of their vertical axis in the interface plane from its equilibrium value.

Any i -th cube ($i = 1, \dots, N$) in the h phase, i.e. the honeycomb lattice with tripole-tripole interacting cubes, has a fixed azimuthal orientation α_i of its vertical axis in the fluid-fluid interface plane. Assuming that the cubes in this phase can experience only small angular variations ω in α_i , with an energy cost $U(\omega) \approx C_h(\vartheta^*)\omega^2/2$, we calculate here the rotational spring constant C_h with respect to ϑ^* . For this, we compute

$$E_\infty^{*(h)} \equiv 2\tilde{E}_\infty^{(h)}(\omega) - 2\tilde{E}_\infty^{(h)}, \quad (5.18)$$

for a honeycomb lattice unit cell [see Fig. 5.10(c)], where the two cubes have azimuthal orientation of their vertical axis given by α_1 and $\alpha_2 + \omega$, respectively. With α_1 and α_2 we refer to the minimum energy azimuthal orientations that the two tripole-tripole interacting cubes have in the unit cell of the honeycomb lattice phase, and $\tilde{E}_\infty^{(h)}$ is the capillary interaction energy per cube [Eq.(5.3)] when the two cubes have such orientations. With $\tilde{E}_\infty^{(h)}(\omega)$ we refer to $\tilde{E}_\infty^{(h)}$ calculated when the second cube has out-of-equilibrium azimuthal orientation given by $\alpha_2 + \omega$. In Fig. 5.14(a) we show $E_\infty^{*(h)}(\omega)$, as obtained by our numerical method, for several values of the distance D between the centers of mass of two closest-neighbor cubes, corresponding to different values of ϑ^* for the lattice. In Fig. 5.14(b), we show the values of $C_h(\vartheta^*)$ obtained by fitting $E_\infty^{*(h)}(\omega)$, for each ϑ^* considered, in a neighborhood of $\pm \pi/10$ around each minimum in ω , with the function $U_h(\omega) = a_h(\vartheta^*) + \omega^2 C_h(\vartheta^*)/2$. Finally, we can fit these values of C_h to express C_h as a function of ϑ^* , obtaining

$$C_h(\vartheta^*) = A e^{B\vartheta^*}, \quad (5.19)$$

with $A = 0.021 \Sigma \gamma$ and $B = 2.70$.

Analogously, any i -th cube ($i = 1, \dots, N$) in the x phase, i.e. the hexagonal lattice with dipole-dipole interacting cubes, has a fixed azimuthal orientation α_i of its vertical axis in the fluid-fluid interface plane. Assuming that the cubes in this phase can experience only small angular variations ω in α_i , with an energy cost $U(\omega) \approx C_x(\vartheta^*)\omega^2/2$, we calculate now the rotational spring constant C_x with respect to ϑ^* . For this, we compute

$$E_7^{*(x)} \equiv 7\tilde{E}_7^{(x)}(\omega) - 7\tilde{E}_7^{(x)}, \quad (5.20)$$

for $N = 7$ adsorbed cubes, with 6 of them placed with their center of mass at the vertexes of a side- D hexagon in the interface plane, and the 7th cube placed with

center of mass at the center of this hexagon. The minimum energy azimuthal orientation of the vertical axis of these cubes in the interface plane is such that they dipole-dipole interact with each other, and $\tilde{E}_7^{(x)}$ is the capillary interaction energy per cube [Eq.(5.3)] when the cubes are in their minimum energy orientation. Instead $\tilde{E}_7^{(x)}(\omega)$ is the capillary interaction energy per cube [Eq.(5.3)] when the azimuthal angle of the vertical axis of the cube in the center of the hexagon is rotated by ω from its equilibrium value. In Fig. 5.15(a) we show $E_7^{*(x)}(\omega)$, as obtained by our numerical method, for several values of the distance D between the centers of mass of two closest-neighbor cubes, corresponding to different values of ϑ^* for the lattice. In Fig. 5.15(b), we show the values of $C_x(\vartheta^*)$ obtained by fitting $E_7^{*(x)}(\omega)$, for each ϑ^* considered, in a neighborhood of $\pm\pi/10$ around each minimum in ω , with the function $U_x(\omega) = a_x(\vartheta^*) + \omega^2 C_x(\vartheta^*)/2$. Finally, we can fit these values of C_x to express C_x as a function of ϑ^* , obtaining

$$C_x(\vartheta^*) = A e^{-B/\vartheta^*} , \quad (5.21)$$

with $A = 55.30 \Sigma \gamma$ and $B = 6.71$.

5.6.5 COMMON TANGENT CONSTRUCTION

In Fig. 5.16 we show the behavior of $F_f/A\gamma$ [Eq. (5.10)], $F_h/A\gamma$ [Eq. (5.14)], and $F_x/A\gamma$ [Eq. (5.17)], for $\{111\}$ -oriented hexapole-generating adsorbed cubes with $\cos \theta = 0$, in the f , h , and x phase, respectively, with respect to ϑ^* [Eq. (5.8)], i.e. the normalized density per unit area of adsorbed cubes, for several values of $\Sigma\gamma/k_B T$ (with Σ the cube surface area and γ the fluid-fluid surface tension).

This representation of the free energy, i.e. free energy density with respect to the particle density, is useful to verify if the system phase separates for certain densities. Indeed, given a system with global density $\vartheta = \Sigma N/A$ and free energy $F(N, A)$, consider two subsystems 1 and 2 with density $\vartheta_1 = \Sigma N_1/A_1$ and $\vartheta_2 = \Sigma N_2/A_2$, respectively, with $N_1 + N_2 = N$ (so $A_1\vartheta_1 + A_2\vartheta_2 = A\vartheta$) and $A_1 + A_2 = A$. These definitions implies

$$\frac{A_2}{A} = \frac{\vartheta - \vartheta_1}{\vartheta_2 - \vartheta_1} . \quad (5.22)$$

Given $f(\vartheta) \equiv F(N, A)/A$, for a certain fixed T , we first note that, if

$$A f(\vartheta) > A_1 f(\vartheta_1) + A_2 f(\vartheta_2) , \quad (5.23)$$

then

$$F(N, A) > F(N_1, A_1) + F(N_2, A_2) . \quad (5.24)$$

So, Eq. (5.23) implies that the free energy $F(N, A)$ of the global system with N particles and area A is higher than the sum of the free energies $F(N_1, A_1)$ and $F(N_2, A_2)$ of the two subsystems with, respectively, N_1 particles and area A_1 , and N_2 particles and area A_2 . Therefore, if Eq. (5.23) holds, then the global

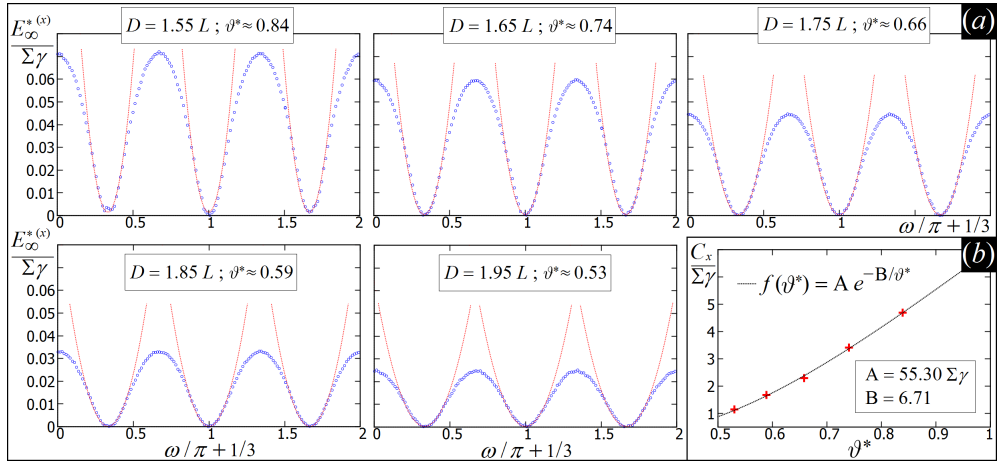
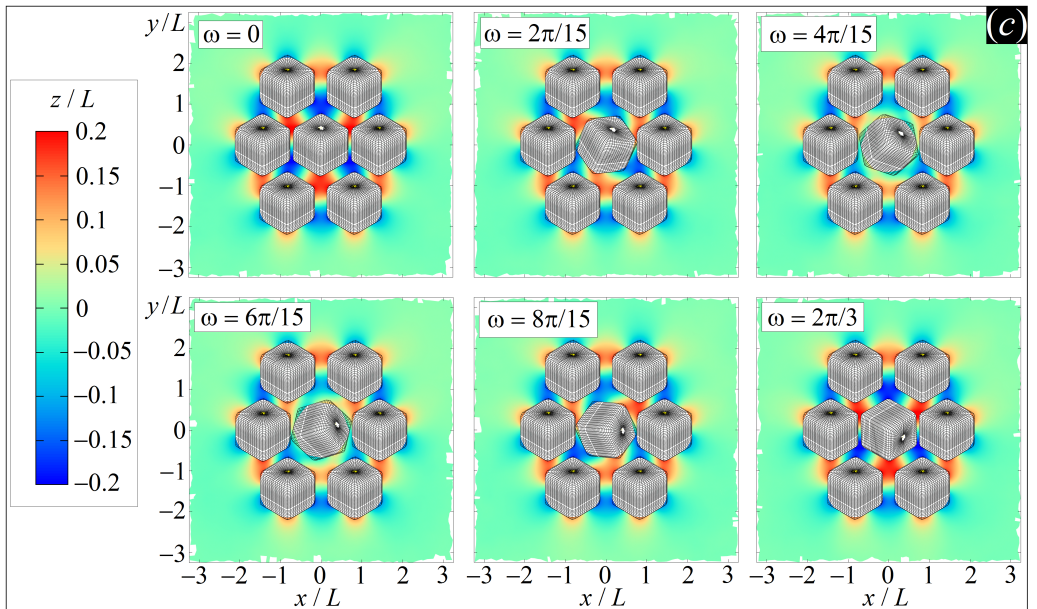


Figure 5.15: (a) Energy $E_7^{*(x)}$ [Eq. (5.20)] for $N = 7$ dipole-dipole interacting cubes disposed like in an hexagonal lattice, where the azimuthal orientation of the vertical axis of the central cube is rotated by ω from its equilibrium value, for several values of the distance D between the centers of mass of two closest-neighbor cubes. The cube contact angle is $\pi/2$, the cube total surface is Σ , and the cube side is L . The red dotted curves represent the fit around each minimum of $E_7^{*(x)}$ with $a_x(\vartheta^*) + \omega^2 C_x(\vartheta^*)/2$. (b) Values of $C_x(\vartheta^*)$, as obtained for the various D considered. The dotted curve is the fit of these values using $A e^{-B/\vartheta^*}$. (c) Contour plots of the interface height profile, as obtained through our numerical method, for $D = 1.65L$ and for different values of ω . The plane $z = 0$ correspond to the fluid-fluid interface when no cubes are adsorbed.



system prefers to phase separate into the two subsystems. In this argument we are, of course, neglecting the energy contributions due to the interface that would form between the two subsystems. Equation (5.23) can be rewritten, using Eq. (5.22), as

$$f(\vartheta) > f(\vartheta_1) + \frac{\vartheta - \vartheta_1}{\vartheta_2 - \vartheta_1} [f(\vartheta_2) - f(\vartheta_1)] . \quad (5.25)$$

Equation (5.25) shows that a system with density ϑ phase separates into two subsystems with densities ϑ_1 and ϑ_2 , if the linear combination of $f(\vartheta_1)$ and $f(\vartheta_2)$ in ϑ is lower than $f(\vartheta)$. By geometrical argument one can see that, for any ϑ such that Eq. (5.25) holds, the two most convenient ϑ_1 and ϑ_2 for phase separating are the ones that ensure

$$\frac{f(\vartheta_2) - f(\vartheta_1)}{\vartheta_2 - \vartheta_1} = \left. \frac{\partial f}{\partial \vartheta} \right|_{\vartheta_1} = \left. \frac{\partial f}{\partial \vartheta} \right|_{\vartheta_2} . \quad (5.26)$$

Therefore, the tendency of a system, with a certain density ϑ and at a certain temperature T , to phase separate is indicated by the presence of the so-called *common tangents* in the plot of its free energy density $f(\vartheta)$. If in the system there are, like in our case, phases with different structures which are described by different free energy densities $f_i(\vartheta)$, then the same argument illustrated above can be applied also to the presence of common tangents between, say, $f_\alpha(\vartheta)$ and $f_\beta(\vartheta)$: if a common tangent exists between $f_\alpha(\vartheta_1)$ and $f_\beta(\vartheta_2)$, then for $\vartheta \in [\vartheta_1, \vartheta_2]$ the system phase separates into the phase with structure α and density ϑ_1 , and into the phase with structure β and density ϑ_2 . Of course if a common tangent can be found, for example, for the single free energy density $f_\alpha(\vartheta)$, then the system phase separates into two phases with structure α and different densities. If more than one common tangents exist for a given ϑ , then the system phase separates accordingly to the common tangent with the lowest free energy density for such a ϑ . For a ϑ such that no common tangents exist, the system stays in a single phase, which has density ϑ and structure corresponding to the lowest $f_i(\vartheta)$.

In Fig. 5.16, for each value of $\Sigma\gamma/k_B T$ considered, the common tangents between $F_f(\vartheta^*)/A\gamma$, $F_h(\vartheta^*)/A\gamma$, and $F_x(\vartheta^*)/A\gamma$, are shown with black dotted lines when they lead to a lower free-energy state, more convenient than any of the three phases, f , h and x . As we explained in this Section, when for a certain ϑ^* a common tangent exists, the cubes phase separates into the two phases corresponding to the free energies at the contact points of the common tangent, and the densities of these two coexisting phases are indicated by such contact points. As shown in Fig. 5.16, for $\Sigma\gamma/k_B T \gg 500$ the cubes form an almost close-packed phase x coexisting with a very dilute phase f , which is indeed the result expected in the limit of low T , where capillary interactions dominate over entropic forces. However, in the regime $\Sigma\gamma/k_B T \approx 500$, the presence of common tangents between $F_h(\vartheta^*)/A\gamma$ and $F_f(\vartheta^*)/A\gamma$ or $F_x(\vartheta^*)/A\gamma$ indicates, as we speculated, that for certain densities the cubes prefer the phase h . These results are summed up in the next Section, where we extract from Fig. 5.16 a temperature-density phase diagram for the adsorbed cubes.

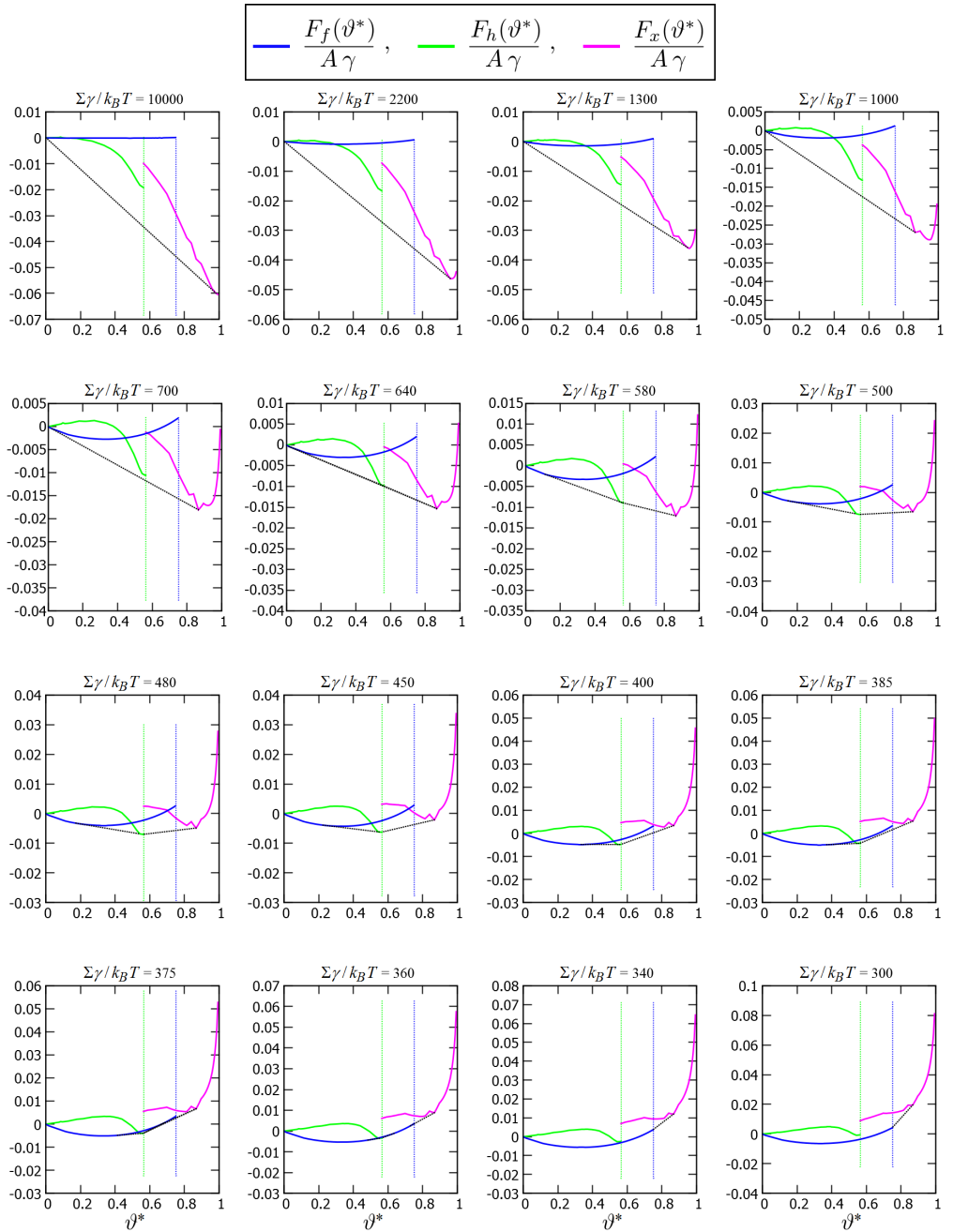


Figure 5.16: Plots of $F_f(\vartheta^*)/A\gamma$ [Eq. (5.10)], $F_h(\vartheta^*)/A\gamma$ [Eq. (5.14)], and $F_x(\vartheta^*)/A\gamma$ [Eq. (5.17)], shown with a blue, green, and violet line, respectively, with respect to the normalized density ϑ^* [Eq. (5.8)], for different values of $\Sigma\gamma/k_B T$. The dotted vertical blue line represents the value of ϑ^* for which the phase f can no longer occur. The dotted vertical green line represents the value of ϑ^* corresponding to the closest packing fraction for the phase h . The closest packing fraction for the phase x corresponds to $\vartheta^* = 1$. With black dotted lines we show the common tangents, which indicate phase coexistence.

5.6.6 TEMPERATURE-DENSITY DIAGRAM FOR THE x , h AND f PHASES

In this Section we sum up the results obtained in the previous Section for the free energy of the adsorbed $\{111\}$ -oriented hexapole-generating cubes with Young's contact angle $\theta = \pi/2$. Assuming that such cubes can be in three possible phases, i.e. a disordered (2D) fluid phase (phase f), a honeycomb lattice with tripole-tripole interacting cubes (phase h), and a hexagonal lattice with dipole-dipole interacting cubes (phase x), in Fig. 5.17 we report the phase diagram, extracted by the common tangents calculations shown in Fig. 5.16, for the adsorbed cubes with respect to ϑ^* [Eq. (5.8)], i.e. the density per unit area of adsorbed cubes normalized such that $\vartheta^* = 1$ for the close packed phase x , and with respect to $\Sigma\gamma/k_B T$ (with Σ the cube total surface area, γ the fluid-fluid surface tension, k_B the Boltzmann constant, and T the system temperature). The temperature range goes from $\Sigma\gamma = 1300 k_B T$ to $\Sigma\gamma = 300 k_B T$, as this was the meaningful part of the diagram. The blue, green and purple areas denote one-phase f , h , and x regions, and the gray areas indicate two-phase regions of coexisting phases that can be found by horizontal tie lines. For $\Sigma\gamma/k_B T \lesssim 350$ and $\Sigma\gamma/k_B T \gtrsim 650$, the phase behavior is in the high-temperature and low-temperature limit, where the highest-density phase x coexists with the high-density and low-density phase f , respectively. Interestingly, however, in the intermediate regime $350 \lesssim \Sigma\gamma/k_B T \lesssim 650$, that is bounded by an $h - f - x$ and a $f - h - x$ triple point, the phase h is, as speculated, thermodynamically stable in a huge density regime, either in coexistence with the phase f or with the phase x , or as an homogeneous phase for a small density regime. Note that, for temperatures in this regime, cubes are still strongly adsorbed at the interface, as the single particle adsorption energy

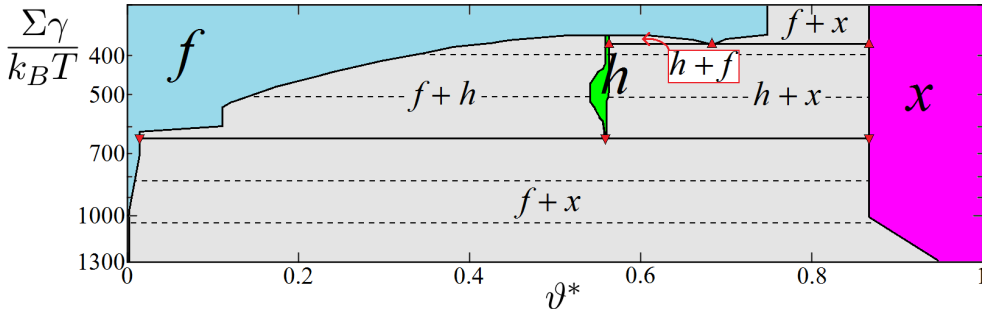


Figure 5.17: Temperature-density phase diagram for adsorbed $\{111\}$ -oriented hexapole-generating cubes with Young's contact angle $\theta = \pi/2$, extracted from the common tangent calculations shown in Fig. 5.16. In colors we show the phase h (honeycomb lattice with tripole-tripole interacting cubes), phase x (hexagonal lattice with dipole-dipole interacting cubes) and phase f [disordered (2D) fluid phase]. The gray areas indicate phase coexistence. The density ϑ^* of adsorbed cubes per unit area is normalized such that $\vartheta^* = 1$ for the close packed phase x . Going up along the y axis means to increase the temperature of the system (Σ is the cube total surface area, γ is the fluid-fluid surface tension, k_B is the Boltzmann constant, and T is the system temperature).

E_1 [Eq. (5.1)] is $E_1 \approx -0.25\Sigma\gamma$ for $\theta = \pi/2$ (see Fig. 5.2 for $\cos\theta = 0$). To find a stable phase h of cubes with side $L = 5$ nm, a typical tension $\gamma \approx 0.01 - 0.02$ N/m is required at room temperature, which is indeed a reasonable estimate for γ in the experiments in Refs. [75,76], where both hexagonal and honeycomb lattices of truncated nanocubes were observed. For cubes with $L = 1$ μm , instead, a much lower tension $\gamma \approx 0.2 - 0.5$ $\mu\text{N/m}$ is needed to obtain the h phase, which could however be possibly achieved in the extreme case of e.g. water-water interfaces [29].

5.7 EFFECTS DUE TO TRUNCATION OF THE CUBE SHAPE

In this Section, we study the effects of truncating the shape of a cubic particle on its adsorption energy E_1 [Eq. (5.1)]. By tuning the parameter q , which corresponds to the percentage of each cube side that is removed by the truncation (see Fig. 5.18), we go from a cubic shape with sharp edges for $q = 0$ to a bipyramid shape with square base for $q = 1$. We call L the side of the cubic shape for $q = 0$. So, L corresponds also to the height of the bipyramid shape. We consider a single adsorbed particle with Young's contact angle $\theta = \pi/2$, and with a truncated-cube shape obtained for, respectively, $q = 0.01$, $q = 0.25$, $q = 0.50$, $q = 0.75$, and $q = 0.99$ (see Fig. 5.18). As usual, the plane $z = 0$ corresponds to the flat interface, i.e. when no particles are adsorbed. In Fig. 5.19 we show the single-particle adsorption energy E_1 [Eq. (5.1)] with respect to the cube configuration φ , ψ at the interface (see Fig. 5.1). The center of mass height z_c is kept at the interface level for these calculations, because here we consider only

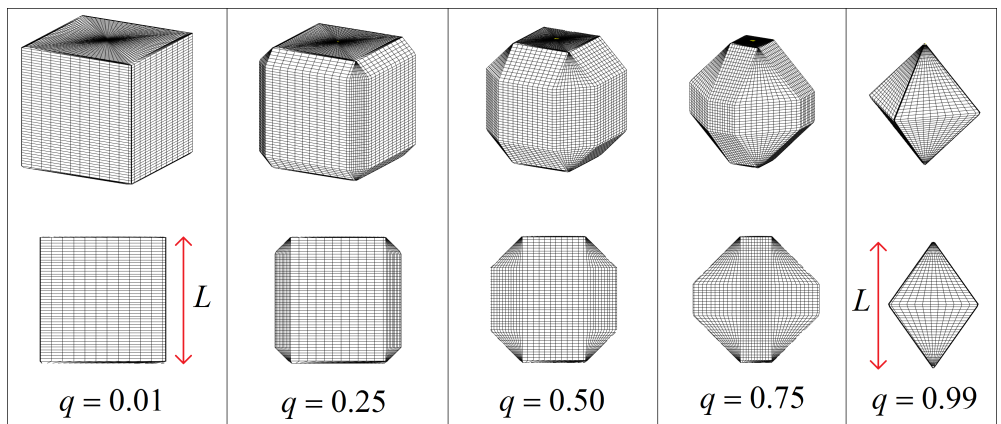


Figure 5.18: Profile and 3D view of the truncated-cube shapes (black grid) corresponding to $q = 0.01$, $q = 0.25$, $q = 0.50$, $q = 0.75$, and $q = 0.99$, respectively, where q is the parameter we tune to go from a cubic shape with sharp edges and side L ($q = 0$) to a bipyramid shape with square base and height L ($q = 1$).

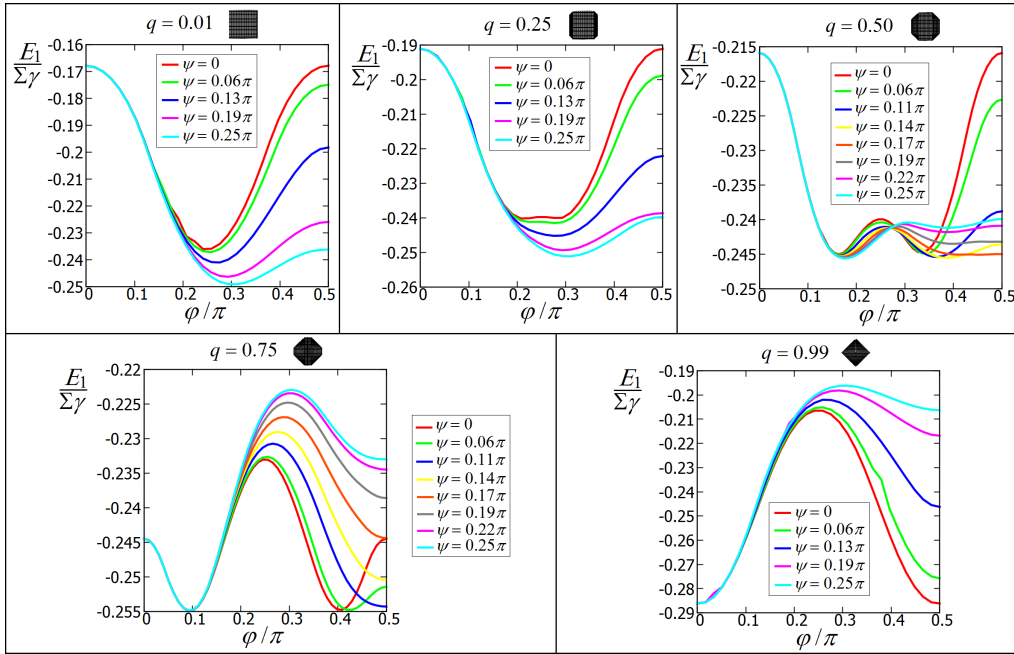


Figure 5.19: Energy E_1 [Eq. (5.1)] of a single-adsorbed truncated cube, for $q = 0.01$, $q = 0.25$, $q = 0.50$, $q = 0.75$, and $q = 0.99$, respectively (see Fig. 5.18), for $z_c = 0$ and with respect to φ and ψ (see Fig. 5.1), for various Young's contact angles θ . We plot E_1 in units of $\gamma\Sigma$, with γ the fluid-fluid surface tension and Σ the particle total surface area. The minima in the energy corresponds to the equilibrium and metastable configurations φ , ψ of the particle.

the case $\theta = \pi/2$, and therefore we already know, by symmetry, that this is the minimum energy value of z_c . In Fig. 5.20 we report E_1 minimized over ψ and with respect to φ , showing 3D views and contour plots of the equilibrium fluid-fluid interface height profile close to the particle, for the particle's equilibrium and metastable configurations at the interface, i.e. corresponding to the minima in E_1 . As shown, the results for the cube with sharp edges ($q = 0.01$) and for the slightly truncated cube ($q = 0.25$) are analogous to the results we shown in Sec. 5.3 for a cube with smooth edges. For all these three shapes, indeed, we obtain that the equilibrium orientation of the cube at the interface is the $\{111\}$ (see Fig. 5.3), which induce a hexapolar capillary deformation in the fluid-fluid interface height profile. The only effects of truncation we note for the truncated cube with $q = 0.25$ are a slight reduction of the hexapolar deformation amplitude in z , which likely implies slightly weaker capillary interactions between these truncated cubes, compared to the sharp-edge cubes. For the highly-truncated cubes, we find that the minimum energy configuration of the particle at the interface is still given by a tilted hexapole-inducing orientation. However, the hexapole generated by these highly-truncated cubes in the interface height profile does not seem 3-fold symmetric, while it was for $q \leq 0.25$ and for the smooth-edge cube of Sec. 5.3.

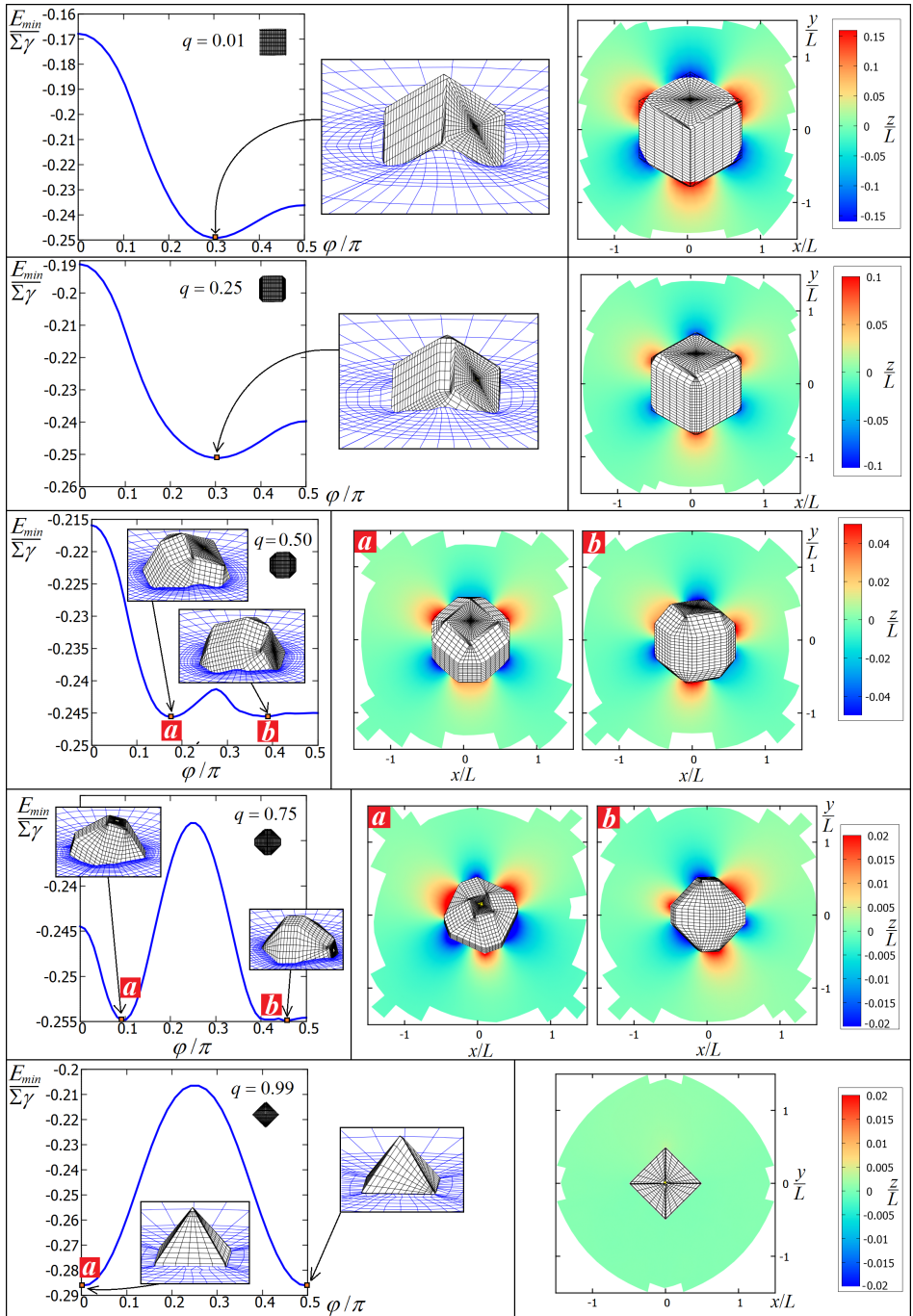


Figure 5.20: Energy $E_{min}(\varphi)$, which is E_1 [Eq. (5.1)] for $z_c = 0$ and minimized over ψ , of a single-adsorbed truncated cube, for $q = 0.01$, $q = 0.25$, $q = 0.50$, $q = 0.75$, and $q = 0.99$, respectively (see Fig. 5.18), for various Young's contact angles θ . In the insets and in the right panels we show a 3D view and a contour plot, respectively, of the fluid-fluid interface height profile close to the particle, for its equilibrium and metastable configurations, i.e. corresponding to the minima of E_{min} .

This could imply that the capillary interactions between such highly-truncated cubes also lose their 3-fold symmetry, inducing in this way the particles to self-assemble into tetragonal or chain-like structures (like experimentally observed for truncated nanocubes in Ref. [75]), rather than into hexagonal or honeycomb lattices. This hypothesis needs, of course, to be verified by calculations analogous to Secs. 5.4 and 5.5, but we leave this study for future research. Note also that the capillary deformations induced by such highly-truncated cubes are significantly reduced in their amplitude in z , compared to the cases for $q \leq 0.25$. Finally, for the bipyramid shapes with square base ($q = 0.99$), we find that the equilibrium orientation of the particle is no longer tilted, but the particle stands vertically at the interface. In this configuration, the capillary deformations induced by the particle in the height profile of the interface are negligible, therefore we do not expect capillary interactions, and the self-assembly structures of many of these particles adsorbed at the interface should be dictated by the close packing fraction. It is interesting, though, to study if this behavior changes by varying the Young's contact angle from the value of $\pi/2$ considered here, but we leave also this study for future research.

5.8 CASIMIR-LIKE AND VAN DER WAALS FORCES

In this Chapter we studied capillary interactions and self-assembly of particles adsorbed at fluid-fluid interfaces. However, in our analysis we did not include other possible kinds of particle-particle interactions. In general, to study these systems it is important be aware whether they are negligible or not, compared to interactions due to capillary deformations. In this Section, we quickly address this point for van der Waals interactions and Casimir-like forces.

In Fig. 5.21 we show the van der Waals potential Φ_{vdw} between two spheres of diameter $\sigma \equiv 2R$, with respect to the particle center-of-mass distance $D \equiv d + \sigma$, calculated with a Hamaker-de Boer approach [122] as

$$\Phi_{vdw}(d) = -\frac{A}{6} \left[\frac{2R^2}{d^2 + 4Rd} + \frac{2R^2}{d^2 + 4Rd + 4R^2} + \ln \left(\frac{d^2 + 4Rd}{d^2 + 4Rd + 4R^2} \right) \right], \quad (5.27)$$

for a system with surface tension $\gamma = 0.02$ N/m and Hamaker constant $A = 0.15$ eV (which is an estimation for a PbSe/Hexane/PbSe system [123]). These values are an order-of-magnitude estimate for the experimental systems in Refs. [75, 76], and a more accurate estimation should take into account that the cubes are adsorbed at a fluid-fluid interface and therefore the effective Hamaker constant can be slightly different. We plot $\Phi_{vdw}/2$ in units of $\Gamma\gamma$, where $\Gamma = 4\pi\sigma^2$, such that $\Gamma\gamma \approx 1.5 \cdot 10^5 k_B T$ for $\sigma = 100$ nm and $\Gamma\gamma \approx 1.5 \cdot 10^3 k_B T$ for $\sigma = 10$ nm. Compared with capillary forces, see Fig. 5.6(a), van der Waals interactions are completely negligible for spheres with $\sigma = 100$ nm, while they may become relevant for spheres with $\sigma = 10$ nm, i.e. with size comparable to the nano-cubes in Refs. [75, 76]. Note however that the range of capillary interactions goes far

beyond the range of van der Waals forces [compare Fig. 5.6(a) and 5.21]. So, for such experiments, capillarity remains the leading driving force, while van der Waals forces may come into play only when the particles get very close to each other.

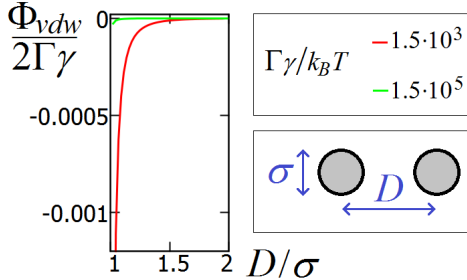


Figure 5.21: van der Waals interaction potential Φ_{vdw} between two spheres of diameter σ and at a center-of-mass distance D (see Eq. (5.27)), for a system with Hamaker constant $A = 0.15$ eV, in units of $\Gamma\gamma$, with $\gamma = 0.02$ N/m and $\Gamma = 4\pi\sigma^2$ the sphere surface area.

Another kind of particle-particle interactions that we did not include in our analysis are Casimir-like forces, which arise between adsorbed particles as a consequence of the thermal fluctuations (called capillary waves) experienced by the fluid-fluid interface equilibrium profile. We show here that these forces are indeed negligible compared to the capillary interactions induced by the hexapolar deformations considered in our work. Following Ref. [124], we can express the fluctuation-induced potential between two spheres adsorbed at a fluid-fluid interface as

$$V_{fluc} \approx -k_B T \frac{R^4}{D^4}, \quad (5.28)$$

with R the sphere radius and D the distance between the centers of mass of the two spheres. For our cubes (with side L and total surface area Σ) adsorbed at a fluid-fluid interface with surface tension γ , we can use $R \approx L/2$ to rewrite this expression, as an order-of-magnitude estimation, as

$$\frac{V_{fluc}}{\Sigma\gamma} \approx -\frac{k_B T}{\Sigma\gamma} \frac{L^4}{16D^4}. \quad (5.29)$$

Using for example $k_B T / \Sigma\gamma \approx 350$, which corresponds to the high-temperature limit for the honeycomb-hexagonal phase-coexistence area in the phase diagram of Fig. 3, and $D = 1.5L$, i.e. almost the contact distance for the cubes, we obtain $V_{fluc} \approx 0.000035 \Sigma\gamma$, which is definitely negligible compared to the cube-cube attractive pair potential $2\tilde{E}_2 = \mathcal{O}(0.01\Sigma\gamma)$ [see Fig. 5.6(a)].

5.9 CONCLUSION

In this Chapter, we exploited our numerical method, introduced in Chapter 4, to study systems of particles with cubic shape adsorbed at a fluid-fluid interface, demonstrating the importance of capillarity for studying the behavior of a single adsorbed cube, see Sec. 5.3, as well as the self-assembly of many adsorbed cubes, see Secs. 5.4 and 5.5. In particular, we showed that cubes with contact angle close to $\pi/2$ prefer the $\{111\}$ orientation, defined in Fig. 5.3, generating a hexapolar capillary deformation in the interface height profile which leads the cubes to self-assemble into hexagonal and honeycomb lattices. Experiments [125–127] showed that hexagonal platelets self-assemble into honeycomb or hexagonal lattices, depending on whether 3 or 6 of the side facets were made hydrophobic. However here we theoretically demonstrated that also adsorbed cubes with homogeneous surface properties can self-assemble through capillary interactions into lattices with hexagonal and honeycomb symmetries, rather than tetragonal. In addition, in Sec. 5.6 we introduced a simple free-energy model, where both configurational entropy and capillary interactions are included, and from this we predicted a phase diagram that features both the honeycomb and hexagonal lattices as stable structures. Interestingly, in Refs. [75, 76], where hexagonal and honeycomb lattices of adsorbed cubes are actually observed, capillarity is not taken into account to justify such structures, rather ligand adsorption and van der Waals forces between specific facets of the truncated cubes are suggested. Although we cannot exclude other possible driving forces, our results strongly suggest that capillarity could generate the observed structures. In fact, our phase diagram even features a well-defined parameter range in which the honeycomb lattice is to be expected, and this region is consistent with the experiments in Refs. [75, 76]. Finally, in Sec. 5.7 we explored the effects of shape truncation, for a cubic particle, on its single-adsorbed behavior, observing, in particular, that an asymmetric hexapole arises for highly-truncated cubes.

CHAPTER 6

WETTING OF DROPLETS ON COMPLEX SUBSTRATES

In this Chapter, we apply the numerical method introduced in Chapter 4 to study the behavior of (3D) droplets wetting solid particles with a non-trivial shape, and (3D) droplets wetting solid surfaces with heterogeneous chemical properties. In particular, we will present results for the equilibrium position of droplets on rod-like particles, and for the equilibrium shape of droplets wetting ellipsoidal hydrophilic patches.

6.1 INTRODUCTION

In Chapter 4, we introduced a new numerical method to calculate the equilibrium shape of fluid-fluid interfaces, given as input parameters the geometry and Young's contact angle of the solid surfaces in the system, and the volume of the fluids. So far in this Thesis, we have focused mainly on applying this numerical method for studying adsorbed particles at fluid-fluid interfaces. In this Chapter, instead, we show its applicability to study droplets wetting complex solid substrates. Firstly, we will briefly illustrate how we adapted the algorithm we reported in Chapter 4 for adsorbed particles at fluid-fluid interfaces, to study 3D droplets wetting complex solid surfaces. Then, we will present results for the equilibrium, i.e. minimum energy, position of a droplet on solid bullet-shaped particles. These results are an important extension of the theoretical calculations shown in Ref. [71], where the adsorption configuration of bullet-shaped particles at flat fluid-fluid interfaces (i.e. corresponding to infinite-volume droplets) was computed in the approximation of no capillary deformations. In Ref. [71], the particle flat-end attachment, experimentally observed, was theoretically found to be the equilibrium configuration only assuming heterogeneous chemical properties for the particle surface. Here, instead, where capillarity and finite-volume droplet effects are included, we show that such a configuration can be equilibrium also for particles with homogeneous chemical properties. In particular, we will show how the specific geometry of the particle (wider or narrower flat base) influences the preferred position of the droplet on the particle, i.e. if attached to the particle flat end or to the particle long side, and our predictions seem confirmed by recent experimental results [128]. These results are important for the synthesis of new odd-shaped colloidal particles, currently a very hot research field [129]. Finally, to point out the applicability of our method to study the wetting of solid surfaces with heterogeneous chemical properties, we will present results for the equilibrium shape of droplets wetting ellipsoidal hydrophilic patches, illustrating in particular the different behavior of the droplet with respect to the ellipsoid aspect ratio.

6.2 NUMERICAL METHOD

In this Chapter, we use the numerical method introduced in Chapter 4 to calculate the equilibrium shape of 3D droplets in contact with complex substrates. The algorithm used to implement our numerical method for this kind of calculations is an adaptation of the algorithm presented in Appendix B of Chapter 4 for the equilibrium shape of a fluid-fluid interface around an adsorbed 3D colloidal particle. In this Section, we briefly describe the modifications introduced in the algorithm to calculate the equilibrium shape of a 3D droplet (for more details, see Appendix B of Chapter 4). The shape and position of the solid surface in contact with the droplet is an input parameter of the simulation, and it is defined

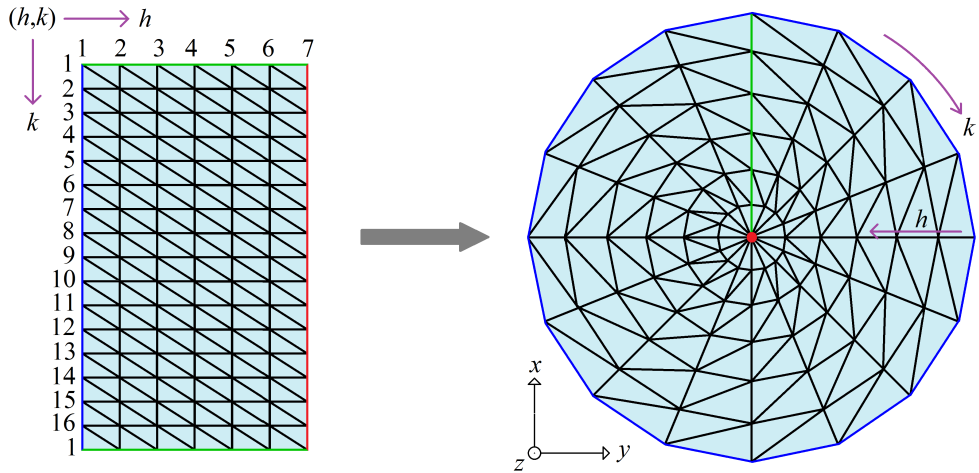


Figure 6.1: Sketch of a 16×7 triangulated grid of points to define the fluid-fluid interface of the droplet. The points of the grid with $h = 1$ are constrained to move only on the grid defining the solid surface in contact with the droplet. The point in the center of the grid, i.e. corresponding to the highest value of h ($h = 7$ here), moves only along the z axis, i.e. the direction pointing out of the paper in this sketch. All the other points of the grid move freely in the 3D space, but keeping constant their azimuthal angle with respect to the z axis.

by a triangulated grid of points. The fluid-fluid interface, i.e. the droplet surface, is represented by another triangulated grid of points, as sketched in Fig. 6.1. The basic mechanism of the method is the same described in Chapter 4, that is a simulated annealing algorithm is used to find the position of the fluid-fluid interface points which minimizes the energy functional Ξ [Eq. (4.3)], with the constraint of a given volume for the droplet. The desired volume V for the droplet is defined by the initial position of the fluid-fluid interface grid points. The points at the extremes of the fluid-fluid interface grid, i.e. corresponding to $h = 1$ in the sketch of Fig. 6.1, are constrained to move only on the grid defining the solid surface, with a mechanism analogous to the one described in Appendix B of Chapter 4 for moving the three-phase contact points on the solid particle surface. The point in the center of the fluid-fluid interface grid, see sketch in Fig. 6.1, is constrained to move only along the z axis. All the remaining points of the fluid-fluid interface grid can move freely in the 3D space. However, to have a higher control on the numerical solution, they are forced to move with constant azimuthal angle in the $[x, y]$ plane.ⁱ The Young's contact angle θ , taken inside the droplet, is also an input parameter required by the program, and it appears in the expression of the energy functional Ξ [Eq. (4.3)]. Possibly,

ⁱAlso, if required, during the simulation it is checked that their position satisfy the constraints imposed by the model, e.g. they are not allowed to move inside the solid.

surfaces with heterogeneous chemical properties, i.e. different contact angles, can be considered, as shown for example in Sec. 6.4. To perform this kind of calculations, a certain Young's contact angle, possibly different, is associated to each triangle of the solid surface grid. Then, during the simulated annealing, whenever a fluid-fluid interface grid point constrained on the solid surface is moved, the Young's contact angle used in the expression of $\Delta\Xi$, i.e. the variation of the energy functional Ξ [Eq. (4.3)] due to the point move, is the contact angle associated to the triangle of the solid surface grid where the new position of the moved point is located. Of course, the triangles of the solid surface grid need to be small enough to describe the heterogeneous properties of the solid surface with the desired approximation. In the calculations presented in this Chapter, we do not include the gravitational energy of the fluid-fluid interface, i.e. we consider the limit $\ell \rightarrow \infty$ for the capillary length, as this is the case for the experimental systems of interest. However, as shown in Chapter 4, gravity can easily be included in the method.

6.3 DROPLETS WETTING NON-TRIVIALY-CURVED SOLID PARTICLES

In this Section, we study the wetting of a droplet on solid particles with non-trivial curved surfaces. In particular, we consider the three particle shapes shown in Fig. 6.2, i.e. a nail-shaped particle with aspect ratioⁱⁱ $m = 5.8$, a bullet-shaped particle with aspect ratio $m = 6.0$, and a bullet-shaped particle with aspect ratio $m = 2.1$. As suggested by recent experiments [71, 128], where droplets are nucleated on solid particles with shapes similar to the ones in Fig. 6.2, the droplet can stay attached at the particle flat end, or at the particle long side. Here we elucidate this phenomenon, by predicting which of these two is the preferred position of the droplet, for the three particle shapes considered, and with respect to the droplet volume V and Young's contact angle θ (assumed constant on the whole particle surface). Using our numerical method, we calculate, for a given V and θ , the droplet equilibrium shape when the droplet is placed at the particle flat end, and

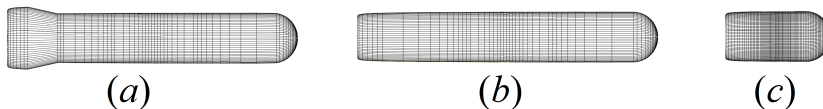


Figure 6.2: (a) Nail-shaped particle with aspect ratio $m = 5.8$. (b) Bullet-shaped particle with aspect ratio $m = 6.0$. (c) Bullet-shaped particle with aspect ratio $m = 2.1$. The equations used to define these surfaces are reported in Sec. 6.3.1.

ⁱⁱThe aspect ratio is measured as height over width of the particle, where the height is the distance between the two extrema of the particle along its long side, and the width is the particle diameter measured in the center.

when the droplet is placed at the particle long side. Then, the equilibrium shape that minimizes the (free) energy E [Eq. (2.24)] of this solid-fluid-fluid system corresponds to the preferred position of the droplet.ⁱⁱⁱ Explicitly written, the energy E is

$$E = \gamma (S - W \cos \theta) - V \Delta P , \quad (6.1)$$

where γ is the fluid-fluid surface tension, S and W are the areas of the droplet-external fluid interface and droplet-particle interface, respectively, and ΔP is the difference between the bulk pressure of the droplet and the bulk pressure of the external fluid. Note that, with respect to Eq. (2.24), E is shifted by a constant in Eq. (6.1), to rewrite it in a more compact way. When the droplet is at the particle flat end, we define its energy E_e as

$$E_e \equiv \gamma (S_e - W_e \cos \theta) , \quad (6.2)$$

and when the droplet is at the particle long side, we define its energy E_s as

$$E_s \equiv \gamma (S_s - W_s \cos \theta) . \quad (6.3)$$

Here S_e , W_e , and S_s , W_s , are the areas S , W when the particle is at the flat end and at the long side of the particle, respectively. Then, given

$$\Delta E \equiv E_s - E_e , \quad (6.4)$$

the droplet prefers to stay in the position that minimizes E [Eq. (6.1)], which is at the particle long side if $\Delta E < 0$, and at the particle flat end if $\Delta E > 0$. Note that in E_s [Eq. (6.3)] and E_e [Eq. (6.2)] we did not include the $V \Delta P$ term of Eq. (6.1), because in ΔE [Eq. (6.4)] this is canceled out, as we are comparing energies of droplets with the same volume, and so it is not relevant for our analysis.^{iv} In Figs. 6.3, 6.4, and 6.5, we show, for the three particle shapes shown in Fig. 6.2, the values of E_s [Eq. (6.3)], E_e [Eq. (6.2)] and ΔE [Eq. (6.4)] with respect to the volume V of the droplet, and for several values of $\cos \theta$. For each value of V and θ , the values of E_s and E_e are numerically computed from the equilibrium shape of the droplet obtained from our numerical method. For comparison, we plot also the energy E_c [Eq. (6.11)] obtained analytically for a

ⁱⁱⁱIn our algorithm for calculating the droplet equilibrium shape, the central point of the droplet surface grid can move only in the vertical direction, and all the other points can move only in directions with constant azimuthal angle with respect to the z axis (see Fig. 6.1). Given the initial position of the droplet, the simulation finds the minimum energy shape of the droplet that satisfies these constraints. So, the droplet cannot migrate, during the simulated annealing, from the flat end to the long side of the particle, or viceversa, accordingly to which is the minimum energy position. Therefore, we need to calculate the droplet equilibrium shape in both positions, and then compare their energy.

^{iv}If desired, the term $V \Delta P$ can be computed using the Young-Laplace Equation in absence of gravity [Eq. (2.21)], from which $\Delta P = 2\gamma/R$, where R is the radius of curvature of the droplet with a given volume V when forming a sphere, i.e. when not in contact to the particle, and therefore is given by $R = \sqrt[3]{3V/4\pi}$.

droplet with a spherical cap shape, with respect to V and θ (see Sec. 6.3.2). As expected, for small volumes E_c matches E_e . Indeed, when the droplet is small enough to stay within the edges of the particle flat base, it has a spherical cap equilibrium shape, as it is in contact with a flat substrate. These results show that, for a droplet volume V such that $0.1V_p \lesssim V \lesssim V_p$, with V_p the particle volume, the droplet prefers to attach at the particle flat end rather than at the particle long side, because $\Delta E > 0$. The precise range of volumes V such that $\Delta E > 0$ depends, as shown, by the specific particle shape and by the Young's contact angle θ . In the limit of very big droplets ($V \gg V_p$), our results suggest that the attachment at the long side of the particle is always preferred by the droplet, for any particle shape and value of θ , in agreement with the theoretical results presented in [71] and valid for flat interfaces, i.e. for $V \rightarrow \infty$.^v The energy unit used in the graphs of Figs. 6.3, 6.4 and 6.5, is $\Sigma\gamma$, with Σ the particle total surface area and γ the fluid-fluid surface tension. Considering for example a micron-sized particle with $\Sigma \approx 2 \mu\text{m}^2$ and a typical surface tension $\gamma \approx 0.01$ N/m, we obtain $\Sigma\gamma \approx 5 \cdot 10^6 k_B T$, with k_B the Boltzmann constant and T the room temperature. In Fig. 6.6 we sum up these results in three phase diagrams, one for each particle shape, where we indicate if ΔE is positive or negative, with respect to V and θ . As shown, the nail-shaped particle and the shortest bullet-shaped particle have a larger region, than the longest bullet-shaped particle, of V - $\cos\theta$ combinations such that the droplet prefers to stay at the particle flat end. This result seems in agreement with recent experimental findings [128], and it is reasonably connected with the larger ratio between the particle flat-end diameter and the particle length, proving how, just by slightly playing with the particle geometry, it is possible to change the most favorable position for the attachment of the droplet on the particle surface. Finally, in Figs. 6.7, 6.8, and 6.9, we show, for the three particle shapes considered, a 3D view of the equilibrium shape of the droplet, as obtained by our numerical method, attached at its preferred position on the particle (i.e. flat end or long side), for some values of V and θ .

^vAlthough in [71] capillary deformation effects in the flat interface due to the particle are neglected.

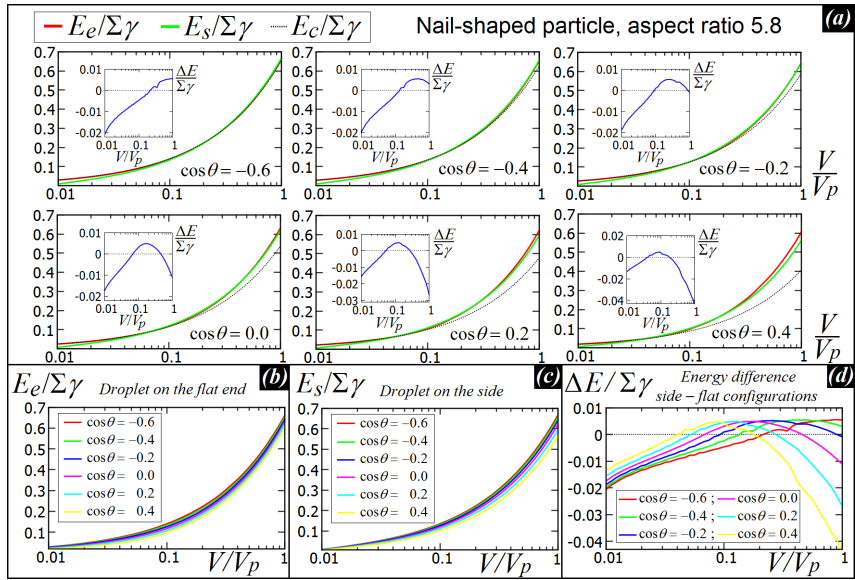


Figure 6.3: Results for the nail-shaped particle of aspect ratio 5.8.

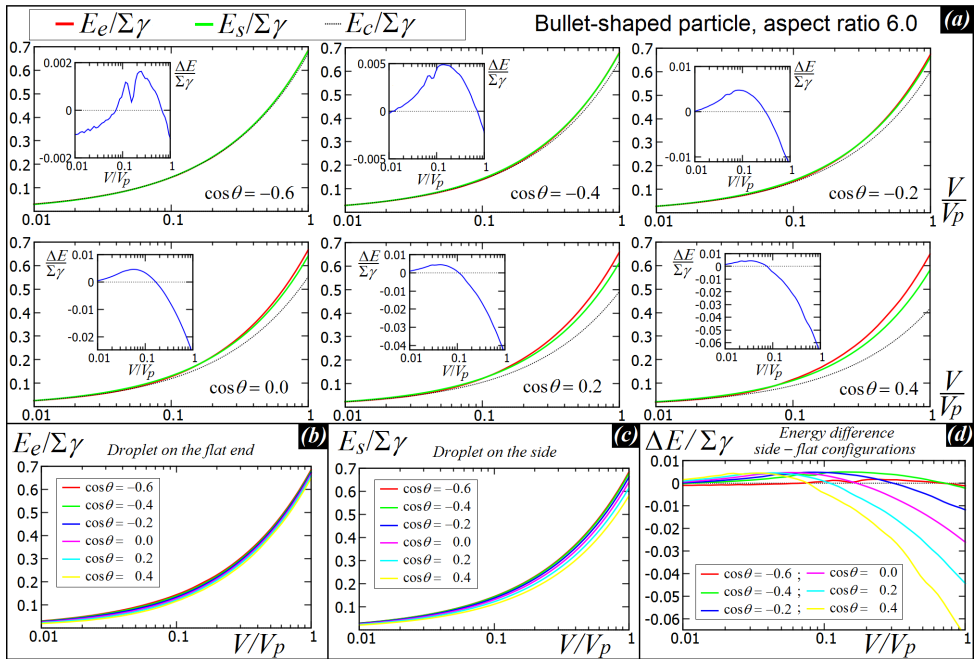


Figure 6.4: Results for the bullet-shaped particle of aspect ratio 6.0 [see Fig. 6.2(b)]. (a) Energy E_s [Eq. (6.3)] and E_e [Eq. (6.2)] of a droplet in contact with the particle long side and with the particle flat end, respectively, for various Young's contact angles θ , and with respect to the droplet volume V , where V_p is the particle volume, Σ the particle total surface area, and γ the fluid-fluid surface tension. For comparison, with the dotted line we plot the energy E_c [Eq. (6.11)], analytically obtained for a droplet with a spherical cap shape of volume V and contact angle θ . In the insets, $\Delta E \equiv E_s - E_e$ is shown. (b)-(c)-(d) Plots of E_e , E_s , and ΔE , respectively, for the various θ considered.

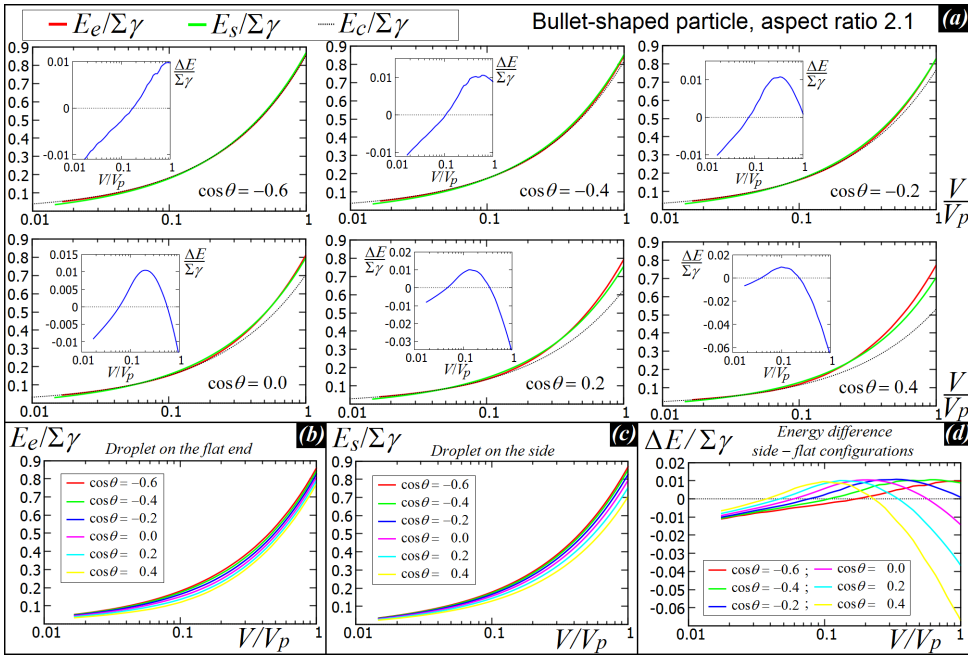


Figure 6.5: Results for the bullet-shaped particle of aspect ratio 2.1 [see Fig. 6.2(c)]. (a) Energy E_s [Eq. (6.3)] and E_e [Eq. (6.2)] of a droplet in contact with the particle long side and with the particle flat end, respectively, for various Young's contact angles θ , and with respect to the droplet volume V , where V_p is the particle volume, Σ the particle total surface area, and γ the fluid-fluid surface tension. For comparison, with the dotted line we plot the energy E_c [Eq. (6.11)], analytically obtained for a droplet with a spherical cap shape of volume V and contact angle θ . In the insets, $\Delta E \equiv E_s - E_e$ is shown. (b)-(c)-(d) Plots of E_e , E_s , and ΔE , respectively, for the various θ considered.

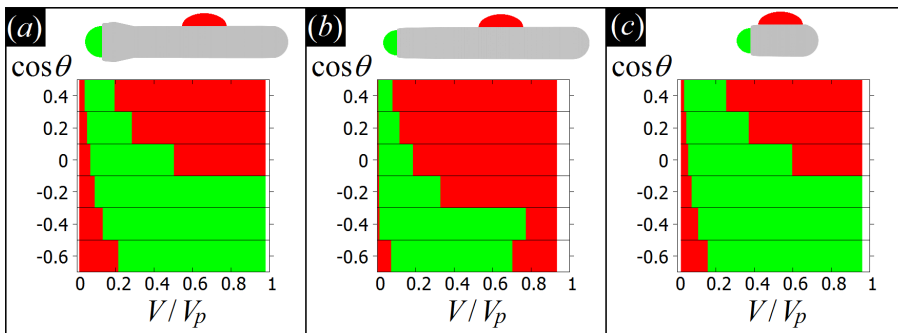


Figure 6.6: In this phase diagrams we sum up the results of Figs. 6.3, 6.4, and 6.5. We indicate with red the $\cos\theta$ - V combinations such that the droplet prefers to attach at the long side of the particle (i.e. $\Delta E < 0$), and in green the $\cos\theta$ - V combinations such that the droplet prefers to attach at the flat end of the particle (i.e. $\Delta E > 0$). The particle shape considered is (a) the nail-shaped particle with aspect ratio 5.8, (b) the bullet-shaped particle with aspect ratio 6.0, (c) the bullet-shaped particle with aspect ratio 2.1.

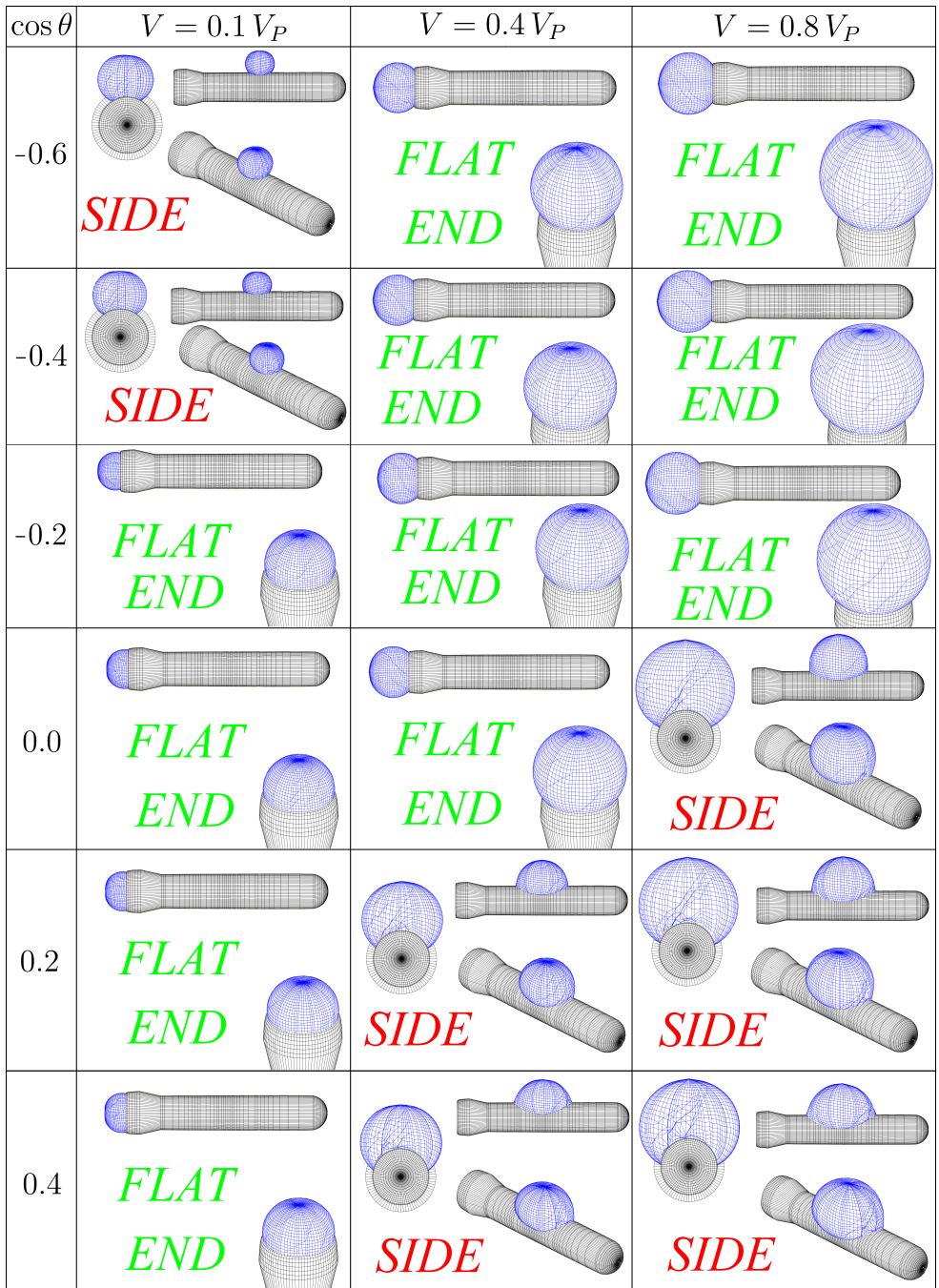


Figure 6.7: 3D view of the equilibrium shape, as computed through our numerical method, of the droplet attached at its preferred position (i.e. flat end or long side) of the nail-shaped particle with aspect ratio 5.8, for a droplet volume $V = 0.1, 0.4, 0.8 V_P$, with V_P the particle volume, and for $\cos \theta = -0.6, -0.4, -0.2, 0.0, 0.2, 0.4$, with θ the Young's contact angle.

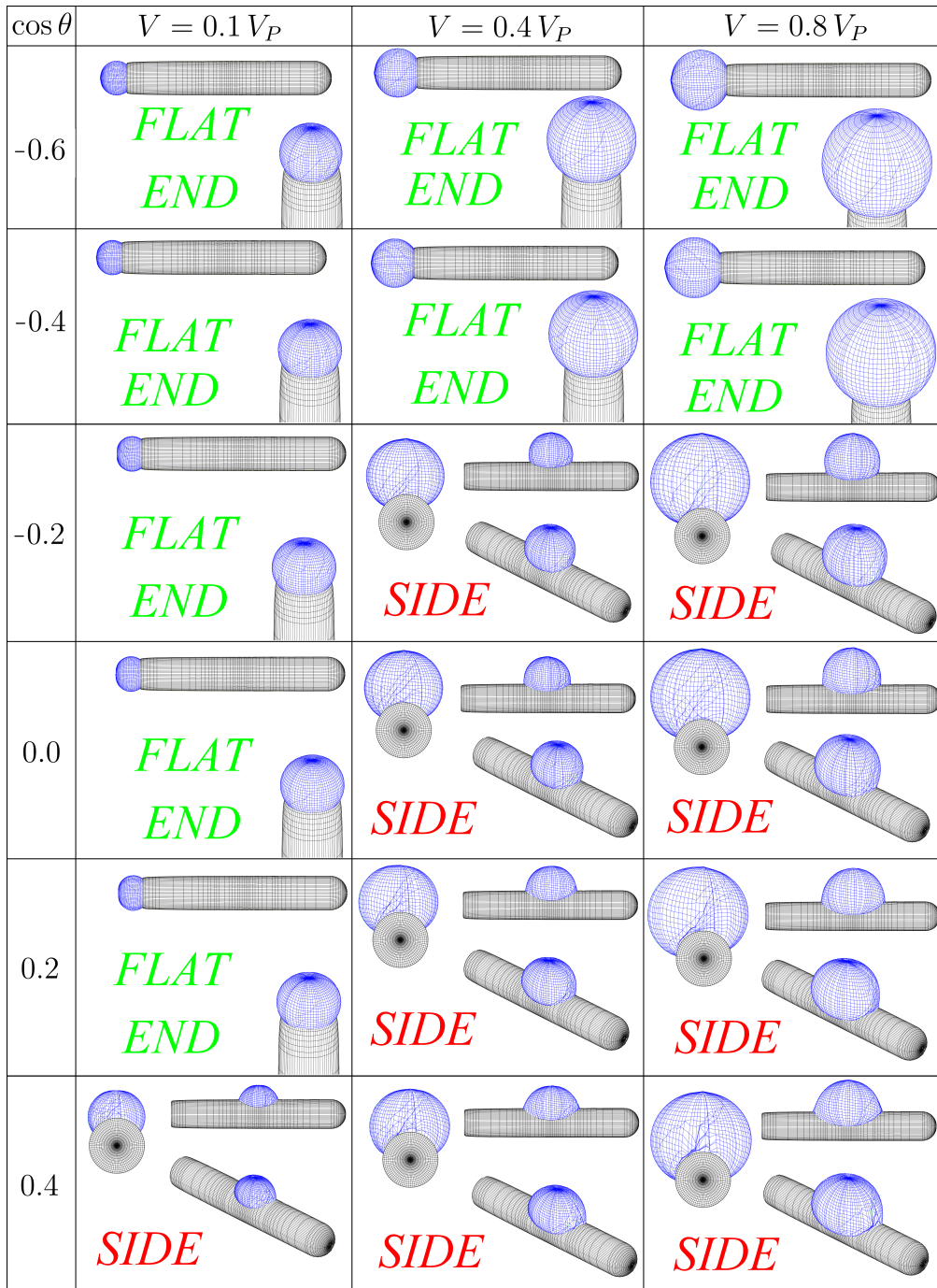


Figure 6.8: 3D view of the equilibrium shape, as computed through our numerical method, of the droplet attached at its preferred position (i.e. flat end or long side) of the bullet-shaped particle with aspect ratio 6.0, for a droplet volume $V = 0.1, 0.4, 0.8 V_P$, with V_P the particle volume, and for $\cos \theta = -0.6, -0.4, -0.2, 0.0, 0.2, 0.4$, with θ the Young's contact angle.

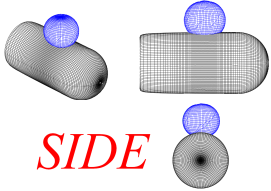
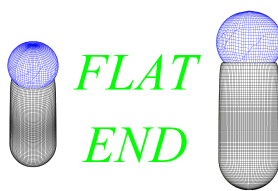
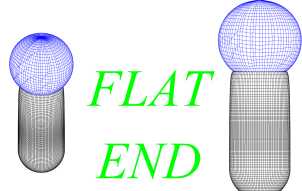
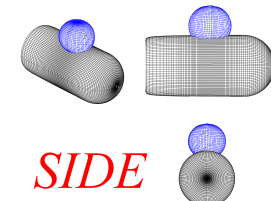
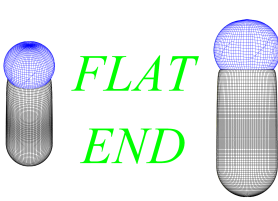
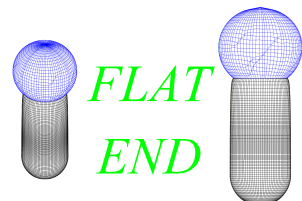
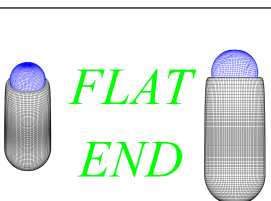
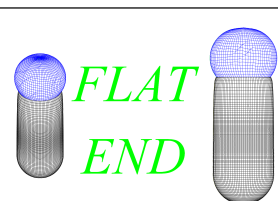
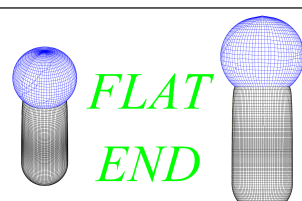
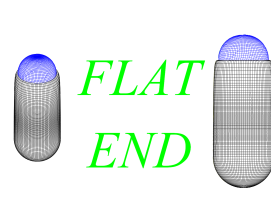
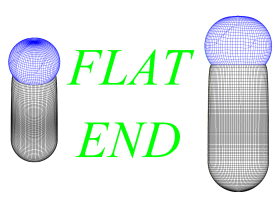
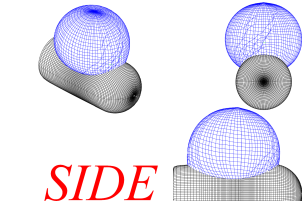
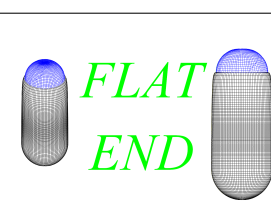
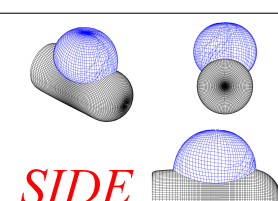
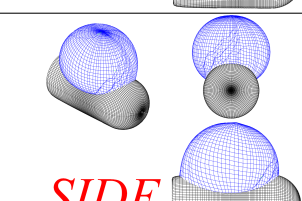
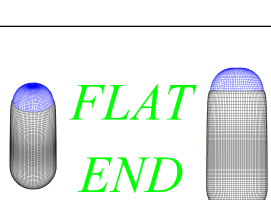
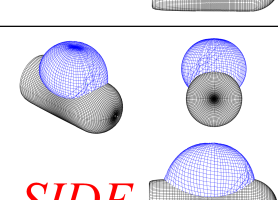
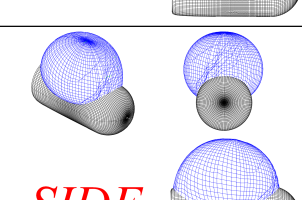
| $\cos \theta$ | $V = 0.1 V_P$ | $V = 0.4 V_P$ | $V = 0.8 V_P$ |
|---------------|--|---|---|
| -0.6 |  <i>SIDE</i> |  <i>FLAT</i> <i>END</i> |  <i>FLAT</i> <i>END</i> |
| -0.4 |  <i>SIDE</i> |  <i>FLAT</i> <i>END</i> |  <i>FLAT</i> <i>END</i> |
| -0.2 |  <i>FLAT</i> <i>END</i> |  <i>FLAT</i> <i>END</i> |  <i>FLAT</i> <i>END</i> |
| 0.0 |  <i>FLAT</i> <i>END</i> |  <i>FLAT</i> <i>END</i> |  <i>SIDE</i> |
| 0.2 |  <i>FLAT</i> <i>END</i> |  <i>SIDE</i> |  <i>SIDE</i> |
| 0.4 |  <i>FLAT</i> <i>END</i> |  <i>SIDE</i> |  <i>SIDE</i> |

Figure 6.9: 3D view of the equilibrium shape, as computed through our numerical method, of the droplet attached at its preferred position (i.e. flat end or long side) of the bullet-shaped particle with aspect ratio 2.1, for a droplet volume $V = 0.1, 0.4, 0.8 V_P$, with V_P the particle volume, and for $\cos \theta = -0.6, -0.4, -0.2, 0.0, 0.2, 0.4$, with θ the Young's contact angle.

6.3.1 SHAPE OF THE SOLID PARTICLES

In this Section we report how we defined the surface of the solid particles shown in Fig. 6.2. The triangular grid used to represent the particle surface is 400×400 points. The generic position $\mathbf{p} = (p_x, p_y, p_z)$ of each point of the particle grid is defined using the following parametric equations

$$\begin{aligned} p_x &= a s[\cos(u\pi - \pi/2) \cos(2v\pi)] |\cos(2v\pi)| |\cos(u\pi - \pi/2)|^\epsilon \\ p_y &= a s[\cos(u\pi - \pi/2) \sin(2v\pi)] |\sin(2v\pi)| |\cos(u\pi - \pi/2)|^\epsilon \\ p_z &= b s[\sin(u\pi - \pi/2)] |\sin(u\pi - \pi/2)| + m - 1 \end{aligned} \quad (6.5)$$

where $u, v \in [0, 1]$, and

$$b = \begin{cases} 1, & \text{if } u\pi - \pi/2 > 0, \\ 2m - 1, & \text{otherwise;} \end{cases} \quad (6.6)$$

$$\epsilon = \begin{cases} 1.0, & \text{if } u\pi - \pi/2 > 0, \\ 0.05, & \text{otherwise;} \end{cases} \quad (6.7)$$

$$s(x) = \begin{cases} 1, & \text{if } x \geq 0, \\ -1, & \text{if } x < 0. \end{cases} \quad (6.8)$$

For the bullet-shaped particles $a = 1$, while for the nail-shaped particle

$$a = \begin{cases} 1.3, & \text{if } u\pi < 0.4, \\ 1, & \text{otherwise;} \end{cases} \quad (6.9)$$

The value of m is the aspect ratio of the particle, which is 5.8 for the nail-shaped particle [Fig. 6.2(a)], 2.1 for the longest bullet-shaped particle [Fig. 6.2(b)], and 6.0 for the shortest bullet-shaped particle [Fig. 6.2(c)].

6.3.2 ENERGY OF A SPHERICAL-CAP DROPLET

As already discussed in Chapter 2, when a droplet is in contact with a flat solid surface, and gravity is negligible, the shape of the droplet is a spherical cap, see Fig. 6.10, with contact angle determined by Young's Law. The energy $E_c \equiv E - P\Delta V$ [with E given in Eq. (6.1)] of a droplet with a spherical cap shape of volume V and contact angle θ is

$$E_c(V, \theta) = \gamma [S(V, \theta) - \cos \theta W(V, \theta)] , \quad (6.10)$$

where $S_c(V, \theta) = 2\pi(1 - \cos \theta)R^2(V, \theta)$ is the fluid-fluid interface area of the spherical cap-shaped droplet, and $W_c(V, \theta) = \pi(R \sin \theta)^2$ the solid-droplet interface area. Therefore

$$E_c(V, \theta) = \gamma [2(1 - \cos \theta) - \cos \theta(\sin \theta)^2] \pi R^2(V, \theta) . \quad (6.11)$$

The volume V of a spherical cap is

$$V = \left(\frac{2 + \cos \theta}{3} \right) (1 - \cos \theta)^2 \pi R^3 , \quad (6.12)$$

from which

$$R(V, \theta) = \sqrt[3]{\frac{3V}{\pi(2 + \cos \theta)(1 - \cos \theta)^2}} . \quad (6.13)$$

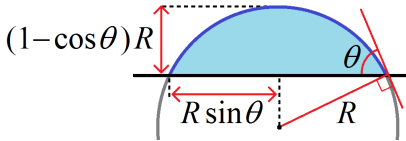
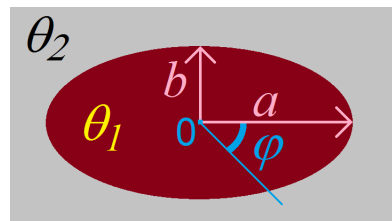


Figure 6.10: Section of a spherical cap with curvature radius R and contact angle θ .

6.4 DROPLETS ON HYDROPHILIC ELLIPSOIDAL PATCHES

In the previous Section we applied our numerical method to study the wetting of a droplet on a curved solid surface. In this Section, instead, we study the wetting of a droplet on a flat solid substrate, but with heterogeneous chemical surface properties, with the main aim of testing our numerical method for this kind of calculations. In particular, we consider an ellipsoidal patch with Young's contact angle $\theta_1 = 30^\circ$ with the droplet, while the external substrate has Young's contact angle $\theta_2 = 60^\circ$ with the droplet (see Fig. 6.11). Therefore, the droplet prefers to wet the ellipsoidal patch rather than the remaining solid surface. We study the droplet equilibrium shape with respect to the droplet volume V , and with respect to the aspect ratio b/a of the ellipsoidal patch, where b and a are the minor and major semi-axis of the ellipsoid, respectively. In Fig. 6.12, we show $R(\varphi)$ and $\theta(\varphi)$ for different volumes V of a droplet wetting the ellipsoidal patch with $b = 0.3a$, where φ is the azimuthal angle (see Fig. 6.11) in the solid surface plane. Here, R and θ are numerically computed from the equilibrium shape of the droplet, obtained by our numerical method, and they are, respectively, the distance of the three-phase contact line from the droplet center (intended as the average position of the three-phase contact line), and the droplet Young's contact angle (measured as the angle between the solid surface plane and the droplet surface grid in contact with the solid). In Fig. 6.13, we show analogous results, but for an ellipsoidal patch with $b = 0.7a$. For both patches, the droplet has a spherical cap shape with contact angle 30° , when it has a small volume, such that it is completely contained inside the patch, and a spherical cap shape with contact angle 60° , when it has a big volume, such that it completely encloses the patch. However between these two (trivial) regimes, the droplet deviates from the spherical cap shape, due to the presence of two different Young's contact angles in the substrate. In particular, we observe two different behaviors for the droplet wetting the two different patches. In the case of the more elongated ellipsoid, $b = 0.3a$, the droplet, while growing in volume, starts spreading outside the patch from the ellipsoid long sides already before than the patch is completely wet, see Fig. 6.12. Instead, for the ellipsoid with $b = 0.7a$, first the droplet completely wet the patch, and only after it starts spreading on the external substrate, again from the ellipsoid long sides, see Fig. 6.13. Note indeed that, in Fig. 6.13(a), $R(\varphi)$ exceeds the ellipsoidal patch rim for $\varphi = 90^\circ$ and $\varphi = 270^\circ$ (i.e. at the

Figure 6.11: Top view of a solid flat surface with an ellipsoidal patch (dark red area) of major semi-axis a and minor semi-axis b . The patch has Young's contact angle $\theta_1 = 30^\circ$, while the external surface (gray area) has Young's contact angle $\theta_2 = 60^\circ$. Therefore, a droplet on this solid surface has a higher wettability with the patch.



ellipsoid long side) only if $R(0^\circ) = R(180^\circ) = a$, that is only if the droplet has spread already until the rim of the ellipsoidal patch short side. Instead, in Fig. 6.12(a), $R(\varphi)$ exceeds the ellipsoidal patch rim for $\varphi = 90^\circ$ and $\varphi = 270^\circ$ (i.e. at the ellipsoid long side) for $R(0^\circ) = R(180^\circ) < a$, that is when the droplet still has not spread until the rim of the ellipsoidal patch short side. This different behavior of the droplet for the two different patches is also clearly shown by the 3D plots of the droplet equilibrium shape shown in Figs. 6.12 and 6.13. The behavior of Young's contact angle θ with respect to the azimuthal angle φ , see Figs. 6.12(b) and 6.13(b), shows that for small volumes the droplet has $\theta \approx 30^\circ$ for any φ , i.e. it is still in the spherical cap regime, with 30° the Young's contact angle of the patch. Then, by growing the droplet volume, the value of θ starts increasing first at the ellipsoidal patch long side, once the droplet has reached the rim, and only after (i.e. for bigger droplet volumes) its value increases also at the ellipsoidal patch short side. As shown, θ increases, while growing the droplet volume, until it reaches the maximum value of about 60° , corresponding to the Young's contact angle of the external substrate to the patch. The droplet is again in the spherical cap regime when θ is 60° for any φ . To sum up, outside from the spherical-cap regime, there are four different possible phases for the droplet:

- *phase A*: the droplet is completely inside the patch, and does not wet the patch completely;
- *phase B*: the droplet is partially outside the patch, and does not wet the patch completely;
- *phase C*: the droplet is completely inside the patch, and does wet the patch completely;
- *phase D*: the droplet is partially outside the patch, and does wet the patch completely.

To sum up, while growing in volume, the droplet first it is a spherical cap with contact angle 30° and completely inside the patch. Then, once it touches the patch rim, the droplet goes into phase *A*. Then, depending on the ellipsoidal patch aspect ratio, the droplet goes into phase *B* or *C*. Finally, the droplet goes into phase *D*, before assuming again the shape of a spherical cap, now with contact angle 60° and completely surrounding the patch. These results are shown more in detail in the phase diagram of Fig. 6.14, where we indicated the droplet phase, as obtained by calculating the droplet equilibrium shapes through our numerical method, with respect to the droplet volume V and the ellipsoidal patch aspect ratio b/a . This phase diagram confirms that, for a certain value of b/a between 0.3 and 0.7, there is a transition in the behavior of the droplet, such that for the more elongated patches it goes from phase *A* to phase *B* and then phase *D*, while for the less elongated patches the droplet goes from phase *A* to phase *C* and then phase *D*.

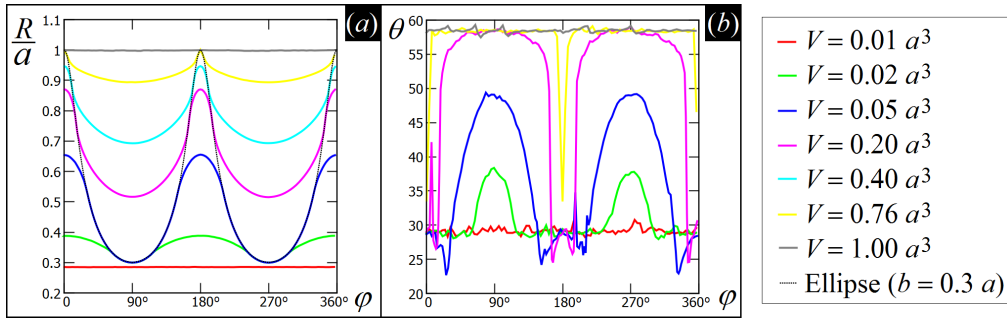
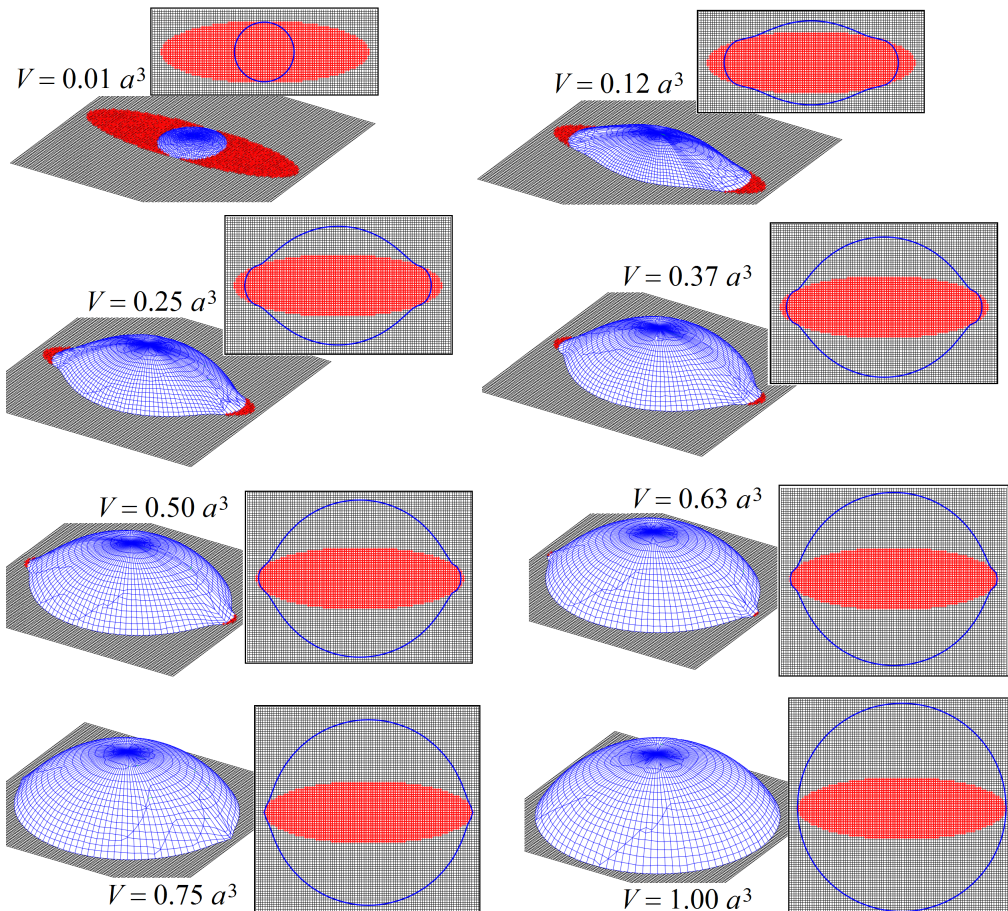


Figure 6.12: Results for a droplet of volume V wetting a flat solid surface with Young's contact angle 60° , with an ellipsoidal patch, of aspect ratio $b/a = 0.3$, with Young's contact angle 30° . Below we show a 3D view of the equilibrium shape of the droplet (blue grid) for different V , as computed by our numerical method, with the insets showing a top view of the three-phase contact line (blue line). The black grid represents the solid surface, with the red area indicating the ellipsoidal patch. In (a) we plot the distance R of the three-phase contact line from the droplet center, with respect to the azimuthal angle φ , see Fig. 6.11. In (b) we report the droplet contact angle θ , with respect to φ , as numerically computed from our numerical solutions.



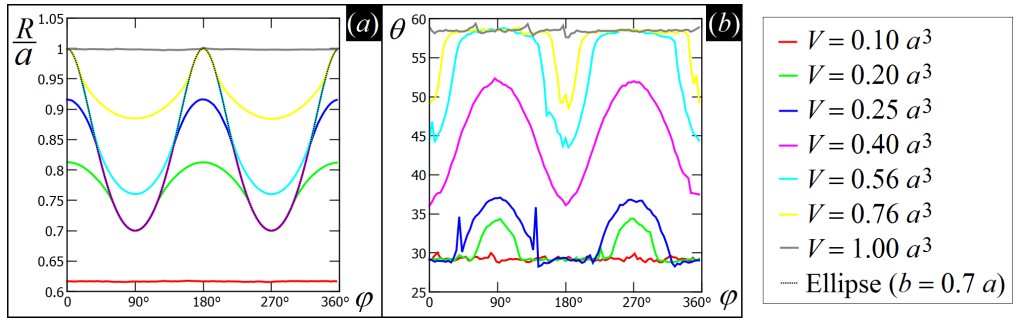
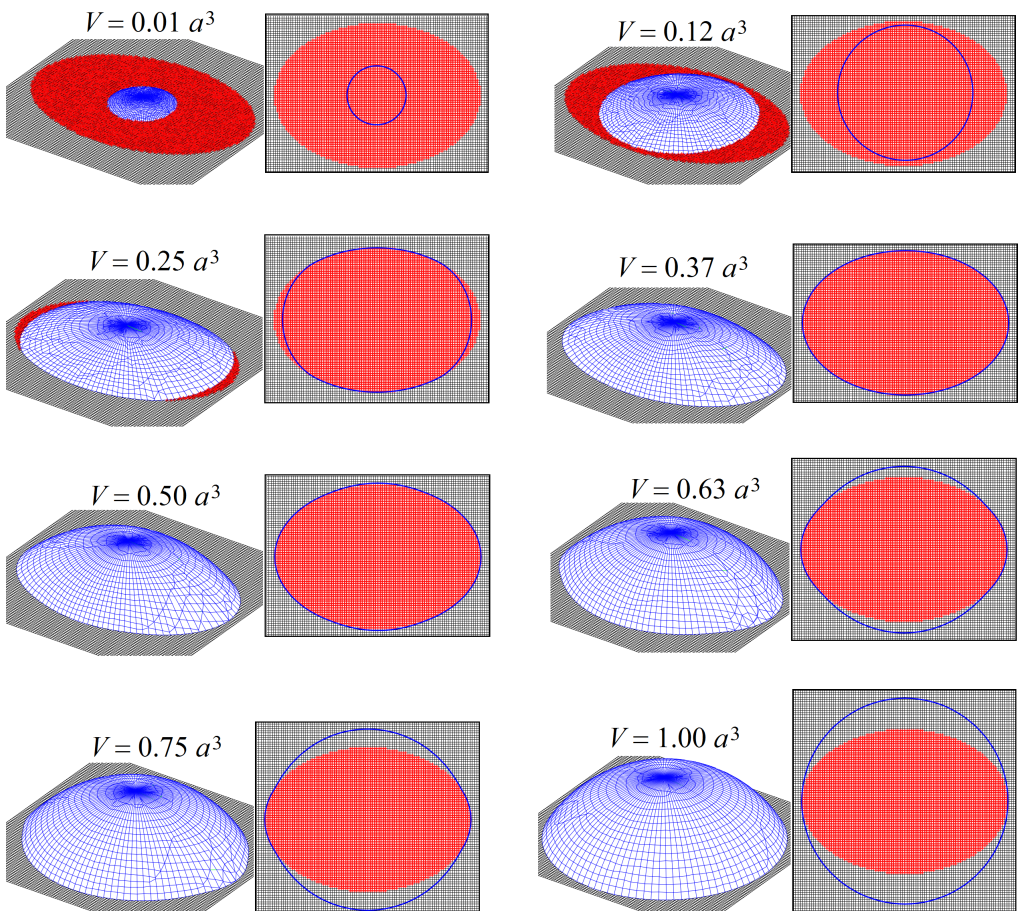


Figure 6.13: Results for a droplet of volume V wetting a flat solid surface with Young's contact angle 60° , with an ellipsoidal patch, of aspect ratio $b/a = 0.7$, with Young's contact angle 30° . Below we show a 3D view of the equilibrium shape of the droplet (blue grid) for different V , as computed by our numerical method, with the insets showing a top view of the three-phase contact line (blue line). The black grid represents the solid surface, with the red area indicating the ellipsoidal patch. In (a) we plot the distance R of the three-phase contact line from the droplet center, with respect to the azimuthal angle φ , see Fig. 6.11. In (b) we report the droplet contact angle θ , with respect to φ , as numerically computed from our numerical solutions.



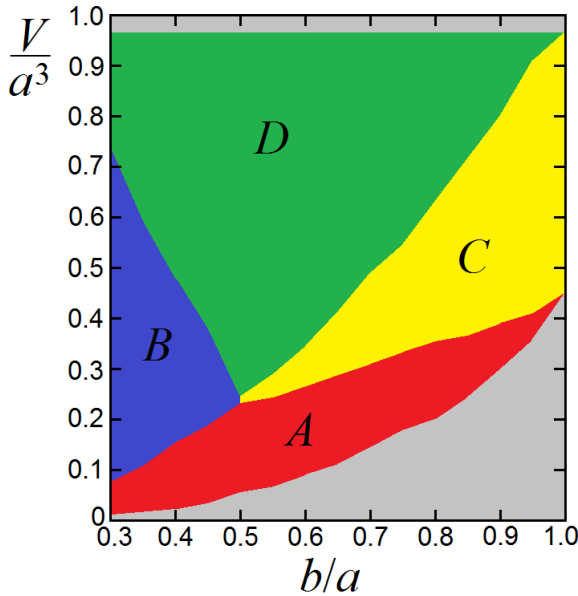
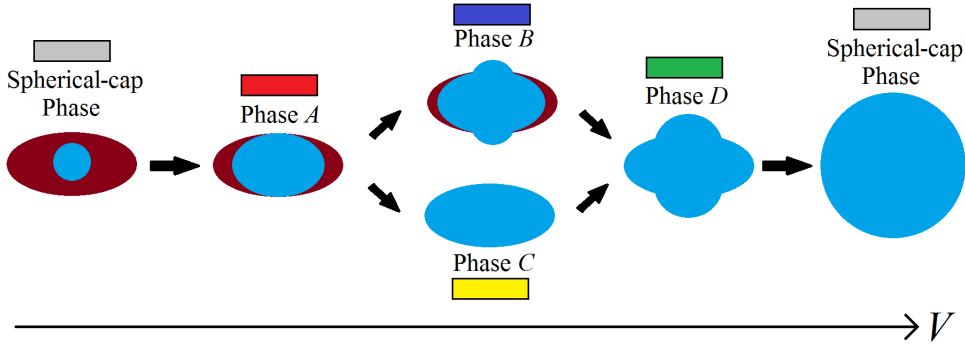


Figure 6.14: Phase diagram for a droplet wetting an ellipsoidal patch of Young's contact angle 30° and an external substrate of Young's contact angle 60° , with respect to the ellipsoid aspect ratio b/a and the droplet volume V . The gray areas indicate the spherical-cap regime of the droplet, either with contact angle 30° and completely inside the patch, or with contact angle 60° and completely outside the patch. The colored area indicates the four possible phases for the droplet when it deviates from the spherical cap shape, that is: the *phase A*, when the droplet is completely inside the patch and does not wet the patch completely, the *phase B*, when the droplet is partially outside the patch and does not wet the patch completely, the *phase C*, when the droplet is completely inside the patch and does wet the patch completely, and the *phase D*, when the droplet is partially outside the patch, and does wet the patch completely. The sketch above the phase diagram shows the different droplet phases.

6.5 CONCLUSION

In this Chapter we studied the wetting of 3D droplets on complex solid substrates, exploiting the numerical method introduced in Chapter 4. In particular, in Sec. 6.3 we presented results for a droplet attached to a solid bullet-shaped particle, calculating its equilibrium configuration, i.e. if to the particle flat end or to the particle long side, with respect to the Young's contact angle and to the droplet volume. These results are an important extension of the calculations presented in Ref. [71], where the limit of flat fluid-fluid interfaces (i.e. infinite-volume droplets) and the approximation of no capillarity were used. Here, we showed that the attachment of the droplet to the flat end of the particle, rather than to its long side, can be achieved just by slightly tuning the specific geometry of the particle, even assuming homogeneous chemical properties for the particle surface. Instead, in Ref. [71], the flat-end attachment of the droplet was theoretically predicted to be the equilibrium one only if different Young's contact angles for the particle surface were assumed. Our predictions seem to be confirmed by recent experimental results [128]. Then, in Sec. 6.4, with the main aim of pointing out the applicability of our method to study the wetting of solid surfaces with heterogeneous chemical properties, we studied the equilibrium shape of a droplet on a flat solid surface with an ellipsoidal patch of higher wettability than the external surface. As shown, the behavior of a droplet, nucleating inside the patch and growing until the patch is completely covered, varies with respect to the ellipsoid aspect ratio. Note that we considered an ellipsoidal patch for illustrative purpose, however our method can be used to study the wetting on (possibly curved) surfaces with patches of any shape and Young's contact angle. See for example in Fig. 6.15 the equilibrium shape of a droplet wetting a flat surface with four circular patches with higher wettability than the external surface. As a final remark, we point out that in this Chapter, and in the whole thesis in general, we always considered undeformable solids. An interesting development for our numerical method is to calculate the equilibrium shape of fluid-fluid interfaces in contact with soft (i.e. deformable) solids, as this is a very important and recurrent research problem in the Soft Matter field (e.g. see Refs. [83, 130–135]). We leave for future work the adaptation of our method for such calculations.

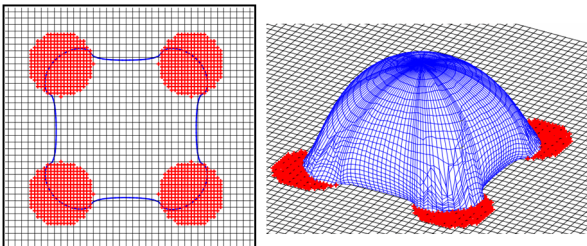


Figure 6.15: Equilibrium shape of a droplet (blue grid), as computed by our numerical method, on a flat solid surface with four circular patches (red area) of higher wettability than the external surface (black grid). In the inset, top view of the equilibrium three-phase contact line (blue line).

BIBLIOGRAPHY

- [1] P. Lang and I. Liu, *Soft Matter at Aqueous Interfaces*, Lecture Notes in Physics 917, Springer, 2015.
- [2] L. D. Landau and E. M. Lifshitz, *Statistical Physics - Part I*, Pergamon Press, 3rd revised and enlarged edition, 1980.
- [3] R. Defay and I. Prigogine, *Surface Tension and Adsorption*, Longmans, 1966.
- [4] C. Pozrikidis, *Introduction to Theoretical and Computational Fluid Dynamics*, Oxford University Press, 2nd edition, 2011.
- [5] M. J. Smith, *Am. J. Phys.* **38**, 1153 (1970).
- [6] P. Roura, *Am. J. Phys.* **73**, 1139 (2005).
- [7] G. Whyman and E. Bormashenko, *J. Colloid Interface Sci.* **331**, 174 (2009).
- [8] A. K. Das and P. K. Das, *Chem. Eng. Sci.* **65**, 4027 (2010).
- [9] J. Guzowski, M. Tasinkevych, and S. Dietrich, *Soft Matter* **7**, 4189 (2011).
- [10] V. A. Lubarda, *Langmuir* **27**, 10705 (2011).
- [11] V. A. Lubarda, *Soft Matter* **8**, 10288 (2012).
- [12] A. Eddi, K. G. Winkels, and J. H. Snoeijer, *Phys. Rev. Lett.* **111**, 144502 (2013).
- [13] X. Zhang, H. Lhuissier, C. Sun, and D. Lohse, *Phys. Rev. Lett.* **112**, 144503 (2014).
- [14] E. Dietrich, S. Wildeman, C. W. Visser, K. Hofhuis, E. S. Kooij, H. J. W. Zandvliet, and D. Lohse, *Journal of Fluid Mechanics* **794**, 45 (2016).
- [15] W. Ramsden, *Proc. R. Soc. Lond.* **72**, 156 (1903).
- [16] S. Pickering, *J. Chem. Soc.* **91**, 2001 (1907).
- [17] K. Du, E. Glogowski, T. Emrick, T. P. Russell, and A. D. Dinsmore, *Langmuir* **26**, 12518 (2010).

- [18] G. B. Davies, T. Krueger, P. V. Coveney, and J. Harting, *The Journal of Chemical Physics* **141**, 154902 (2014).
- [19] A. J. Mendoza, E. Guzmán, F. Martínez-Pedrero, H. Ritacco, R. G. Rubio, F. Ortega, V. M. Starov, and R. Miller, *Advances in Colloid and Interface Science* **206**, 303 (2014), Manuel G. Velarde.
- [20] P. Pieranski, *Phys. Rev. Lett.* **45**, 569 (1980).
- [21] S. Sacanna, W. K. Kegel, and A. P. Philipse, *Phys. Rev. Lett.* **98**, 158301 (2007).
- [22] M. G. Basavaraj, S. Vandebril, J. Fransaer, and J. Vermant, *Soft Matter* **5**, 1717 (2009).
- [23] E. Dickinson, *Trends in Food Science & Technology* **24**, 4 (2012).
- [24] R. Aveyard, *Soft Matter* **8**, 5233 (2012).
- [25] F. Günther, S. Frijters, and J. Harting, *Soft Matter* **10**, 4977 (2014).
- [26] S. Bai, C. Pappas, S. Debnath, P. W. J. M. Frederix, J. Leckie, S. Fleming, and R. V. Ulijn, *ACS Nano* **8**, 7005 (2014).
- [27] E. Santini, E. Guzmán, M. Ferrari, and L. Liggieri, *Colloids and Surfaces A: Physicochemical and Engineering Aspects* **460**, 333 (2014).
- [28] Z. Li, D. Harbottle, E. Pensini, T. Ngai, W. Richtering, and Z. Xu, *Langmuir* **31**, 6282 (2015).
- [29] M. Vis, J. Opdam, I. S. J. van 't Oor, G. Soligno, R. van Roij, R. H. Tromp, and B. H. Ern, *ACS Macro Letters* (2015).
- [30] J. Vermant, *Nature* **476**, 286 (2011).
- [31] P. J. Yunker, T. Still, M. A. Lohr, and A. G. Yodh, *Nature* **476**, 308 (2011).
- [32] P. Fang, S. Chen, H. Deng, M. D. Scanlon, F. Gumy, H. J. Lee, D. Momotenko, V. Amstutz, F. Cortes-Salazar, C. M. Pereira, Z. Yang, and H. H. Girault, *ACS Nano* **7**, 9241 (2013).
- [33] K. Stratford, R. Adhikari, I. Pagonabarraga, J. C. Desplat, and M. E. Cates, *Science* **309**, 2198 (2005).
- [34] R. Di Leonardo, F. Saglimbeni, and G. Ruocco, *Phys. Rev. Lett.* **100**, 106103 (2008).
- [35] L. Yao, L. Botto, M. Cavallaro, B. J. Bleier, V. Garbin, and K. J. Stebe, *Soft Matter* **9**, 779 (2013).
- [36] V. R. Dugyala and M. G. Basavaraj, *Langmuir* **30**, 8680 (2014).
- [37] K. Schwenke, L. Isa, D. L. Cheung, and E. D. Gado, *Langmuir* **30**, 12578 (2014).
- [38] G. B. Davies, T. Krger, P. V. Coveney, J. Harting, and F. Bresme, *Advanced Materials* **26**, 6715 (2014).
- [39] G. B. Davies, T. Kruger, P. V. Coveney, J. Harting, and F. Bresme, *Soft Matter* **10**, 6742 (2014).
- [40] M. Anyfantakis, Z. Geng, M. Morel, S. Rudiuk, and D. Baigl, *Langmuir* **31**, 4113 (2015).

- [41] G. B. Davies and L. Botto, *Soft Matter* **11**, 7969 (2015).
- [42] R. McGorty, J. Fung, D. Kaz, and V. N. Manoharan, *Materials Today* **13**, 34 (2010).
- [43] E. M. Furst, *PNAS* **108**, 20853 (2011).
- [44] A. D. Law, M. Auriol, D. Smith, T. S. Horozov, and D. M. A. Buzza, *Phys. Rev. Lett.* **110**, 138301 (2013).
- [45] E. Koos, *Current Opinion in Colloid & Interface Science* **19**, 575 (2014).
- [46] N. Sharifi-Mood, I. B. Liu, and K. J. Stebe, arXiv preprint arXiv:1510.05500 (2015).
- [47] N. Bizmark, M. A. Ioannidis, and D. E. Henneke, *Langmuir* **30**, 710 (2014).
- [48] J.-J. Shao, W. Lv, and Q.-H. Yang, *Advanced Materials* **26**, 5586 (2014).
- [49] K. Schwenke, L. Isa, and E. D. Gado, *Langmuir* **30**, 3069 (2014).
- [50] X.-C. Luu and A. Striolo, *The Journal of Physical Chemistry B* **118**, 13737 (2014).
- [51] J. Vermant, *Nature* **476**, 286 (2011).
- [52] A. Kumar, B. J. Park, F. Tu, and D. Lee, *Soft Matter* **9**, 6604 (2013).
- [53] S. Coertjens, P. Moldenaers, J. Vermant, and L. Isa, *Langmuir* **30**, 4289 (2014).
- [54] G. Morris, K. Hadler, and J. Cilliers, *Current Opinion in Colloid & Interface Science* **20**, 98 (2015).
- [55] M. Cavallaro, L. Botto, E. P. Lewandowski, M. Wang, and K. J. Stebe, *PNAS* **108**, 20923 (2011).
- [56] C. Blanc, D. Fedorenko, M. Gross, M. In, M. Abkarian, M. A. Gharbi, J. Fournier, P. Galatola, and M. Nobili, *Phys. Rev. Lett.* **111**, 058302 (2013).
- [57] D. Ershov, J. Sprakel, J. Appel, M. A. Cohen Stuart, and J. van der Gucht, *PNAS* **110**, 9220 (2013).
- [58] L. Yao, N. Sharifi-Mood, I. B. Liu, and K. J. Stebe, *Journal of Colloid and Interface Science* **449**, 436 (2015).
- [59] N. Sharifi-Mood, I. B. Liu, and K. J. Stebe, *Soft Matter* **11**, 6768 (2015).
- [60] I. B. Liu, N. Sharifi-Mood, and K. J. Stebe, *Phil. Trans. R. Soc. A* **374**, 20150133 (2016).
- [61] G. Morris, S. J. Neethling, and J. J. Cilliers, *Minerals Engineering* **33**, 87 (2012).
- [62] B. J. Park, C. Choi, S. Kang, K. E. Tettey, C. Lee, and D. Lee, *Langmuir* **29**, 1841 (2013).
- [63] L. Isa, N. Samudrala, and E. R. Dufresne, *Langmuir* **30**, 5057 (2014).
- [64] E. L. Sharp, H. Al-Shehri, T. S. Horozov, S. D. Stoyanov, and V. N. Paunov, *RSC Adv.* **4**, 2205 (2014).
- [65] G. Morris, K. Hadler, and J. Cilliers, *Current Opinion in Colloid & Interface Science* **20**, 98 (2015).

- [66] L. Isa, E. Amstad, K. Schwenke, E. Del Gado, P. Ilg, M. Krger, and E. Reimhult, *Soft Matter* **7**, 7663 (2011).
- [67] J. Reguera, E. Ponomarev, T. Geue, F. Stellacci, F. Bresme, and M. Moglianetti, *Nanoscale* **7**, 5665 (2015).
- [68] J. de Graaf, M. Dijkstra, and R. van Roij, *J. Chem. Phys.* **132**, 164902 (2010).
- [69] A. R. Morgan, N. Ballard, L. A. Rochford, G. Nurumbetov, T. S. Skelhon, and S. A. F. Bon, *Soft Matter* **9**, 487 (2013).
- [70] W. van der Stam, A. Gantapara, Q. A. Akkerman, G. Soligno, J. M. Meeldijk, R. van Roij, M. Dijkstra, and C. de Mello Donega, *Nanoletters* **14**, 1032 (2014).
- [71] B. Peng, G. Soligno, M. Kamp, B. de Nijs, J. de Graaf, M. Dijkstra, R. van Roij, A. van Blaaderen, and A. Imhof, *Soft Matter* **10**, 9644 (2014).
- [72] N. Ballard and S. A. F. Bon, *Journal of Colloid and Interface Science* **448**, 533 (2015).
- [73] B. J. Park and D. Lee, *Soft Matter* **8**, 7690 (2012).
- [74] B. J. Park and D. Lee, *ACS Nano* **6**, 782 (2012).
- [75] H. Evers, B. Goris, S. Bals, J. Casavola, M. de Graaf, R. van Roij, M. Dijkstra, and D. Vanmaekelbergh, *Nano Letters* **13**, 2317 (2013).
- [76] M. P. Boneschanscher, W. H. Evers, J. J. Geuchies, T. Altantzis, B. Goris, F. T. Rabouw, S. A. P. van Rossum, H. S. J. van der Zant, L. D. A. Siebbeles, G. Van Tendeloo, I. Swart, J. Hilhorst, A. V. Petukhov, S. Bals, and D. Vanmaekelbergh, *Science* **344**, 1377 (2014).
- [77] J. de Graaf, M. Dijkstra, and R. van Roij, *J. Chem. Phys.* **132**, 164902 (2010).
- [78] V. D. Nguyen, M. T. Dang, T. A. Nguyen, and P. Schall, *Journal of Physics: Condensed Matter* **28**, 043001 (2016).
- [79] R. Goldman, *Computer Aided Geometric Design* **22**, 632 (2005).
- [80] Kühnel, *Differential Geometry, Curves - Surfaces - Manifolds*, Chapter 3, American Mathematical Society, 2006.
- [81] Z. Li and T. Ngai, *Nanoscale* **5**, 1399 (2013).
- [82] O. S. Deshmukh, A. Maestro, M. H. G. Duits, D. van den Ende, M. C. Stuart, and F. Mugele, *Soft Matter* **10**, 7045 (2014).
- [83] R. W. Style, L. Isa, and E. R. Dufresne, *Soft Matter* **11**, 7412 (2015).
- [84] J. C. F. Gauss, *Principia Generalia Theoriae Figurae Fluidorum*, Dieterich, 1830.
- [85] O. Pitois and X. Chateau, *Langmuir* **18**, 9751 (2002).
- [86] D. Stamou, C. Duschl, and D. Johannsmann, *Phys. Rev. E* **62**, 5263 (2000).
- [87] P. A. Kralchevsky and N. D. Denkov, *Current Opinion in Colloid & Interface Science* **6**, 383 (2001).
- [88] K. D. Danov, B. Pouligny, and P. A. Kralchevsky, *Langmuir* **17**, 6599 (2001).

- [89] N. D. Vassileva, D. van den Ende, F. Mugele, and J. Mellema, *Langmuir* **21**, 11190 (2005).
- [90] K. D. Danov, P. A. Kralchevsky, B. N. Naydenov, and G. Brenn, *Journal of Colloid and Interface Science* **287**, 121 (2005).
- [91] K. D. Danov and P. A. Kralchevsky, *Advances in Colloid and Interface Science* **154**, 91 (2010).
- [92] G. S. Barozzi and D. Angeli, *Energy Procedia* **45**, 548 (2014).
- [93] D. Sharp, *Physica D: Nonlinear Phenomena* **12**, 3 (1984).
- [94] A. Friedman, *Notices Amer. Math. Soc.*, 854 (2000).
- [95] K. A. Brakke, *Experimental Mathematics* **1**, 141 (1992).
- [96] H. Matsui, Y. Noda, and T. Hasegawa, *Langmuir* **28**, 15450 (2012).
- [97] M. Sussman, P. Smereka, and S. Osher, *Journal of Computational Physics* **114**, 146 (1994).
- [98] S. V. Shepel and B. L. Smith, *Journal of Computational Physics* **218**, 479 (2006).
- [99] R. Scardovelli and S. Zaleski, *Annual Review of Fluid Mechanics* **31**, 567 (1999).
- [100] D. Jacqmin, *Journal of Computational Physics* **155**, 96 (1999).
- [101] S. Chen and G. D. Doolen, *Annual Review of Fluid Mechanics* **30**, 329 (1998).
- [102] M. Sega, M. Sbragaglia, S. S. Kantorovich, and A. O. Ivanov, *Soft Matter* **9**, 10092 (2013).
- [103] F. Günther, F. Janoschek, S. Frijters, and J. Harting, *Computers & Fluids* **80**, 184 (2013).
- [104] C. Semperebon, T. Krüger, and H. Kusumaatmaja, *Phys. Rev. E* **93**, 033305 (2016).
- [105] D. S. Frost and L. L. Dai, *The Journal of Chemical Physics* **136**, 084706 (2012).
- [106] S. Razavi, J. Koplik, and I. Kretzschmar, *Soft Matter* **9**, 4585 (2013).
- [107] S. Razavi, I. Kretzschmar, J. Koplik, and C. E. Colosqui, *The Journal of Chemical Physics* **140** (2014).
- [108] S. Maheshwari, M. van der Hoef, X. Zhang, and D. Lohse, *Langmuir* **32**, 11116 (2016).
- [109] C. Chen, K. Lu, J. Li, X. Dong, J. Lu, and L. Zhuang, *RSC Adv.* **4**, 6545 (2014).
- [110] T. Cheng and Y. U. Wang, *Journal of Colloid and Interface Science* **402**, 267 (2013).
- [111] L. D. G. Sigalotti, J. Troconis, E. Sira, F. Peña Polo, and J. Klapp, *Phys. Rev. E* **90**, 013021 (2014).
- [112] J. Brannick, C. Liu, T. Qian, and H. Sun, *Numerical Mathematics: Theory, Methods and Applications* **8**, 220 (2015).
- [113] S. Kirkpatrick, C. D. Gelatt, and M. P. Vecchi, *Science* **220**, 671 (1983).
- [114] J. de Graaf, M. Dijkstra, and R. van Roij, *Phys. Rev. E* **80**, 051405 (2009).

- [115] W. Beugeling, E. Kalesaki, C. Delerue, Y. M. Niquet, D. Vanmaekelbergh, and C. Morais Smith, *Nature Communications* **6**, 1 (2015).
- [116] J. de Graaf, M. Dijkstra, and R. van Roij, *Phys. Rev. E* **80**, 051405 (2009).
- [117] J. W. J. de Folter, E. M. Hutter, S. I. R. Castillo, K. E. Klop, A. P. Philipse, and W. K. Kegel, *Langmuir* **30**, 955 (2013).
- [118] M. Pang, A. J. Cairns, Y. Liu, Y. Belmabkhout, H. C. Zeng, and M. Eddaoudi, *JACS* **135**, 10234 (2013).
- [119] G. Morris, S. Neethling, and J. Cilliers, *Journal of Colloid and Interface Science* **361**, 370 (2011).
- [120] Y. Rosenfeld, *Phys. Rev. A* **42**, 5978 (1990).
- [121] D. A. Young and B. J. Alder, *The Journal of Chemical Physics* **70**, 473 (1979).
- [122] P. C. Hiemenz and R. Rajagopalan, *Principles of Colloid and Surface Chemistry*, Marcel Dekker, Inc., 3rd edition, 1997.
- [123] D. V. Talapin and E. V. Shevchenko, *Nano Letters* **7**, 1213 (2007).
- [124] M. Oettel, A. Domínguez, and S. Dietrich, *Phys. Rev. E* **71**, 051401 (2005).
- [125] N. Bowden, A. Terfort, J. Carbeck, and G. M. Whitesides, *Science* **276**, 233 (1997).
- [126] N. Bowden, I. S. Choi, B. A. Grzybowski, and G. M. Whitesides, *J. Am. Chem. Soc.* **121**, 5373 (1999).
- [127] D. B. Wolfe, A. Snead, C. Mao, N. B. Bowden, and G. M. Whitesides, *Langmuir* **19**, 2206 (2003).
- [128] M. Kamp, G. Soligno, F. Hagemans, B. Peng, A. Imhof, R. van Roij, and A. van Blaaderen, *submitted*.
- [129] S. Sacanna, M. Korpics, K. Rodriguez, L. Coln-Melndez, S.-H. Kim, D. J. Pine, and G.-R. Yi, *Nature Communications* **4**, 1688 (2013).
- [130] M. Rivetti and A. Antkowiak, *Soft Matter* **9**, 6226 (2013).
- [131] O. S. Deshmukh, D. van den Ende, M. C. Stuart, F. Mugele, and M. H. Duits, *Advances in Colloid and Interface Science* **222**, 215 (2015).
- [132] S. Karpitschka, S. Das, M. van Gorcum, H. Perrin, B. Andreotti, and J. Snoeijer, *Nature communications* **6** (2015).
- [133] H. Mehrabian, J. Harting, and J. H. Snoeijer, *Soft Matter* **12**, 1062 (2016).
- [134] S. Karpitschka, A. Pandey, L. A. Lubbers, J. H. Weijs, L. Botto, S. Das, B. Andreotti, and J. H. Snoeijer, *PNAS* **113**, 7403 (2016).
- [135] B. Andreotti, O. Baumchen, F. Boulogne, K. E. Daniels, E. R. Dufresne, H. Perrin, T. Salez, J. H. Snoeijer, and R. W. Style, *Soft Matter* **12**, 2993 (2016).

SUMMARY / SAMENVATTING

Summary: In this thesis, first we provide a theoretical introduction about fluid-fluid interfaces, and the mathematical models to describe them using a macroscopic approach. Then, we introduce a new numerical method for calculating the equilibrium shape of fluid-fluid interfaces, proving its correctness and pointing out its applicability to study systems of colloidal particles adsorbed at fluid-fluid interfaces, and droplets in contact with solid surfaces, possibly curved and with heterogeneous chemical properties.

A very important result presented in this thesis, and obtained through such a new numerical method, is the prediction that capillary interactions can drive cubic particles adsorbed at fluid-fluid interfaces to self-assembly into thermodynamically-stable honeycomb and hexagonal lattices. The capability of experimentally producing honeycomb (i.e. graphene-like) lattices of nanoparticles would be an extremely important achievement, and indeed it is currently a very hot research topic, because of the semiconductor properties that these materials would have. Other relevant results presented in this thesis, and obtained from our new numerical method, regard the equilibrium shape of droplets in contact with complex substrates. In particular, we study the equilibrium position of a droplet on a bullet-shaped particle, predicting that the droplet position can shift from the long side of the particle to its flat end just by slightly tuning the bullet geometry. The ability of tuning the droplet position on the particle surface is an important result for the synthesis of odd-shaped colloidal particles, which is a very active field of research. Then, we also study the equilibrium shape of a droplet wetting a flat solid substrate with an ellipsoidal patch with higher wettability than the remaining substrate, showing the different behavior of the droplet with respect to the aspect ratio of the patch shape.

Samenvatting: Ten eerste geven we in deze thesis een theoretische introductie over vloeistof-vloeistofgrensvlakken, en de wiskundige modellen om deze te omschrijven met het gebruik van een macroscopische benadering. Vervolgens introduceren we een nieuwe numerieke methode om de evenwichtsvorm van vloeistof-vloeistofgrensvlakken te berekenen, de juistheid te controleren en te wijzen op de toepasbaarheid om systemen van colloïdale deeltjes geadsorbeerd door vloeistof-vloeistofgrensvlakken, en druppels in contact met solide oppervlakten, mogelijk gebogen en met heterogene chemische eigenschappen, te bestuderen.

Een zeer belangrijk resultaat gepresenteerd in deze thesis, en door een zodanig nieuwe numerieke methode verkregen, is de verwachting dat capillaire wisselwerkingen, kubieke deeltjes geabsorbeerd in vloeistof-vloeistofgrensvlakken, kunnen induceren tot zelfassemblage in thermodynamisch stabiele honingraat en zeshoekige roosters. De capaciteit van het experimenteel produceren van honingraat (d.w.z. grafeen-achtige) roosters van nanodeeltjes zou een extreem belangrijke prestatie zijn en is momenteel een hot topic in de wetenschap, door de halfgeleider eigenschappen die deze materialen zouden hebben.

Andere relevante resultaten in deze thesis, en verkregen van onze nieuwe numerieke method, betreft de evenwichtsvorm van druppels in contact met complexe substraten. In het bijzonder, bestuderen we de evenwichtspositie van een druppel op een kogel-vormig deeltje, en voorspellen we dat de druppel positie kan verschuiven van de lange zijde van het deeltje naar het platte uiteinde door het enigzins afstemmen van de kogel vorm. De mogelijkheid van het afstemmen van de druppel positie op het deeltjesoppervlak is een belangrijk resultaat voor de synthese van vreemd gevormde colloïdale deeltjes, wat een zeer actief veld van onderzoek is.

Vervolgens, bestuderen we de evenwichtsvorm van een deeltje dat een platte vaste substraat met een ellipsvormige plek met hogere bevochtigbaarheid dan het resterende substraat bevochtigt, waarmee het verschillende gedrag van de druppel met betrekking tot de beeldvorming van de vlek vorm aangetoond wordt.ⁱ

ⁱThanks to Eline van der Drift for helping with the translation.

ACKNOWLEDGMENTS

To begin, I would like to thank my supervisor, René (van Roij), first of all for giving me the opportunity of doing this PhD, and then for being an excellent mentor during these four years of PhD, both from a professional and human point of view, and for the extremely high quality of his comments and suggestions, which have always helped me to improve my research and work.

Then, I would like to thank my co-supervisor, Marjolein (Dijkstra), for her always expert advice and useful suggestions, and for helping in connecting my theoretical results with experimental ongoing works, leading to many fruitful collaborations. I would also like to thank the supervisor of my Master thesis, Giorgio (Pastore), for directing me in the first place toward the Soft Matter community here in Utrecht, as I would have not been here without his advice.

Then, I would like to thank the coordinator, Peter (Lang), and all the other PIs and the administrative staff of the SOMATAI (SOft Matter AT Aqueous Interfaces), for putting together this Marie Curie Initial Training Network, which financed the major part of my PhD, and for organizing for the SOMATAI fellows many useful and interesting workshops, schools and conferences in the past four years, spread across half Europe. Of course, a special thank to all the SOMATAI fellows, for all the fun meetings and nice time spent together.

Then, I want to thank all the colleagues, professors and administrative staff at the Institute for Theoretical Physics, Utrecht University, which is the where my PhD activity has been mainly located, and all the colleagues and professors in the Soft Matter group of the University of Utrecht.

I would like to thank Ward (van der Stam), Anjan (Gantapara), Quinten (Akkerman), Johannes (Meeldijk) and Celso (de Mello Donega) for a very nice collaboration on the adsorption of bipyramid-shaped particles at a fluid-fluid interface, where I contributed with theoretical calculations for the adsorption energy us-

ing the Triangular Tessellation technique, and the results have been published in *Nano Letters* in 2014. I also contributed with analogous calculations for a very interesting work about the adsorption of droplets on bullet-shaped particles, published in *Soft Matter* in 2014, and I would like to thank Bo (Peng), Marlous (Kamp), Bart (de Nijs), Joost (de Graaf), Alfons (van Blaaderen) and Arnout (Imhof) for this collaboration. Then I would like to thank Marlous (Kamp), Fabian (Hagemans), Bo (Peng), Arnout (Imhof) and Alfons (van Blaaderen) for a new collaboration on this same topic, submitted for a publications in 2016, where new and very relevant theoretical and experimental insights have been presented. I would like to thank Mark (Vis), Joeri (Opdam), Ingo (van t Oor), Hans (Tromp) and Ben (Erne) for a very nice collaboration, published in *ACS Macro Letters* in 2015, where the adsorption of nano-plates at water-water interfaces has been exploited to stabilize experimental water-in-water emulsions, and I contributed to this work with numerical predictions obtained from the method introduced in this thesis. I would like to thank Ivan (Devic), Xuehua (Zhang) and Detlef (Lohse) for a very interesting collaboration about droplets wetting elliptical patches of enhanced lyophilicity, where Ivan and me compared the theoretical predictions obtained from the numerical method introduced in this thesis, and obtained exploiting the free-software Surface Evolver. These results are likely to be submitted for a publication in the 2016/2017 winter.

Finally, I would like to thank all the colleagues met during meetings, conferences, schools and workshops, for all the useful discussions we had. In particular, Leon (Bremer), Remco (Tuinier) and Alvaro (Gonzalez Garcia) from DSM in Geleen, then Lucio (Isa), Michele (Zanini), Ivan (Lesov) from ETH Zurich, Ciro (Semprebon) from Durham University, Stefano (Cappelli) from TU Eindhoven.

Of course, I would like to thank my family, and my parents Francesco and Antonia in particular, for always supporting me.

Finally, as these last four years have been an incredible experience also from an human point of view and outside university, I would like to thank all the wonderful friends that I have met during this time. Thank you all for making my last four years such an amazing time!

AUTHOR'S PUBLICATIONS

The work contained in this thesis is (partly) based on the following publicationsⁱ of the author:

- **G. Soligno**, M. Dijkstra and R. van Roij, *The Equilibrium Shape of Fluid-Fluid Interfaces: Derivation and a New Numerical Method for the Young's and Young-Laplace Equations*, *The Journal of Chemical Physics* **141**, 244702 (2014);
- **G. Soligno**, M. Dijkstra and R. van Roij, *Self-assembly of Cubes into 2D Hexagonal and Honeycomb Lattices by Hexapolar Capillary Interactions*, *Physical Review Letters* **116**, 258001 (2016) [Editors' suggestion; Featured of the cover];



ⁱSee also next page.

- M. Kamp*, **G. Soligno***, F. Hagemans*, B. Peng, A. Imhof, R. van Roij and A. van Blaaderen, *Regiospecific Nucleation and Growth of Silane Coupling Agent Droplets onto Colloidal Particles*, [submitted](#) [*These authors equally contributed];
- I. Devic*, **G. Soligno***, M. Dijkstra, R. van Roij, X. Zhang and D. Lohse *Sessile Nanodroplets on Elliptical Patches of Enhanced Lyophobicity*, [in preparation](#) [*These authors equally contributed];
- **G. Soligno**, M. Dijkstra and R. van Roij, *Capillary Interactions and Self-assembly of Possibly-truncated Cubes at Fluid-Fluid Interfaces*, [in preparation](#);
- **G. Soligno**, M. Dijkstra and R. van Roij, *How the Linear Approximation of the Young-Laplace Equation Affects the Prediction of Capillary Forces*, [in preparation](#).

Other publications of the author are:

- W. van der Stam, A. P. Gantapara, Q. A. Akkerman, **G. Soligno**, J. D. Meeldijk, R. van Roij, M. Dijkstra and C. de Mello Donega, *Self-Assembly of Colloidal Hexagonal Bipyramid- and Bifrustum-Shaped ZnS Nanocrystals into Two-Dimensional Superstructures*, [Nano Letters](#) **14**, 1032 (2014);
- B. Peng, **G. Soligno**, M. Kamp, B. van Nijs, J. de Graaf, M. Dijkstra, R. van Roij, A. van Blaaderen and A. Imhof, *Site-specific growth of polymers on silica rods*, [Soft Matter](#) **10**, 9644 (2014);
- M. Vis, J. Opdam, I. S. J. vant Oor, **G. Soligno**, R. van Roij, R. H. Tromp and B. H. Ern e, *Water-in-Water Emulsions Stabilized by Nanoplates*, [ACS Macro Letters](#) **4**, 965 (2015).

AUTHOR'S PRESENTATIONS

The work contained in this thesis has been (partly) presented by the author with **oral presentations** at the following national and international conferences:

- *Capillary-induced Self-assembly of Particles Adsorbed at Fluid-Fluid Interfaces (20 min)*, SOMATAI Conference, Crete, 29th May-3rd June 2016;
- *Self-Assembly of Cubes into 2D Hexagonal and Honeycomb Lattices by Hexapolar Capillary Interactions (20 min)*, SACS Conference, San Sebastian, 25th-27th October 2016;
- *Self-Assembly of Cubes into 2D Hexagonal and Honeycomb Lattices by Hexapolar Capillary Interactions (15 min)*, Physics@FOM, Veldhoven, 17th-18th January 2017;

and with **poster presentations** at the following conferences and symposia:

- Trends in Theory, 16th-17th May 2013, Dalfsen;
- International Soft Matter Conference, 15th-19th September 2013, Rome;
- Physics@FOM, 21st-22nd January 2014, Veldhoven;
- Liquid Matter Conference, 21st-25th July 2014, Lisbon;
- Physics@FOM, 20th-21st January 2015, Veldhoven;
- Trends in Theory, 28th-29th May 2015, Dalfsen.

ABOUT THE AUTHOR

Giuseppe was born the 22nd of September 1986 in Venosa, a town in the south of Italy already known for giving birth to the Roman poet Horace. In 1987, Giuseppe moved with his family in the north-east of Italy, close to Venice, where he lived until he was 18 years old, and then he moved to Trieste (Italy) for his university studies. In Trieste, Giuseppe lived six years, and during this period he achieved first a Bachelor in Physics, and then a Master in Theoretical Physics with full marks and *cum laude*, i.e. the highest honor in the Italian university system. For his Master thesis work, carried out under the supervision of Prof. Dr. Giorgio Pastore, Giuseppe used theoretical and numerical models to study hydrodynamic interactions in colloidal systems. In February 2013, Giuseppe moved to Utrecht (the Netherlands) to start a PhD of four years under the supervision of Prof. Dr. René van Roij and the co-supervision of Prof. Dr. Marjolein Dijkstra. During his PhD, Giuseppe developed a new numerical method to calculate the equilibrium shape of fluid-fluid interfaces. Among the many results he obtained exploiting this method, his predictions for the self-assembly of cubes adsorbed at fluid-fluid interfaces into hexagonal and honeycomb lattices have been featured on the cover of the 24th of June 2016 issue of Physical Review Letters, one of the most prestigious journals in Physics. The 23rd of January 2017 Giuseppe will defend his PhD thesis.

